AN EFFICIENT UNIT CELL BASED NUMERICAL MODEL FOR CONTINUUM REPRESENTATION OF FABRIC SYSTEMS

by

Ali Shahkarami Noori

B.Sc., Sharif University of Technology, 1995
M.A.Sc., The University of British Columbia, 1999

A THESIS SUBMITTED IN PARTIAL FULFILLMENT OF THE REQUIREMENTS FOR THE DEGREE OF

DOCTOR OF PHILOSOPHY

in

THE FACULTY OF GRADUATE STUDIES

(Civil Engineering)

THE UNIVERSITY OF BRITISH COLUMBIA

July 2006

Abstract

Flexible personal armour systems are used everyday by police forces, military personnel, paramedics, and others in their line of duty. The introduction of high-performance polymer-based fibres and yarns has paved the way for the design of lightweight, yet strong body armours that can defeat a wide range of threats. However, despite the relatively high cost of materials used in bullet resistant vests, their design is completely based on experiments. Addition of simulation capability to the design process of bullet resistant vests should introduce significant savings in the time and cost associated with this activity and lead to more optimized armour systems.

A novel numerical approach is introduced in this thesis that is comprised of two distinct numerical models developed in parallel and verified against each other. Experimental data are used to characterize the behaviour of fabrics and to validate the predictions of the numerical models. This combination of the numerical and experimental efforts has resulted in a unique modelling technique to capture the deformational response of fabric panels.

A detailed 3D model of the fabric unit cell is created to investigate the interaction of the crossing yarns under extensional in-plane displacements. This continuum-based model explicitly considers the geometry of the yarns as an assembly of solid and bar elements and upon successful calibration, predicts the response of the fabric unit cell under the applied displacements.

An efficient 2D shell crossover model is also developed that implicitly incorporates the extensional and shearing response of the crossing yarns. The governing constitutive equations for this shell element are derived considering sinusoidal compressible yarns subjected to symmetric displacements in the fabric's plane. The efficient shell elements are used to create finite element models of fabric under static and dynamic loading scenarios.

Simulations of single and multi-ply fabric targets subjected to impact are carried out and the model predictions are compared against the data from instrumented ballistic experiments. The model is found to be successful in capturing the deformational behaviour of fabric targets. Parametric analysis is performed on various geometric and mechanical properties of the fabric to investigate the sensitivity of its response to such values. Recommendations are made for setting up models of fabric to be used in industrial design process, in order to make the approach available to armour designers.

Table of Contents

List of Tables

List of Figures

List of Symbols

Chapter 2 – Experimental Data

a ..... Fitting constant in the proposed compression model

b ..... Fitting constant in the proposed compression model

d_c ..... Transverse compressive deformation of the fabric

m ..... Mass of fibres

n ..... The exponent of the proposed compression model

p ..... Transverse pressure applied to the fabric

p_0 ..... Defined as "latent pressure" at zero pressure

t_0 ..... Initial fabric thickness

v ..... Current volume of the fabric

v_0 ..... Initial volume of the fabric

A ..... Loading area in the transverse compression tests

A_d ..... Areal density of the fabric

E ..... Elastic modulus of the fibres

F_c ..... Transverse compressive force Applied to the fabric

K ..... A dimensionless constant (see Section 2.2.2)

K' ..... Constant used in the transverse compression model (see Section 2.2.2)

K'' ..... A fitting constant in the transverse compression model developed in this study

P ..... Pressure applied to the fabric in the proposed transverse compression model

V_a ..... Maximum available fibre volume fraction

V_f ..... Fibre volume fraction of the fabric

V_{min} ..... Minimum compressed volume of the fabric in compression

V_0 ..... Initial fibre volume fraction

V ..... Current volume of the fabric in compression

β ..... A constant determined empirically

γ ..... Exponent in the general pressure-volume relationship for the fabrics

ρ ..... Density of fibres

σ_b ..... Applied bulk stress of the fabric

Chapter 3 – 3D Fabric Crossover Model

a_E ..... Model parameter for the transverse modulus of the solid elements

b_E ..... Model parameter for the transverse modulus of the solid elements

d_1 ..... Normal in-plane displacement applied to the fabric unit cell in the local 1-direction (warp)

d_2 ..... Normal in-plane displacement applied to the fabric unit cell in the local 2-direction (weft)

$\underline{x}$ ..... Material coordinate system in the deformed state

A^n ..... Cross-sectional area of a solid element perpendicular to the yarn axial direction at time-step n

A^0 ..... Initial cross-sectional area of a solid element perpendicular to the yarn axial direction

C ..... Speed of sound wave in the material

E_a ..... Initial modulus of a solid element in the axial yarn direction

E_c ..... Upper limit of the transverse modulus of the solid elements

E_1^n ..... Modulus in the yarn axial direction at time-step n

E_2^n ..... Secant modulus of a solid element in the transverse direction (local 2-dir.) at time-step n

E_3^n ..... Secant modulus of a solid element in the transverse direction (local 3-dir.) at time-step n

$\underline{F}$ ..... Deformation gradient matrix

G_i ..... Shear modulus of the solid element material in the plane perpendicular to i local axis

J ..... Jacobian, defined as the determinant of $\underline{F}$

K_G ..... Reduction factor for the shear modulus of the solid elements

K_r ..... Reduction factor for the transverse yarn modulus when subjected to tension

L ..... Nominal length of an element in the finite element mesh

L^n ..... Length of a solid element in the yarn axial direction at time-step n

L^0 ..... Initial length of a solid element in the yarn axial direction

V^n ..... Volume of a solid element at time-step n

V^0 ..... Initial Volume of a solid element

V_c ..... Solid element volume corresponding to the maximum transverse modulus

V_f^n ..... Yarn's fibre volume fraction at time-step n

V_f^0 ..... Initial fibre volume fraction of the yarn

$\underline{X}$ ..... Material coordinate system in the undeformed state

ε^n ..... Logarithmic normal strain in the yarn axial direction at time-step n

ε_f ..... Instantaneous strain to failure of the yarn

σ_i^n ..... Component i of the solid element stress vector at time-step n

Δt ..... Time step size in explicit finite element analysis

Chapter 4 – 2D Shell Crossover Model

$( )_i$ ..... Quantity referring to warp ($i = 1$) and weft ($i = 2$)

a ..... Constant used in the definition of the transverse compression model

b ..... Constant used in the definition of the transverse compression model

cr_i ..... Crimp value of yarn i of the unit cell

d_{c_i} ..... Transverse compression of yarn i of the unit cell

d_i ..... Extensional in-plane displacement applied to the fabric unit cell in i direction

f_1 ..... Objective function obtained from the equilibrium of yarn contact forces

f_2 ..... Objective function obtained from the compatibility of the distance between the yarn centrelines

g ..... Transverse gap between the warp and weft yarns of a unit cell

h_i ..... Centreline height of yarn i at the centre of the unit cell

h_{0_i} ..... Initial centreline height of yarn i at the centre of the unit cell

m_i ..... Yarn count in i direction (threads per unit length)

p ..... In-plane gap between neighbouring parallel yarns

$\underline{q_i}^n$ ..... Vector defining the i material direction at time step n

$q_{i_x}{}^n$ and $q_{i_y}{}^n$ ..... Components of the material vector i in the local x and y directions at time step n

u ..... In-plane normal distance between parallel yarns

u_1 ..... In-plane normal distance between parallel yarns at the onset of parallel yarn contact

u_2 ..... In-plane normal distance between parallel yarns at shear locking

w_i ..... Unit cell length the i direction

x, y, z ..... Local coordinate system of the representative shell element

x_i ..... Unit cell coordinate axis along yarn i

z_i ..... Unit cell coordinate axis perpendicular to the fabric plane

A_p ..... Equivalent compacted cross-sectional area of a yarn

A_s ..... Solid cross-sectional area of a yarn

A_{sh} ..... Cross-sectional area of the shell element representing the fabric unit cell

A_{si} ..... Solid cross-sectional area of yarn i of the unit cell

E_i ..... Elastic modulus of yarn i of the unit cell

F_{c_i} ..... Contact force of yarn i of the unit cell

$\underline{F}^n$ ..... Incremental deformation gradient at time step n

G_1 ..... Initial shear modulus of the unit cell

G_2 ..... Unit cell shear modulus for strains beyond shear locking

$\underline{I}$ ..... 2x2 unit matrix

$\underline{J}$ ..... Jacobian matrix, with components $J_{kl} = \frac{\partial f_k}{\partial h_l}$ (where $k = 1,2$ and $l = 1,2$)

L ..... Side-length of the square fabric sample used in the picture-frame shear test

T_i ..... Tension in yarn i of the unit cell

S_i ..... Length of yarn i of the unit cell

S_{0i} ..... Initial crimped length of yarn i of the unit cell

α_i ..... Slope between the fabric's plane and the centreline of yarn i at the edge of the unit cell

β ..... Instantaneous in-plane angle between the warp and weft yarns

β_0 ..... Initial in-plane angle between the warp and weft yarns (90° for plain weave fabric)

β_1 ..... Warp-to-weft angle corresponding to the onset of contact between parallel yarns in a sheared fabric

β_2 ..... Warp-to-weft angle corresponding to the onset of shear locking (full compaction of parallel yarns) in a sheared fabric

γ_1 ..... Shear strain corresponding to the onset of contact between parallel yarns

γ_2 ..... Shear strain corresponding to the onset of shear locking

λ_i^n ..... Stretch increment in the i material direction at time step n

θ_i^n ..... Angle between the material vector i and the local x axes at time step n

$\underline{\sigma_i}^n$ ..... Stress matrix obtained from the yarn in the i material direction at time step n

$\underline{\overline{\sigma}_i}^n$ ..... Stress matrix obtained from the yarn in the i material direction at time step n, transformed into the local coordinate system

$\underline{\sigma_{avg}}^n$ ..... Total average stress matrix in at time step n

$\Delta\varepsilon_{i11}^n$ ..... Element on the row 1 and column 1 of the i material direction strain increment matrix at time step n

$\Delta\varepsilon_x^n$ ..... Normal strain increment in the local x-direction at time step n

$\Delta\varepsilon_y^n$ ..... Normal strain increment in the local y-direction at time step n

$\Delta\varepsilon_{xy}^n$ ..... Shear strain increment in the local xy-direction at time step n

$\underline{\Delta\varepsilon}^n$ ..... Strain increment matrix at time step n

$\underline{\Delta\varepsilon_i}^n$ ..... Strain increment matrix in the i material direction at time step n

Λ_i^n ..... Total stretch in the i material direction at time step n

$\underline{\Theta_i}^n$ ..... Transformation matrix between the local and material coordinate systems at time step n

Chapter 5 – Ballistic Response of Fabric Panels

${}^n d_c$ ..... Total transverse compression of an n-ply fabric specimen

K_{ff} ..... Spring stiffness representing the inter-ply fabric deformation

K_{fm} ..... Spring stiffness representing the deformation resulting from the interaction of the fabric and the loading cell

d_{ff} ..... Inter-ply fabric transverse deformation

d_{fm} ..... Transverse deformation resulting from the interaction of the fabric and the loading cell

N ..... Number of layer in a multi-ply fabric pack

C ..... Speed of sound in material

E ..... Yarn elastic modulus

ρ ..... Yarn material density

k ..... Ratio of warp to weft strain applied in the biaxial extension experiments (see Section 5.3)

Acknowledgements

This thesis was made possible with the unlimited support and guidance of my supervisors, especially Dr. Reza Vaziri, to whom I am deeply grateful. Thank you Reza, for the opportunity and for trusting me throughout this journey. I would also like to thank Dr. Anoush Poursartip who supported me over the years and helped me along when I needed it the most. Many thanks go to the other members of my supervisory committee, Dr. Goran Fernlund and Dr. Terje Haukaas, for their role throughout the course of this thesis.

I would like to thank the Natural Sciences and Engineering Research Council of Canada, Defence Research and Development Canada, DuPont Advanced Fiber Systems Inc., Pacific Safety Products Inc., and The University of British Columbia for the financial support of this project.

I shared this experience with many other people, to whom I am thankful. I would like to thank Dr. Elvis Cepus, Mr. Roger Bennett and Ms. Ingrid Kongshavn who have been instrumental in exposing me to the world of ballistic experiments. I would like to thank all the past and current members of the Composites Group for their support and friendship, especially Dr. Anthony Floyd and Mr. Mehdi Haghshenas for their friendship and for the endless technical discussions.

And finally I would like to thank my family, specially my mother, who has always believed in me and given me her unconditional love.

Dedication

To my mother, who instilled in me the determination to follow my dreams, and devoted her life to ensure I get a chance to do so.

And to my late father, who always believed in me and is greatly missed.

CHAPTER 1 - DYNAMIC ANALYSIS OF FABRIC SYSTEMS

Modelling the ballistic response of fabrics has been the focus of many studies over the years. In this chapter, a review of the various modelling approaches undertaken to capture the dynamic behaviour of fabrics is provided and an overall picture of the evolution of body armour analysis and design is sketched. Following this introduction, the goals of the current study is discussed and the overall modelling methodology and its several components are introduced.

1.1 MODELLING BALLISTIC FABRICS – A HISTORIC BACKGROUND

Fabric-based body armour systems are used by police officers, military personnel and many others to reduce the risk of threats they are exposed to everyday in their line of duty. Historically, body armours were made from metals and mainly used by soldiers to provide protection in the battles of ancient wars. With the advancement in weapons and the rising need to defeat these harmful threats, the metallic body armours grew bigger and heavier, to the point that they were almost impractical, as they critically limited the mobility and flexibility of the soldiers (for a full review of the armour history,

see [1]). Introduction of soft personal body armours in the form used today was made possible by the introduction of high-performance fibres and fabrics in the early 1970's. Since then, many studies have been focused on the understanding of the complex mechanical behaviour of woven fabrics and on quantifying their performance as the building block of fabric-based armour systems. However, it is only fair to say that the knowledge of such behaviour is still under-developed and there are numerous avenues to be explored on the dynamic behaviour of woven fabrics.

The designers of bullet-proof vests follow strict guidelines to demonstrate the capability of the armour to defeat the threats they are designed for. The design process is highly experiment-based despite the high price of the material used in the bullet-proof vests. This is perhaps due to the absence of a robust numerical tool to analyse the ballistic performance of fabrics. Availability of a reliable fabric model can help the designers to save the cost of material by redirecting the design and manufacturing in a desired direction, as well as by reducing the time required to demonstrate the capability of their design in defeating a set of preconceived threats.

Prediction of the complex behaviour of fabrics under dynamic loading scenarios has been the centre of many studies over the years. Fabrics used in a variety of military and civil applications pose a certain challenge for the designers due to their specific non-homogeneity and multifaceted interaction of their components. The ever-increasing demand for high-performance fabrics over the past few decades has revealed the immaturity of the design tools and inability to fully optimize the armour systems. This has created much interest

over the past decades in exploring various aspects of the fabric's ballistic performance. The studies geared towards predicting the dynamic behaviour of fabrics can be divided into analytical and numerical approaches. Since this thesis is focused on the development of a new computational approach, only a review of the relevant numerical approaches in the literature is presented in this chapter.

The numerical models developed to capture the response of fabric systems has evolved significantly over the past decades. However, predicting the behaviour of these constantly-evolving lightweight structures under high-speed impact is a formidable task. Maturing of finite element analysis methodology along with the massive improvement of the available computational resources in the form of faster computers and large storage devices have enabled the modellers to incorporate more details of the structure and materials into their consideration. This has resulted in the development of different generations of fabric models, categorized here as Discrete models and Unit-cell Continuum models, discussed separately below.

1.1.1 Discrete models

The Discrete modelling technique is one of the earliest approaches considering the fabric as an assembly of discrete masses connected to each other by cable or spring elements (see Figure 1 - 1). This net-like mass-spring approximation of the fabrics provided a simple and efficient platform for studying the dynamic behaviour of fabric systems. Although many different versions of discrete models have been developed over the years, they all share a very similar mathematical basis. While spatial characteristics of the fabric are more or less at

the discretion of the user, the temporal discretization is controlled by the convergence of the mathematical solution of the physical system. Stable results are obtained only if the time step size is smaller than the one needed for the strain wave to travel the smallest element nominal dimension in the finite element mesh (see Section 3.3). Upon impact, nodes directly in contact with the projectile start to move with it, and the equilibrium of the nodes are sought based on the impulse-momentum equations. At each time-step, the coordinates of the nodes are updated from their velocities and the tensile forces in the cables are determined. The calculations are completed by determining the new nodal velocities and the analysis moves to the next time-step. The same procedure is followed for the duration of the impact event. The numerical model allows the user to obtain various target and projectile information during the event and gain a better understanding of the mechanics of the fabric deformation.

Work of Roylance et al. [2] was fundamental in introducing the discretized mass-spring model of fabrics and more or less transformed the ballistic textile industry to focus more efforts on this modelling approach. For this purpose, effects of the projectile geometry, yarn bending, slippage at the crossovers, etc. were initially ignored. Roylance et al. [2, 3] used this model to investigate the energy absorption mechanisms of fabric panels and concluded that despite the limitations of the approach, it is a useful tool to study the behaviour of fabric systems and can be used in the preliminary design of armour systems.

After Roylance et al. [2], many other researchers used the discrete modelling approach to study various characteristics of fabric panels. Some examples of

such studies can be found in the works of Billon and Robinson [4], and Johnson et al. [5]. Tan, Shim and co-workers [6-11] extensively used the discrete mass-cable model to study the effects of fabric crimp, boundary conditions, projectile obliquity and a variety of other factors on the behaviour of fabric targets. Shahkarami et al. [1, 12] developed a similar pin-jointed mass-string model for impact simulation of fabric, called TEXIM, and studied the effect of fabric boundary conditions on the overall energy absorption of the system and perforation of the projectile. TEXIM was later used by Novotny et al. [13, 14] to study the behaviour of hybrid panels, comprised of two different materials, and their possible advantages over ordinary monolithic fabric packs in absorbing the impact energy.

The major shortcoming of the discrete models is their failure to capture the biaxial nature of the fabric response. To overcome this deficiency, some researchers have introduced crimped yarns with a zigzag profile where the crossing yarns interact during the deformation. Cunniff, Ting and co-workers [15, 16] developed a numerical model where the warp and weft yarns were non-coplanar to capture the crimp in the yarns. The warp and weft yarn coupling was then incorporated via spring elements. Tan and Ching [17] presented a discrete model where the fabric was created from a network of linear bar elements, with the warp and weft yarns initially in contact with, but not jointed to, one another. This model allowed for the consideration of yarn crimp, as well as the sliding contact between the crossing yarns.

All the modelling attempts using the discrete approach, some of which discussed above, have tremendously contributed to the general knowledge on

the ballistic behaviour of fabrics. However, the discrete modelling techniques are oversimplified for the current needs of the high-performance fabric industry and are abandoned by many scientists in favour of more complex models, discussed in the next section.

1.1.2 Unit-cell continuum models

The unit cell models are generally based on a continuum representation of the fabrics. Based on the scale of such representation, different modelling techniques are formulized (see Figure 1 - 2). Some 3D models of fabric and fabric unit cells usually incorporate the weave details at the yarn level in their structure definition. In these models, individual yarns are meshed based on their respective geometry inside the weave, and proper material properties are assigned to them. The complexity of these models and the level of structural details they consider make them an excellent tool for analysing the deformational behaviour of fabric unit cells. However, the explicit representation of the yarns and the amount of details they consider eventually leads to an extreme inefficiency, up to a point that they become impractical for real-size problems.

Shockey et al. [18, 19] presented the results of their study on the fabric barriers to contain turbine engine fragments of the aircrafts. To complement the extensive experimental effort carried out in that study, a detailed 3D model and a simple shell model were also developed. The detailed 3D model was perhaps one of the first attempts to capture the deformational response of the fabrics by explicitly modelling the yarns in the weave. In a separate study, Duan et al. [20-23] recently used the same modelling approach to investigate the influence of

intra-ply friction (i.e. friction between the crossing yarns) on the energy absorption characteristics of fabric panels. Similar modelling technique was used by Boisse and co-workers [24-27], Peng and Cao [28], and others. In all these cases, the 3D unit cell model of the fabric or fabric composites appeared to be very inefficient and limited to studying only the fabric unit cell or fabric specimen with very small dimensions.

To overcome the prohibiting inefficiency of the 3D model, shell-based unit cell models were developed for simulation of fabrics in ballistic impact and for the analysis of woven composites forming process. In this approach, the fabric unit cell is replaced by a representative shell element, whose material constitutive relationship is a representation of the orthotropic fabric behaviour in a smeared approach. The material model developed for the shell element can be as simple as a basic orthotropic model (equivalent of the discrete pin-jointed model) to a fully inclusive mechanistic model of the fabric crossover. As a result, a varying level of complexity can be achieved by these models which would inversely affect their efficiency. Examples of such models include the work by Tabiei and Ivanov [29, 30], King et al. [31-33], Lim et al. [34], Tanov and Brueggert [35, 36], Buet-Gautier and Boisse [37], Xue et al. [38], Luo [39], Stubbs [40], Simons and co-workers [18, 41], etc.

Overall, the unit cell fabric modelling approaches are used more widely in a variety of applications. The efficient shell-based models appear to be extremely versatile in terms of their applicability and efficiency. The shell elements can be formulated to be as simple as the discrete bar models, or almost as comprehensive as the 3D solid models, thus offering a wide spectrum of

options to the user. As a result, the shell-based continuum models currently seem to be a perfect modelling approach for a wide range of applications.

1.2 CURRENT STATE-OF-THE-ART

The need for a robust numerical model that can truly capture the realistic response of the fabric structure without sacrificing efficiency still exists. Despite the development of various modelling techniques to date, a robust numerical approach that is efficient and can incorporate various deformational and failure mechanisms of fabrics is still lacking in the engineering community. The pool of available ballistic experimental data on various fabric types and target configurations is extremely large, leading to a vast discontinuity between the experimental fabric research and the advancement of the numerical modelling techniques. However, the significant evolution of the fabric models over the past decade has the promise of the numerical models that are an inseparable part of the armour analysis and design process in the near future.

1.3 RESEARCH OBJECTIVES

The main objective of this study is to develop an efficient and robust numerical analysis tool to aid with the design of fabric-based personal protective systems. The availability of such predictive tools would be useful for the engineers and designers of body armours to reduce the time and material costs involved in arriving at an optimum solution.

To achieve the above goals, this work intends to link the valuable experimental data on the mechanical behaviour of fabrics under a variety of loading scenarios to the numerical analysis, both in terms of providing input values and for validation purposes. The computational study established is aimed to be fully exercised, in order to better understand the characteristics of the fabric targets and to contribute to the current body of knowledge on their ballistic behaviour and the complex mechanics of bullet-proof vests.

1.4 METHODOLOGY

The work presented in this thesis is an effort to establish a new technique to evaluate the performance of fabrics under quasi-static and dynamic loadings. The methodology proposed is a mix of numerical and experimental effort, shown in Figure 1 - 3. The main component of the current approach is the highly efficient shell element that represents a fabric unit-cell, capturing the response of a single yarn crossover in the case of plain weave fabric. In parallel to the 2D shell model, a more detailed finite element representation of the fabric unit cell is provided through a 3D solid-based model of the yarns in a single fabric crossover. This 3D crossover model is used to provide some of the input variables to the 2D shell crossover model. Moreover, it serves to verify the 2D shell's predictions of the fabric biaxial response. In doing so, detailed experimental measurements are used to provide the information needed by these two models and for validation of their predictions. The verification of the 2D shell crossover response using the 3D crossover model predictions and its validation using the experimental data would provide confidence in the

accuracy of the numerical model proposed and makes it a useful tool to create detailed multi-ply models of fabric subjected to different loading scenarios in a variety of applications.

The main tasks that are envisaged to achieve the objectives of this study are as follows:

- Introduce a new constitutive model for the yarn material represented by solid elements in the 3D model of fabric crossover. This constitutive model would be capable of capturing the transverse mechanical response of the yarns woven into a fabric as they interact with each other under the applied loading.

- Formulate the mechanical response of a single yarn crossover under biaxial and shear loading conditions and implement this mathematical representation into a single shell element that represents an individual fabric unit cell.

- Use the developed shell elements to create real-size models of fabrics and study their behaviour under quasi-static and dynamic loadings. This task would not only serve as a validation for the 2D shell crossover model, but it would also provide more insight into the complex behaviour of fabrics.

- Utilize the shell elements to perform parametric studies, in order to identify the sensitivity of the fabric behaviour to a variety of geometrical and mechanical properties. This would help identify the influencing factors affecting the energy absorption and deformational characteristics

of fabric structures and facilitate the design of more efficient fabric systems.

1.5 OUTLINE OF THE THESIS

This thesis consists of seven chapters that in addition to the current first chapter, provides the experimental data (Chapter 2), the details of the model development, verification and validation (Chapters 3 to 5), the sensitivity analysis and case-studies (Chapter 6), and the conclusions and future work (Chapter 7).

Chapter 2 provides the information regarding the experimental data used throughout the thesis. This chapter covers some general information on the material that is the focus of this study, along with the methodology used to measure the transverse compression of the fabrics (tests performed by Kongshavn [42]). A phenomenological model is developed to capture the fabric's transverse compression behaviour. The ballistic impact experiments (performed by Cepus [42]) are introduced and the basics of the data acquisition system, ELVS (Enhanced Laser Velocity System) are briefly discussed.

Chapter 3 presents the development of the 3D solid crossover model. The components of the 3D crossover model are presented and the simplifying assumptions made to formulate the axial and transverse mechanical behaviour of the yarns in a single fabric crossover are provided. The biaxial nature of the fabric crossover extensional response is discussed and the interaction of the yarns during such loading is studied.

Chapter 4 discusses the details of the 2D shell crossover model development, along with its formulation and implementation into a shell element's material constitutive model. The predictions of the shell elements are then verified against those of the 3D solid model and the pin-jointed cable model on a unit cell and fabric level under biaxial and ballistic impact loadings.

Chapter 5 presents the validation of the static and dynamic response predictions of the 2D shell crossover model through comparisons with the relevant experimental data. The efficiencies of the model are highlighted and its limitations are identified by comparing the numerical simulations to fabric biaxial extension and ballistic impact data.

Chapter 6 presents the sensitivity analysis performed on a variety of fabric's geometrical and mechanical properties, in an effort to determine the influence of different fabric parameters on its static and dynamic responses. The 2D shell crossover is then used to study pencilling phenomenon, a problem that is the side-effect of the recent advancements in the design of the personal body armours.

Chapter 7 provides a summary of the findings throughout the work presented in this thesis, along with the conclusions that can be drawn from those findings. Recommendations are made for the refinement of the modelling approach proposed and to find solutions to the unanswered questions.

Discrete Models

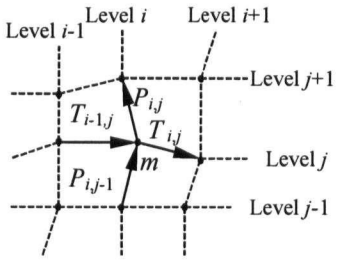

Roylance et al. (1973)
Tan, Shim, and coworkers (1995-2005)
Shahkarami (1999)
Johnson et al. (1999)
Billon and Robinson (2001)
Cunniff, Ting and coworkers (1998-1999)

Figure 1 - 1: Discrete modelling approach adopted by many researchers to study the dynamic behaviour of fabrics.

Continuum Models

Unit-Cell Shell Models

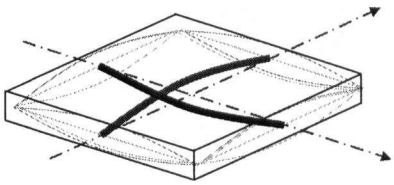

Tabiei & Ivanov (2002-2004)
King et al. (2003-2005)
Lim et al. (2003)
Tanov & Brueggert (2001-2003)
Luo (2000)
Stubbs (1989)
Shockey & coworkers (2000-2001)

3D Solid Models

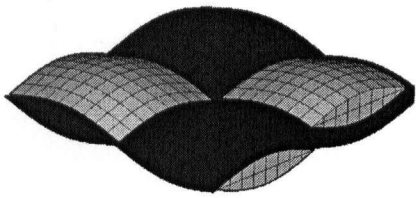

Shockey et al. (2000-2001)
Duan et al. (2005-2006)
Boisse & coworkers (2000-2005)
Peng and Cao (2002)

Figure 1 - 2: Continuum modelling approach, further subdivided into 3D solid models and unit-cell shell models, used by many to capture the dynamic response of fabrics and fabric composites.

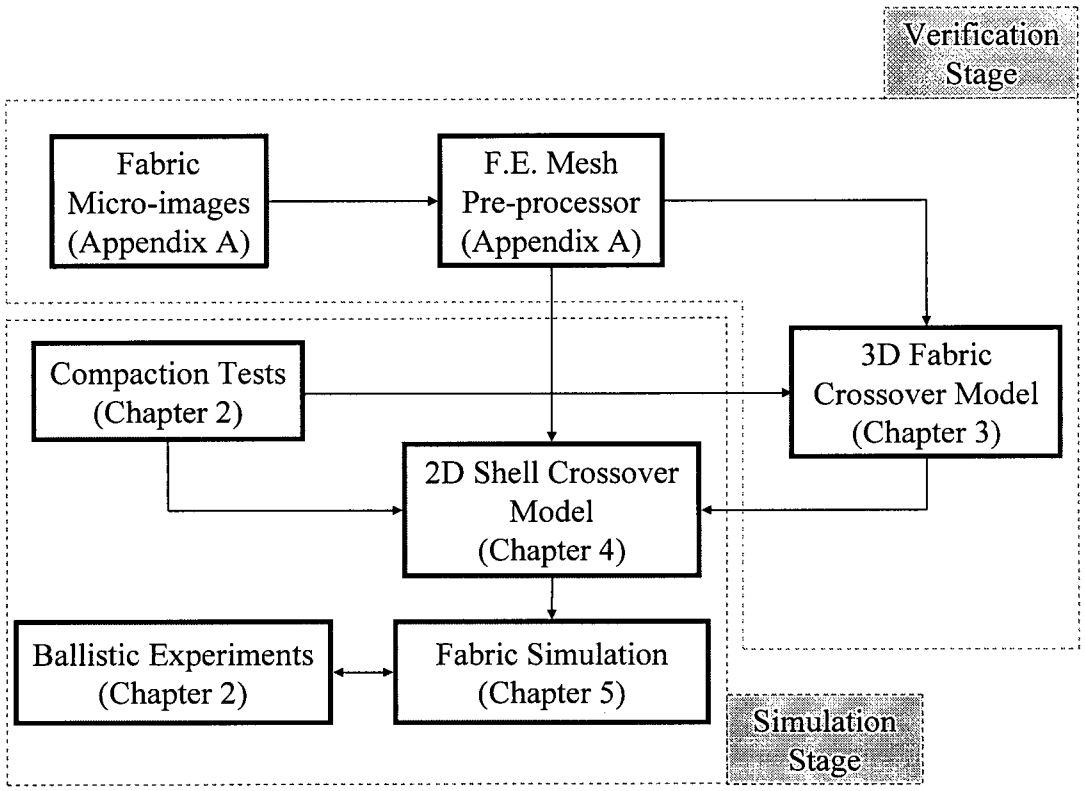

Figure 1 - 3: A summary of the numerical approach presented in this study.

CHAPTER 2 - EXPERIMENTAL DATA

This chapter highlights the experimental data that was extensively used in the development and validation of the fabric numerical model presented throughout this thesis. Only the results obtained from special experiments, such as transverse compression tests and ballistic tests, are covered here. Other data generated from standard tests, such as fibre density, elastic modulus, strain-to-failure, etc., have been taken from various sources in the literature. The original data of the transverse compression test analysed in Section 2.2 were obtained by Kongshavn [42]. The ballistic impact experiments on single and multi-ply panels discussed in Section 2.3 were performed by Cepus [42]. These experimental data were generated as part of a combined experimental/numerical research project sponsored by the Natural Sciences and Engineering Research Council of Canada (NSERC) and DuPont Advanced Fiber Systems Inc.

It should be noted once again that the experimental data presented in this chapter are obtained by Kongshavn and Cepus [42] in the case of transverse compression and ballistic tests, respectively. The author used these data to

perform model development and experimental data fitting, as presented in the following sections.

2.1 FABRIC MATERIAL

Kevlar® is perhaps one of the most common high-strength fibres widely used in ballistic applications. Kevlar® para-aramid fibres were first manufactured by DuPont in 1965. Kevlar® fibres are made of highly oriented chains of poly-paraphenylene terephthalamide molecules with strong inter-chain bonding [43]. The specific arrangement of polymeric chains has given lightweight Kevlar® fibre such superior physical properties that make it the material of choice in a variety of applications. In addition to applications in protection and defence industry, Kevlar® is widely used in tires, fibre optics and aircraft construction.

The study presented here focuses mainly on fabrics woven from Kevlar® 129 yarns for ballistic applications. The yarn densities of the fabrics tested in ballistic experiments range from 840 to 3000 denier, and the fabrics are all woven into a plain weave structure. Basic properties of the panels as reported by the manufacturer or measured in the laboratory are presented in Table 2 - 1.

2.2 TRANSVERSE COMPRESSION OF FABRICS

Transverse yarn deformation is one of the influential parameters that affect the overall response of fabrics during ballistic impact events. Compression of the crossing yarns as they interact under in-plane extensional displacements that result from the dynamic loading of single and multi-layer fabric targets

determines the degree of their compliance and hence their energy absorption capabilities. This interaction, which affects the overall response of fabric systems, is commonly neglected by many researchers. This section discusses the development of a suitable mathematical model to capture the transverse compression of the yarns in the Kevlar® fabrics studied using the experimental data obtained by Kongshavn [42].

2.2.1 Transverse Compression Experiments

The experimental set-up for the transverse compression tests is depicted in Figure 2 - 1. Squares of 55 mm by 55mm were cut from the fabrics and stacked on top of each other with the warp yarns running in the same direction. Samples of 1, 4, 8, and 16-ply packs were prepared and placed between two steel platens of size 19mm by 19mm in an MTS™ Servohydraulic machine. Teflon™ layers were placed at the interface of the loading head and the top and bottom layers, to minimize the friction between them and allow in-plane movement of fabrics. The displacement of the loading head was measured using an Instron™ extensometer, and the load applied to the target was measured from the load-cell mounted on the loading head.

Figure 2 - 2 shows the raw data for transverse compressive force-displacement response of 1 to 16-ply panels of S-720 fabric. As seen in the figure, the loading of the panels at a constant displacement-controlled rate of 1 mm/minute was stopped at 7 kN. The loading was maintained at 7 kN for 0.2 minutes, followed by unloading phase back to zero force at the same rate. The loading and unloading branches showed different characteristics, which is mainly attributed to the compaction of the panels during the loading process. As

expected, the pack shows an increasingly more compliant response with the addition of more plies.

Since Teflon™ was added to the pack, the influence of the Teflon™ panels should be extracted from the experimental data. Compressive tests were performed on samples of only two layers of Teflon™ to obtain the transverse compliance of the Teflon™ along with that of the test set up. Pure compressive response of the fabrics can thus be obtained by subtracting the Teflon™ response from that of the fabric pack with added layers of Teflon™, as shown in Figure 2 - 3.

2.2.2 Transverse Compression Model

The experimental data from the transverse compression tests were studied by only considering the loading part of the tests, since no significant transverse unloading takes place during a ballistic event. In order to obtain a suitable realistic model for the transverse behaviour of fabrics, similar work previously done by other researchers in the literature needs to be reviewed.

Numerous studies have been conducted on the transverse compression of the yarns and fabrics. These can mostly be found in the textile science literature pertaining to various applications in fabric industry (Van Wyk [44], Hoffman and Beste [45]) or to manufacturing of textile composites (Gutowski et al. [46], Saunders et al. [47, 48], Pearce and Summerscales [49]). These models generally adopt either an empirical or micromechanical approach. In 1946, van Wyk [44] presented a compression model to capture the pressure-volume response of wool, where special attention was given to its "handle" as a part of wool

quality assessment. Van Wyk's model is a relationship based on a power law, where the pressure is related to the cube of the inverse of the volume in the high pressure range as follows:

$$p = \frac{KEm^3}{\rho^3}\left(\frac{1}{v^3} - \frac{1}{v_0{}^3}\right) \tag{2 - 1}$$

where p is the pressure, E is the modulus of elasticity of the fibres, m and ρ are respectively the mass and density of wool, v and v_0 are the current and initial volumes, and K is a dimensionless constant. Van Wyk concluded that the above equation is similar to the general relation employed by others with an exponent of $\gamma = 3$ in the general form given below:

$$\left(\frac{v}{v_0}\right)^{\gamma}(p + p_0) = p_0 \tag{2 - 2}$$

where p_0 was termed "latent pressure" of wool at zero pressure. For the low pressure range, a different compressive behaviour dominated the response that was best represented by a simple inverse relation:

$$p = \frac{K'Em^3}{\rho^3 v_0{}^2}\left(\frac{1}{v} - \frac{1}{v_0}\right) \tag{2 - 3}$$

with K' being a constant. Hoffman and Beste [45] also observed that the response of fabrics to pressure can be expressed by a power function, with the exponent changing suddenly from 5/4 at low pressures to 3 at high pressures.

The compressibility of the reinforcing fabrics in the processing of composite materials has been the focus of many studies, since the compression of the fibre-bed/fabric reinforcement would greatly affect the permeability and other

properties of the composite structure during both its processing and load bearing life. One of the pioneering works in this field was performed by Gutowski [46] who provided a micro-mechanical model to capture the compression of fibre beds based on bending of single fibres. For instance, Gutowski derived the following relation between the applied bulk stress, σ_b, and the fibre volume fraction, V_f, in the absence of any axial stress in the fibre bundle:

$$\sigma_b = \frac{3\pi E}{\beta^4} \frac{\left(1-\sqrt{\frac{V_f}{V_0}}\right)}{\left(\sqrt{\frac{V_a}{V_f}}-1\right)^4} \qquad (2-4)$$

where E is the elastic modulus of the fibres, V_0 and V_a are respectively the initial and the maximum available fibre volume fractions, and β is a constant determined empirically.

Pearce and Summerscales [49] studied the compression of glass-fibre woven fabrics used in RTM (Resin Transfer Molding) processes. In their study, they used a power-law expression to fit the measured pressure to the fibre volume fraction of the fabric. The exponent of the power function used in data fitting was found to be in the range of 7 to 11. From these experiments, they reported that the transverse thickness change due to the applied pressure would not result in a lateral spreading. They also observed noticeable relaxation in the fabrics under pressure, and achieved higher fibre volume fraction after each loading cycle. Saunders et al. [47] performed compression tests on dry and wet glass woven fabrics with different weave structure (plain, twill, five-harness

satin), and concluded that the response is best represented by a power function. The exponent of the function obtained from the fitting to the experimental data was found to be between 9 and 10.5 in this study. Saunders et al. commented on the effect of additional layers on the response of the fabrics, and concluded that the higher compression in multi-layer packs can be related to nesting of the layers, specifically in plain woven fabrics.

One major common finding of all studies cited above is that the relationship between the pressure applied to the fabric and fibre volume fraction can be best expressed by a power function. For the Kevlar® 129 fabrics studied in this work, the power function adopted has the following mathematical form:

$$P = \frac{K''}{(V - V_{\min})^n} \qquad (2 - 5)$$

where P is the applied pressure, V is the fabric current volume, $V_{\min}$ is a minimum compression volume, K'' is a fitting constant, and n is an exponent. The minimum compressive volume, $V_{\min}$, is chosen such that a best fit with an exponent of 3 is obtained. The minimum volume and the exponent are merely fitting parameters; however, they reflect the properties of the fabric yarns and the specific weave characteristics. This is evident in Figure 2 - 4, where a linear relationship seems to exist between the minimum volume, $V_{\min}$, and the areal density of the six different Kevlar® 129 fabrics investigated.

The parameter K'' obtained from the fitting of the above function to the experimental data also shows dependence to the cube of the fabric areal density, A_d. This dependence, as shown in Figure 2 - 5, is critical in

extrapolating the transverse compression model to any other plain weave Kevlar® 129 fabric in the absence of transverse compression test data.

The best-fit line shown in Figure 2 - 5 is used to determine the transverse compression response of the fabrics. The best-fit line for the one-ply panels is presented below:

$$K'' = c_1 A_d^{\ 3} + c_2 = 12259 \cdot A_d^{\ 3} - 4 \times 10^{10} \qquad (2 - 6)$$

with c_1 and c_2 being the fitting constants. Having established the relationship between the pressure and the volume of the fabric panels, their transverse force-displacement relation can be obtained knowing the initial or final thicknesses of the fabric packs, as:

$$d_c = a - \frac{b}{\sqrt[3]{F_c}} \qquad (2 - 7)$$

where the parameter a is

$$a = t_0 - \frac{V_{\min}}{A} \qquad (2 - 8)$$

with t_0 being the initial fabric thickness and A the loading area. The parameter b can also be calculated as follows:

$$b = \sqrt[3]{\frac{K''}{A^2}} \qquad (2 - 9)$$

Final values of a and b are provided in Table 2 - 2 for 1, 4, 8, and 16 plies of fabric. The transverse compression model is used to calibrate the transverse properties of the yarns in the 3D solid crossover model (Section 3.4.3.2), and

eventually to obtain true compression response of yarns subjected to biaxial in-plane loading during ballistic events.

2.3 BALLISTIC IMPACT EXPERIMENTS

Ballistic impact experiments were performed on all six Kevlar® 129 fabric types with properties presented in Table 2 - 1. The experiments, conducted by Cepus [42], were instrumented with two Enhanced Laser Velocity System (ELVS), placed on the strike and exit faces of the target [50]. The projectiles used in these experiments were flat-nosed cylindrical steel projectiles (Right Circular Cylinders, RCC), with a base diameter of 5.5 mm and length of 42 mm. The projectiles were partially cored to reduce their weight to 3 grams. The panels were held in a fixture depicted in Figure 2 - 6 with an opening of 203mm by 203 mm (8"x8"), which is capable of providing various levels of end fixity for each side of the panel.

The ELVS systems allow for continuous measurement of the projectile displacement during an impact event [50]. Figure 2 - 7 shows a schematic of the dual ELVS system with laser sheet placed on both sides of the target. The diode laser produces a sheet of light that is collimated in the horizontal and vertical directions passing through two plano-cylindrical lenses. This provides a sheet of light with a uniform intensity and constant width and thickness. The light intensity of the sheet is then measured by a photo detector and recorded as voltage by an oscilloscope. As the projectile enters the sheet before impacting the target, the recorded voltage drops down since the intensity of the light entering the photo detector reduces. The location of the projectile before and

during the impact is then traced from these voltage recordings and its displacement time-history is obtained. Figure 2 - 8 to Figure 2 - 10 show typical displacement, velocity, and energy-time curves for RCC projectiles impacting 1-ply S-726 targets at 96 m/s and 110 m/s resulting in a non-perforating and a perforating impact respectively. The displacement-time response of the projectile is directly calculated from the voltage-time data, while the velocity-time information is obtained through numerical differentiation of the displacement data. The absorbed energy by the target is determined from the reduced velocity of the projectile. Further differentiation of the velocity-time data provides the acceleration-time response of the projectile, and in parallel, the resultant decelerating force imposed on the projectile by the target. Traditional plots such as residual vs. strike velocity (V_s-V_r) and absorbed vs. strike energy (E_s-E_a) can also be plotted as a testament of the inclusiveness of the ELVS data acquisition system, as presented in Figure 2 - 11 and Figure 2 - 12 for S-720 panels. The ELVS data obtained from the instrumented ballistic impact experiments are used later in Chapter 6 to validate the predictions of the shell-based fabric model developed in this study.

2.4 SUMMARY

The details of the laboratory test data used throughout this thesis were introduced in this chapter. The experiments reported are the transverse compression of fabrics and instrumented ballistic impact tests, performed by Kongshavn and Cepus [42], respectively. The fabric compression tests were conducted to characterize the transverse behaviour of yarns within the fabric. These tests were done on fabric packs of 1 to 16 plies using a standard MTS

machine, and the load carrying capacity of the fabric versus its transverse deformation was recorded. A mathematical function was fitted to the experimental data which will be used later in this thesis to obtain certain input parameters to the numerical models of fabric unit-cell. Representative ballistic impact experiments on single fabric targets and the basics of ELVS data acquisition system were introduced. The data from the ballistic impact tests will be used to measure the success of the numerical model developed in this study capturing the true dynamic behaviour of the fabrics.

Table 2 - 1: Properties of the Kevlar® 129 plain weave fabric panels investigated in this study.

Panel	S-720	S-726	S-727	S-728	S-731	S-745
Yarn (denier†)	1420	840	1000	1500	1000	3000
Warp count (tpi*)	20	26	26	17	31	17
Weft count (tpi*)	20	27	26	17	31	17
Areal density (g/m^2)	266.5	203.7	238.9	232.4	293.0	474.0
Warp crimp (%)	2.18	3.44	3.38	1.76	8.16	5.27
Weft crimp (%)	1.39	0.50	0.74	0.94	0.56	1.38

†Denier: mass of 9000 meters of the yarn in grams.
*tpi: threads per inch.

Table 2 - 2: The fitting parameters a and b for the transverse compression of the fabric model (Equation 2 - 7) for single and multi-ply panels of Kevlar® 129.

Layers	a (mm)	b ($mm.N^{1/3}$)
1	1.21E+04	-3.92E+04
4	4.43E+05	-1.03E+06
8	1.96E+06	5.5E+06
16	2.21E+07	0

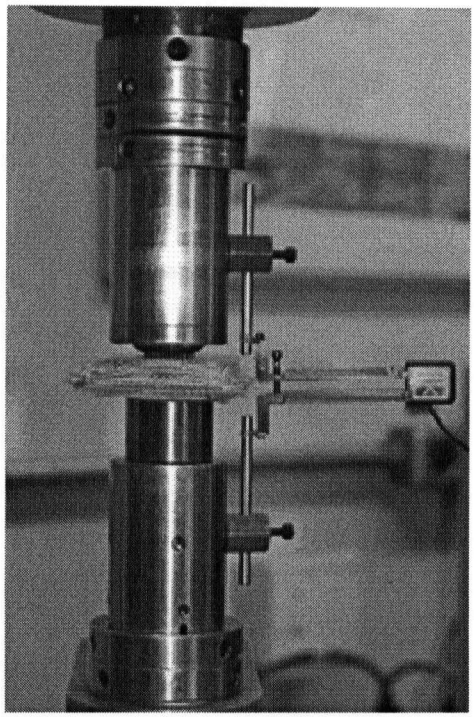

Figure 2 - 1: Experimental set-up for the transverse compression tests conducted by Kongshavn [42].

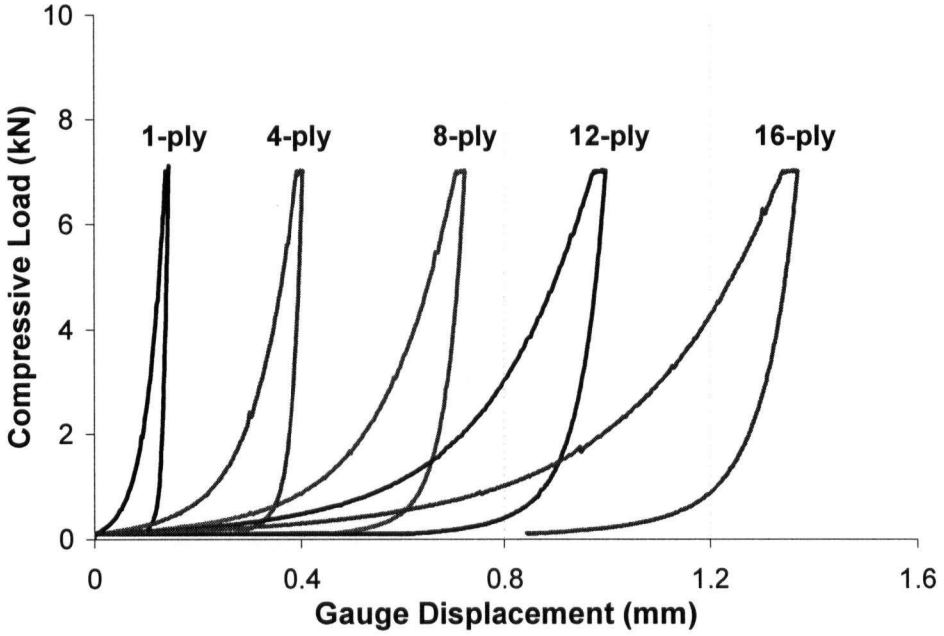

Figure 2 - 2: Transverse compressive force-displacement response of S-720 panels conducted by Kongshavn for fabric packs of 1 to 16 plies [42].

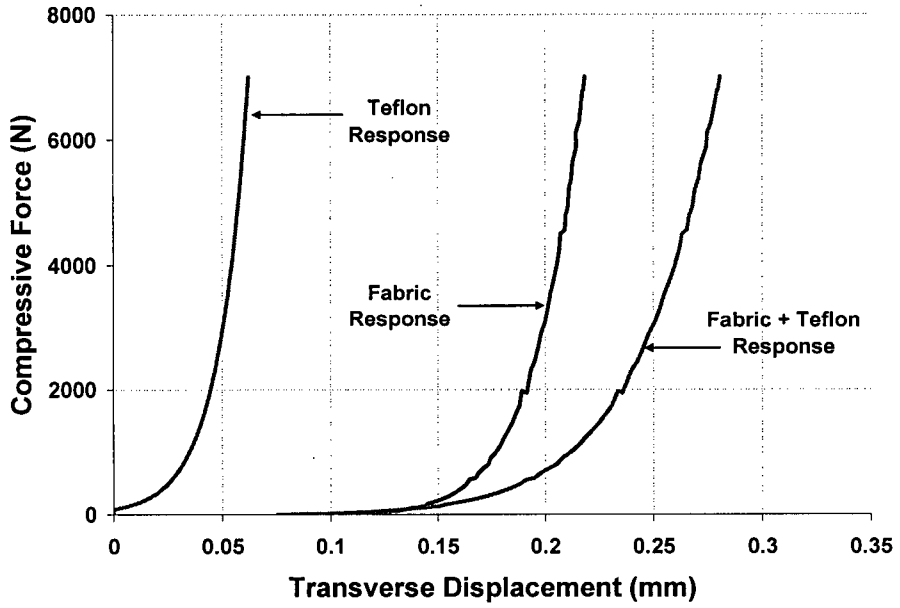

Figure 2 - 3: Transverse compressive response of a single-ply of S-720 fabric before and after extracting the compliance of the Teflon™ layers (experimental data obtained from Kongshavn [42]).

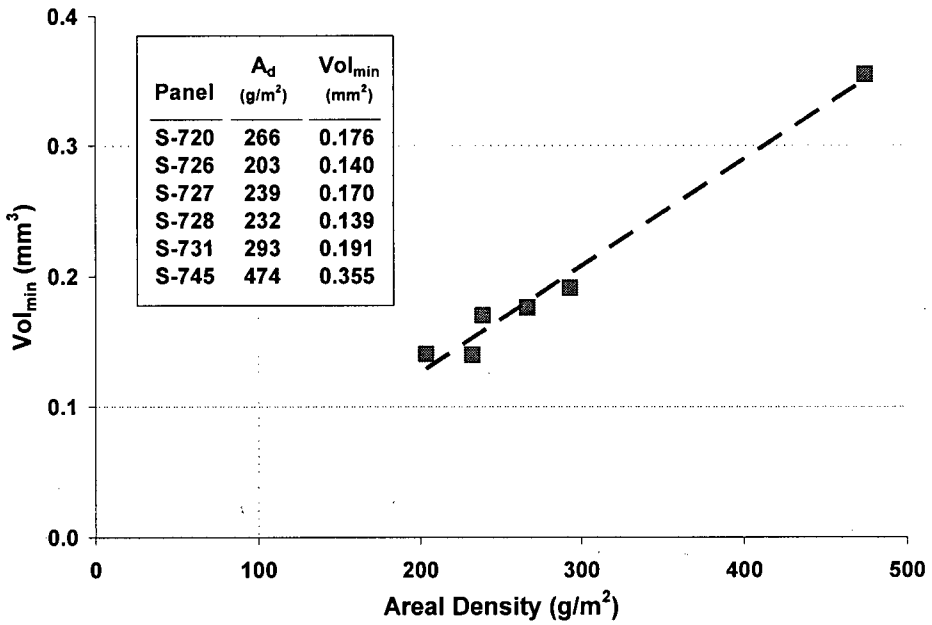

Figure 2 - 4: Linear function representing the relationship between the minimum compression volume of a unit area of the fabrics (obtained from compression model) and their areal density.

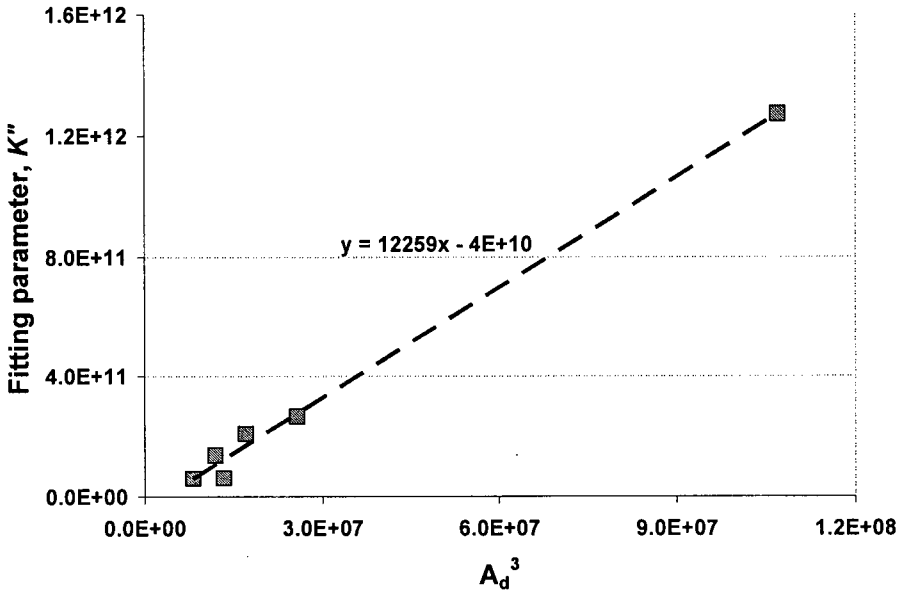

Figure 2 - 5: Fitting parameter K'' as a function of the third power of areal density (A_d^3) for the six different Kevlar® 129 fabrics.

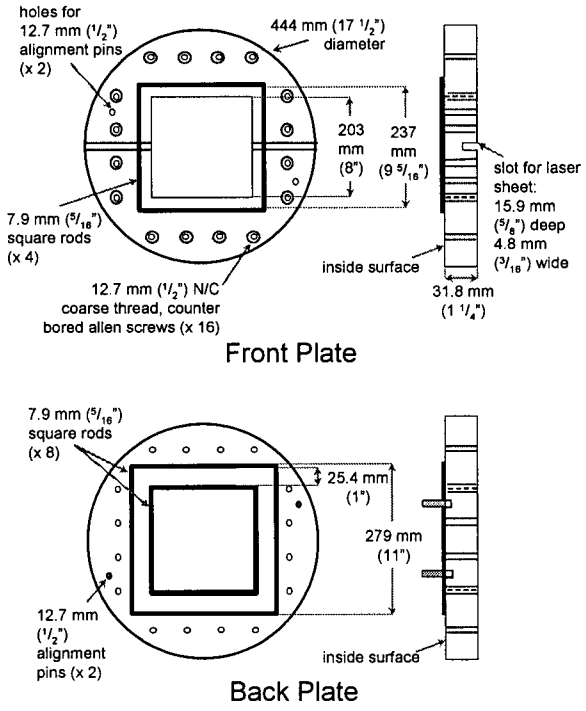

Figure 2 - 6: Schematic of the test fixture used in the ballistic experiments [51].

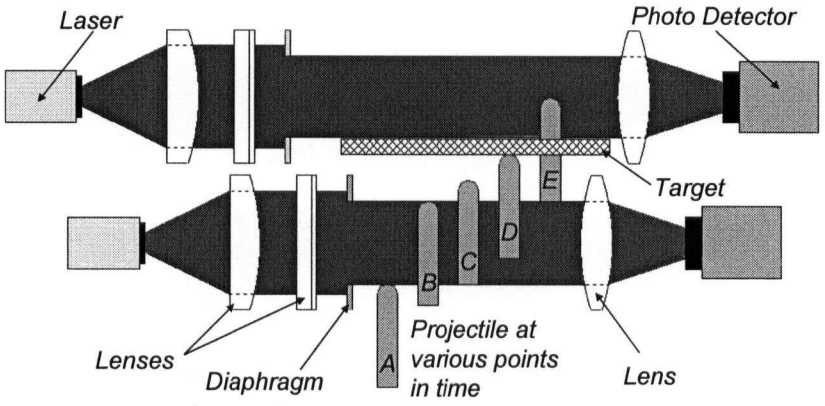

Figure 2 - 7: Dual ELVS system setup with tracking the displacement of the projectile striking the front-side of the target (front ELVS) and the tip of the deformation cone on the back-side of the target (back ELVS) [51].

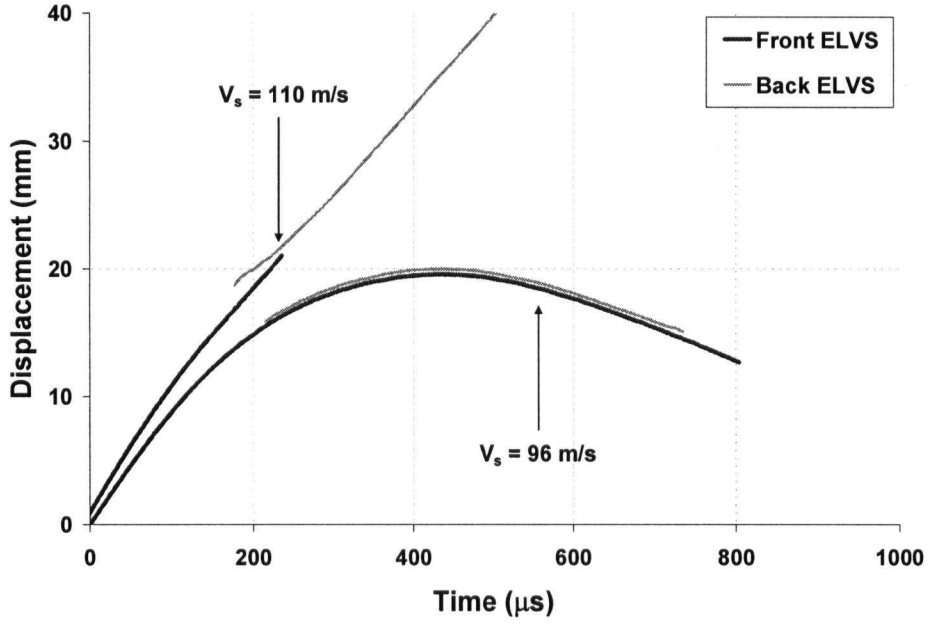

Figure 2 - 8: Displacement-time response of 1-layer S-726 panels impacted at 96 m/s and 110 m/s obtained from an ELVS-instrumented ballistic experiment (performed by Cepus [42]).

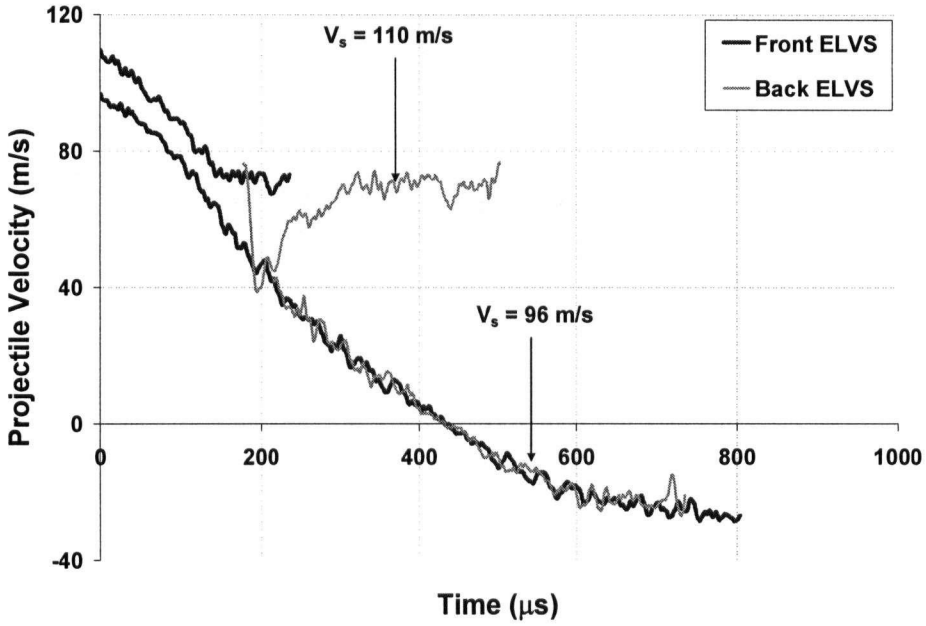

Figure 2 - 9: Velocity-time response of 1-layer S-726 panels impacted at 96 m/s and 110 m/s obtained from an ELVS-instrumented ballistic experiment (performed by Cepus [42]).

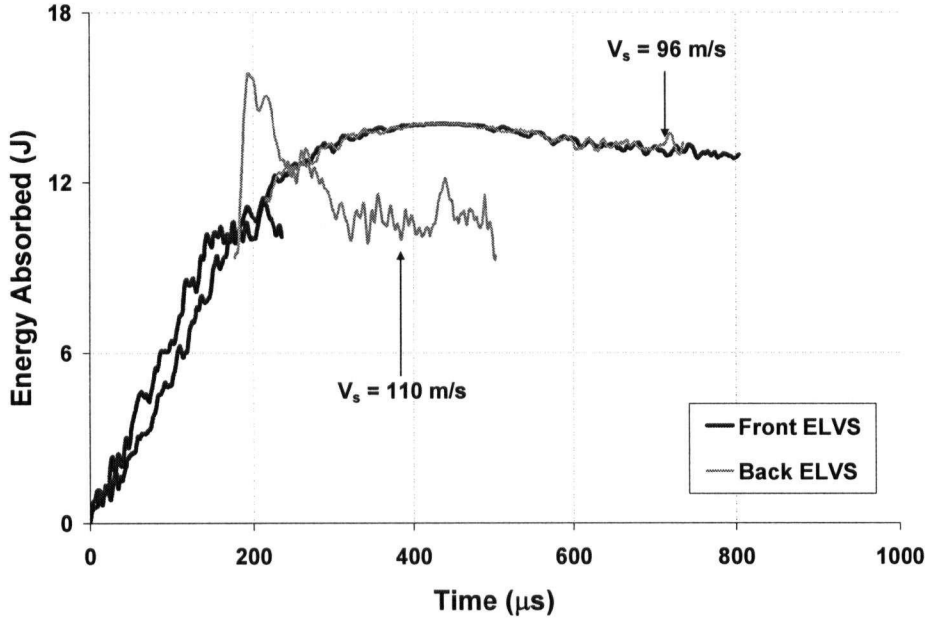

Figure 2 - 10: Energy absorbed-time response of 1-layer S-726 panels impacted at 96 m/s and 110 m/s obtained from an ELVS-instrumented ballistic experiment (performed by Cepus [42]).

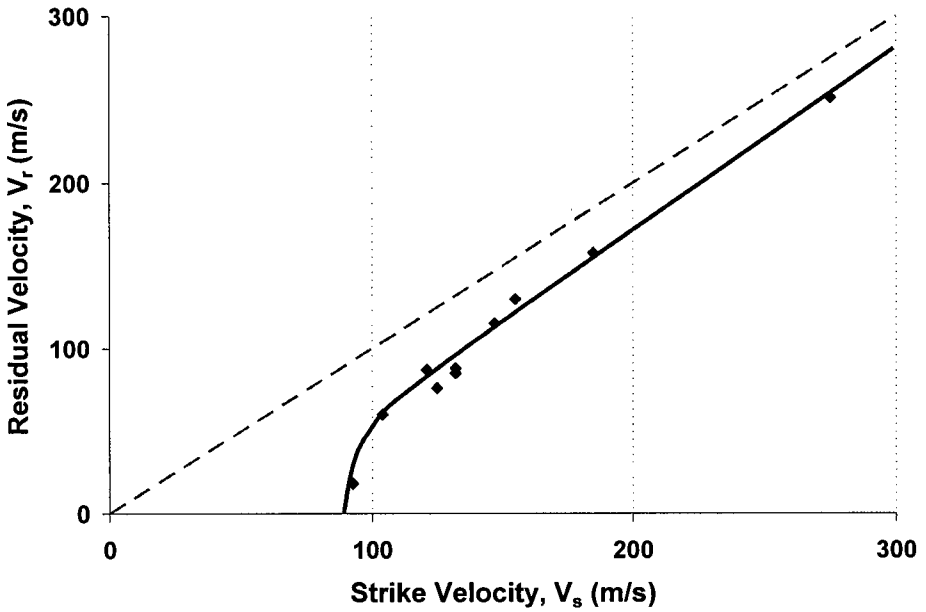

Figure 2 - 11: Projectile strike velocity versus its residual velocity in the ballistic impact tests for the 1-ply S-720 panels (Experiments performed by Cepus [42], data summarized by the author).

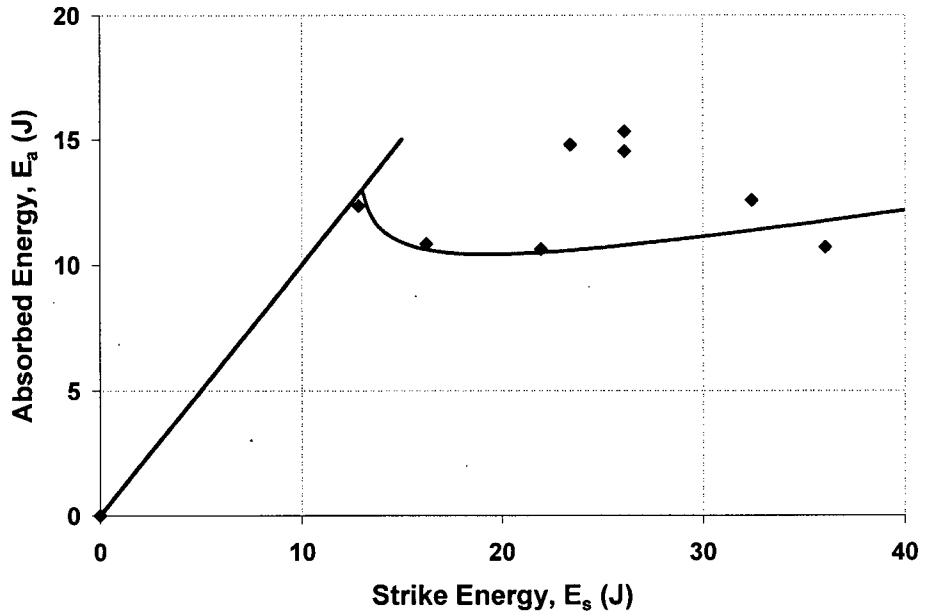

Figure 2 - 12: Projectile strike energy versus the absorbed energy by the target in the ballistic impact tests for the 1-ply S-720 panels (Experiments performed by Cepus [42], data summarized by the author).

CHAPTER 3 - 3D FABRIC CROSSOVER MODEL

3.1 INTRODUCTION

One of the most detailed modelling techniques to capture the dynamic behaviour of fabrics is to model the individual yarns as continuum bodies, woven into the fabrics in a specific architecture. This approach takes advantage of the realistic yarn geometry definition by explicitly including the individual yarns in a woven fabric in the finite element model. As a result, the complicated interactions of the yarns are inherently captured in such analysis.

This chapter reviews the basics of a 3D model specifically developed to capture the mechanical response of a plain-weave fabric crossover. The specific constitutive relationship implemented in the beam and solid element components of the model is discussed. The calibration process including input data determination for the 3D model is discussed and the advantages and limitations of the approach are highlighted.

3.2 3D FABRIC UNIT-CELL MODELS

Finite element analysis methods have proven to be invaluable tools to simulate a wide range of physical phenomena by means of mathematical formulations. In order to achieve that, a series of simplifying assumptions are to be made and a number of initial parameters need to be defined. It is rather intuitive that the outcome of any simulation is only as good as suitability of the initial assumptions and the accuracy of the input parameters. Since the finite element models are only mathematical approximations of the physical reality, there are always some degree of deviation from the true response of a system (other than the inherent error of the F.E. formulations) that stems from user's knowledge of the physical event and the wealth of details considered.

Several researchers have attempted to incorporate the many details of the complicated structure of a fabric through continuum representation of the yarns in the weave. In these unit-cell based 3D models, solid (brick) elements replace the fibres in a yarn in a smeared approach to capture the behaviour of dry fabrics or fabric composites. In simulating fabric composite manufacturing, many of the models developed focus on determination of fabric deformation during the processing of textile composites. These fabrics might be in dry state (in the case of Resin Transfer Molding), or in a fluid/semi-fluid resin base (in case of prepreg draping). Regardless of the application, the fabric may be subjected to extreme shearing and some stretching, leading to yarn rotation and fabric compaction. In the case of ballistic impact, dry fabrics are used to arrest the flying objects through membrane stretching. In this application, the fabric undergoes a large amount of stretch and a moderate amount of shear

depending on the boundary conditions. Considering the resemblances of the above mentioned applications, similar 3D solid models of fabrics have been developed in both fields.

Shockey et al. [18, 19] presented a combined experimental/numerical study to evaluate the performance of high strength polymeric fabric panels in containing the turbine engine fragments on commercial aircrafts. Along with impact and quasi-static tests, a detailed 3D solid model of fabrics was developed to study the response of fabric panels. The model was implemented in LS-DYNA and the material model employed for the solid elements was chosen to be elastic orthotropic, with reduced shear and transverse normal moduli. The profile and shape of the yarns in the fabric were obtained from cross-sectional imaging studies of the fabrics, while their properties were calibrated from the mechanical properties tests performed on single yarns. The failure model implemented was based on a cumulative damage model to capture the gradual rupture of the fibres in the yarn as it is stretched to failure. The model developed by Shockey et al. [18, 19] was successful in providing insight into the physics of fabric energy absorption; however, it lacked a robust constitutive model for the yarns, specifically due to their simplified transverse compression response. Shockey et al. further reported that the computational requirements for their detailed 3D model are considerable due to the large number of nodes and elements, significantly limiting the applicability of the model to larger fabric targets.

Duan et al. [20-23] developed a model very similar to that of Shockey et al. [18, 19] for a square patch of fabric of size 32.7 mm x 32.7 mm. The aim of their

study was to consider the yarn-to-yarn and fabric-projectile friction to investigate the energy absorption and failure of the fabric. The finite element fabric mesh used for their study was made up of 46,800 eight-noded solid elements. The findings of their studies indicated that the addition of friction would enhance the energy absorption of the fabric and reduce the projectile residual velocity. The role of boundary conditions on the performance of the target was also investigated. The study by Duan et al. further highlights the inefficiency of the 3D solid modelling, since a small panel size and very high impact velocity (800 m/s) was needed to decrease the execution time to within a practical range.

In fabric composite manufacturing, it is highly advantageous to have a numerical model to predict the deformed fabric configuration; to know the final angle between the yarns which would affect the permeability of the reinforcement and determine the final mechanical properties of the composite. Boisse and co-workers. [24-27] presented a meso/macro-mechanical approach to capture the deformation of plain and twill weave panels. In their approach, they take advantage of the available biaxial and shear response of the fabrics to calibrate a detailed 3D solid model of fabric unit-cell. A parallel meso-mechanical model powered by an analytical model of plain weave yarn crossover is developed to simulate the forming process of fabric composites. In effect, Boisse et al. use the 3D solid model validated by the experimental data to either feed the biaxial response to an equivalent representative element, or to verify the response of their biaxial analytical model.

Peng and Cao [28] adopted a unit-cell approach to predict the nonlinear elastic properties of fabric composites. In this study, they used the homogenization method to estimate the moduli of the yarns in the composite based on the properties of its constituents. Numerical tests were then performed on the 3D unit-cell to obtain the extensional and trellis behaviour of the fabric. These responses were then correlated with an equivalent shell element to evaluate its effective properties.

All the models discussed above suffer from the extreme inefficiency problem acknowledged by many researchers. The 3D unit-cell proves to be very powerful due to the wealth of geometry and material details it considers, while for modeling practical engineering systems, the resulting inefficiency proves to be its Achilles heal. The following sections highlight the basics and results of the 3D solid crossover model developed in this study, as a part of the overall modelling approach discussed earlier (Figure 1 - 3).

3.3 EXPLICIT FINITE ELEMENT ANALYSIS

Any structure, in theory, can be represented by a series of mathematical equations along with specific boundary conditions, solution of which can characterize the state of the body under the specific physical conditions. Solving these mathematical equations, however, is not an easy task. Finite element analysis method is an efficient approach for analysing the state of a physical body under an applied set of loading and boundary conditions. The analysis procedure is to discretize a continuum body into a finite number of components (elements) connected to each other at certain points along their

edges, usually referred to as nodes. Temporal and spatial field parameters are considered and their relationship with the mechanical properties of the body is formulated into mathematical equations. Temporal and spatial discretization of the problem would lead to a solution of the mathematical equations resulting in the values of the field parameters at the common nodes of the elements. Within the domain of an element, the values of all parameters are approximated through the adoption of appropriate shape functions. In a structure, since the true state of stress and strain in the material would correspond to the minimum energy of the system, any other approximation of this state would lead to higher energy than the real case. As a result, the finite element solution would always exhibit a stiffer response compared to that of the real physical system.

To analyse the dynamic response of any structure, temporal discretization should be performed on the equations of motion to deal with the time dependency of the mathematical equations. Details on these well-established methods, briefly discussed in this section, can be found in any finite element references [52, 53]. The choice of temporal discretization scheme for the finite element analysis is usually based on the nature of the dynamic event. In general, two main methods are usually adopted, commonly referred to as Implicit and Explicit time-integration schemes. Implicit schemes take advantage of the trapezoidal rule to approximate the time derivatives in the equation of motion. The result is a discretized scheme that is unconditionally stable, and the time-step-size is only defined based on accuracy considerations. Explicit schemes, on the other hand, utilize the central difference method for temporal discretization. The analysis with this method is conditionally stable,

meaning that the accuracy and convergence of the solution is time-step-size dependent. The criterion to achieve stability in the explicit time-integration scheme is based on the speed of sound wave in the material, C, as follows:

$$\Delta t \leq \frac{L}{C} \tag{3 - 1}$$

where Δt is the time step size, L is the smallest element length. The time-step-size of a finite element problem is chosen to be equal to the smallest value calculated amongst all the elements in the model. The explicit scheme is suitable for wave propagation problems where the response is dominated by high-frequency modes. In these types of events, the time scale is usually very small and in the same order as the wave propagation across an element. For these problems, where the behaviour of the wave front is important, the explicit time-integration method is more suitable since the stability requirement leads to a time-step-size during which the wave in the system can travel less than the smallest dimension of any element in the model. In structural dynamics problems, the response of the system is usually dominated by lower frequency components. For these problems, implicit methods are more suitable since the analysis time is much longer than in the wave propagation problems and the time-step size obtained considering accuracy criteria is usually much larger than the largest time-step size from the explicit methods.

This study is based on developing constitutive relationships for elements that are aimed to represent the behaviour of yarns and fabrics. For this purpose, LS-DYNA explicit finite element code is used as the main analysis tool, since the impact problems investigated here are more of a wave propagation nature. The main reason in choosing LS-DYNA as the analysis platform is its versatility and

excellent capability in simulating impact events, combined with its well-established contact algorithms that would allow for a more realistic representation of the colliding bodies. Figure 3 - 1 shows a schematic of the analysis process in LS-DYNA, as an explicit wave propagation code.

LS-DYNA allows the users to define the material constitutive relationship for beam, shell and solid elements within a user-defined material model (UMAT). This option is fully exploited in this chapter to modify the behaviour of beam and solid elements to match specific characteristics of the fibres of a yarn. The following sections provide the basic components of a yarn model and highlight the details of UMAT development for beams and solid elements.

3.4 Model Basics

A 3D micro-mechanical model of a fabric unit-cell is developed to capture the biaxial response of plain weave fabrics. As seen in Figure 3 - 2, the model is based on representation of a single fabric crossover and is comprised of solid (brick) and bar elements. This approach, developed for the plain weave fabrics, is not weave specific and can be readily applied to any other fabric structure. The finite element mesh of the unit-cell is created by a specialized pre-processor presented in Appendix A. The basic assumptions considered in the creation of the yarn cross-sections and longitudinal profiles are obtained from the study of the micro-images of the fabric cross-sections. As a result, it is assumed that the yarn profiles follow a sine function, while their cross-section can be elliptical or sinusoidal. It appears from the fabric micro-images that the cross-sectional areas of the yarns are considerably larger than the solid area of

the fibres, implying that there is a significant amount of voids between the fibres. Thus the cross-sectional area of the yarns in the finite element mesh is inflated to account for the voids between fibres. The pre-processor is also capable of generating crossover meshes of unbalanced fabrics with varying dimensions and crimp values in warp and weft yarns. However, one of the basic limitations of the pre-processor is its inability to consider varying yarn cross-sections along its profile. As a result, yarn overlays cannot be created in the finite element mesh of the crossovers.

The key to the success of the fabric crossover model is capturing the true response of the individual yarns that form a crossover. The finite element model of each yarn is made from a combination of bar and solid elements. The bar elements represent the axial stiffness of the fibres in the yarn and make up the tensile stiffness of the yarns. The solid elements, on the other hand, provide the transverse compressive resistance of the yarns, as they interact with each other in a fabric crossover. The following sections highlight the basics of the bar and solid elements developed for the finite element representation of the yarns.

3.4.1 Discrete Bar Elements

Due to the complex nature of the yarns as an assembly of fibres, many of their mechanical properties are not uniquely available. In finite element analysis, the absence of a meaningful mechanical property would cause instabilities in the calculations and lead to spurious modes of deformation without significant energy absorption. This phenomenon occurs commonly for strongly orthotropic materials and specifically in 3D solid elements of yarns as reported by some researchers (e.g. Gasser et al. [26]). This phenomenon is shown in

Figure 3 - 3 (right) for a single crimped yarn made of orthotropic solid elements with low shear modulus under tensile loading. The unstable load-displacement response of such a yarn is also shown in Figure 3 - 4 . Boisse et al. [25] state that "because some rigidities are nearly equal to zero, some numerical instabilities often appear. This is avoided by hourglass control." Lack of sufficient shear stiffness in the yarns would lead to unstable element shapes that closely resemble hourglass deformation modes that occur in under-integrated (or reduced-integration) elements. As a result, one possible solution to this problem could be the addition of hourglass-control stiffness component to an element's stiffness which would resist the initiation of such deformations. Due to the non-physical nature of the added hourglass stiffness, it is preferred that the energy consumed by these modes of deformation be limited to a small amount. This fact is usually overlooked by many users, leading to unreliable structural responses.

Reinforcing the solid elements by addition of rebars is an efficient method of controlling unrealistic hourglass-like deformation modes. In doing so, reinforcing bar elements are added to the yarns in the axial direction to play the role of the reinforcement. Figure 3 - 3 (left) shows the stable deformed shape of the same crimped yarn under axial displacement after the addition of the reinforcing bars. The axial tensile force in the yarn also shows a monotonic rise with increasing displacements, as depicted in Figure 3 - 4.

The reinforcing bar elements are formulated to provide the axial tensile stiffness of the yarns. As these bars should closely represent the axial response of a bundle of fibres, they would have the same tensile modulus and area of the

fibre bundle they represent (see Table 3 - 1), while exhibit no resistance (due to fibre buckling) in compression. A user material routine (UMAT) is developed to modify the response of beam elements in LS-DYNA (see flowchart in Appendix B). The goal of this transformation is to take advantage of the many capabilities of beam elements such as element erosion, while implementing the non-conventional tension, compression and shear behaviour of the fibre bundles in the reinforcing bars. In general, erosion of elements from the mesh in LS-DYNA is performed based on a user-defined criterion that prompts the code to physically remove an element from the finite element mesh. In this process, the code eliminates the element from the calculation while retains its mass properties on the nodes attached to it. For the case of beams, the erosion is activated based on an instantaneous failure strain criterion, where the beam is eliminated from the mesh when its axial strain exceeds a predefined failure strain.

The UMAT developed takes advantage of a visco-elastic material model along with an instantaneous strain-to-failure criterion. The UMAT is considered in conjunction with a beam element based on the Hughes-Liu beam formulation available in LS-DYNA. The specific type of beam formulation is based on a degenerated 8-noded iso-parametric solid element formulation, although the choice of beam formulation is not expected to affect the results in the current analysis. In order to convert the behaviour of the beam elements to that of a bar, the bending and shear resistance of the beam should be eliminated. This is achieved through considering a single integration point in the thickness of the beam, since lack of stress gradient through the thickness of the beam eliminates the bending moments in the beam. The shear stresses and axial stiffness of the

beam in compression are also set to very small values manually. The final result is a beam element that along with the UMAT developed behaves similar to a cable that is ideal for representing the axial response of the fibres in the yarn.

3.4.2 Continuum Solid Elements

The key part in developing a successful 3D model of the fabric is the yarn's constitutive model. The structure of a non-twisted yarn is based on an assembly of long parallel fibres bundled (entangled) together. As a result, the individual fibres are more or less free to move and interact with each other within a yarn, only exhibiting a high axial stiffness in tension. In axial compression, owing to the absence of any lateral confinement, the fibres of a single yarn easily buckle and show little resistance. This lack of bonding between the fibres also translates into near zero shearing or bending stiffness in the yarn. In the transverse direction, the presence of voids between the fibres along with their extensive relative motion leads to an extremely complex non-linear response. The challenge in setting up a realistic model of a fabric crossover is to provide a material model that can capture this complex behaviour of yarns, in all possible loading modes and directions.

The solid elements used in this study are the reduced integration constant stress solid elements. In this type of elements, the volume integration is carried out using Gaussian approximation considering only a single integration point. This leads to an element that provides a high efficiency compared to other elements, e.g. fully integrated (2x2 integration point) element. However, the one-point quadrature algorithm is accompanied by some zero-energy

deformation (hourglass) modes in the elements that lead to unstable results. For more information on the constant stress solid elements and other available choices the reader is referred to the LS-DYNA Theoretical Manual [54].

While the yarns exhibit strong overall orthotropic characteristics, their behaviour can be considered isotropic in the transverse direction. In this study, it is assumed that the axial and transverse yarn responses are completely decoupled, and the Poisson's ratios are assumed to be zero in all directions. As mentioned previously, the axial stiffness of the yarns is provided by the bar elements, thus the modulus of solid elements along the axis of the yarn is set to a small value. However, due to the presence of voids in the yarn and occurrence of large strains in the transverse direction, the rule of mixtures is used to adjust the modulus of the solid elements in the yarn axial direction according to the yarn cross-sectional area. At any instant of time t (time-step n), the axial modulus (E_1^n) is obtained from current fibre volume fraction (V_f^n) as follows:

$$E_1^n = E_a V_f^n \tag{3 - 2}$$

where (E_a) is the initial modulus of the solid elements along the yarn axis. The fibre volume fraction is monitored as the yarns cross-section deforms due to contact and the axial modulus is updated at each time-step. Using the basics of continuum mechanics, the compression of the yarns are tracked using the deformation gradient, $\underline{F}$, defined as (using indicial notation):

$$F_{ij} = \frac{\partial x_i}{\partial X_j} \tag{3 - 3}$$

where $\underline{X}$ and $\underline{x}$ correspond to the material coordinates before and after deformation, respectively. The volume of an element can be calculated as follows:

$$V^n = JV^0 \tag{3 - 4}$$

where V^n and V^0 are the calculated current and initial volumes respectively, and J is the Jacobian defined as the determinant of $\underline{F}$

$$J = |\underline{F}| \tag{3 - 5}$$

Considering the current and old axial dimensions of the yarn L^n and L^0, one can estimate the current yarn cross-section, A^n from its original value, A^0 as

$$A^n = \left(J\frac{L^0}{L^n}\right)A^0 \tag{3 - 6}$$

The updated fibre volume fraction can then be calculated as:

$$V_f^n = \left(\frac{L^n}{JL^0}\right)V_f^0 \tag{3 - 7}$$

Adopting an incremental strain algorithm, the total logarithmic strain is calculated by the accumulation of the strain increments as follows:

$$\varepsilon^n = \int_0^n \frac{dL}{L} = \ln\left(\frac{L^n}{L^0}\right) \tag{3 - 8}$$

where ε^n is the logarithmic strain at time-step n along the yarn axis. Using the two equations above, we can calculate the updated nominal fibre volume fraction as:

$$V_f^n = \left(\frac{\exp(\varepsilon^n)}{J}\right)V_f^0 \tag{3 - 9}$$

In the transverse direction, the material representing the fibres in a yarn is assumed to be isotropic. There is not much information available on the transverse modulus of Kevlar® 129 fibres.

The transverse elastic modulus is assumed to be a function of the nominal fibre volume fraction of the yarns in a non-linear fashion. The behaviour of the yarn subjected to transverse loading is schematically shown in Figure 3 - 5. Based on the loading conditions (tension versus compression) and its amplitude, an effective transverse secant modulus is determined. The conditional function defining the instantaneous transverse modulus is presented below.

1. If $V_f^n < V_f^0$, the yarn is subjected to transverse tension. In reality, this type of loading would separate the fibres of a non-twisted yarn (such as the Kevlar® 129 yarns in the six fabrics studied here) and not much resistance is displayed by the yarn. As a result, the yarn is assumed to have a very soft response defined as:

$$E_2^n = E_3^n = K_r E_c \qquad (3 - 10)$$

where E_c is an upper limit for the modulus and K_r is a reduction factor.

2. If $V_f^0 < V_f^n < V_c$, where V_c is referred to as the minimum nominal fibre volume fraction and is merely a fitting parameter, then the yarn easily deforms under the applied compressive loading. The deformation of the yarn is combined of fibre displacement and realignment, along with some transverse fibre compression. This zone is similar to the initial soft response of foams. The transverse modulus in this zone is assumed to follow a non-linear function of the form:

$$E_2^n = E_3^n = \frac{a_E}{b_E - V_f^n} \tag{3 - 11}$$

where a_E and b_E are calculated below:

$$a_E = E_c\left(b_E - V_c\right) \tag{3 - 12}$$

$$b_E = \frac{V_c - K_r V_f^0}{1 - K_r} \tag{3 - 13}$$

It should be noted that V_c can be higher than the maximum packing ratios for square or hexagonal packing, since it is assumed that a certain level of fibre compression does also occur at V_c and beyond.

3. If $V_f^n > V_c$, then the yarn is subjected to high compression. The resistance in this case is high, as the fibres of the yarn have reached maximum packing ratio and have been compressed transversely. The transverse fabric modulus is at its maximum value, E_c

$$E_2^n = E_c \tag{3 - 14}$$

Figure 3 - 6 shows the transverse modulus of the yarns as a function of the nominal fibre volume fraction for the input values presented on the figure inset. It should be noted that the nominal fibre volume fraction is merely a fitting parameter and can exceed the value of 1.0 in the presence of fibre compression, since it is calculated using the compressed volume of the yarn compared to the uncompressed net area of the fibres in the yarn. Adopting the above function for the transverse modulus, the fitting parameters V_c, E_c, and K_r are determined by simulating the 1-layer transverse compression tests and the predicted force-displacement response to that of the experiments. The

transverse elastic modulus estimated is then used to calculate the state of stress as follows:

$$\sigma_i^n = E_2^n \varepsilon_i^n \text{ where } i = 2,3 \qquad (3 - 15)$$

where E_2^n is the secant modulus defining the transverse stress in the yarn as a function of applied strains.

As mentioned earlier, the shear stiffness of a yarn is generally extremely low due to the lack of any bonding between the fibres. The shear resistance of the yarn should have some dependency to the axial and transverse state of stress as they are affected by the fibre-to-fibre interaction and friction. This is ignored in this study due to absence of any experimental or analytical evidence, and the shear moduli in all directions are set to a low value. These moduli are determined from the compacted transverse elastic modulus E_c as follows:

$$G_i = K_G \frac{E_c}{2} \qquad (3 - 16)$$

where K_G is a reduction factor, and $i = 1,2,3$. In this study, this reduction factor is assumed to be $K_G = 0.1\%$ to simulate the lack cohesion between the fibres of a yarn in shear. The shear modulus of this magnitude would not be able to provide any significant resistance to the yarn deformation, similar to the behaviour of a real yarn.

3.4.3 Determination of Material Properties

Perhaps the biggest challenge in setting up the 3D solid model of fabrics is determination of the materials properties. The behaviour of the yarns in a fabric is so complicated that the modellers are forced to estimate some values or

resort to model calibration using experimental data. The following sections discuss the procedure to obtain the input parameters for solid and beam elements.

3.4.3.1 Single yarn tensile test simulation

Tensile tests are performed on single yarns to validate the axial properties of the yarns. In solids, the modulus in the direction of the yarn axis is set to a very low value since the bar elements are taking all the tension. The axial tensile modulus of the bars is set equal to the modulus of the fibres and their cross-sectional area estimated from the solid area of the fibres. This ensures that the virtual yarns exhibit the same stiffness as the actual ones in the axial direction.

Figure 3 - 7 shows the single yarn response of the crimped warp and weft yarns of S-720 panel. It can be seen that the yarns show very little resistance while they are crimped and stiffen up when taut. The tensile responses also reflect the difference in the crimp values of the warp and weft yarns, as the S-720 panel has non-balanced crimp values. The corresponding responses predicted by an analytical model are superimposed on the graph for comparison. This analytical model assumes zero stiffness for strains less than the crimp value and linear Kevlar® yarn stiffness for strains higher than the crimp strain (see bar properties provided in Table 3 - 1 for the S-720 fabric). Good agreement is observed between the analytical model and the predictions of the 3D finite element model of the crimped yarn. Erosion of the bar elements are also incorporated in this model which results in the failure of the yarns at a predefined failure strain value (taken to be 3% in this study, as seen in Table 3 - 1).

3.4.3.2 Transverse compression test simulation

Determination of the transverse properties of yarns in a woven fabric is one of the most challenging aspects of yarn modelling. Overlooked by many of the existing numerical models, the transverse response of yarns affects the interaction of the crossing yarns and defines the shape of the nonlinear biaxial response of a fabric. This fact can perhaps be further explained by comparing the yarn interaction for two extreme cases: transversely incompressible versus over-compressible yarns. In fabrics woven from incompressible yarns, stretching of the yarns in one direction leads only to pure crimp exchange between them while the transverse distance between the yarn centrelines remains constant. For over-compressible yarns, interaction of the crossing yarns due to in-plane extension disappears in their transverse deformation. As a result, the fabrics woven from over-compressible yarns exhibit decoupled warp and weft yarn responses, while the ones with incompressible yarns show the highest level of coupling between the two directions. Regardless of the level of yarn transverse compliancy, capturing the true transverse yarn response is a crucial step in developing a realistic fabric model. This fact is also reiterated by other researchers, e.g. Boisse et al. [25] who quotes "The transverse law appears to be an important point for a good modelling of the unit woven shell."

Some researchers have tried to design experiments that would realistically capture the transverse compressive behaviour of yarns. Perhaps one of the earliest investigations into this matter is that of Kawabata [55]. The proposed method, referred to as the wire method, consists of hanging the yarn on a horizontal steel wire at a certain angle. Weights are added to the yarn successively and the change in the yarn thickness is measured as a function of

the contact force. This method, however, fails to represent the true state of yarn in the fabric and capture the interaction of the yarns as they get compressed. Despite the efforts to establish a standard experiment for measurement of transverse compressive response of yarns in a woven fabric, little can be said about their success since none of them can produce the true compressive behaviour of yarns during the biaxial loading of a fabric (as seen in Figure 3 - 8).

Several simulations of the compression experiments were conducted to calibrate the transverse moduli of the solid elements. In these simulations, the modelled yarn crossover is transversely compacted between two rigid plates and the contact force exerted on the plates by the yarns is plotted against the applied transverse displacement.

In effect, the value of the transverse modulus is back calculated from the transverse compression data (discussed in Section 2.2.1), by matching the force-displacement response of the yarn crossover predicted from the numerical simulation to that of the experiments. The comparison of the two responses is presented in Figure 3 - 9 for a single crossover of S-720 fabric.

3.4.3.3 Biaxial Response of the 3D Crossover Model

The 3D crossover model assembled from yarns with solid and bar elements is used to study the biaxial response of fabrics at a unit-cell level. The contact between the yarns is activated through surface-to-surface option in LS-DYNA which is based on a penalty method, i.e. placing normal interface springs between the contacting bodies. The friction between the yarns is ignored and

symmetric displacements are applied to the yarns in the biaxial deformation mode.

Figure 3 - 10 shows the development of tensile force in the warp yarn as it is displaced while the weft yarn is kept fixed at both ends. Comparing the tensile response of the warp yarn inside the weave (crossover response) and outside (single crimped yarn response), it appears that the yarn exhibits a stiffer response inside the fabric due to the interaction with the crossing (weft) yarn. At the same time, tension also builds up in the weft yarn as a result of this interaction. Due to the biaxial state of the in-plane extensional response in the fabrics, the tension in each yarn is a function of its own displacement (d_1) as well as that of the crossing yarn (d_2). This results in response surfaces for each yarn, as shown in Figure 3 - 11. These surfaces are a product of various geometrical and mechanical properties of the yarns and fabric, and are the basis of the specific characteristics of a fabric. The response surfaces obtained here are used in the following chapter to verify the predictions of the meso-mechanical model developed to capture the interaction of the crossing yarns and the biaxial behaviour of fabrics.

3.5 ADVANTAGES AND LIMITATIONS

The 3D crossover model incorporates many details of the yarns in the weave and provides a large amount of information on the mechanics of their deformation under various applied loads. Due to the generality of the assumption made in setting up the 3D crossover model, there is almost no limitation on the loading scenarios that could be considered.

The 3D solid-bar modeling approach brings along several challenges and limitations. Some of these issues are listed below:

- Generating the shape of the yarns as they are in the fabric is not an easy task. Plain fabric cross-section micro-imaging (see Appendix A) reveals that the yarns in the warp and weft directions interact even before any loading is applied. This is evident from the non-uniform profiles, yarn overlays, etc.

- The properties of the continuum representation of the yarns cannot be easily determined. This is mainly due to the complex, highly non-homogeneous nature of the yarns and lack of understanding of the physics of fibre interactions in a yarn.

- Due to the small scale of the fabric unit-cell and the number of solid and bar elements used to capture the shape of the yarns, the finite element mesh of fabrics, even with small dimensions, would contain a large number of elements. This results in unrealistic computational requirements leading to extremely time-consuming analysis even for models with modest dimensions.

Despite all the limitations discussed above, the 3D solid-bar model is perhaps one of the best tools to get insight into the behaviour of yarns in fabrics of different weave structure. With the everyday advancement of computing machines, this issue will become less and less limiting and 3D models will perhaps replace the other simplified approaches in the near future.

3.6 SUMMARY

This chapter introduced the basics of a detailed 3D model of the fabric unit-cell (a single crossover in the case of plain weave fabric) that is comprised of bar and solid elements. Representing bundles of fibres in the yarn, the bar elements are aligned with the yarn axial direction and would provide its tensile stiffness. The solid elements are placed in the space between these bar elements and provide the soft transverse compressible response of the yarns. The modeling technique established can be applied to any type of fabric, since it is not dependent on the geometry of the yarns or the fabric structure. The 3D crossover model was successful in capturing the biaxial response of fabrics due to the interaction of the crossing yarns. The 3D crossover model will be used in the following chapter to verify the predictions of the computationally more efficient 2D shell crossover model.

Table 3 - 1: Beam element input parameters used for the 3D crossover model of S-720 fabric unit-cell.

Parameter	Warp	Weft
Elastic Modulus (GPa)	96.0E+09	96.0E+09
Number of bars/yarn	44	38
Yarn Density (denier)	1420	1420
Fibre Area (mm^2)	1.096E-01	1.096E-01
Bar Area (mm^2)	2.49E-03	2.88E-03
Failure strain, ε_f	3.0%	3.0%

Table 3 - 2: Solid element input parameters used for the 3D crossover model of S-720 fabric unit-cell.

Parameter	Warp	Weft
E_a (Pa)	1.0E+06	1.0E+06
E_c (Pa)	2.0E+09	2.0E09
K_r	0.02	0.02
V_f^0	0.70	0.62
V_c	1.00	1.00

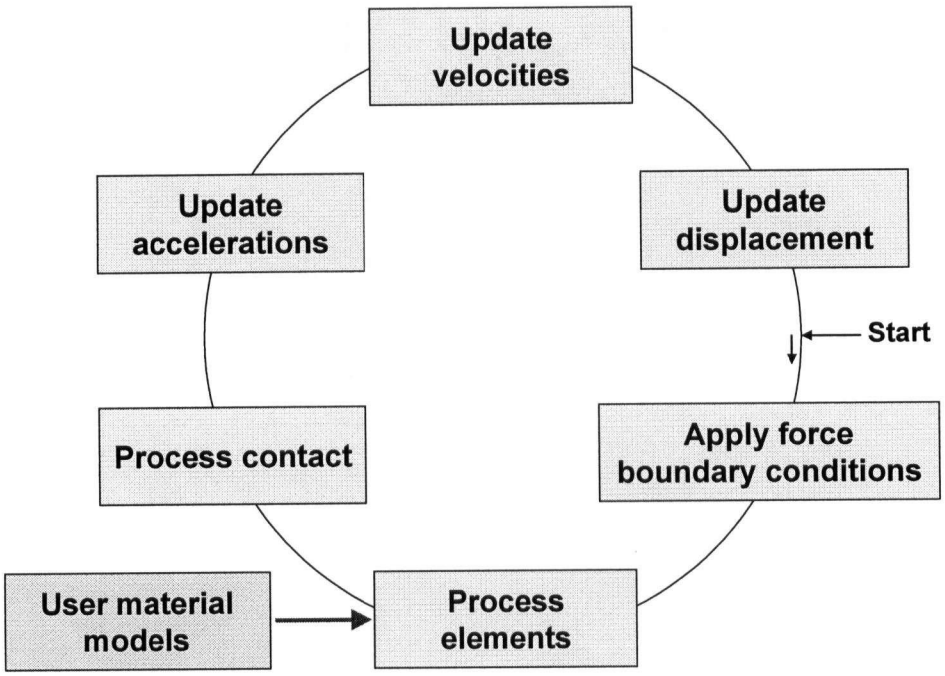

Figure 3 - 1: schematic representation of LS-DYNA explicit finite element analysis [56].

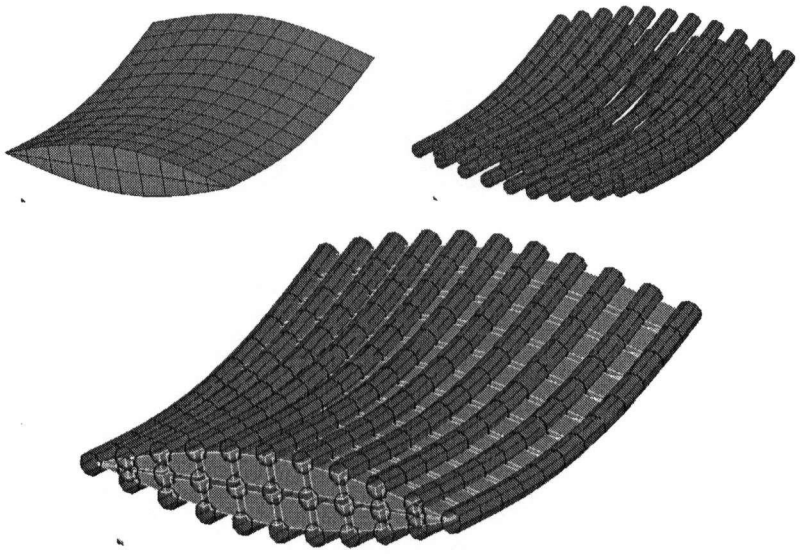

Figure 3 - 2: Solid (top left) and bar (top right) elements combined to make up a 3D model of a yarn (bottom).

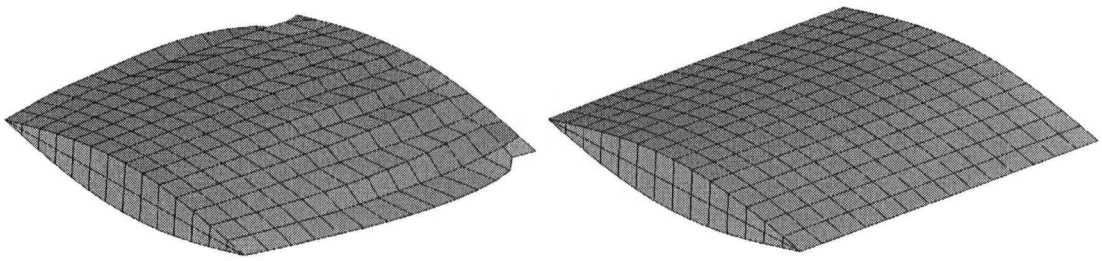

Figure 3 - 3: Hourglass-type deformation shapes (left) eliminated by the addition of bar elements (right).

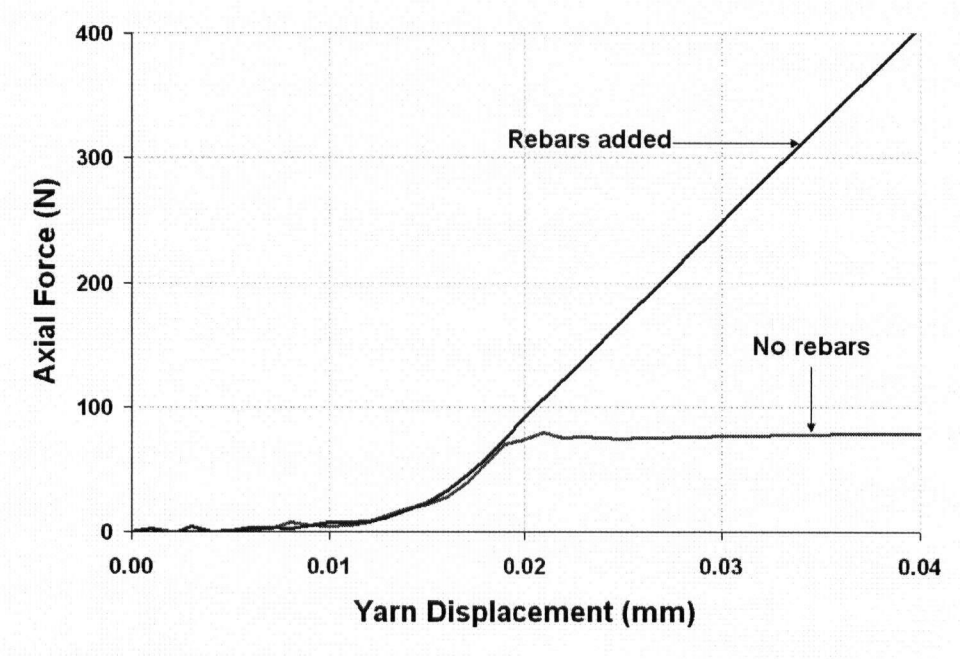

Figure 3 - 4: Force-displacement response of a single crimped yarn showing the instability of the yarn model without the bar elements.

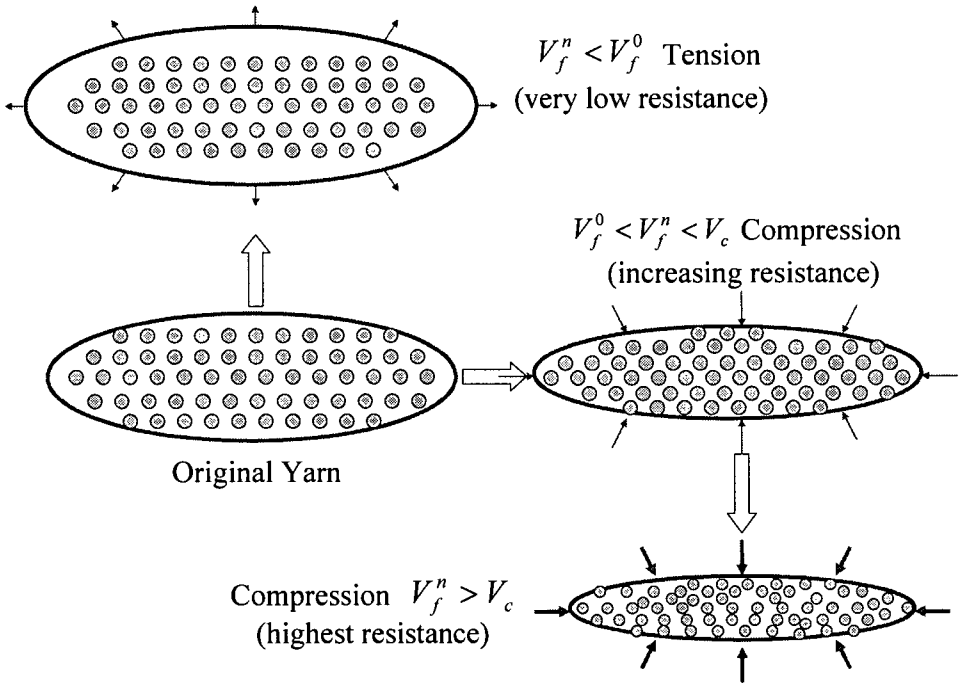

Figure 3 - 5: Schematic representation of fibre realignment and compression in a yarn subjected to transverse compression.

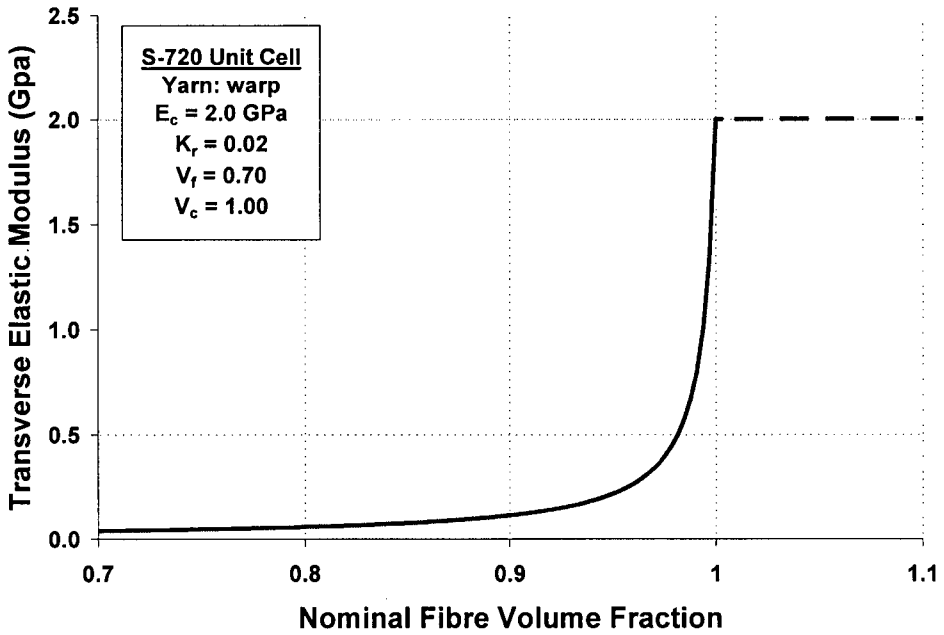

Figure 3 - 6: Relationship between transverse elastic modulus and the fibre volume fraction for the S-720 warp yarn.

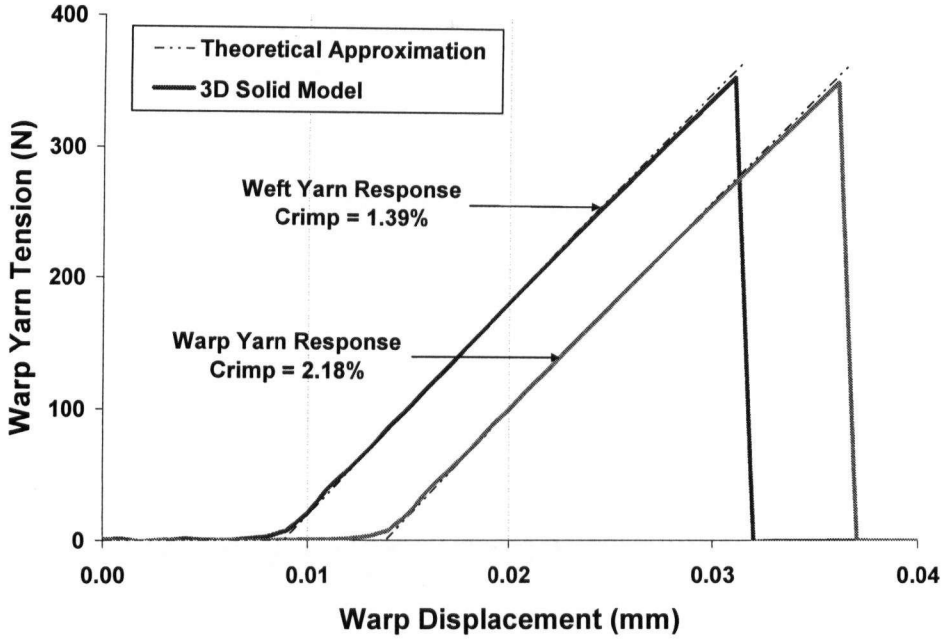

Figure 3 - 7: Single-yarn tensile test predictions for S-720 warp and weft yarns with 2.18% and 1.39% crimp, respectively.

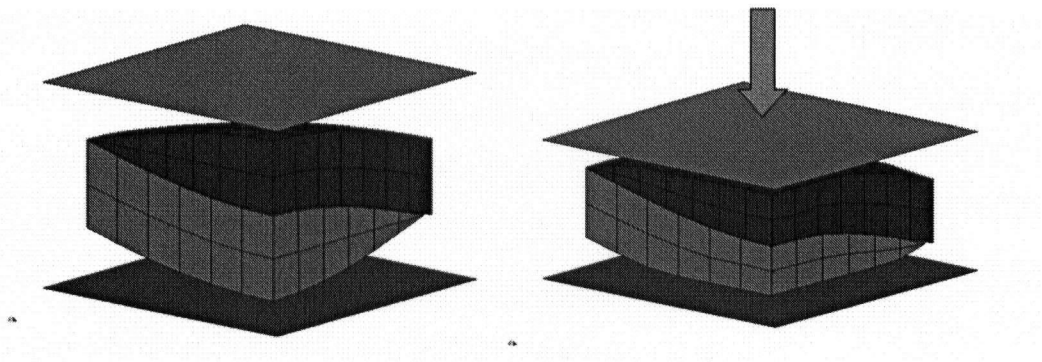

Figure 3 - 8: Simulation of the transverse compression test of a fabric unit cell (note that only a quarter of the unit cell is shown due to symmetry).

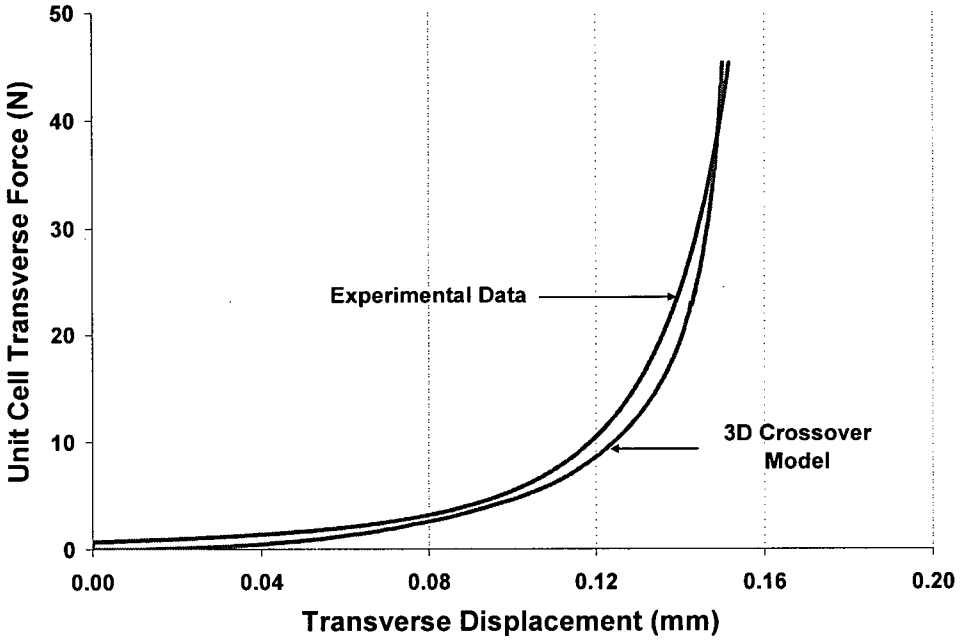

Figure 3 - 9: Transverse compression response of S-720 fabric unit cell, experiments compared to prediction of the 3D crossover model.

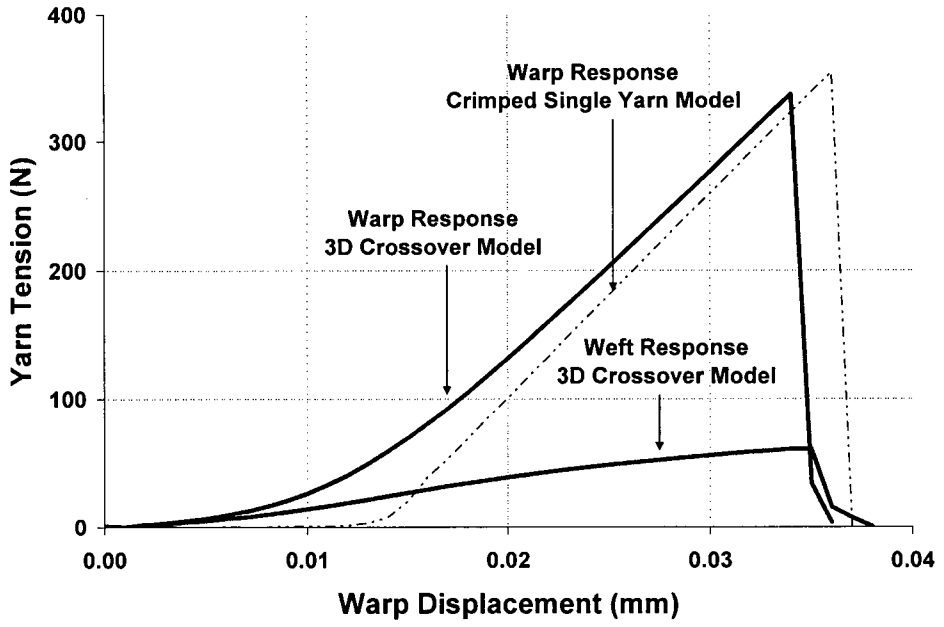

Figure 3 - 10: Tensile force developed in the warp and weft yarn of a single crossover model extracted from S-720 fabric.

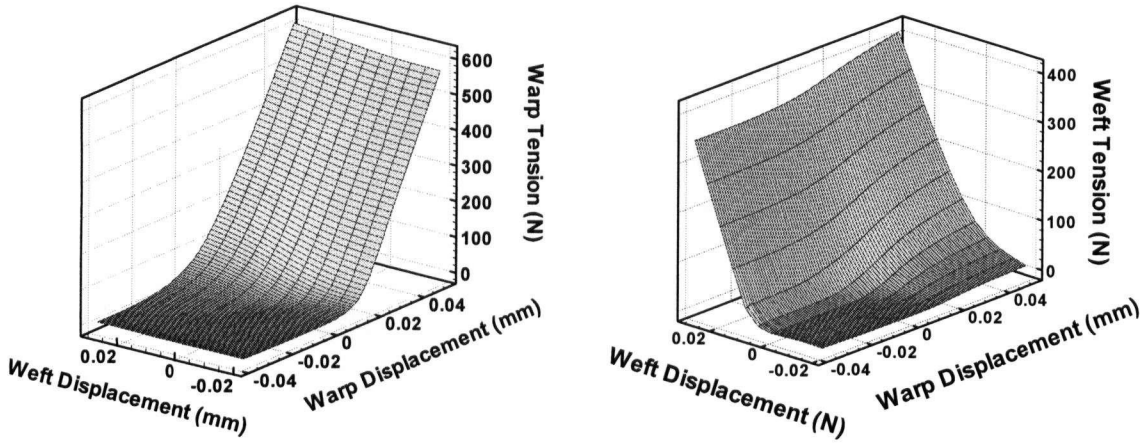

Figure 3 - 11: Warp and weft yarn tensile response surfaces as a function of yarn displacements, calculated for S-720 fabric unit-cell.

CHAPTER 4 - 2D SHELL CROSSOVER MODEL

4.1 INTRODUCTION

In this chapter, a meso-mechanical model of fabric crossover is developed that is implemented as a constitutive material model for an efficient shell element in LS-DYNA to capture the biaxial response of a fabric unit-cell. A comprehensive review of the relevant literature is first presented, to highlight the strengths and shortcomings of the unit-cell models currently studied by other scientists. The details of the shell constitutive model are then presented, followed by the verification of its response through comparison with the 3D unit-cell discussed in the previous chapter. A critical review of the capabilities and limitations of the model is presented along with some future recommendation for further improvements of the model.

4.2 SHELL-BASED FABRIC UNIT-CELL MODELS

Most fabrics possess a periodic geometry due to the specific pattern that the yarns are woven into, making them an excellent candidate for unit-cell analysis approach. Many researchers have tried to duplicate the mechanical response of fabrics in efficient membrane/shell elements. The elements developed are generally a continuum representation of the fabric through smearing the effects of warp and weft yarns into a two dimensional homogeneous material. While pin-jointed bar models of fabrics generally consider the response of warp and weft yarns to be decoupled, shell/membrane elements can accommodate the biaxial behaviour of the fabrics through implementation of appropriate constitutive models. This section includes a brief review of some of the unit-cell models that have employed shell/membrane elements as the basis to predict the fabric response.

Fabrics exhibit a non-linear structural response when stretched in the in-plane direction. Perhaps some of the earliest models of fabric crossover to capture the biaxial behaviour of the fabrics response under extensional and shear deformation modes are those of Kawabata et al. [57-59]. In a series of papers published in 1973, Kawabata et al. presented simple analytical models to capture the biaxial and uniaxial behaviour of symmetrically loaded yarn crossovers, as well as their shear response. Considering a linear representation of the yarn centrelines (Figure 4 - 1), the equilibrium of the crossing yarns under biaxial extension was satisfied through balancing the yarns tensile forces with the contact force developed between them. Kawabata et al. [57] accommodated the transverse deformation of the yarns due to the inter-yarn

contact force in determining the transverse position of the yarns satisfying the equilibrium of forces and compatibility of the deformations. This model was expanded in a following paper [58] to incorporate the bending resistance of yarns, most dominant in the uniaxial extension of the fabrics. The model developed to capture the shear response of the fabric [59] is discussed in Section 4.3.2.

Since the early work of Kawabata et al. [57], many other studies have adopted a similar, if not identical, approach to capture the biaxial response of fabrics using finite element analysis approach. Ivanov and Tabiei [30] developed a model that in their words was "a computational micro-mechanical material model for loosely woven fabric", with a unit-cell consisting of a crossover with the yarns interacting under the applied displacements. The yarn material was considered to be visco-elastic and its response modelled by a three-element spring/dashpot model. The model was implemented in the shell element and used to simulate ballistic impact experiments on Kevlar® 129 fabric targets.

King et al. [31, 32] published the details of a continuum-based model of a fabric unit-cell used to capture the deformational response of woven fabrics. The model relies on the selection of a representative model of weave geometry along with a constitutive relationship to capture the biaxial response of the fabric crossover. In this multi-scale approach, King et al. adopted a similar geometry to that of Kawabata et al. [57] to identify the in-plane extensional response of the yarns. The yarns were represented by an assembly of trusses pin-jointed together to make up the geometry of a certain weave. Other aspects of fabric response such as lateral compression and bending of yarns were

considered through individual springs in the unit-cell. With the knowledge of macroscopic deformations and displacements of the fabric at any time, the internal forces can be calculated from the unique configuration of the yarn network by minimizing the energy stored in the system. King et al. [57] compared and obtained good agreement between the predictions of their numerical model and the laboratory data for a variety of different experiments.

A detailed mesoscopic model for biaxial analysis of fabric deformation during the forming process was developed by Boisse et al. [27]. The initial geometry of yarns was represented by a combination of circular arcs and straight lines. The tensile response of the yarn was measured from simple tension tests. The model considered for transverse crushing law of the yarns was dependent on both the compressive state of the yarn and its axial tension. The friction between the yarns were considered implicitly to prevent relative sliding of the yarns, however, it was assumed that the frictional dissipative energy was too small compared to other energy components. Boisse et al. used this model to determine the forming of a fabric with a square punch and die. They reported that their biaxial unit-cell model was in good agreement with the experimental data and the predictions of a 3D micromechanical unit-cell model they developed for the same purpose (discussed in Chapter 4).

Xue et al. [38] proposed a combined micro/macro-mechanical non-orthogonal constitutive model to capture the large deformation behaviour of the fabrics in the thermo-forming process. The constitutive model developed considered details of the weave such as the dimensions of the fibres, yarns and the unit-cell, their material properties and the orientation of the yarns. The shear

properties of the fabric were then obtained from a mechanistic analysis of the unit-cell and the tensile properties of the fabric was obtained from a simplified analytical model. The tensile model is based on incorporating the interaction of the crossing yarns through correlation parameters determined by performing fabric uniaxial tensile tests.

Stubbs [40] presented the details of a model developed to capture the response of coated fabrics under multi-axial loading. This model represented the interlacing yarns and the added stiffness of the coating material through an assembly of truss elements. Stubbs' approach is very similar to that of Kawabata et al. [57] in principle, with only the addition of two horizontal bars (springs) connecting the yarn ends that would characterize the effect of the resin coating of the fabric.

Luo [39] developed a constitutive model for the unit-cell of fabric-reinforced flexible composites under biaxial loads. The response of the unit-cell was obtained using a strain energy approach, accounting for the yarn deformation through rigid body displacement resulting from the crimp exchange between the interacting yarns, and their cross-sectional changes under the contact force.

Tanov and Brueggert [36] proposed a model based on a representative cell approach to capture the extreme shearing of loosely woven fabrics during the expansion of side airbags in cars. The representative cell was embedded into a User Material model for membrane elements in LS-DYNA. The axial response of the yarns was represented by four bar members along the sides of the element and the shear response including the locking of fabric was captured by diagonal springs. Tanov and Brueggert considered the rotation of the fibres

during the shearing of the fabric, but seem to have overlooked the interaction of the crossing yarns during extension. The model developed by Tanov and Brueggert seems to be successful in capturing the response of airbags and appear to be in good agreement with the experimental measurements.

The continuum-based fabric unit-cell models discussed above are a few of many useful approaches to simulate the biaxial response of fabrics. The invaluable research and scientific development in the field of computational modeling of fabrics, some of which briefly discussed above, has been instrumental in the evolution of the approach presented in this thesis.

4.3 2D Shell Fabric Unit-cell - Model Basics

The 2D shell crossover model developed is based on a continuum representation of the fabric unit-cells using shell elements. The model captures the micromechanics of the fibres and yarns in the fabric through a smeared continuum approach. In establishing the basis of the model, it is assumed that the in-plane extensional mode of deformation is decoupled from the shearing mode. As a result, the constitutive relations developed for these two modes of deformation are derived separately. The following sections review the material models developed to capture the extensional and shearing response of a plain weave fabric unit-cell comprised of a single yarn crossover.

4.3.1 In-plane Extensional Response

Plain weave fabrics exhibit strong biaxial behaviour when extended in their plane. An analytical model is developed here to capture this biaxial response

considering the interaction of warp and weft yarns at fabric crossovers. The model presented here is inspired by Kawabata's linear crossover model [57], with further expansion to accommodate the non-linear geometry of the yarns. The model is based on tracking the location of the yarn centrelines (with geometries illustrated in Figure 4 - 2), as the two yarns interact under the applied displacements. The initial geometry of each yarn centreline is determined by its initial crimp value, obtained from the laboratory measurements. The analytical model developed here is aimed to capture the interaction of the warp and weft yarns and to determine their in-plane extensional response. In establishing the mathematical formulation of the model, several simplifying assumptions are considered, as listed below:

- It is assumed that the yarn profiles of the woven fabric are initially sinusoidal, based on the observations made through studying the fabric cross-sectional micro-images (see Appendix A). It is further assumed that the yarn profiles stay sinusoidal at all times, independent from the details of micro and macroscopic unit-cell displacements.

- The in-plane warp and weft displacements are assumed to be symmetrically applied at the two yarn ends, preventing any sliding between the two crossing yarns. This assumption results in an effectively pin-jointed model, since no relative in-plane yarn displacement occurs at the point of contact between the two yarns.

- As the warp and weft yarns interact, a contact force develops along their entire contact length while stretching under the applied displacements. It is assumed that there is no friction between the contacting yarns so that the

contact force at any point is perpendicular to the surface of the yarns. For the analysis of the crossover mechanics, only the resultant contact force acting at the centre-point of the crossover is considered.

- Figure 4 - 3 shows the free-body diagram of a yarn, with a continuous support system representing the effects of the crossing yarn. Since the contact between the two yarns is assumed to be frictionless, the supports act as rollers. Transverse compression of the yarns is illustrated by the springs between the supports and the yarn centreline. Due to symmetry, the resultant contact force acting on the yarn only has a component in the z-direction (normal to the fabric plane). The absence of friction between the yarns results in a constant tensile force along the yarn. Global equilibrium of the forces acting on the yarn is satisfied when the z-component of the yarn tension equals the resultant contact force, summed over the entire length of the yarn.

Taking the origin of the coordinates to be at the centre of the unit-cell, the shape of the yarn can be expressed with a cosine function, as depicted in Figure 4 - 4. For a unit-cell of width $2w_i$ in the i direction ($i = 1, 2$ for warp and weft, respectively), the profile of the yarn centreline can be expressed as:

$$f(x_i) = z_i = h_i \cos\left(\frac{\pi}{2w_i} x_i\right) \qquad (4 - 1)$$

where h_i is the height of the yarn centreline at the centre of the unit-cell ($x_i = 0$). The parameter w_i (in mm) can be calculated from the thread count of the crossing yarns, m_j (in threads/mm), as

$$2w_i = \frac{1}{m_j} \tag{4 - 2}$$

where $j = 2,1$ defines the perpendicular direction to yarn i. The initial value of h_i can be calculated mathematically from the crimped length of the yarn. Considering the yarn profile function presented in Equation 4 – 1, the length, S_i, of the yarn at any moment can be calculated from the equation below.

$$S_i = 2\int_0^{w_i} \sqrt{1 + \left(\frac{\pi h_i}{2w_i}\right)^2 \sin^2\left(\frac{\pi}{2w_i}x\right)}\,dx \tag{4 - 3}$$

The initial length of the yarn can also be determined from yarn crimp, cr_i:

$$S_{0i} = 2w_i(1 + cr_i) \tag{4 - 4}$$

From Equations 4 – 3 and 4 – 4, the nonlinear equation needed to calculate the value of h_{0i} is obtained:

$$w_i(1 + cr_i) = \int_0^{w_i} \sqrt{1 + \left(\frac{\pi h_{0i}}{2w_i}\right)^2 \sin^2\left(\frac{\pi}{2w_i}x\right)}\,dx \tag{4 - 5}$$

It is basically assumed that the yarns maintain their sinusoidal profile during deformation. Application of a set of symmetric displacements to the warp and weft yarns would lead to the development of contact force between them as a result of their interaction with each other. The consequent motion of the central point of the crossover in the out-of-plane direction is an outcome of this meso-mechanical interaction in a fabric crossover. Figure 4 - 5 depicts the geometry of the yarns in the warp and weft directions before and after the application of symmetric displacements. Note that the two perpendicular yarns are shown in the same plane for illustration purposes. The geometry of the yarns after the

application of symmetric displacements d_1 and d_2 can be expressed in terms of their new heights h_1 and h_2. The challenge at this point is to determine the values of the two unknowns, h_1 and h_2 for a given set of displacements d_1 and d_2.

For any displacement d_i applied to the yarn i $(i=1,2)$ of the crossover, there is an equilibrium configuration with a yarn height of h_i. The applied displacement leads to the development of a tensile force, T_i, and a contact force, F_{c_i}, in the yarn. This contact between the two yarns leads to their deformation in the transverse direction denoted by d_{c_i}. By equilibrium, the resultant contact forces acting on the two yarns should be equal; in other words:

$$F_{c_1} = F_{c_2} \tag{4 - 6}$$

The tensile forces developed in the yarns due to their in-plane deformations are functions of the yarn material and geometrical properties. The bending/shear mechanical properties of the yarns are usually very small compared to their axial tensile stiffness and thus considered to be negligible in this study. However, due to the potential numerical instabilities resulting from this assumption, the user is provided with the option of including some bending resistance to the yarns as a percentage of the yarn tensile stiffness. This has proven to be useful in significantly reducing the numerical oscillations, especially where the fabric is subjected to low levels of load or when the yarns lose contact due to buckling in a compressed unit-cell. For the case of Kevlar®

129 material, the tensile behaviour of the yarns is assumed to simply follow a linear elastic model, defined by the equation below:

$$T_i = \frac{E_i A_{si}}{S_{0i}}(S_i - S_{0i}) \tag{4 - 7}$$

where E_i is the elastic modulus of the fibres in yarn i, A_{si} is the cross-sectional area of the fibres in the yarn, and S_{0i} and S_i are the initial and the current length of the yarn. The equivalent contact force that develops between the two yarns, F_{c_i}, can be estimated by enforcing the equilibrium of yarn i, as follows:

$$F_{c_i} = 2T_i \sin\alpha_i \tag{4 - 8}$$

where α_i is the yarn-end slope (see Figure 4 - 5). This slope is calculated using the first derivative of the yarn shape function calculated at the yarn end, i.e.

$$\tan\alpha_i = \left.\frac{dz}{dw}\right|_{w=-w_i} = \frac{\pi h_i}{2w_i} \tag{4 - 9}$$

Therefore,

$$\sin\alpha_i = \frac{\tan\alpha_i}{\sqrt{1+\tan^2\alpha_i}} = \frac{\pi h_i}{\sqrt{(2w_i)^2 + (\pi h_i)^2}} \tag{4 - 10}$$

The relationship between the transverse contact force acting on the yarns and their compression d_{ci} can be generally expressed as:

$$d_{c_i} = Q(F_{c_i}) \tag{4 - 11}$$

The compression model developed for the transverse mechanical response of the yarns was discussed in detail in Chapter 3. This relationship can be expressed in the following form:

$$d_{c_i} = a - \frac{b}{\sqrt[3]{F_{c_i}}} \tag{4 - 12}$$

where a and b are constants. The method to determine a and b is discussed later in this chapter.

In addition to the equilibrium condition expressed in Equation 4 – 6, the geometric compatibility of the yarn centerlines should also be satisfied. For this purpose, the original and current shape of the yarns (h_1 and h_2), transverse deformation of the two yarns and the initial gap, g, between them are considered in the compatibility expression given below:

$$h_1 + h_2 = h_{01} + h_{02} - d_{c1} - d_{c2} - g \tag{4 - 13}$$

Equations 4 – 6 and 4 – 13 are used to determine the two unknowns h_1 and h_2. Due to the complex nature of these two equations, an explicit closed-form solution is not readily obtainable. Therefore, h_1 and h_2 are calculated using a numerical approach that is capable of solving such multi-variable non-linear system of equations. The Newton-Raphson technique is used to estimate the unknowns h_1 and h_2 by solving a system of nonlinear equations applied to the objective functions f_1 and f_2, defined as:

$$f_1 = F_{c_1} - F_{c_2} \tag{4 - 14}$$

$$f_2 = h_1 + h_2 + d_{c_1} + d_{c_2} + g - h_{01} - h_{02} \tag{4 - 15}$$

Details of the Newton-Raphson iterative technique can be found in the literature (e.g. see [60]). The first step in setting up the iterative scheme is to determine the Jacobian matrix, $\underline{J}$, defined as:

$$\underline{J} = \begin{bmatrix} \frac{\partial f_1}{\partial h_1} & \frac{\partial f_1}{\partial h_2} \\ \frac{\partial f_2}{\partial h_1} & \frac{\partial f_2}{\partial h_2} \end{bmatrix} \tag{4 - 16}$$

The components of the Jacobian matrix can be calculated from the partial derivatives of equations developed earlier. The terms on the first row of the Jacobian matrix J_{11} and J_{12} can be determined as:

$$J_{11} = \frac{\partial f_1}{\partial h_1} = \frac{\partial}{\partial h_1}\left(F_{c_1} - F_{c_2}\right) = \frac{\partial F_{c_1}}{\partial h_1} \tag{4 - 17}$$

$$J_{12} = \frac{\partial f_1}{\partial h_2} = \frac{\partial}{\partial h_2}\left(F_{c_1} - F_{c_2}\right) = -\frac{\partial F_{c_2}}{\partial h_2} \tag{4 - 18}$$

since the contact force acting on a yarn is only a function of the geometry of that yarn, in other words:

$$\frac{\partial F_{c_1}}{\partial h_2} = \frac{\partial F_{c_2}}{\partial h_1} = 0 \tag{4 - 19}$$

The derivative of the contact force with respect to the height is needed for each yarn to be substituted in Equations 4 – 17 and 4 – 18. Differentiating Equation 4 – 8 with respect to h_i using the chain rule results in the following relation:

$$\frac{dF_{c_i}}{dh_i} = 2\sin\alpha_i \frac{dT_i}{dh_i} + 2T_i \frac{d(\sin\alpha_i)}{dh_i} \tag{4 - 20}$$

Differentiating Equation 4 – 10 results in

$$\frac{d(\sin\alpha_i)}{dh_i} = \frac{4\pi w_i^{\,2}}{\left[(2w_i)^2 + (\pi h_i)^2\right]^{1.5}} \tag{4 - 21}$$

and using Equation 4 – 7,

$$\frac{dT_i}{dh_i} = \frac{E_i A_{si}}{S_{0i}} \frac{dS_i}{dh_i} \tag{4 - 22}$$

Using Leibniz Integral Rule [61]:

$$\frac{\partial}{\partial z} \int_{a(z)}^{b(z)} f(x,z)dx = \int_{a(z)}^{b(z)} \frac{\partial f}{\partial z} dx + f(b(z),z)\frac{\partial b}{\partial z} - f(a(z),z)\frac{\partial a}{\partial z} \tag{4 - 23}$$

the term $\frac{dS_i}{dh_i}$ can be evaluated as

$$\frac{dS_i}{dh_i} = \left(\frac{\pi}{2w_i}\right)^2 h_i \int_0^{w_i} \frac{1}{\sqrt{1+\left(\frac{\pi h_i}{2w_i}\right)^2 \sin^2\left(\frac{\pi}{2w_i}x\right)}} \sin^2\left(\frac{\pi}{2w_i}x\right)dx \tag{4 - 24}$$

Thus, Equation 4 – 22 can be evaluated as

$$\frac{dT_i}{dh_i} = \frac{E_i A_{si}}{S_{0i}} \left(\left(\frac{\pi}{2w_i}\right)^2 h_i \int_0^{w_i} \frac{1}{\sqrt{1+\left(\frac{\pi h_i}{2w_i}\right)^2 \sin^2\left(\frac{\pi}{2w_i}x\right)}} \sin^2\left(\frac{\pi}{2w_i}x\right)dx \right) \tag{4 - 25}$$

Equations 4 – 21 and 4 – 25 are inserted into 4 – 20 to evaluate J_{11} and J_{12}. The other components of the Jacobian matrix can now be determined:

$$J_{21} = \frac{\partial f_2}{\partial h_1} = \frac{\partial}{\partial h_1}\left(h_1 + h_2 + d_{c_1} + d_{c_2} + g - h_{01} - h_{02}\right) \tag{4 - 26}$$

using the chain rule,

$$J_{21} = 1 + \frac{d(d_{c_1})}{dh_1} = 1 + \frac{d(d_{c_1})}{dF_{c_1}} \frac{dF_{c_1}}{dh_1} \tag{4 - 27}$$

The value of $\frac{dF_{c_1}}{dh_1}$ is obtained from Equation 4 – 20, and $\frac{d(d_{c_1})}{dF_{c_1}}$ is evaluated from differentiation of Equation 4 – 12:

$$\frac{d(d_{c_1})}{dF_{c_1}} = \frac{b}{3}\frac{1}{(F_{c_1})^{4/3}} \tag{4 - 28}$$

Similarly for J_{22} we have

$$J_{22} = \frac{df_2}{dh_2} = 1 + \frac{d(d_{c_2})}{dh_2} = 1 + \frac{d(d_{c_2})}{dF_{c_2}}\frac{dF_{c_2}}{dh_2} \tag{4 - 29}$$

where

$$\frac{d(d_{c_2})}{dF_{c_2}} = \frac{b}{3}\frac{1}{(F_{c_2})^{4/3}} \tag{4 - 30}$$

With all the components of the Jacobian matrix determined, one can perform an iterative numerical scheme to find the values of h_1 and h_2 for a given set of d_1 and d_2 according to the algorithm outlines in Appendix B. Other physical and geometrical characteristics of the crossover such as the contact force and yarn tension can then be calculated, resulting in a biaxial response that incorporates the interaction of the yarns in a single crossover.

4.3.2 Shear Response

One of the distinctive attributes of plain weave fabrics is their unconventional shear behaviour. Due to the specific arrangement of the yarns in the weave structure, the fabric can shear easily up to a certain locking angle where the compacted yarns resist further shearing. Many scientists in the textile industry and the field of textile composites manufacturing have studied this behaviour, some of which are reviewed here.

Kawabata et al. [59] introduced a semi-empirical model to capture the shear deformation response of fabrics. The overall shear behaviour of fabrics under

biaxial tensile and shear deformations was approximated based on utilizing a linear empirical relationship to estimate the torque required to change the angle between the crossing yarns. The unknown parameters in this empirical relationship, comprised of a frictional and an elastic component, were calibrated through experimental measurements.

Prodromou and Chen [62] studied the relationship between shear angle and wrinkling of textile composite performs. They performed frame shear tests on glass fabrics with plain weave, four- and eight-harness satin weaves. Their experimental results showed that two distinct regions can be distinguished on the load versus shear angle response of the fabrics: prior to locking where the trellis mechanism dominates the response and post-locking where the fabric starts to wrinkle out-of-plane due to high shear modulus in the fabric. They found that more conformable weaves such as satin would reach the shear locking at larger deformations, as is also the case for smaller yarn size at a given yarn count. The shear tests performed by Prodromou and Chen [62] indicated that the relative motion of the yarns at the centre of a fabric crossover does not occur during the trellising, meaning that the crossing yarns can effectively be considered pinned. Based on these observations, Prodromou and Chen [62] proposed a method for calculating the locking angle. In their proposed pin-jointed model, they assumed that shear locking occurs when the space between the parallel yarns closes, and moved on to calculate the locking angle by setting the distance between the yarns of the deformed fabric equal to their width. Based on the results obtained from this mechanistic pin-jointed model, they concluded that other factors not considered such as friction and

changes in the yarn width and their spacing can result in a different measured locking angle compared to the predicted value.

McBride and Chen [63] proposed a pin-jointed shear model that would consider the geometry of the fabric unit-cell with sinusoidal yarn shapes during the shearing deformation. In this model, transverse yarn compaction was included as a deformation mechanism in addition to the trellising. The model predictions of yarns width and fibre volume fraction as a function of shear angle showed good agreement with the observed values, despite the inaccuracies stemming from other factors not accounted for, such as friction and fibre waviness within a yarn.

The model presented in this study is motivated by the two models of Prodromou and Chen [62] and McBride and Chen [63]. A trellis mechanism is considered where the shear response of a crossover is subdivided into three distinct regions. Initially, due to the presence of gap between parallel yarns, the lone resisting mechanism against shearing is considered to be friction, leading to a very small initial shear modulus (referred to here as zone I). Further shearing of the unit-cell would give rise to the shear modulus, as the yarns start to interact and compact each other transversely (zone II). Eventually, the compaction of the yarns reaches a maximum value, after which the shear modulus is at its maximum and further shearing deformation of the fabric would lead to wrinkling (zone III).

The information obtained from the picture-frame tests are used to set up a shear model for the plain weave fabric. The fabric geometry changes from its initial state to deformed state are schematically shown in Figure 4 - 6. As the

fabric shears, the warp-to-weft angle β decreases from its original value, β_0., thus reducing the spacing between the adjacent parallel yarns. This distance, u, and its reduction are shown in Figure 4 - 6. The relationship between the shear angle and yarn spacing can be derived from the fabric deformed geometry, as:

$$\sin\beta = \frac{u}{L} \tag{4 - 31}$$

where L is the side-length of the fabric in picture frame shear test. The presence of in-plane gap, p, between adjacent yarns in the undeformed configuration allows the fabric to shear freely to a certain angle, β_1. At this angle, the inter-yarn gap diminishes and the parallel yarns start to get in contact with each other. Angle β_1 can be calculated as

$$\sin\beta_1 = \frac{u_0 - p}{L} \tag{4 - 32}$$

where u_0 is the initial distance between the yarns. Further shearing of the fabric leads to gradual compaction of the yarns, up to an angle β_2, where the yarns reach their maximum compaction. This angle can be calculated from the following equation:

$$\sin\beta_2 = \frac{u_2}{L} \tag{4 - 33}$$

where u_2 corresponds to the yarns spacing at maximum compaction. In order to calculate u_2, certain assumptions need to be made. It is assumed that the fabric thickness, as reported in many other studies, remains more or less constant and is decoupled from the shear deformation. Based on this assumption, it is concluded that the amplitude of the sine function representing

the yarn profiles remains constant during shear. It is further assumed that the yarn cross-sectional shape becomes elliptical at the point of full compaction. In reality, the yarn compaction would not be uniform along its length due to the localized interaction of the crossing yarns and their specific configuration in a highly sheared fabric. To account for this effect, an area reduction factor, K_s, is considered which results in a yarn packed area of . Using the schematic of the yarns in the sheared unit cell shown in Figure 4 - 7, the compacted area can be calculated from the formula below:

$$A_p = K_s A_s = \pi u_2 \frac{t}{2} \tag{4 - 34}$$

The values of u_2 calculated from the above equation can be substituted in Equation 4 – 33 to determine the locking angle β_2.

Using the locking angles β_1 and β_2, the corresponding shear strains γ_1 and γ_2 can be determined. The shear stress-strain relationship is formulated such that the instantaneous shear strain γ is related to the secant shear modulus G by the function below (also schematically shown in Figure 4 - 8):

$$G = \begin{cases} G_1 & 0 < \gamma \le \gamma_1 \\ G_1 + \dfrac{G_2 - G_1}{\gamma_2 - \gamma_1}(\gamma - \gamma_1) & \gamma_1 < \gamma < \gamma_2 \\ G_2 & \gamma \ge \gamma_2 \end{cases} \tag{4 - 35}$$

A similar relation exists between the shear strain γ and shear modulus for values smaller than zero, in other words, the shear model is the same for positive and negative values of shear strain.

4.3.3 Development of User Material Model for Shell Elements

The main goal of this work is to develop an efficient shell element that performs similar to that of a yarn crossover. This shell element takes advantage of a meso-mechanical model of the fabric crossover and can be categorized between the simple pin-jointed cable model and the detailed 3D fabric crossover model of the fabric unit-cell both in terms of complexity and efficiency. In other words, the shell crossover model would be able to capture many details of the weave and yarns that the pin-jointed bar model would overlook, while it is significantly more efficient numerically compared to the 3D fabric crossover model. This section discusses the details of the User Material Model (UMAT) development to provide the constitutive relationship for the smeared shell element that represents a fabric unit-cell.

In developing the UMAT for the shell element, several simplifying assumptions are made based on the physical behaviour of a fabric. Since fabrics generally have very low bending and shear stiffness, it is assumed that their out-of-plane stiffness is insignificant compared to their in-plane stiffness. The in-plane extensional and shear responses of the fabric are decoupled and treated separately based on the mathematical models developed in the preceding sections.

The interface between the main engine of the finite element code, LS-DYNA and the user developed material routine, UMAT, is simple and efficient. At each time step, LS-DYNA passes the element strain increments evaluated at the shell element integration point (centre of the element for the constant stress shell elements used in this study) in the local coordinate system to the user

material routine. In return, the components of the element stress tensor are computed by the UMAT and returned to the code for continuation of the analysis. The goal in setting up the UMAT is to use the strain increments to determine the unit-cell displacements and warp-to-weft angle needed, respectively, by the extensional and the shear models discussed.

The basic knowledge of stretches in the crossing yarns and their relative angles are essential for determination of the forces developed in the crossover. To capture the extension and rotation of warp and weft yarns at each time step, two vectors are attached to the crossing virtual yarns, whose configuration is constantly updated throughout the analysis. The deformation gradient, $\underline{F}^n$, pertaining to the incremental changes in the displacement field between the two consecutive time steps n and $n-1$ can be assembled from the strain increments as follows:

$$\underline{F}^n = \left(\underline{I} + 2\underline{\Delta\varepsilon}^n\right)^{0.5} \approx \underline{I} + \underline{\Delta\varepsilon}^n = \begin{bmatrix} 1+\Delta\varepsilon_x{}^n & \Delta\varepsilon_{xy}{}^n \\ 0 & 1+\Delta\varepsilon_y{}^n \end{bmatrix} \qquad (4-36)$$

where $\underline{\Delta\varepsilon}^n$ is the tensor of the strain increments with components $\Delta\varepsilon_x{}^n$, $\Delta\varepsilon_y{}^n$ and $\Delta\varepsilon_{xy}{}^n$ in the local coordinate system, xyz, and $\underline{I}$ is the unit matrix. In the convention used in this study, the local x-axis is defined parallel to the $n_1 - n_2$ edge, as shown in Figure 4 - 9. The z-axis is taken to be normal to the element mid-plane and the y-axis is determined by the cross product

$$y = z \times x \qquad (4-37)$$

This local axes system in LS-DYNA is based on the shell node numbering, as defined in the User's Manual [54]. The material axes, on the other hand, are

assumed to be parallel to the warp and weft yarns. The strain increments obtained from the deformation of the element need to be converted into the unit-cell displacement in the material directions (along warp and weft yarns) to determine the biaxial response of the crossover. In the un-deformed configuration, the material and local axes coincide in the case of uniform rectangular elements. As the element undergoes large displacements and rotations, the angle between the local and the material axes (defined by the warp and the weft) changes. The angle between the material and local axes of the element is thus updated at each time step in order to determine the displacements applied to the warp and weft yarns.

To track the configuration of the material axes in the local coordinate system during the analysis, two vectors q_{01} and q_{02} are considered parallel to the warp and weft yarns, respectively. The coordinates of these two vectors are updated at each time step in the local coordinate system (Figure 4 - 9) using the deformation gradient as follows:

$$\underline{q_i}^n = \underline{F}^n \underline{q_i}^{n-1} \tag{4 - 38}$$

where $\underline{q_i}^n$ and $\underline{q_i}^{n-1}$ are the i material vector ($i = 1,2$ for warp and weft) at time steps n and $n-1$, respectively. The angle between each material vector and the local x-axis can be determined as follows:

$$\theta_i^n = \tan^{-1}\left(\frac{q_{i_y}^n}{q_{i_x}^n}\right) \tag{4 - 39}$$

where

$$\underline{q_i}^n = \begin{bmatrix} q_{i_x}^n & q_{i_y}^n \end{bmatrix}^T \tag{4 - 40}$$

The strain increment tensor needs to be transformed into the direction of the two material vectors. The appropriate transformation matrix is calculated for each material vector based on its current angle:

$$\underline{\Theta_i}^n = \begin{bmatrix} \cos\theta_i^n & \sin\theta_i^n \\ -\sin\theta_i^n & \cos\theta_i^n \end{bmatrix} \tag{4 - 41}$$

The strain increments are subsequently rotated to the material directions using the transformation matrix as follows:

$$\underline{\Delta\varepsilon_i}^n = \underline{\Theta_i}^n \underline{\Delta\varepsilon}^n \underline{\Theta_i}^{nT} \tag{4 - 42}$$

The displacements along the yarns can then be calculated using the basics of continuum mechanics. The incremental stretch of a unit vector in the material directions from time step $n-1$ to n can be calculated from the equation below:

$$\lambda_i^n = \sqrt{1 + 2\Delta\varepsilon_{i11}^n} \approx 1 + \Delta\varepsilon_{i11}^n \tag{4 - 43}$$

The total stretch in the material directions is updated at each time step using the incremental stretch values of Equation 4 – 43, as shown below:

$$\Lambda_i^n = \Lambda_i^{n-1} \lambda_i^n \tag{4 - 44}$$

Displacement along yarn i at time step n would then be equal to

$$d_i^n = \left(\Lambda_i^n - 1\right) w_i \tag{4 - 45}$$

where w_i is the initial unit cell width obtained from Equation 4 -2. Knowing the displacements d_1 and d_2, the meso-mechanical crossover model can be used to calculate the tensile forces developed in the warp and weft yarns. In order to determine equivalent stress components that would result from these yarn

tensions, it is assumed that each yarn occupies only half of the shell thickness. As depicted in Figure 4 - 10, independent stress tensors in the top and bottom halves of the smeared shell are assembled that represent the contribution of the warp and weft (fill) yarns to the overall stress tensor. The components of the yarn tensors are calculated from the forces exerted on the yarn, in this case, the axial yarn tension:

$$\underline{\sigma_i}^n = \begin{bmatrix} \frac{T_i}{A_i} & 0 \\ 0 & 0 \end{bmatrix} \tag{4 - 46}$$

where A_i is the cross-sectional area of the equivalent top or bottom half-thickness. The above tensor can also accommodate future model developments in a case where definition of other yarn stress components (e.g. resulting from contact between the yarns due to shearing of the crossover, etc.) is required.

The individual yarn stress tensors are then transformed back into the local coordinate system using the transformation matrix, $\underline{\Theta_i}$:

$$\underline{\bar{\sigma}_i}^n = \underline{\Theta_i}^T \underline{\sigma_i}^n \underline{\Theta_i} \tag{4 - 47}$$

The total element stress tensor is the volume average of the two yarn stress tensors, as calculated below:

$$\underline{\sigma_{avg}}^n = \frac{\underline{\bar{\sigma}_1}^n + \underline{\bar{\sigma}_2}^n}{2} \tag{4 - 48}$$

However, an extra term should be added to the in-plane shear stress that would represent the interaction of the crossing yarns in shear, as discussed in Section 4.3.2. This additional shear term can easily be determined from the

current angle between the two yarns, calculated from the updated coordinates of the two material vectors.

Failure of individual yarns in warp and weft directions is activated based on an instantaneous failure criterion, i.e. comparing the tensile force of every yarn to their ultimate tensile load reported by the yarn manufacturer. Once the yarn tension has surpassed its ultimate tensile load, it is flagged and permanently eliminated from the shell element. As a result, the shell element is only capable of carrying load in the direction where the yarn has not failed. Once both the warp and weft yarns tensile forces exceed their failure threshold, they are eliminated from the shell element, which is no longer capable of carrying any extensional load. Such a shell element is then eroded from the finite element mesh. In general finite element terms, erosion of an element implies that the code removes the element from the calculation while retains its mass properties on the nodes attached to it. Every node that becomes unconstrained as a result of eroding all the elements attached to it is also eliminated from the analysis. Erosion of shell elements in LS-DYNA can be activated from within UMAT based on a user-defined criterion that prompts the code to physically eliminate an element from the finite element mesh. Erosion of the shell elements with extensive unrealistic deformation (usually occurring due to the failure of one yarn only) is also triggered via a user-controlled parameter, to avoid numerical instabilities.

The representative shell element, consisting of the analytical model described above, provides the biaxial extensional and shear responses of the fabric unit-cell under the applied deformation. Figure 4 - 11 shows a simple flowchart

generally highlighting the process of calculating element stresses at each time step from the applied strains (more details can be found in Appendix B).

LS-DYNA provides an extensive library of shell elements with different formulations. The main two element types considered for this study are Hughes-Liu (HL) and Belytschko-Tsay (BT) four-noded shell elements:

BT shell elements are one of the most efficient elements implemented in LS-DYNA. Taken from the work by Belytschko et al. [64], these elements take advantage of a combined co-rotational and velocity-strain formulation to provide an efficient algorithm for small element strains. The formulation is based on a co-planar geometry, so erroneous results may result from non-coplanar deformations.

HL elements, taken from the work by Hughes and Liu [65, 66], are based on an incrementally objective formulation, incorporating transverse shear and thickness thinning. Since no geometric assumptions are considered in developing the formulation of the HL elements, these shells can handle warpage when the nodes are not coplanar. However, the under-integrated HL elements with 4066 operations are more demanding computationally than the BT elements with 725 mathematical operations [54]. In this study, the selectively-reduced HL formulation is used for the shell element, although the response of the model does not seem to be specifically affected by the choice of the shell element formulation (HL or BT).

4.3.4 Determination of the input parameters

The input parameters for the representative shell model are determined either directly from the results of mechanical tests on yarns or indirectly from the analysis of the 3D unit-cell. The process of obtaining the input data is highlighted in this section.

4.3.4.1 Extensional Response of the Fabric Unit-cell

The extensional response of the individual yarns is determined by simulating single-yarn extensional tests in the warp and weft directions. The values of elastic modulus and failure strain of the yarns are supplied to the shell elements and the single yarn tensile response of the warp and weft yarns are simulated and compared to the simple analytical prediction of the tensile response of crimped single yarns (previously discussed in Section 3.4.3.1). Figure 4 - 12 shows the tension-displacement response of the S-726 warp and weft yarns with crimp values reported in Table 2 - 1. Good agreement was found between the crimped yarn tensile responses obtained from the above two methods.

4.3.4.2 Transverse Compression of the Yarns

The transverse compression behaviour of yarns during biaxial extension inside the fabric is extremely complicated. Examination of the yarns responses in the 3D crossover model revealed that the relationship between the contact force between the yarns and their deformation changes based on the type of loading the fabric is subjected to. This is especially true for the two loading cases of transverse compression and biaxial extension of the fabric since the different contact areas and yarn geometries (as seen in Figure 4 - 13) lead to different

compressive responses. The implication of this discrepancy is that the test results from the fabric compression tests cannot be used directly for the fabric biaxial extension simulations. In order to obtain a yarn compression response that truly represents the transverse behaviour of yarns in unit-cell biaxial extension, the 3D crossover model is used. After calibrating the transverse mechanical properties of the yarns (see Section 3.4.3.2), biaxial tests are performed and the contact force developed between the two yarns is monitored against the compression of the yarns. The transverse compressive responses of the yarns are plotted in Figure 4 - 14 for the two loading cases. The best fit to the compression data obtained from biaxial simulation of the unit-cell using the 3D crossover model is fed into the shell element as a refined transverse force-displacement response of the yarns.

4.3.4.3 Shear Response of the Fabric Unit-cell

The response of the unit-cell to pure shear deformation follows the model discussed in Section 4.3.2. The shear modulus in the locked position, G_2, is calculated based on the assumption that the fabric crossover deformed beyond the locking angle behaves as an isotropic media upon further deformation. G_2 is thus chosen to be equal to:

$$G_2 = \frac{E}{2}\frac{A_s}{A_{sh}} \tag{4 - 49}$$

where A_s and A_{sh} are the yarn and shell cross-sectional areas, respectively, and E is the yarn elastic modulus. The initial shear modulus G_1 is chosen to be a fraction of G_2 (e.g. $G_1 = 0.1\% \times G_2$ in most cases), since the yarns easily rotate with respect to each other prior to shear locking. Limit strains γ_1 and γ_2 are

evaluated from the weave geometric parameters, specifically the initial gap between the yarns and the yarn width. For this purpose, the area reduction factor, K_s needed to be estimated. In this study, K_s was evaluated by simply shearing a single fabric layer by hand on a flat frictionless surface until the occurrence of wrinkles. The shear angles corresponding to the onset of wrinkling were then recorded for all six fabrics and upon further analysis, it was found that an area reduction factor of 0.65 would best capture the measured locking angles. This compaction ratio is smaller than the packing ratio of 0.907 for hexagonal and 0.785 for square packing of cylindrical fibres in a yarn. This discrepancy was attributed to the fact that the specific weave geometry and the interlacing of warp and weft yarns would introduce an extremely non-uniform compaction along the length of each yarn, leading to a lower equivalent compaction ratio. The input values to the shear model for all six Kevlar® 129 fabric types are presented in Table 4 - 1.

4.4 SIMULATIONS AND VERIFICATIONS

The representative shell element developed in the previous sections is checked against various other models to verify the accuracy of its predictions. This section reviews the important details of such verifications and highlights the capabilities and limitations of the shell crossover model.

4.4.1 Comparison with 3D crossover model

One of the main fabric modes of deformation in ballistic impact is its in-plane biaxial extension. Any continuum model of woven fabrics should be able to

realistically capture the coupled warp and weft behaviour and their interaction as they are loaded. This section presents the verification studies of the 2D crossover model embedded in the representative shell element with the predictions of the 3D crossover model presented in Chapter 3.

The tensile response of the warp and weft yarns of a fabric unit-cell predicted using the shell element is compared to that of the 3D crossover model. Figure 4 - 15 shows the yarn tensions in the warp and weft directions of S-726 fabric unit-cell as a function of the warp displacement applied to the crossover while the weft yarn is held fixed. Other mechanical and/or geometrical parameters governing the interaction of the two yarns can also be investigated. Figure 4 - 16 depicts the changes in the heights of the yarn mid-plane profile (h_1 and h_2) showing the crimp exchange between the two crossing yarns with the warp displacement applied. It can be seen that with increasing warp displacement, h_1 decreases and the interaction of the two yarns results in increasing h_2. The work required to stretch the fabric unit-cell is also plotted as a function of the warp displacement in Figure 4 - 17. It can be seen in these figures that the two models predict very similar responses for the fabric unit-cell despite their different approaches. However, the subtle differences between the two models stem from the many assumptions embedded in their specific approach. Some of these differences are listed below:

- Yarn cross-section can change in the 3D solid model due to the interaction of the two yarns and the presence of the contact force. This is shown in Figure 4 - 18, for a single S-726 fabric unit-cell during biaxial extension simulation using the 3D crossover model. The change in the cross-sectional

shape of the yarn can further result in a non-uniform contact force distribution along the yarns and lead to non-prismatic yarn cross-sections. This phenomenon is considered to have a minimal effect on the response of the unit-cell and thus ignored in the shell crossover model.

- One of the major assumptions in developing the extensional response of the fabric crossover is that the yarn profiles remain sinusoidal throughout the deformation. This theory can easily breakdown, especially if the cross-sectional shape of the yarns change and lead to an irregular contact between the yarns, e.g. contact concentrated only in the middle area of the yarn. Figure 4 - 19 and Figure 4 - 20, respectively, show the profiles of warp and weft yarns extracted from S-726 fabric unit-cell predicted by the 3D crossover model and shell element. As evident from these figures, while the predictions of the two models match well for the warp profile, this cannot be said in the case of the weft yarn.

- The transverse compression model implemented in the extensional response of the shell elements assumes identical compression responses for the two yarns. This is clearly not the case in the 3D solid model due to the differences in the warp and weft yarn shapes and their initial void ratio, which in turn can affect the response of the unit-cell.

- The transverse compression model implemented in the shell element expresses the transverse deformation of the yarn only as a function of the contact force. The dependence of the compressive model on the ratio of warp to weft displacement is ignored in the shell model, while this is intrinsically included in the 3D crossover model.

4.4.2 Comparison with pin-jointed cable model

The ballistic response of a single layer of fabric is predicted using shell elements and compared with that of the cable-based pin-jointed model. The discrete pin-jointed bar models are one of the earliest numerical models developed to capture the response of fabrics in a variety of applications. As discussed in Chapter 2, the cable models of fabric are based on representing the fabric layer as a series of masses and cable elements initially arranged in orthogonal directions. In this study, the elements used to construct the pin-jointed cable model of fabric are identical to the bar elements used to represent the axial stiffness of the fibres in the 3D crossover model.

The major difference between the shell-based and cable-based fabric models is the biaxial nature of the response, i.e. the biaxial extensional response embedded in the shell elements is ignored in the cable model due to the decoupled nature of the warp and weft yarns in that approach. This decoupled warp/weft behaviour of the cable model can be reproduced in the shell-based fabric model by over-softening the transverse compression response of the yarns and eliminating the interaction of the warp and weft yarns. In a way, the cable-based pin-jointed fabric model can be recovered from the shell-based model as a special case.

In order to show that the discrete cable model is truly a special case of the biaxial shell model, the dynamic response of a fabric panel in ballistic impact predicted by the shell-based and cable-based models are compared. The impact events modelled in this thesis are simulations of the instrumented ballistic impact experiments performed at The University of British Columbia [42],

details of which are presented in Chapter 2. Targets considered are square-shaped with dimensions of 203 mm by 203 mm (8" by 8"), made of a single or multiple layers of fabric. The projectile is meshed to the exact geometry of the actual RCC projectiles used in the experiments (dimensions given in Section 2.3), using a kinematic plasticity model of LS-DYNA (material type 3, i.e. MAT_PLASTIC_KINEMATIC) to capture the mechanical behaviour of steel (see

Table 4 - 2). Due to Symmetry, only one quarter of the projectile and the target is simulated to reduce the computational cost of the analyses. Proper constraints were applied to the target and the projectile to simulate fixed boundary and symmetry conditions. The projectile was assigned an initial velocity and contact was activated between the target and projectile, as well as the several layers of the multi-ply fabric target.

Figure 4 - 21 shows the velocity-time history of the projectile impacting a single-ply S-720 panel at 100 m/s for a case where the crimp in the panel is ignored. The predictions from the two approaches are clearly very similar, with some subtle differences due to the disparities between the two modeling approaches. These differences are better depicted in Figure 4 - 22 where the reaction force at the boundary of a warp yarn passing through the impact point is shown. The shell based model seems to be more stable and less noisy compared to the cable-based model.

Similar comparisons can be made after inclusion of the crimp in the shell-based and cable-based models. Figure 4 - 23 shows such a comparison, where the prediction of the decoupled shell model seems to be very close to that of the

cable-based model, as expected. The overall stiffness and energy absorption of the fabric increases upon the inclusion of the coupling between warp and weft unit-cell yarns in the shell model. This implies that the cable-based model is ignoring an important feature of the fabric behaviour since it can only provide a decoupled warp/weft response, which can highly influence the performance of plain weave fabric panels.

4.4.3 Bias Extension Test Simulations

The complex shear deformation characteristics of fabrics have been the focus of many studies. Fabrics are subjected to very large shear strains in a variety of applications such as thermoforming/stamping as a part of the processing of fabric composites. Deformation of the fabric under shear leads to realignment of fibres/yarns which in turn would alter the mechanical properties of the finished product. For this reason, and to avoid the occurrence of defects such as fabric wrinkling, etc., a thorough understanding of the fabric shear behaviour is essential in these applications.

Several experimental methods are established to characterize the shear behaviour of fabrics. Amongst these methods, two have been widely studied and commonly used to determine the pre- and post-locking moduli and locking angle of fabrics: picture frame shear and bias extension tests. In picture frame shear testing methodology, a fabric is subjected to shearing deformation inside a square frame with hinges at its corners (see Figure 4 - 24). As the fabric is loaded along on of its diagonals, the frame allows for rotation of the sides while keeping them parallel to each other. The load applied to the fabric is then measured and shearing properties of the fabric is extracted from its picture

frame load-displacement data. In the bias extension tests, a rectangular sample is cut with the warp and weft yarns aligned to make a 45° angle with the sides of the sample. The fabric sample is then loaded in tension and its deformational behaviour as well as the force-displacement response are studied. Based on the kinematics of the bias extension test [67], the fabric can be divided into three distinct shearing regions (zones A, B and C in Figure 4 - 25) during the test. Assuming no yarn slippage occurs during the test, the fabric remains undeformed in zone A due to the constraint applied by the clamping plate at the top and bottom of the sample, while it is in a state of pure shear in zone C. The deformation angle in zone B is the average of the other two zones, A and C.

This section investigates the success of the shear model implemented in the 2D shell crossover model in predicting the response of fabrics in bias extension test simulations. Simulation of the bias extension test was performed on a rectangular S-728 panel with a length of 143.5 mm and a width of 74 mm. in order to obtain symmetric deformation profiles, the fabric was balanced in these simulations by using identical warp and weft yarn properties. The failure of yarns was also deactivated to study the elastic shearing response of the shell-based fabric model in a highly deformed case. Figure 4 - 26 shows the fringe plot of the warp/weft angle after stretching the fabric by 5 mm on each side. As seen in the figure, the three zones (A, B, and C) are distinctly visible and the warp/weft angle in region B is equal to the average of regions A and C.

As highlighted in Section 4.3, the overall shearing resistance of the fabric stems from the rotation of the yarns, as well as the locking of the fabric in a trellis

mechanism. Eliminating the trellis mechanism from the shell element shear response would transform them to behave similar to the cable-based pin-jointed models where only the rotation of the yarns is considered. As seen in Figure 4 - 27, lack of shear locking in bias extension test simulation results in an unstable mode of deformation, where bands of elements at 45° have undergone extreme shearing and the rest of the fabric has stayed undeformed. This observation further emphasises the inability of the cable-based pin-jointed models in capturing the true shear response of the fabrics in simulating quasi-static and dynamic events.

4.4.4 Notes on the Numerical Efficiency of Shell UC

One of the most important factors directly affecting the functionality of a model is its numerical efficiency. In general, as a model gets more complex and more detailed, the computational resources needed to perform a certain set of required analysis amplify. This is clearly the case for all the modeling approaches presented in this study. A comparison of the execution time taken to analyse several fabric models utilizing the three modeling approaches (cable-based fabric, 2D crossover shell and 3D solid and bar fabric models) is presented in Table 4 - 3. Intuitively, the simple cable-based model is the most efficient, while the 3D solid-bar model is extremely inefficient, to the point that it is almost impractical for panels with realistic dimensions. Shell-based fabric models are significantly less time-consuming in comparison to the 3D solid-bar models of fabrics, but are more numerically intensive compared to the cable-based models. However, the inefficiency of the shell model compared to the

cable-based model is justifiable since they incorporate several details of the weave and yarns in capturing the mechanical response of the fabrics.

The efficiency of the shell model is highly dependent on the fabric properties and the user-specified input parameters. Since the calculation of yarn tensile forces in the UMAT is an iterative process, the number of cycles needed to achieve convergence is usually dependent on the fabric geometry and mechanical properties, as well as on the applied displacements. Figure 4 - 28 shows the contours of contact force between the yarns as a function of the symmetric displacements applied to a single yarn crossover in the S-720 fabric unit-cell, considering the failure of the yarns based on the instantaneous failure criterion. As seen in the figure, the yarns interaction is limited to the applied displacements that fall within the area identified as region 1. For displacement pairs outside the boundaries of this region no interaction between the yarns occurs, due to either separation of the crossing yarns in region 2 or failure of one or both yarns in region 3.

Figure 4 - 29 shows the number of iterations needed to achieve convergence for the range of displacements considered. Overlaying the boundaries of region 1 on this plot reveals that many displacement pairs outside this region require a higher number of iterations to satisfy the convergence criteria, while the displacements that result in significant resistance from the unit-cell (in region 1) usually achieve convergence after only a few iterations. An efficiency model is thus developed in the UMAT where the code is instructed to perform the Newton-Raphson iteration scheme only for displacements that fall within region 1. However, using the efficiency model requires some pre-processing to

identify the parameters that identify the boundaries of region 1. A simpler efficiency model can also be activated that would bypass the iterations for negative displacement pairs only (Figure 4 - 30).

In the impact analysis of shell-based fabric models, the displacement pairs that elements experience are mostly located in region 1 and its close vicinity. The most time-consuming elements in terms of iteration convergence are the ones where the applied displacement pairs cause subtle contact between the two yarns, located around the curved edge of region 1. In these cases, the number of iterations needed to reach convergence is quite high, mainly due to the fact that the numerical round-off errors become significant compared to the numeric value of the target functions. The tensile forces associated with these displacements are, however, very small and inconsequential in the overall performance of the panel. As a result, a large portion of the execution time is spent performing iterations to calculate forces that would not contribute much to the overall energy absorption. This emphasizes the importance of the development of more intelligent efficiency model that would bypass these time-consuming elements, and save a considerable amount of time and computing power throughout the analysis process.

4.5 SUMMARY

A shell element based on a continuum representation of a fabric unit-cell, comprised of a single crossover has been developed in this chapter. The proposed model takes advantage of several simplifying assumptions to formulate the biaxial response of a fabric crossover. The interaction of the

yarns, whose shapes are based on sine functions (identical to the observed fabric cross-sections), is considered under displacements that are symmetrically applied to the yarns ends. The biaxial response of the pinned yarn crossover was implemented in the constitutive model developed in the commercial finite element software, LS-DYNA. The developed shell-based model has been verified against the 3-D model and proven to be significantly more efficient in terms of the required numerical resources. This efficiency was reflected in the comparison of the execution times reported for a benchmark impact problem.

The shell model developed here, aside from its simplifying assumptions, is very successful in capturing the in-plane response of a yarn crossover. The model framework is such that it can be easily expanded to consider the bending of the yarns, or take advantage of a more realistic shear model. This expansion should be performed along with relevant experimental effort that would calibrate the new properties needed by the model.

Table 4 - 1: Shell input parameters for the in-plane shear model of all six Kevlar® 129 fabric types.

Panel	S-720	S-726	S-727	S-728	S-731	S-745
G_1 (Pa)	9.67E6	1.07E7	1.15E7	8.66E6	1.17E7	1.14E7
G_2 (Pa)	9.67E9	1.07E10	1.15E10	8.66E9	1.17E10	1.14E10
γ_1	0.24	0.15	0.19	0.12	0.35	0.26
γ_2	0.49	0.40	0.40	0.70	0.40	0.50

Table 4 - 2: Input material properties of the steel RCC projectile used in the impact simulations.

Property (units)	Value
Density (g/cm²)	7.922
Elastic modulus (GPa)	193.0
Poisson's ratio	0.30
Yield stress (MPa)	220.0

Table 4 - 3: Comparison of execution times for simulation of impact of an RCC projectile on square panels of Kevlar® 129 fabric using cable (pin-jointed), 2D shell crossover and 3D solid/bar crossover fabric models.

Panel	Dimension (mm)	Elements		Duration of impact (μs)	No. of CPUs	Execution time (sec)
		number	type			
S-720, 1-ply	100.33	18,723	cable	250	1	1,243
S-720, 1-ply	100.33	6,241	shell	250	1	1,932
S-720, 1-ply	25.4	160,000	solid	42	3	157,424
S-7265, 4-ply	100.66	132,251	cable	400	4	5,297
S-7265, 4-ply	100.66	44,084	shell	400	4	15,258

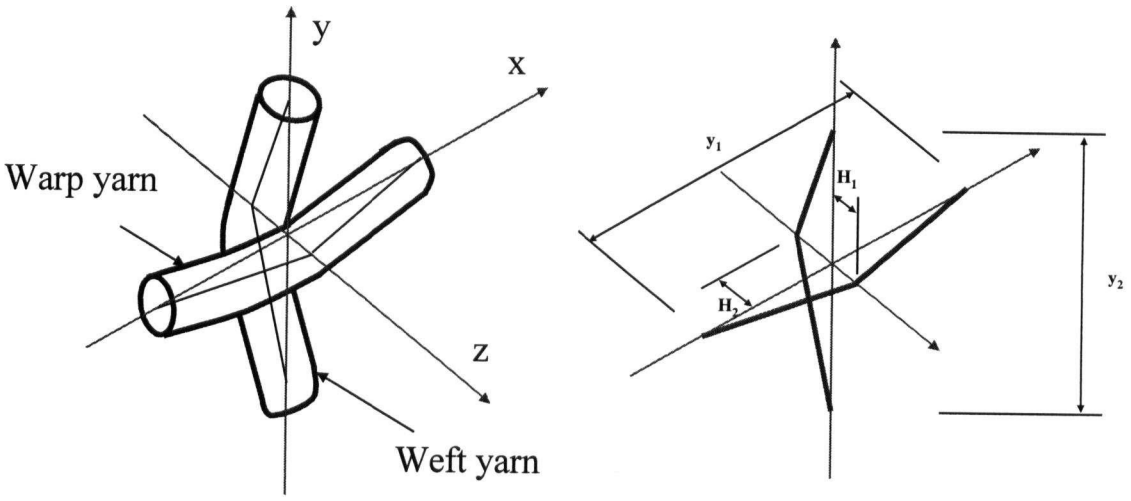

Figure 4 - 1: Illustration of the biaxial crossover model of a single plain weave fabric crossover with linear yarns originally developed by Kawabata et al. [57].

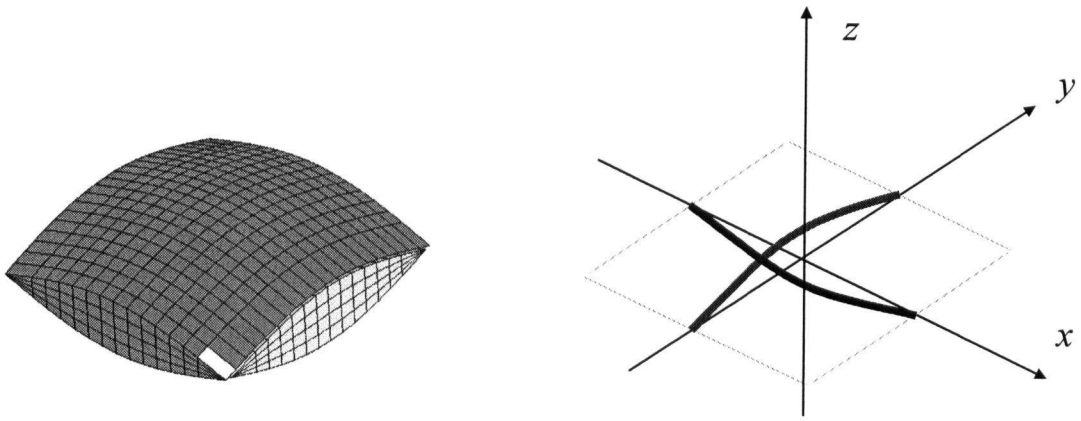

Figure 4 - 2: 3D finite element mesh of a single fabric crossover (left) and the equivalent mathematical representation of the yarns by their centrelines (right).

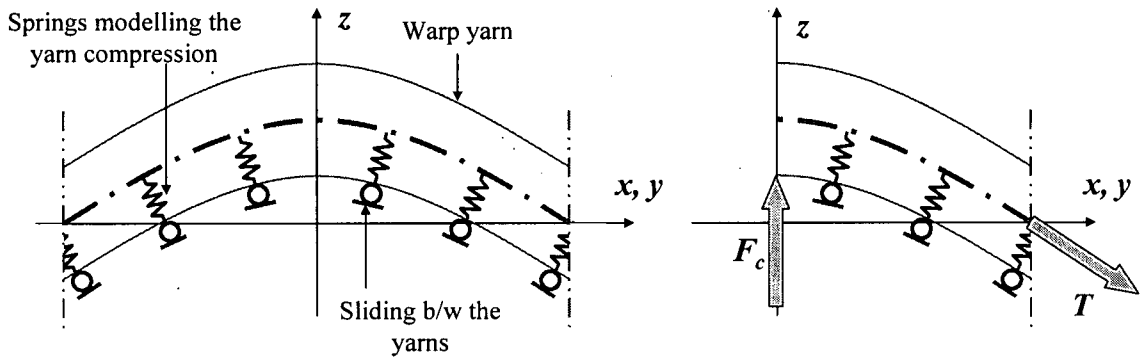

Figure 4 - 3: A schematic model of a yarn in the fabric (left) in contact with the crossing yarn and a free body diagram showing the forces acting on it (right).

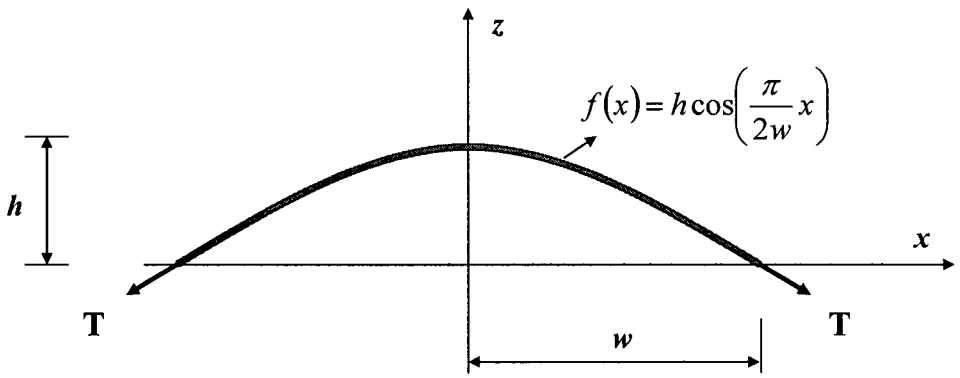

Figure 4 - 4: Cosine-based shape of an arbitrary yarn in a plain weave fabric.

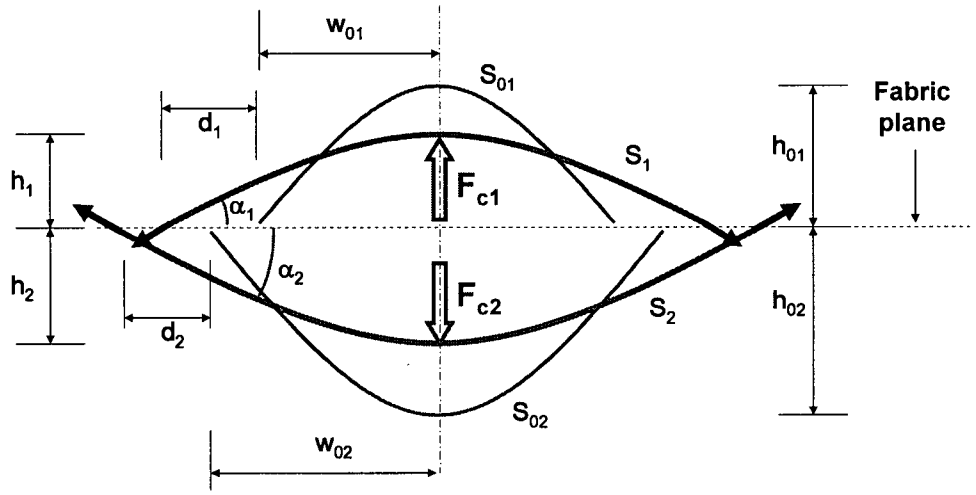

Figure 4 - 5: Warp and weft centreline geometry before (green) and after (red) deformation.

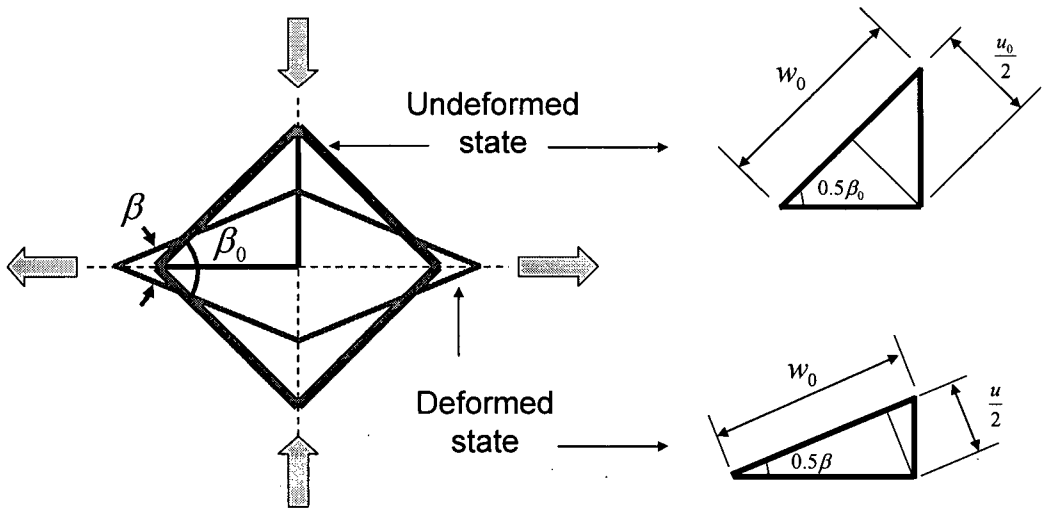

Figure 4 - 6: Shear model developed for the fabric unit-cell based on a picture frame shear test.

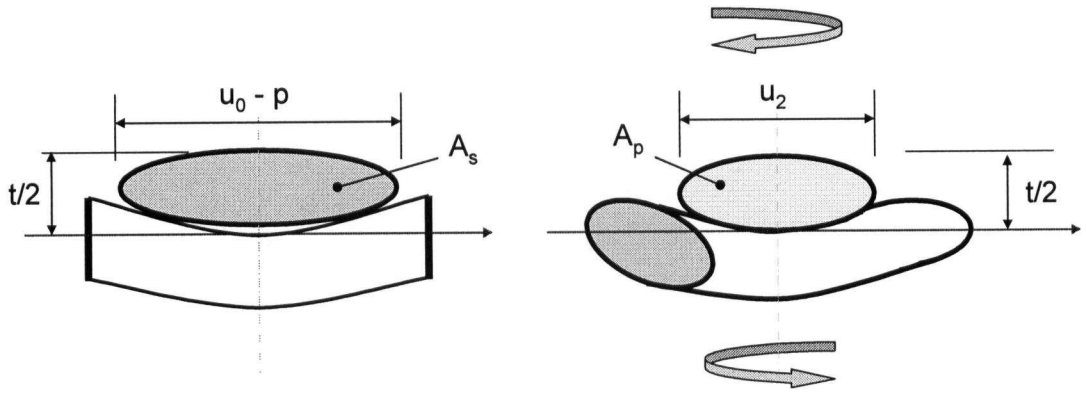

Figure 4 - 7: Compaction of the yarns as a result of the crossover shearing (before (left) and after (right) shearing). Note that the fabric thickness and configuration of yarn centreline are assumed to remain unchanged during shear deformation.

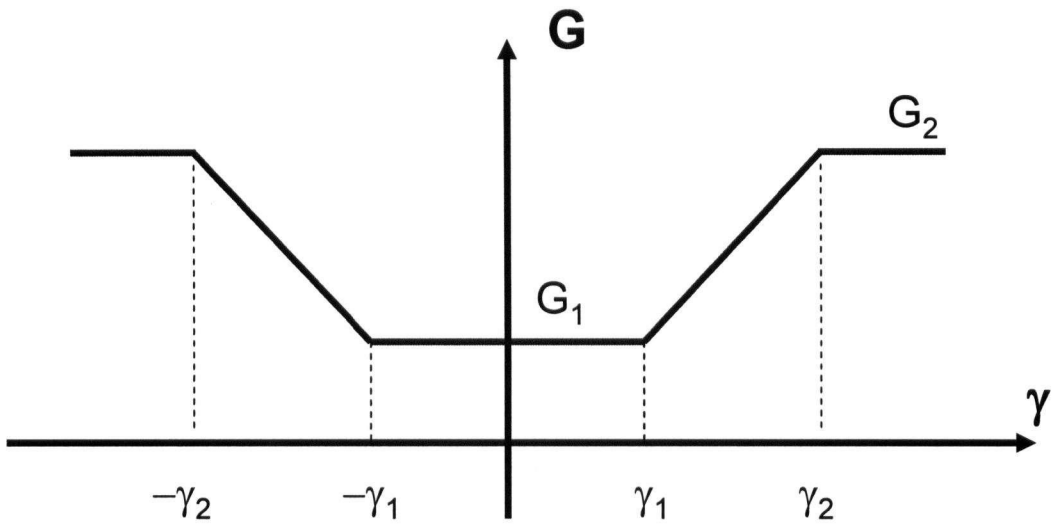

Figure 4 - 8: Secant shear modulus, G, as a function of the shear strain γ, representing the trellis mechanism.

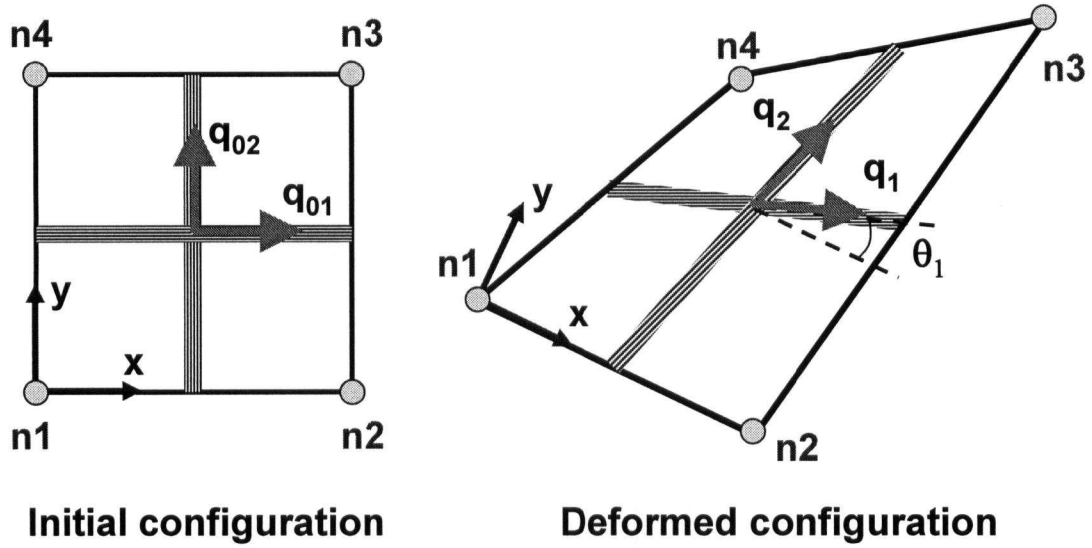

Figure 4 - 9: Definition of the local element and material axes convention assumed for shell elements in LS-DYNA.

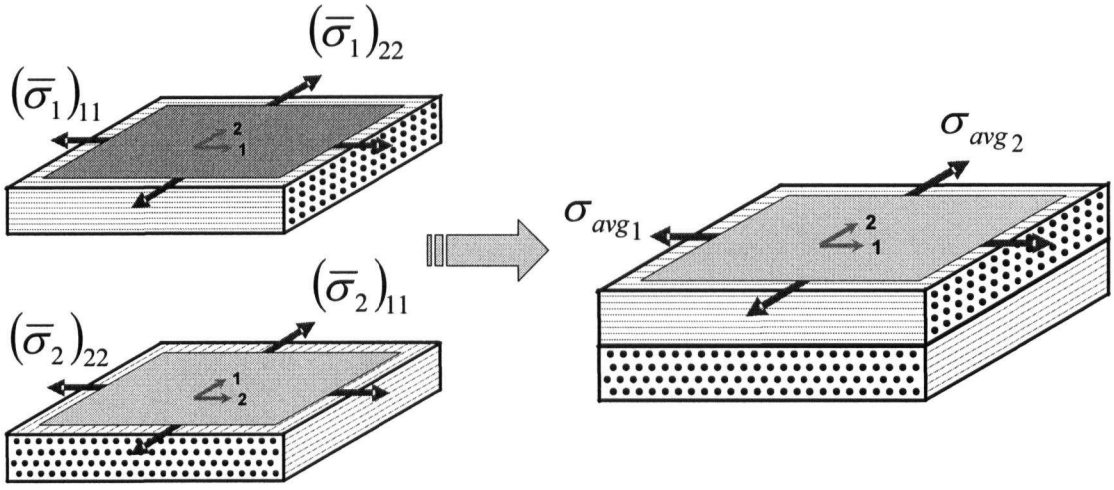

Figure 4 - 10: Definition of element stresses and their relationship with those individual yarns in an equivalent smeared shell approach (w and f in the figure represent the warp and weft yarns, respectively).

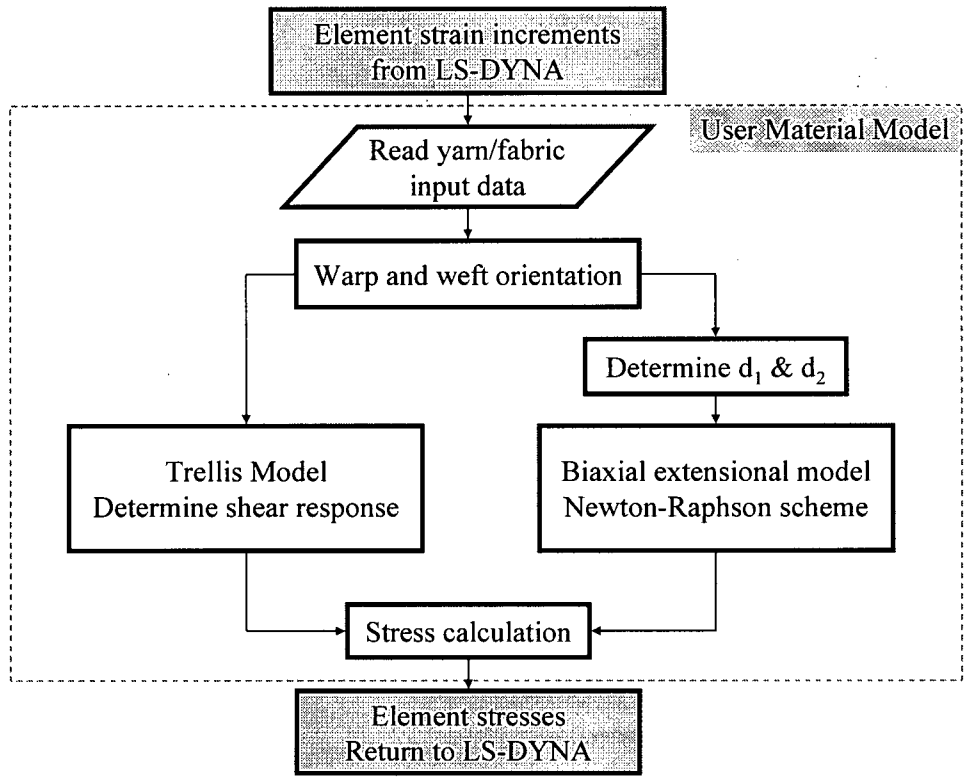

Figure 4 - 11: Flowchart of the UMAT routine specifying the constitutive relationship of the smeared fabric material of the representative shell element (see Appendix B for more details).

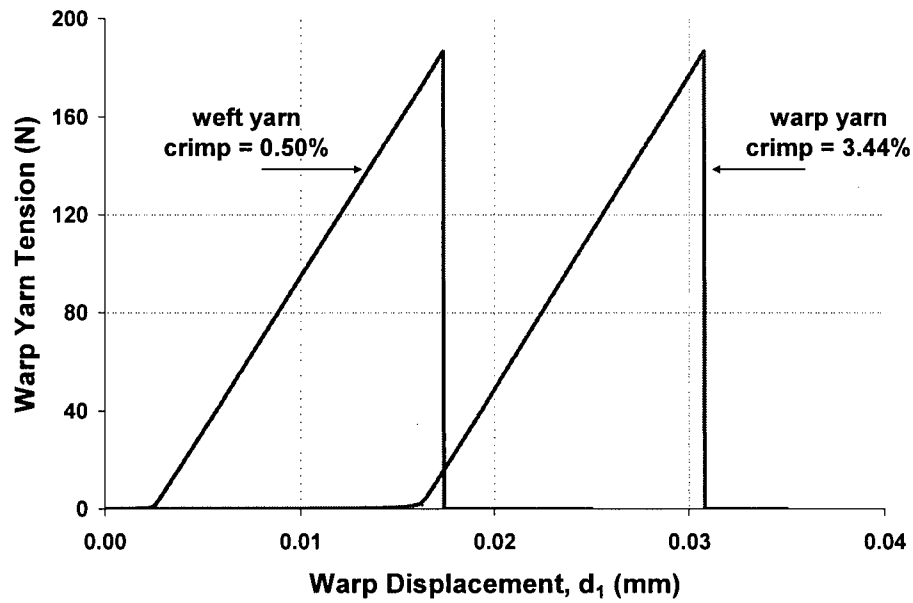

Figure 4 - 12: Tension-displacement response of S-726 single crimped warp and weft yarns predicted by the representative shell element.

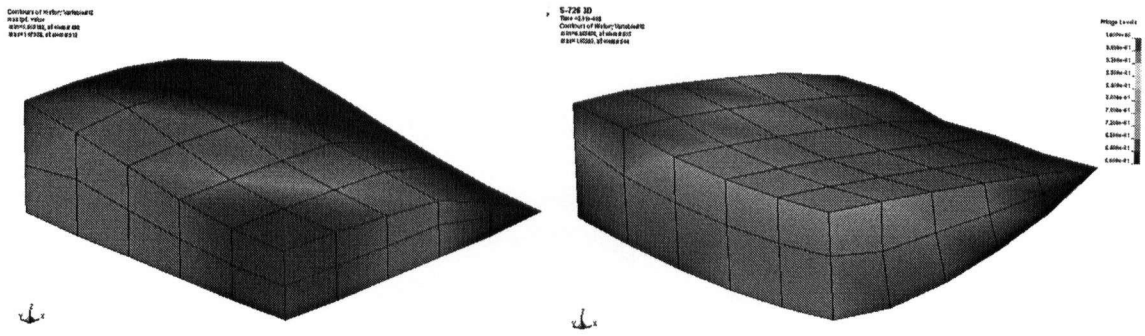

Figure 4 - 13: Deformed shape and contours of element deformation (void ratios) under transverse compression (left) and biaxial extension (right) loading simulations using the 3D crossover model (note that only one quarter of the yarn is shown for illustration purposes).

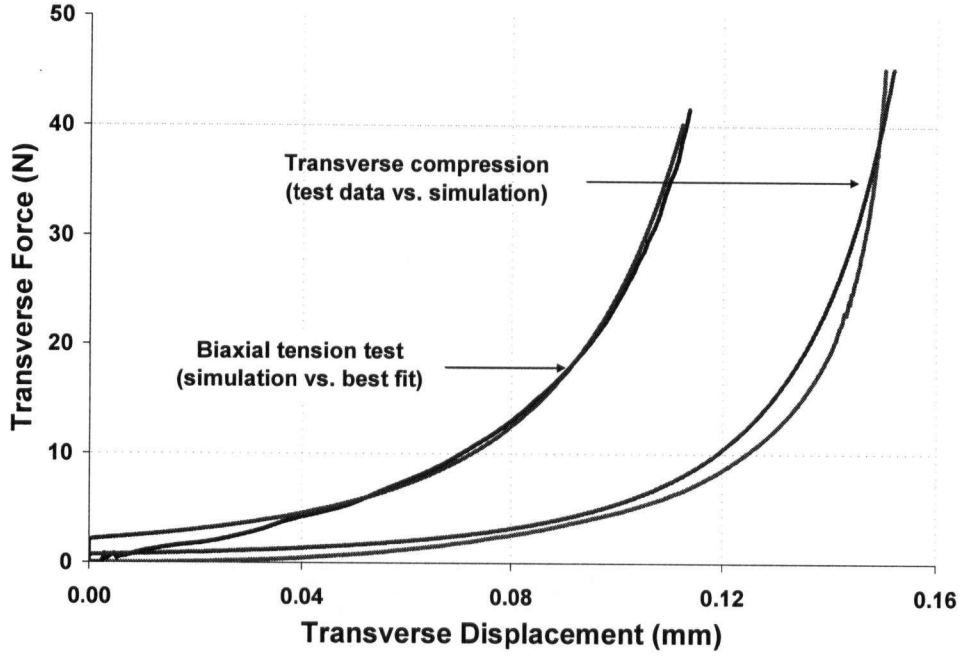

Figure 4 - 14: Transverse force-displacement response predictions (along with the best fit) of the 3D crossover model of S-720 unit-cell obtained from simulations of transverse compression tests and biaxial tension tests, showing the difference in the compressive response of the yarns.

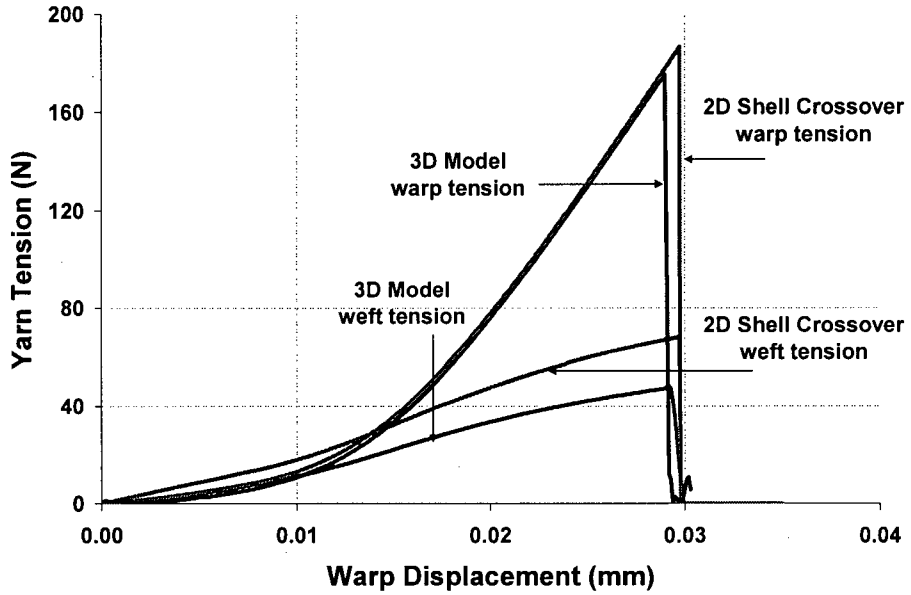

Figure 4 - 15: Biaxial response of S-726 unit-cell as a function of warp displacement (weft yarn fixed, $d_2 = 0$), predicted by the 3D crossover model and the 2D shell model.

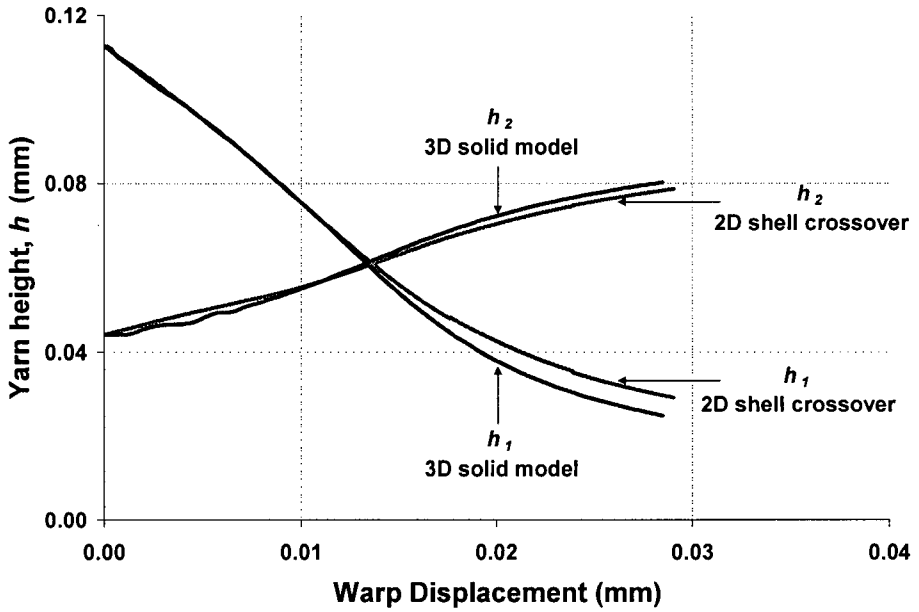

Figure 4 - 16: Variations of h_1 and h_2 with warp displacement, predicted by the shell model during the biaxial extension of an S-726 unit-cell illustrated in Figure 4 - 15.

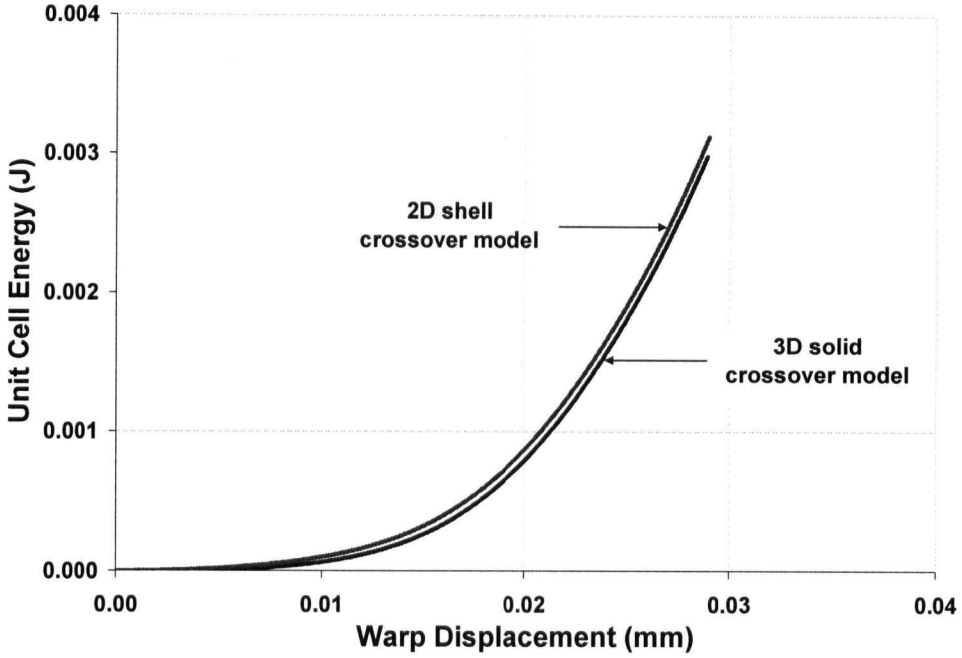

Figure 4 - 17: Energy stored in the unit-cell as a function of warp displacement, comparing the predictions of the shell crossover and 3D solid models during the biaxial extension of an S-726 unit-cell illustrated in Figure 4 - 15.

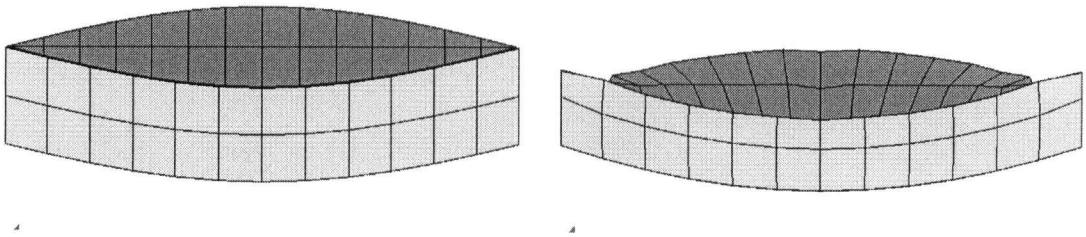

Figure 4 - 18: Yarn cross-sections before (left) and after (right) deformation due to the interaction of the two yarns in biaxial extension, for the biaxial extension of an S-726 unit-cell illustrated in Figure 4 - 15.

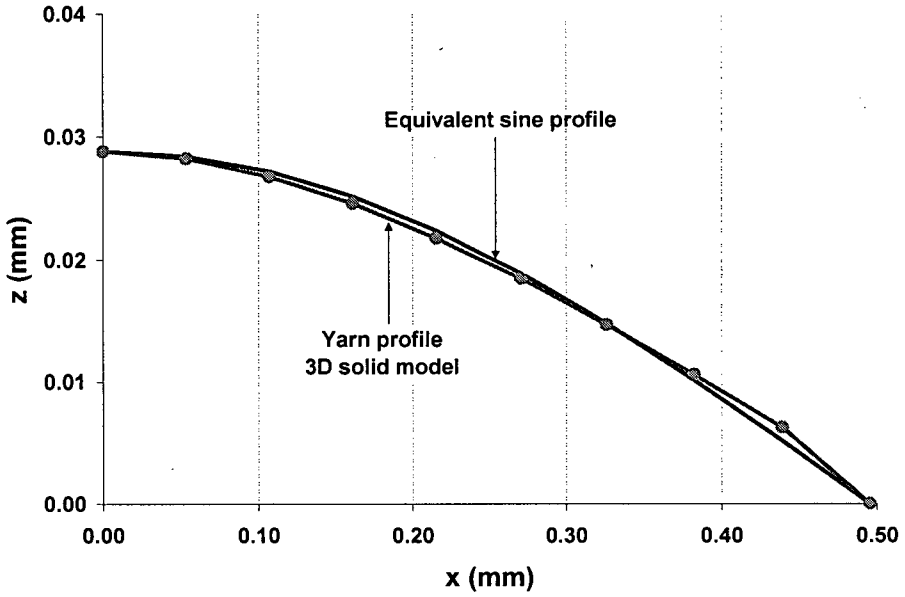

Figure 4 - 19: Deformed profile of the warp yarn predicted by the 3D solid model compared with a sine curve (note that only half of the yarn is shown), for the biaxial extension of an S-726 unit-cell illustrated in Figure 4 - 15.

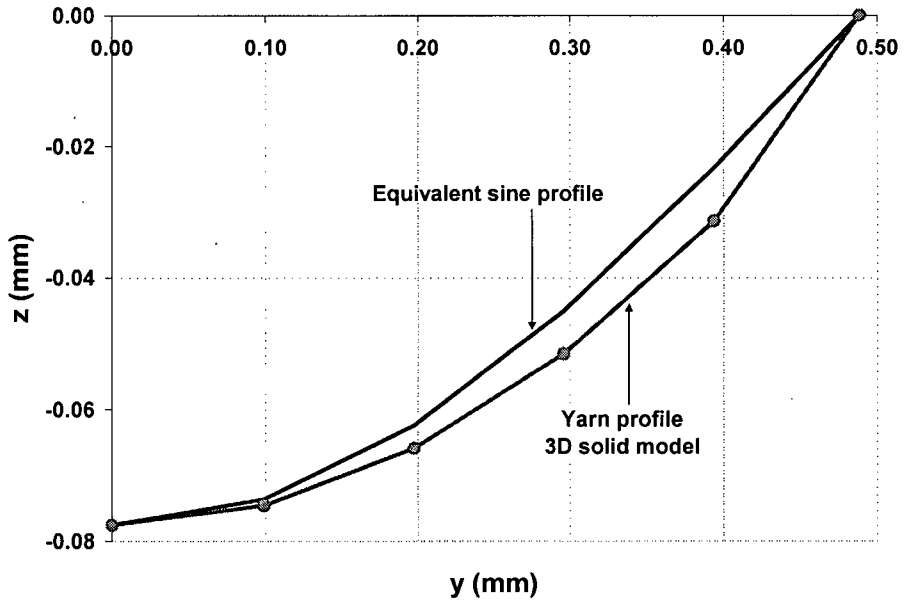

Figure 4 - 20: Deformed profile of the weft yarn predicted by the 3D solid model compared with a sine curve (note that only half of the yarn is shown), for the biaxial extension of an S-726 unit-cell illustrated in Figure 4 - 15.

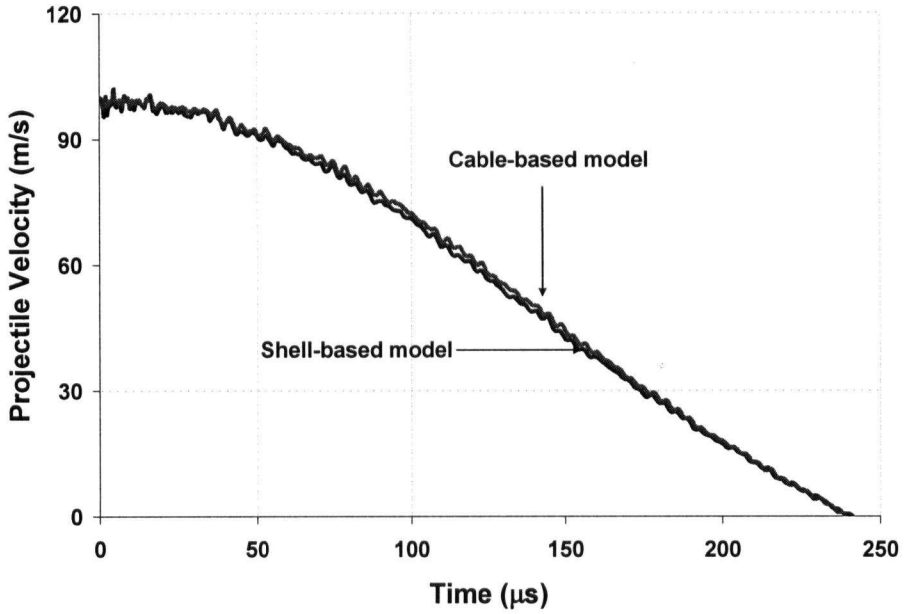

Figure 4 - 21: Velocity-time response of the projectile impacting a single-layer S-720 target, predicted using shell-based and cable-based model (yarn crimp not considered).

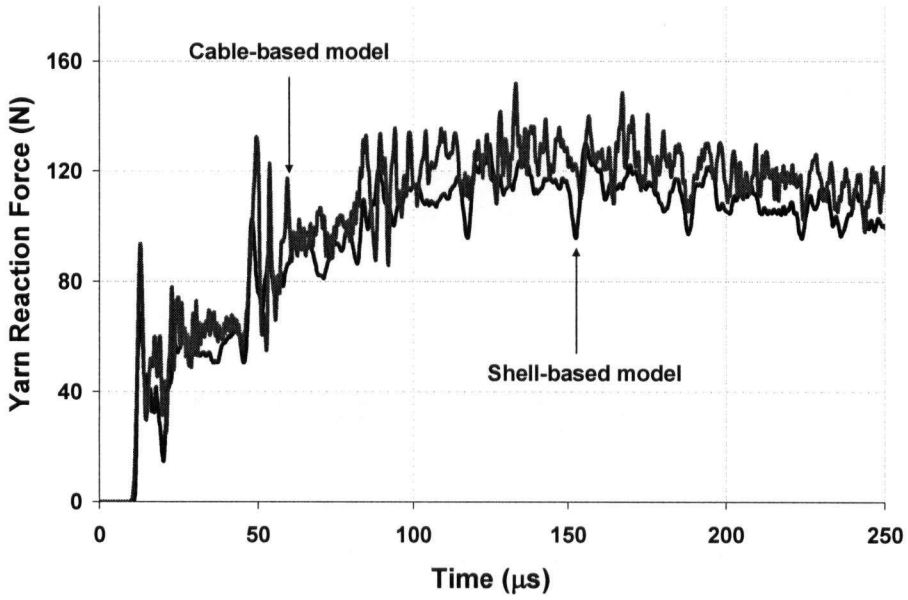

Figure 4 - 22: Comparison of a yarn reaction force in an impact simulation on a single-layer S-720 target, predicted using shell-based and cable-based model (yarn crimp not considered).

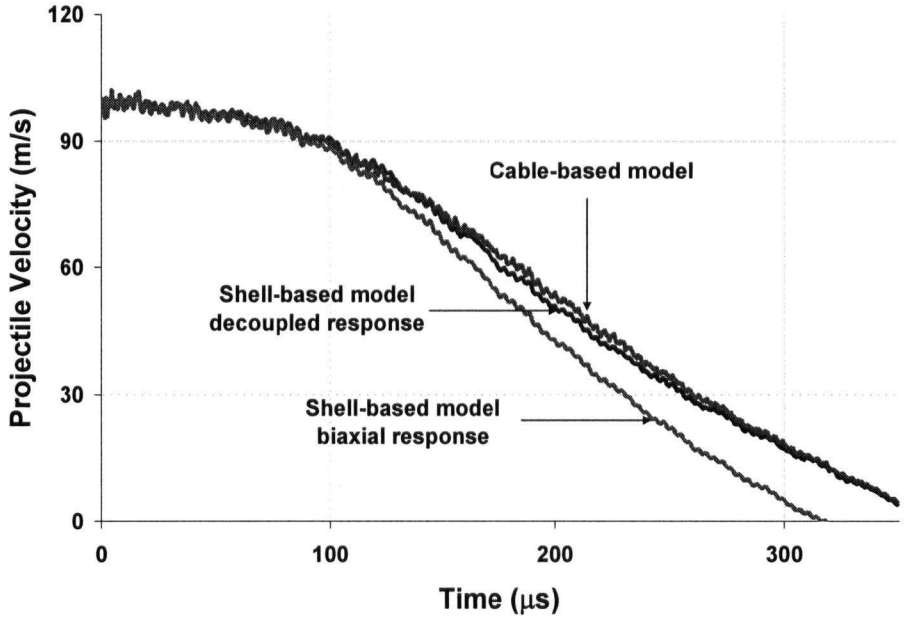

Figure 4 - 23: Velocity-time response of the projectile impacting a single-layer S-720 target, predicted using shell-based and cable-based model (yarn crimp considered).

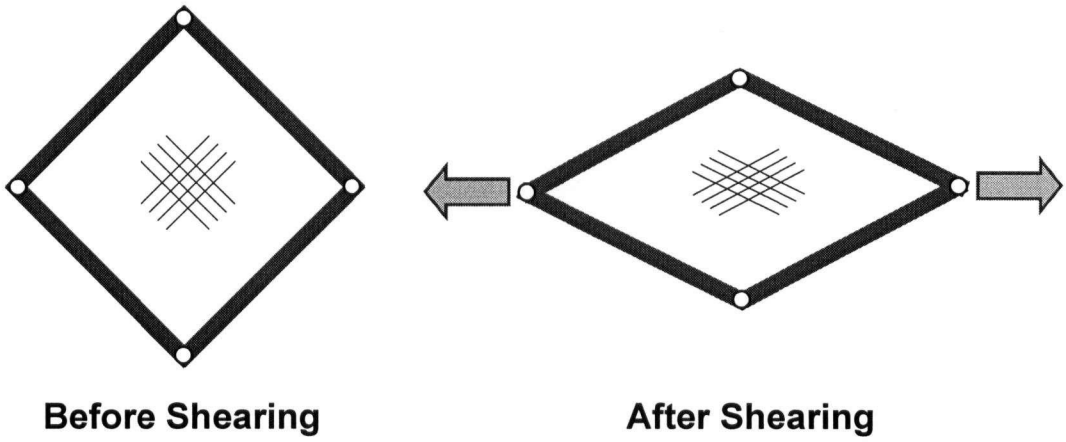

Figure 4 - 24: Schematics of the picture frame shear testing methodology.

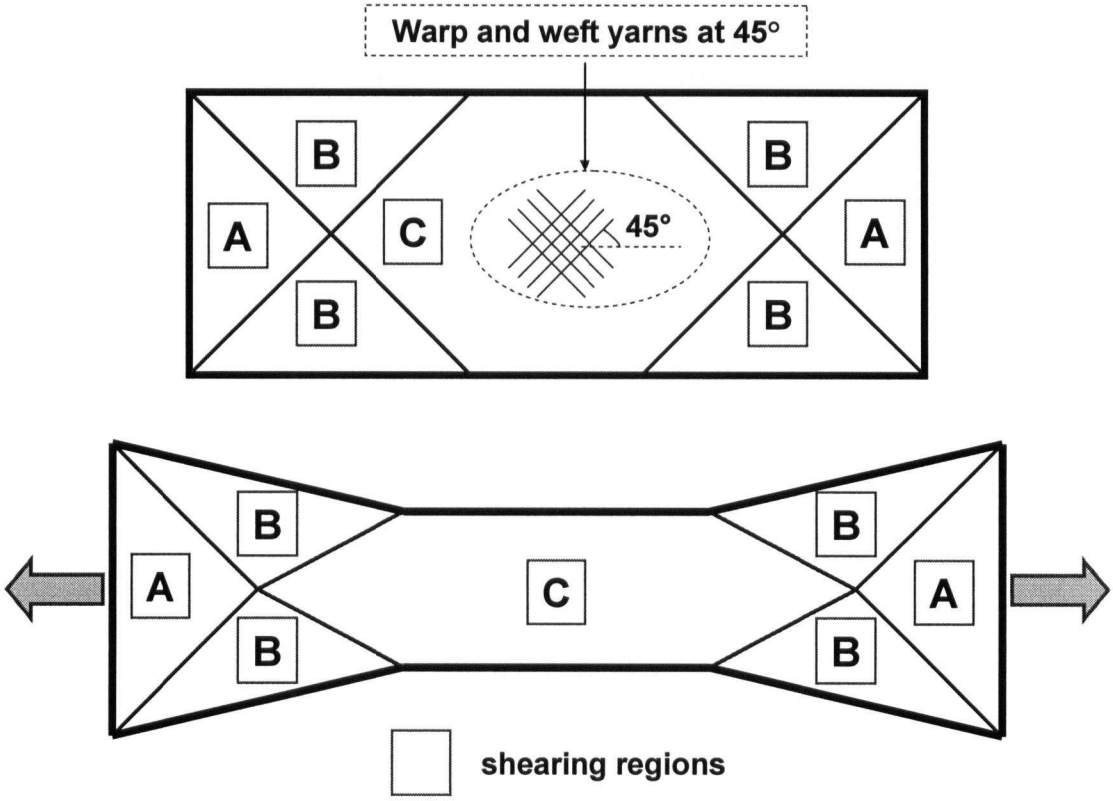

Figure 4 - 25: Schematic representation of undeformed fabric (top) in the bias extension test and the creation of shear zones after deformation (bottom) [67].

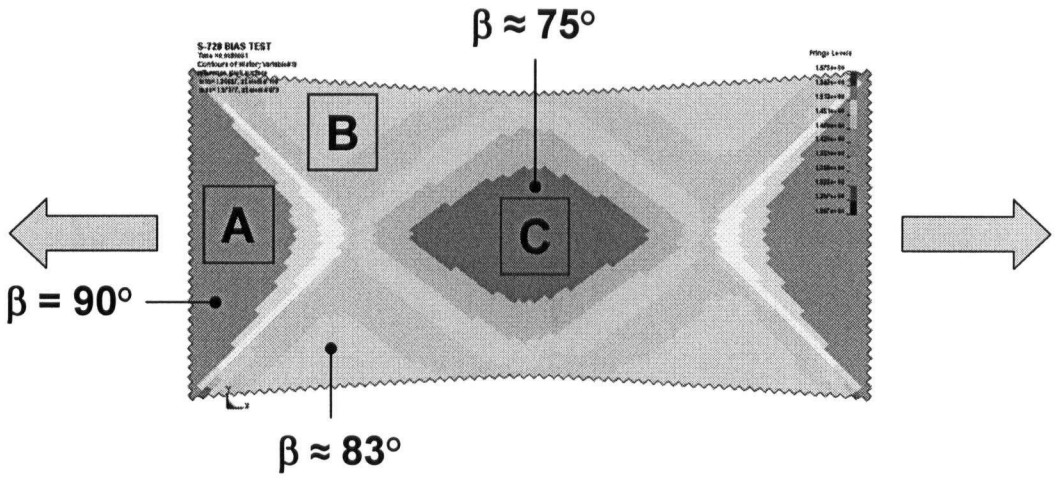

Figure 4 - 26: Contours of warp/weft angle in the deformed balanced S-728 fabric in the bias extension simulation.

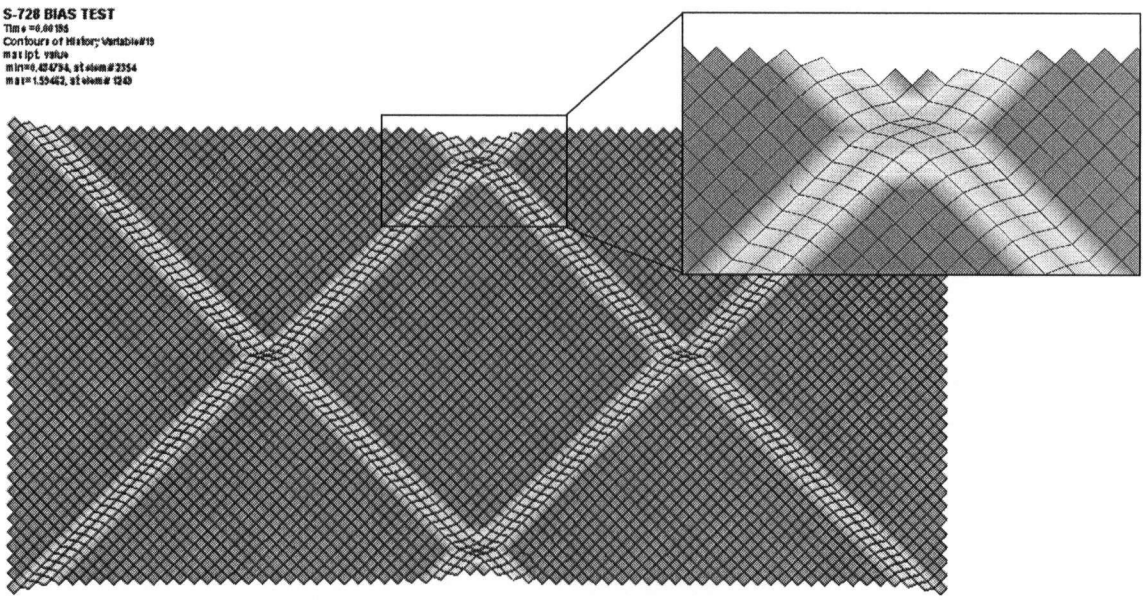

Figure 4 - 27: Unstable deformation mode of the S-728 fabric without considering the shear locking in bias extension simulation.

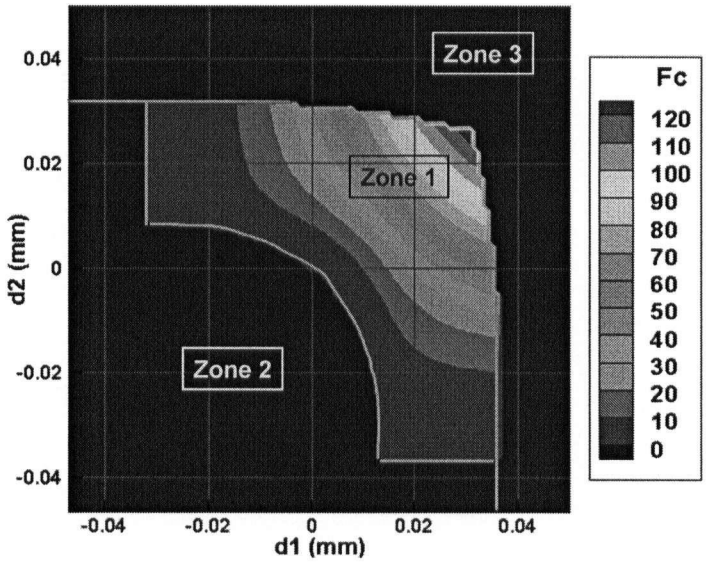

Figure 4 - 28: Contours of contact force between the yarns, computed for biaxial extension of an S-720 fabric crossover ($-0.05 \le d_i \le 0.05$ where $i = 1, 2$).

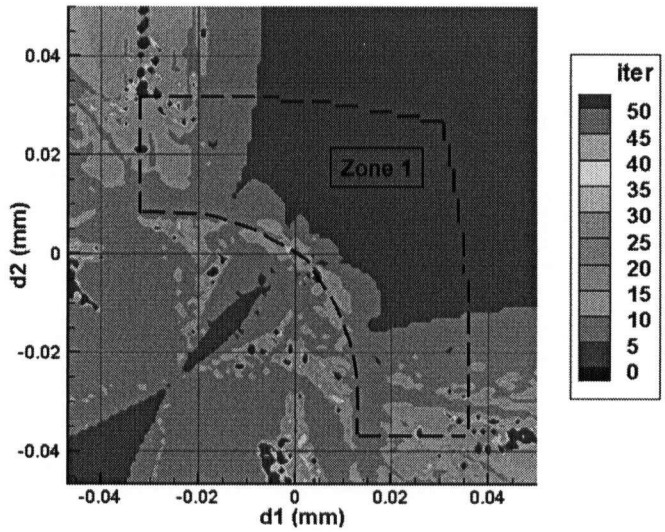

Figure 4 - 29: Contours of the number of iterations needed to gain convergence, when calculating the yarn tensile forces as a function of the symmetric displacements applied to the S-720 fabric unit-cell ($-0.05 \le d_i \le 0.05$ where $i = 1, 2$).

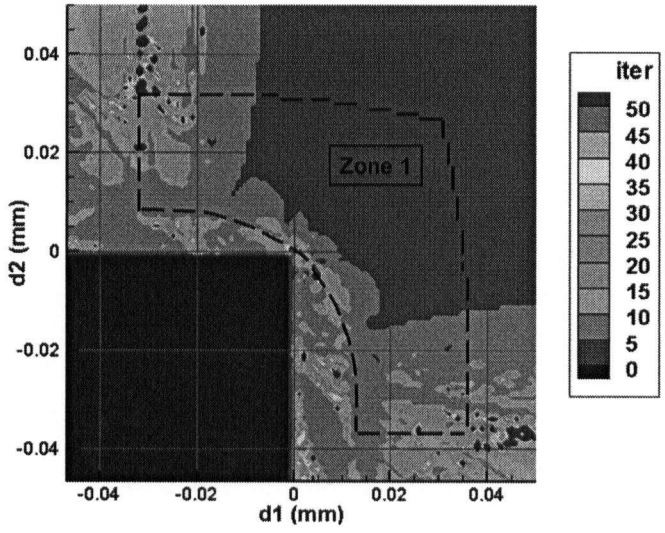

Figure 4 - 30: Contours of the number of iterations needed to gain convergence after bypassing iterations for negative displacement pairs developed for S-720 fabric unit-cell ($-0.05 \le d_i \le 0.05$ where $i = 1, 2$).

CHAPTER 5 - VALIDATION OF THE STATIC AND DYNAMIC RESPONSE PREDICTIONS OF FABRICS

5.1 INTRODUCTION

The meso-mechanical shell fabric model developed in the previous chapter is utilized to study the behaviour of fabrics under two different loading scenarios. In the first part of this chapter, the performance of various Kevlar® 129 panels subjected to ballistic impact of RCC projectiles is investigated. For this purpose, data from instrumented ballistic tests on single and multi-ply fabric targets are used to validate the predictions of the numerical model. The second part of this chapter deals with simulation of the in-plane biaxial extension tests obtained from the literature on balanced and non-balanced fabric panels woven from yarns of glass filaments. The aim of these simulations is to highlight the capabilities of the shell crossover model as well as to probe its limitations in capturing the behaviour of fabric panels with various structures. The findings

of each of these two sections are concluded and summarized at the end of the chapter.

5.2 BALLISTIC IMPACT RESPONSE OF FABRIC PANELS

The meso-mechanical model of fabrics developed and presented in the previous chapter is used here to study the ballistic behaviour of Kevlar® 129 panels. Simulations of ballistic impact experiments on six fabrics panels presented in Section 2.3 (performed by Cepus [42]) are carried out and the energy absorption capacities of the targets are studied. The predictions of the numerical model are presented separately for single and multi-ply target systems, followed by the discussion of the numerical observations.

5.2.1 Ballistic Impact Simulation: 1-ply Targets

The first step in examining the ability of the model to capture the ballistic response of fabric panels is to simulate ballistic impact events on 1-ply target systems. Due to the lack of inter-ply interaction in single-ply targets, direct conclusions can be drawn on the success of the representative shell elements on mimicking the biaxial extensional response of the fabric during impact-induced deformations. This section covers the study of ballistic impact on six different Kevlar® 129 fabric weaves presented earlier in Chapter 2.

The input values chosen for these test simulations are presented in Table 5 - 1. The geometrical symmetry of the target and projectile is used to only consider a quarter of the panel and the projectile in the finite element analysis through application of proper boundary conditions. The geometrical dimensions of each

shell element are set equal to that of a single yarn crossover of the fabric it is meant to represent. The density of the shells is also adjusted to match the total weight of the crossing yarns within its boundaries, resulting in an areal density closely matching the laboratory measurements (see Figure 5 - 1). The contact between the projectile and the target is based on a frictionless surface-to-surface contact model in LS-DYNA [54] activated between the shell elements of the target and solid elements of the projectile. RCC (Right Circular Cylinder) projectiles were meshed into a geometry that closely resembled the shape of the actual steel projectiles used in the experiments [51]. Most input values for the shell elements are obtained directly from the laboratory measurements, except for the constants of the transverse compression model of the yarns, which are obtained from the 3D unit-cell model.

Initial examination of the six Kevlar® 129 fabrics reveals critical differences among them. Figure 5 - 2 shows the value of the total crimp (obtained by the addition of the warp and weft crimp) for the fabrics studied, in order to gain some relative understanding of the level of yarn undulation amongst them. Since almost all panels studied here have identical yarns and mostly equal count numbers in the warp and weft directions, the level of imbalance of each panel would be determined by the difference of yarn undulation between the two directions. Plotting the ratio of warp and weft crimp as shown in Figure 5 - 3, it can be seen that S-720 and S-728 panels have the lowest warp to weft crimp ratios, while S-731 and S-726 panels possess a large ratio showing a significant level of imbalance in the warp and weft directions. The investigation of the impact response of 1-ply panels is thus further divided into two main

categories: relatively balanced fabrics (S-720 & S-728) and highly imbalanced panels (S-726, 727, 731, & 745.)

The S-720 and S-728 panels have a combination of low total crimp and warp/weft ratio amongst the fabrics studied. This implies that the yarns in the warp and weft directions have more or less the same geometries and given that they have equal linear density (denier), intuitively, they are expected to almost equally provide the load-bearing capacity of the fabric.

The velocity-time response prediction of the RCC projectile impacting a 1-ply S-720 fabric panel at a non-perforating speed of 92.5 m/s and a perforating velocity of 155 m/s are shown in Figure 5 - 4 and Figure 5 - 5, respectively. While the numerical model seems to be successful in capturing the impact response of S-720 fabric in the initial stages of impact, it seems to over-estimate the energy absorption capacity of the fabric in the latter portion of the event (see Figure 5 - 4). It was also observed that at higher strike velocity leading to perforation (e.g. Figure 5 - 5), the failure prediction of the numerical model is somehow delayed compared to the experimental data. The sources of such discrepancies are discussed later in this chapter (see Section 5.2.3). Similar conclusions can be drawn for S-728 fabric panel. Figure 5 - 6 and Figure 5 - 7, respectively, show a non-perforating and a perforating event at impact velocities of 76 m/s and 170 m/s.

The deformation profiles (seen in Figure 5 - 8) of the fabrics appear to be symmetric, translating into a balanced distribution of all energy components between the warp and weft yarns. Further examination of the S-720 and S-728 panels during impact reveals that there are slight differences between the warp

and weft responses, evident from the propagation of the tensile wave along the warp and weft yarns and the transverse deformation of the panels. Figure 5 - 9 shows the time-history of the reaction force acting at the boundary of a yarn that goes through the impact point. As seen in this figure, there are minor differences between the reaction forces and a delay in the arrival of the strain wave (indicated by the sudden increase in reaction force) travelling along the warp yarn compared to that of the weft yarn. However, this difference is not significant enough to cause major disparities between the two main material directions and the S-720 and S-728 fabrics can be considered to be relatively balanced.

The other four fabric types have significantly higher crimp values in the warp direction compared to that of weft. Sample model predictions of the projectile velocity-time response for these panels are shown in Figure 5 - 10 to Figure 5 - 17. The agreement between the numerical predictions and experimental data seems to be best in the initial part of the response, with the numerical model slightly over-estimating the energy absorption capacity of the panels.

The existing warp to weft crimp disparity in these fabrics leads to a non-symmetric dynamic behaviour that is readily evident from the transverse deformation profile of the panels (shown for S-731 in Figure 5 - 18). This can also be seen in the reaction force time-histories plotted in Figure 5 - 19 for an S-726 warp and a weft yarn going through the impact point. While the reaction in the weft yarn (with 0.50% undulation) rises quickly at about 30 μs, the warp yarn (at 3.44% crimp) does not see any significant increase until after the 100 μs mark. This clearly indicates the dissimilar tension development in the warp

and weft directions, and as a result, the asymmetric energy distribution in the target. Post-mortem examination of the S-726 panel (Figure 5 - 20) revealed significant yarn slippage at the boundaries holding the weft (low crimp direction) yarns, which is supported by the numerical observation that higher reaction force is needed to contain the weft yarns. At higher velocities, the weft yarns would fail sooner than the warp (high crimp) yarns due to their higher tension, after which point the warp yarns would resist the motion of the projectile, slipping and sliding in the fabric as they are pulled by the projectile (hence a wider de-crimped zone seen in Figure 5 - 20).

The asymmetry inherent in the non-balanced fabrics translates into an efficiency reduction of the fabric system if only the energy absorption is concerned in the absence of any yarn failure. This will be further discussed in Section 5.2.4.2.

5.2.2 Ballistic Impact Simulation: Multi-ply Targets

Personal armour systems, in practice, are usually made from multiple layers of high performance fabrics to defeat the specific types of threats they are exposed to. As a result, a major part of the fabric target energy absorption stems from the interaction of individual layers with each other in the pack. To study such interaction existing in a real vest, the shell crossover model is used to simulate the ballistic impact experiments on multi-ply Kevlar® 129 targets. This section reviews the comparison of the numerical predictions versus the instrumented test data.

One of the challenges of modelling multi-layer fabric targets is the determination of the gap between the adjacent layers. In order to obtain an approximation of the distance between the mid-surfaces of successive layers, transverse compression test data on multi-ply fabrics are used. Figure 5 - 21 shows a schematic of the mechanical model considered in this study to estimate the initial gap between the layers. For a 1-ply model, the interaction of the material between the fabric mid-plane and the surface of the steel loading platen is represented by a spring with a non-linear stiffness of K_{fm}. Addition of one more layer of fabric to the system introduces a supplementary inter-fabric spring with a stiffness of K_{ff}, which represents the interaction of adjacent layers during compression. As a result, one can obtain the pure inter-fabric response of the panels under transverse compression by extracting a 1-ply force-displacement response from that of the multi-ply system. Let us assume that under an arbitrary compressive force F_c applied to an N-ply fabric pack, the total compression turns out to be ${}^{n}d_c$. Considering the system of springs in Figure 5 - 21, the total compression can be divided into two main components:

$$ {}^{n}d_c = 2d_{fm} + (N-1)d_{ff} \qquad (5\text{ - }1) $$

where d_{fm} is the fabric-metal interaction component of deformation and d_{ff} is the fabric-fabric component. For the case of a 1-ply system, $N = 1$ and we have:

$$ {}^{1}d_c = 2d_{fm} \qquad (5\text{ - }2) $$

To obtain the fabric-fabric component of the compression, we subtract the 1-ply response from the N-ply, as follows:

$$ {}^{n}d_c - {}^{1}d_c = (N-1)d_{ff} \qquad (5\text{ - }3) $$

And thus we can conclude that

$$d_{ff} = \frac{{}^{n}d_c - {}^{1}d_c}{(N-1)} \tag{5 - 4}$$

This process is illustrated in Figure 5 - 22, where the compression data for a 4-ply S-728 panel is used to determine the inter-fabric compression response. The value of gap considered between adjacent layers for all multi-ply targets of each fabric is chosen to be equal to its inter-ply deformation corresponding to the maximum load applied in the 4-ply transverse compression experiments. Table 5 - 2 provides the calculated inter-ply gap values for the three panels used in the multi-ply ballistic impact experiments. Subsequent to the implementation of the inter-ply gap, the contact between the adjacent layers in LS-DYNA is activated through the AUTOMATIC_SURFACE_TO_SURFACE option. The contact algorithm used for this purpose is based on the penalty method. This method is based on placing virtual springs normal to the interface of the contacting surfaces, and proved to be successful in maintaining the contact between the layers of the fabric pack, as well as that of the projectile and the target. The configuration of the layers and the projectile is shown in Figure 5 - 23 for a quarter of the problem due to symmetry.

The multi-ply experimental data available to this investigation were limited to only three fabrics types: S-726, S-728, and S-731. In the analysis performed on the multi-layer targets, the apparent stiffness of the fabric panels are correlated to their rate of energy absorption and to projectile deceleration, i.e. a more rapid projectile velocity drop is associated with higher target stiffness. Figure 5 - 24 to Figure 5 - 26 show the velocity-time response of the projectile impacting

a 4-ply target of S-726, S-728, and S-731 fabrics, respectively. It can thus be seen that the predictions seem to be slightly stiffer than the experimental measurements, as was the case for 1-ply targets.

Similarly, velocity-time plots of the RCC projectile impacting 8-ply targets are shown in Figure 5 - 27 to Figure 5 - 29, and 16-ply targets in Figure 5 - 30 to Figure 5 - 32, respectively for S-726, S-728, and S-731 fabrics. It seems that the over-estimation of the target stiffness becomes more pronounced as the number of layers increase. This can be due to under-prediction of the interlayer gap obtained from the method above. Further investigation of the deformed shapes and energy absorption characteristics of the multi-layer panels seem to result in the same conclusions discussed for the case of 1-ply fabric targets. Among the three panels simulated in multi-ply configuration, the S-728 panel is the most balanced. In the case of non-balanced fabrics (S-726 and S-731), the deformation cone appeared to be highly non-symmetric, as was the case in the 1-ply targets.

The failure of the yarns in multi-ply fabrics, however, led to premature perforation of the targets in many cases. Examination of the strains and stresses of the shell elements of the multi-layer models revealed the presence of a significant amount of numerical noise in the tensile response of yarns. The numerical oscillations observed appeared more pronounced in comparison to the 1-ply models, which can stem from the interaction of the fabric layers in the simulations. The excessive noise resulting from the contact algorithms caused the premature failure of the yarns and hence the early perforation of the targets. This problem should be further looked into and remedied by

implementation of more advanced failure criteria, or through averaging or damping out the oscillations.

5.2.3 Discussion of the Ballistic Impact Simulation Results

Some of the fabric panels simulated using shell elements appeared to be stiffer than what was measured in the experiments. Furthermore, while the perforation of the multi-ply targets occurred prematurely due to the presence of numerical noise, the failure prediction of the 1-ply models seemed to occur consistently at a later instance compared to the experiments. The sources of such discrepancies can be linked to several major disparities between the numerical model and the actual fabrics, as listed below:

- The input parameters corresponding to the mechanical properties of the yarns are taken from the ones reported by the manufacturer for virgin yarns before the weaving process. It is known that the weaving of fabrics causes some damage to the yarn in the form of fibre breakage and fibrillation, leading to deteriorated yarn properties [68, 69] in the form of reduced stiffness and tensile strength. The reduction in the yarn stiffness can lead to a softer response of the panel and along with the diminished yarn strength, lead to earlier perforation by the projectile in the case of 1-ply targets. To be able to consider the effects of weaving on the properties of the fabrics, laboratory experiments need to be performed on the yarns extracted from the woven panels.

- The compliance of the experimental fixture and the frequent slippage of the fabric at the boundaries are not considered in the impact simulations

presented in this study. It is known that the slippage of the fabric at the boundary plays a major role in the energy absorption of the targets [42]. Even small slippages at the fixed edges of the target can soften the response of the target and should be considered in a separate study.

- Due to the assumption of symmetry in the extensional responses of the fabric unit-cells, the slippage of the yarns at the crossover level is not allowed. Post-mortem examination of the fabric targets suggests that yarn slippage occurs within a zone including the yarns that go through the impact point. Ignoring the yarn slippage can introduce additional constraints on the motion of the yarns and increase the apparent stiffness of the fabric model.

- The numerical model, however, proved to be successful in capturing the biaxial response of the fabrics and approximating their energy absorption characteristics. The availability of this meso-mechanical fabric model allows for a close internal examination of the targets during the impact event and identification of a fabric's critical material and geometrical parameters.

5.2.4 Overall Comparison of Various Kevlar® 129 Fabrics

Aside from the success of the sine-based yarn crossover meso-mechanical model developed in this study in capturing the ballistic response of fabric panels, one needs to be able to compare the performance of fabrics with various weave parameters. In order to do so, the unit-cell responses and ballistic performances of all six Kevlar® 129 fabrics that are the focus of this study are investigated.

5.2.4.1 Unit-cell mechanical response

Studying the mechanical behaviour of Kevlar® 129 panels with different geometrical and weave properties under biaxial deformation can underscore some of the strengths and weaknesses of each fabric system. The basic characteristics of the panels are thus identified by comparing the warp and weft tension surfaces as their unit-cell is subjected to extensional displacements. These surfaces, shown in Figure 5 - 33 for S-720 fabric system, implicitly incorporate many aspects of the fabrics such as yarn crimp in the two directions, and transverse interaction of the crossing yarns.

A more comprehensive term would be the strain energy stored in the fabric as a function of the applied displacements. This energy is calculated by measuring the external work done to stretch the fabric unit-cell to a known pair of warp and weft displacements. Such energy surface can be plotted against the warp and weft strains as a three-dimensional surface or as a contour plot (see Figure 5 - 34). It should be noted that the energy calculation is only shown for the no-failure zone, where the strains in the warp and weft yarns fall below the failure strain (of 3%, considered in these figures). The value of absorbed energy is set to zero outside this zone for illustration purposes. Comparison of these energy contour plots for all six Kevlar® 129 fabric panels is shown in Figure 5 - 35 and Figure 5 - 36. As can be seen, the size of the no-failure zone is different amongst the fabrics, indicating the varying extension capacity before yarn failure occurs. Since the yarn failure strain is the same in all panels, it is only intuitive that the size of the no-failure zone be directly correlated to the level of crimp in the fabric. Furthermore, the level of energy stored in the system also varies amongst the six fabric systems, appearing to be a direct function of the yarn

linear density. Based on these contour plots, one can conclude that a panel with higher energy absorption capacity would be superior to others. This will be further discussed after the performance of these fabrics is assessed in ballistic impact simulations.

5.2.4.2 Iso-velocity fabric impact simulations

In order to further investigate the performances of the fabrics studied, non-perforating impact simulations were performed on identical panels of various fabric systems at a strike velocity of 100 m/s. Investigating the impact behaviour of fabric panels under iso-velocity conditions would reveal the differences between their energy absorption characteristics, differentiating the superior fabric systems from the others. Figure 5 - 37 shows the projectile's velocity time-history impacting the six different Kevlar® 129 panels at a strike velocity of 100 m/s. From the reduction in the projectile velocity, the energy absorbed by the target can be determined. However, one measure of the efficiency of the target is the energy that it can absorb at a certain projectile displacement.

Figure 5 - 38 shows the plot of total energy absorbed by the fabric against the projectile displacement. It is evident from this figure that S-728 is capable of stopping the projectile with the smallest back-face deformation, while S-731 is the most compliant fabric type in defeating the projectile. Looking further into the energy absorbed by the target and its components, it appears (Figure 5 - 39) that in the panels with high total crimp value (S-745 and S-731) the kinetic to internal energy component ratio is much larger than other panels. Panels with lower crimp value more or less have equal distribution of internal and kinetic

energy. A more in-depth study needs to be performed, however, to highlight more differences amongst the six fabric types.

Before performing an in-depth study on woven fabrics, it is essential to verify some of the predictions of the numerical code. For this matter, single-yarn impact simulations were carried out and predictions of the numerical code were compared with the well-established analytical solutions. It is known that when a yarn is transversely impacted, a longitudinal strain wave is generated that travels at a speed calculated as:

$$C = \sqrt{\frac{E}{\rho}} \tag{5 - 5}$$

where C is the speed of sound in the material, E is the yarn elastic modulus, and ρ is the yarn material density. Material swept by this strain wave moves towards the impact point at a constant speed. In the wake of this strain wave, a transverse wave front develops after which the motion of the material changes from in-plane to transverse at a speed equal to that of the projectile. This behaviour can clearly be seen in the single yarn impact simulation performed using the shell elements. The longitudinal wave speed calculated for an impact on an S-731 yarn is in perfect agreement with the closed form solution.

The propagation of longitudinal wave and the development of the transverse cone are also shown in Figure 5 - 40 and Figure 5 - 41 and their wave front speed is calculated. It can be seen that the transverse deformation cone has linear sides with a slope that show slight reduction in time. For the case of woven fabrics, the longitudinal wave speed decreases due to the presence of

the crossing yarns. Roylance et al. [70] suggests that the strain wave speed should be reduced by a factor of $\sqrt{2}$, as shown below:

$$C = \sqrt{\frac{E}{2\rho}} \tag{5 - 6}$$

After adjusting the mass of the shell elements to include the crossing yarns, a reduction in the longitudinal wave speed was observed which matched the value obtained from Roylance's suggested equation, as shown in Figure 5 - 42.

Yarns are rarely straight in a woven fabric. For the next step, transverse impact on a single crimped yarn is studied. In the absence of any analytical solution for this case, the effect of yarn undulation is investigated using the numerical model. Presence of slack in the yarn due to the undulation causes a reduction in the longitudinal strain wave speed, as every segment of the yarn needs to straighten out before it is able to carry the tension on to the next segment (Figure 5 - 43). The transverse wave speed (U) also gets inversely affected in the presence of yarn undulation. Furthermore, it is observed that the transverse deformation cone has a steeper side-slope in the crimped single-yarn model compared to the no-crimp case (Figure 5 - 44).

The fabric deformational response shows many similarities to the single-yarn impact cases discussed above. The longitudinal and transverse waves are generated as the projectile strikes the target, with a propagation speed that can be calculated from the motion of the nodes along the yarns. The longitudinal wave front is observed to have a distinct sharp front that flattens out as it propagates along a yarn due to wave reflection, refraction and transmission at the crossover points. This is shown for the S-720 panel in the plot of warp and

weft tension along the central yarn going through the impact point in Figure 5 - 45 and Figure 5 - 46. The transverse wave front speed is also observed to be affected by the crimp in the system. This is the main reason behind the non-symmetric shape of the deformation cone in the unbalanced panels such as S-731. As seen in Figure 5 - 47, there is a significant difference in the transverse wave speed between the warp and the weft direction of S-731. The warp direction with higher crimp value clearly has a sharp side angle (similar to the case of single crimped yarn impact discussed earlier) and a lower transverse wave speed, while the less undulated weft direction behaves similar to the no-crimp single yarn impact response.

The reduction of the wave speeds seems to be an inverse function of the yarn crimp. As a matter of fact, a power relation seems to exist between the longitudinal wave speed and the yarns crimp, as shown in Figure 5 - 48 for the C values measured for the warp and weft yarns of all panels impacted at 100 m/s. A similar trend is found for the transverse wave speed, U, as shown in Figure 5 - 49.

Some studies suggest that the energy absorption characteristics of a fabric panel seem to be influenced by the longitudinal wave speed. Comparing the ratio of kinetic to internal energy components in the six Kevlar® 129 fabrics presented in Figure 5 - 39 and the average (warp and weft) longitudinal wave speed plotted in Figure 5 - 50 it can be seen that as the average longitudinal wave speed in a fabric increases, there is a more tendency for the energy components (kinetic and strain energies) to equally contribute to the overall energy absorption of the panels.

Perforation of the fabric panels as a result of yarn failure is of a significant importance in the study of their ballistic performance. As discussed earlier in Section 5.2.3, the numerical model generally overestimates the energy absorption capacity of the panels, resulting in a higher critical velocity than the experimental results, as seen in Figure 5 - 51. By definition, critical velocity is the projectile speed above which the target is perforated and below which the projectile is arrested by the fabric. Due to the deterministic nature of the numerical model, this critical velocity is always a constant value for a specific fabric system. On the other hand, due to the influence of many factors on the perforation of the projectile such as the material flaws in the fabric, the experimental critical velocity is not easy to determine. In this study, the experimental critical velocity is calculated by taking the average of the highest non-perforating and lowest perforating strike velocities recorded for each fabric.

The discrepancy between the predicted critical velocity and the measured value seems to be influenced by the tightness of the fabric. As shown in Figure 5 - 53, the difference between the predicted and measured critical velocity diminishes as the fabric average count number increases. This is mainly attributed to the fact that tighter weaves reduce the occurrence possibility of deformation mechanisms ignored in the shell model, mainly yarn slippage and non-symmetric loading of the unit cells. Post-mortem examination of different perforated panels reveal the difference in the projectile penetration mechanism, as illustrated in Figure 5 - 52, i.e. projectile impacting the panels with looser weave would pull the yarns and wedge through them, while the yarns would rupture in the tighter weaves as the projectile perforates the target.

Although the failure prediction of the model is not in complete agreement with the experimental observation (Figure 5 - 51), they can still be used to investigate the trends amongst the panels. Using the energy surfaces previously shown in Figure 5 - 35 and Figure 5 - 36, one can determine the remaining energy absorption capacity of a panel before any yarn failure occurs. For the case of 100 m/s iso-velocity impact simulations, the energy absorbed by the elements surrounding the projectile at the most critical time (closest to failure) are overlaid on the energy contour plots in Figure 5 - 54. It can be concluded from these plots that while a panel like S-745 still has a significant amount of energy absorption capability, S-731 is very close to experience failure of its weft yarn (maximum d_2). Such analysis also shows the importance of having balanced fabrics, since the capacity of both warp and weft directions are utilized optimally before yarn failure occurs.

As mentioned before, the lack of symmetry in the imbalance panels would result in a less than optimum ballistic performance. However, in the multi-layer packs, this asymmetry can be reduced by increasing the interaction of the consecutive layers. Since the asymmetric deformation cone shapes of every layer tends to nest in the similar profile of its successive layers, one method of increasing the inter-ply interaction is to prevent this nesting phenomenon. Alternating the warp and weft alignments of neighbouring fabric layers within the multi-ply pack would significantly increase the contact between adjacent layers, and would result into a deformation profile that is more symmetric. This hypothesis is examined for the case of a 4-layer S-726 panel, with the deformed shapes illustrated in Figure 5 - 55 for the similar and alternating

packing systems. The deformed shape of the individual layers, specifically those located in the middle of the pack, take a more symmetric shape, as shown in Figure 5 - 56 for the deformation of the third layer of fabric away from the strike face of the S-726 4-ply target. The target with alternating packing sequence also exhibits a higher ballistic efficiency, evident from its improved energy absorption capacity (see the velocity-time response of the projectile in Figure 5 - 57).

5.3 BIAXIAL FABRIC EXTENSION SIMULATIONS

In order to examine the capabilities and limitations of the shell crossover model, an attempt was made to simulate biaxial loading experiments on plain weave fabrics. The experimental data used for this validation exercise is taken from the article of Buet-Gautier and Boisse [37], who presented the results of several biaxial extension tests on woven composite reinforcements. These results included tests on balanced and non-balanced plain weave glass fabric and twill weave carbon fabric. For the purposes of this study, only the test results on plain weave fabrics are investigated.

The biaxial tensile testing device used by Buet-Gautier and Boisse [37] for these experiments is capable of subjecting the fabric to simultaneous prescribed displacements in the warp and weft directions. Square cross-shaped fabric patches with dimensions shown in Figure 5 - 58 were tested and the results were reported in terms of load measured per yarn versus fabric strain. The geometric and mechanical properties of a balanced plain weave glass fabric studied in the biaxial experiments for different strain ratios (k) is provided in

Table 5 - 3. Since this specific fabric is balanced in all aspects, the warp and weft responses are identical and only one set of the results are reported. Table 5 - 3 also provides the properties of a non-balance fabric made from significantly different glass yarns in the warp and weft directions subjected to biaxial loading. Buet-Gautier and Boisse [37] proposed a meso-mechanical model based on the linear model by Kawabata [55] and were successful in predicting the response of the fabrics investigated compared to the experimental data. However, they adopted a transverse compression model that is a function of the yarns axial strain, whose constants were back-calculated from the experimental data for equal warp and weft loading ($k = 1$).

The sine-based meso-mechanical model developed here is used to capture the biaxial response of the fabrics tested by Buet-Gautier and Boisse [37]. To obtain the parameters of the transverse compression model, an inverse calculation approach was used, similar to that of Buet-Gautier and Boisse [37]. The tensile response of the glass yarns were considered to be linear, despite their apparent initial nonlinearities. The bending of yarns was also ignored in the calculations. The input values calculated from the panel properties (such as yarn heights, h_i) and fitted (in the case of transverse compression parameters, a and b) are presented in Table 5 - 4. Figure 5 - 59 shows the single yarn tensile response prediction, as well as that of the fabric where the perpendicular direction is free. Also, the fabric response prediction for iso-displacement loading case ($k = 1$) fitted to the experimental data is depicted in the same figure. With all the material and mechanical parameters determined, the fabric's biaxial

extensional response is obtained using the shell element. As seen in Figure 5 - 60, the predictions are in good agreement with the experimental data.

Similar analysis is performed on a non-balanced glass fabric, where the properties of the warp and weft yarns are significantly different. Figure 5 - 61 and Figure 5 - 62 show the tensile response of the warp and weft extensional responses of single yarns and that of the non-balance glass fabric with free boundary conditions in the perpendicular direction. Similar to other cases, the transverse compression model is calibrated with the biaxial data for $k = 1$. The predictions for other warp to weft strain ratios ($k = 0.5 \& 2$) show some discrepancies. As seen in Figure 5 - 63, while the response prediction of the model for the warp direction for the ratio $k = 2$ matches that of the experiment, the prediction for $k = 0.5$ loading case is not consistent with the test data. A similar trend is also observed for the fabric tension in the weft direction (Figure 5 - 64), showing some discrepancies between the model predictions and the experimental data. Probable sources of such disagreement are listed below:

- The sine-based formulation of the current meso-mechanical model is based on the assumption that the crossing yarns are in contact with each other over a significant portion of their lengths, i.e. little gap exists between parallel yarns. As a result, the sine-based model is usually well suited for tight fabrics with yarns of high linear density and count numbers (as is the case for the Kevlar® 129 fabrics investigated in the ballistic experiments). The non-balanced glass fabric studied by Buet-Gautier and Boisse [37] do not match the above description, pushing the sine-based model to the limits of its validity. For these fabrics, the Kawabata [55] straight-yarn model is

better suited, since the contact is concentrated in the middle area of the unit-cell and the yarns more or less maintain a linear profile.

- The transverse compression force-displacement model implemented by Buet-Gautier and Boisse [37] et al. incorporates the axial strain of the yarns in determining the value of their transverse stiffness. This dependency is related to the change in the contact area of the crossing yarns and the ability of the fibres/filaments to move with respect to each other as they are transversely compressed. The transverse compression model developed in this thesis for the crossing yarns ignores any such dependency.

- The force-strain response of the yarns considered is linear in the current model, while the extension tests on single glass yarns show nonlinearities at low strain values. Using the linear tensile response for the yarns leads to unrealistic values for transverse model parameters after fitting the model prediction to the experimental data for $k = 1$. Poor correlations with experiments thus result when the predictions for other loading ratios are carried out.

- The determination of the beginning of the curve in the experimental data is not an easy task. For these experiments, Buet-Gautier and Boisse [37] chose to use a kinematic criterion where the beginning of the curve is marked at the instant where all the yarns (sagging initially under self-weight) arrive at the mid-plane of the fabric. Slight shifting of the curve to the left and right can alter the error in the numerical predictions, specifically for the $k = 0.5$ case of Figure 5 - 63 and Figure 5 - 64.

5.4 SUMMARY

The efficient shell element developed in the previous chapter was used to perform ballistic impact simulations on single and multi-ply fabric targets. The results were compared with the data from instrumented ballistic impact experiments and found to be in good agreement in capturing the general ballistic response of the fabrics. It was also found that the numerical predictions are always slightly stiffer that the tested panel. This discrepancy was attributed to such factors as using mechanical properties of the virgin yarns, the choice of transverse compression model, and ignoring the compliance of the experimental fixture and sliding at the boundaries.

The six Kevlar® 129 fabric types were also compared with each other at the unit-cell level, as well as the full fabric scale. It was found that the energy absorption of the panels are highly affected by the yarn undulation and that panels with balanced warp and weft properties exhibit a more optimized response. It was also indicated that alternating the warp and weft alignment in a multi-layer pack made from unbalanced fabric would improve its energy absorption characteristics. However, the shell elements proved to be unsuccessful in capturing the failure of the yarns and projectile perforation in multi-layer targets, as the excessive oscillation caused by the contact algorithms lead to premature failure of the yarns. The possibility of incorporating a failure model other than instantaneous erosion strain ought to be investigated.

The biaxial response of fabrics under quasi-static extensional loading was studied using the sine-based shell crossover model. The experimental data for

this analysis was taken from the article by Buet-Gautier and Boisse [37], who applied biaxial displacements in the warp and weft directions (at a variety of different ratios) and measured the load required to do so. While the shell crossover model was successful in capturing the response of a balanced glass fabric, it did not appear to be as successful in the case of an unbalanced fabric. Further investigation of the results and the panels tested showed that the specific properties of the weave and the difference between the warp and weft yarns used in the unbalanced glass fabric would invalidate the basic assumptions of the shell crossover model and hence lead to erroneous results.

Table 5 - 1: Input values used to set up shell-based fabric models to simulate instrumented ballistic impact experiments.

Properties	S-720	S-726	S-727	S-728	S-731	S-745
Elastic modulus (GPa)	96.0					
Shell thickness (mm)	0.43	0.31	0.34	0.44	0.38	0.67
F-d parameter a (mm)	0.045	0.05	0.0425	0.0044	0.046	0.082
F-d parameter b (mm.$\mu N^{1/3}$)	5.8	5.0	5.5	7.8	2.5	9.0
Yarn (denier)	1420	840	1000	1500	1000	3000
Warp count (tpi*)	20	26	26	17	31	17
Weft count (tpi*)	20	27	26	17	31	17
Warp crimp (%)	2.18	3.44	3.38	1.76	8.16	5.27
Weft crimp (%)	1.39	0.50	0.74	0.94	0.56	1.38
H01 (mm)	0.12	0.11	0.12	0.13	0.15	0.22
H02 (mm)	0.10	0.04	0.05	0.09	0.04	0.11
Failure strain	0.03	0.03	0.03	0.03	0.03	0.03
Areal density (g/m^2)	255.2	201.4	238.1	231.1	282.3	473.7

(*tpi: threads per inch)

Table 5 - 2: Interlayer gap determined from the transverse compression test data performed on 4-ply fabric samples.

Fabric Panel	Interlayer gap (mm)
S-726	0.10
S-728	0.12
S-731	0.14

Table 5 - 3: Geometric and mechanical properties of the plain weave glass fabric panels studied by Buet-Gautier and Boisse [37].

Panel		Balanced glass weave	Non-balance glass weave
Count (threads/mm)	warp	0.22	0.22
	weft	0.22	0.16
Crimp (%)	warp	0.40	0.42
	weft	0.40	0.65
Tenacity (N)	warp	350	850
	weft	350	80
Stiffness* (N)	warp	38000	75000
	weft	38000	8900

(*Stiffness is defined as the slope of the tension-strain curve of the yarns)

Table 5 - 4: Shell element input parameters used to carry on simulation of biaxial loading of fabric panels studied by Buet-Gautier and Boisse [37].

Panel		Balanced glass weave	Non-balance glass weave
h (mm)	warp	0.18	0.26
	weft	0.18	0.23
Shell dimension (mm)	warp	4.55	6.25
	weft	4.55	4.55
a (mm)	warp	0.075	0.21
b (mm.$\mu N^{1/3}$)	weft	3.50	16.0

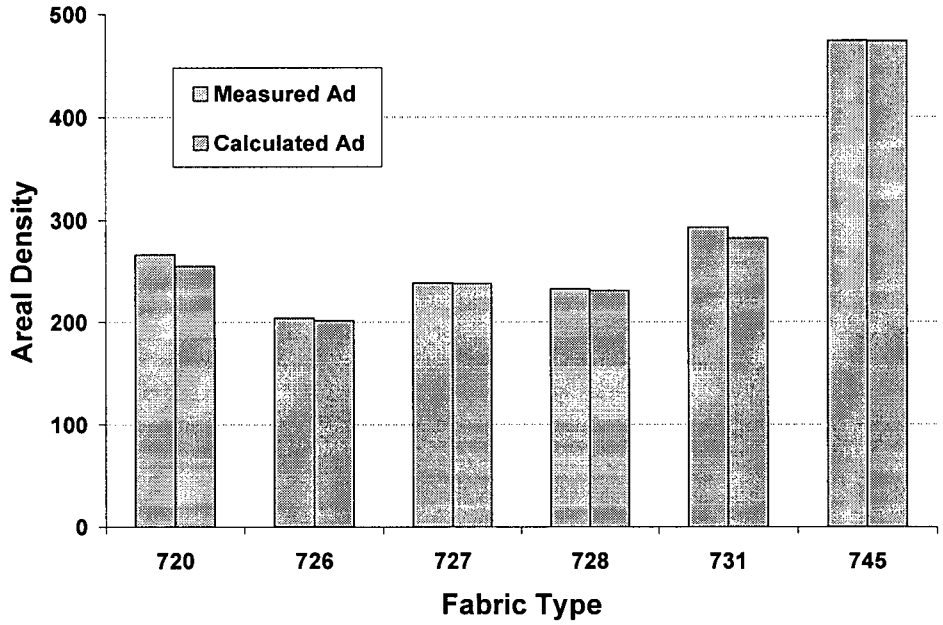

Figure 5 - 1: Areal density comparison of the six Kevlar® 129 panels investigated. Further information on these panels is provided in Chapter 3.

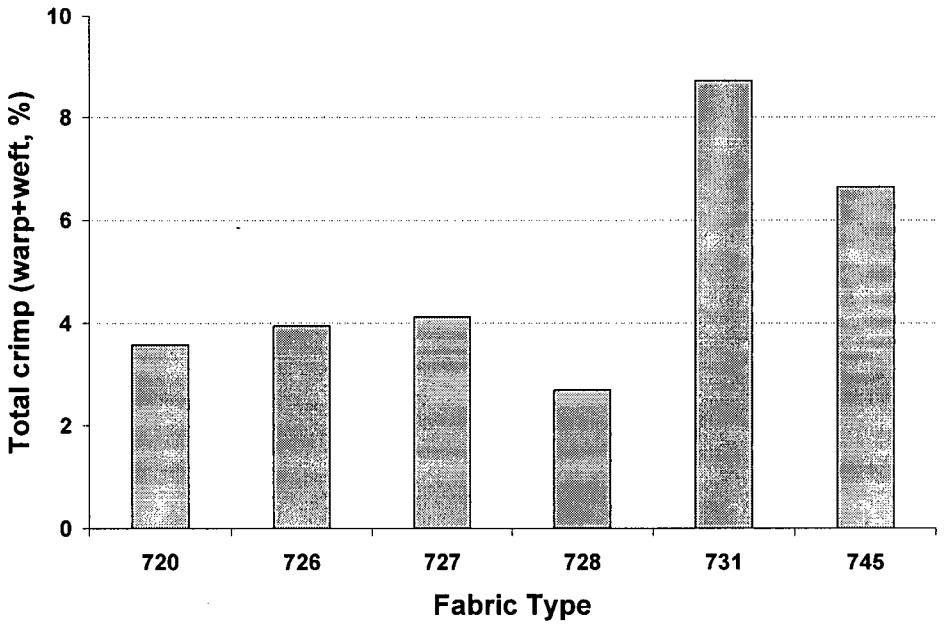

Figure 5 - 2: Crimp comparison of the six Kevlar® 129 panels investigated. Further information on these panels is provided in Chapter 3.

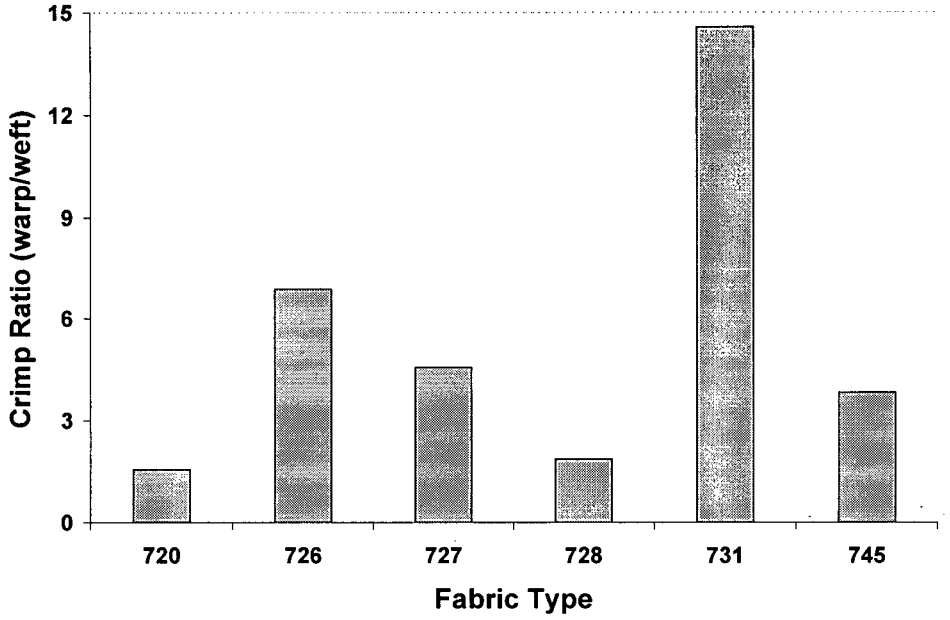

Figure 5 - 3: Crimp ratio (warp/weft) comparison of the six Kevlar® 129 panels investigated. Further information on these panels is provided in Chapter 3.

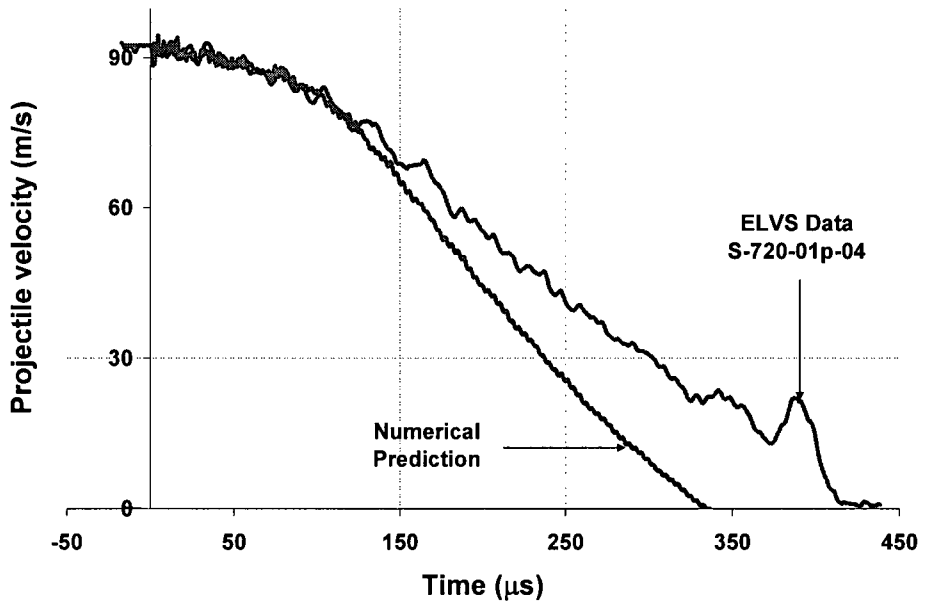

Figure 5 - 4: Velocity-time response of an RCC projectile in a non-perforating impact simulation of a 1-layer S-720 target struck at 92.5 m/s.

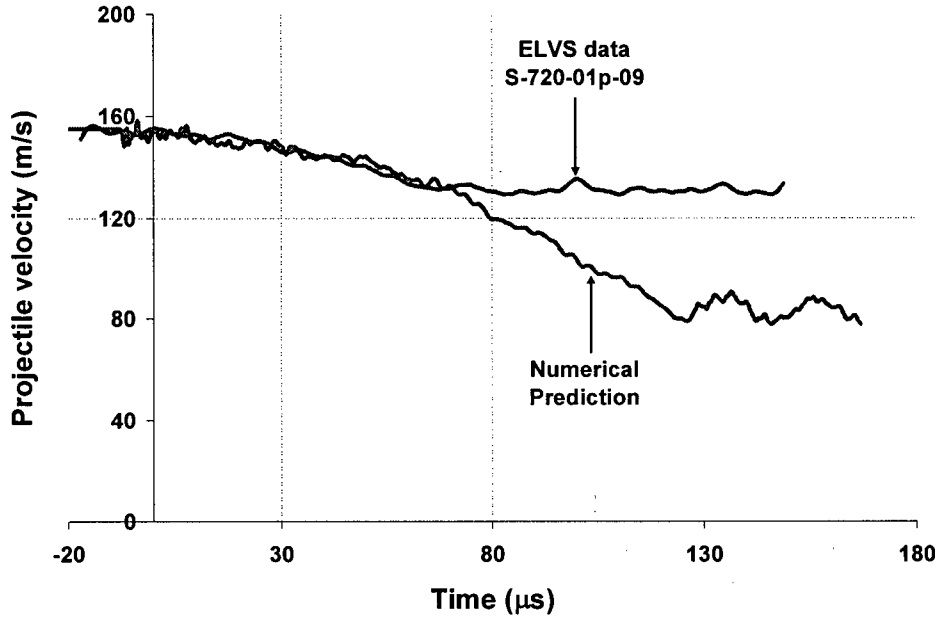

Figure 5 - 5: Velocity-time response of an RCC projectile in a perforating impact simulation of a 1-layer S-720 target struck at 155 m/s.

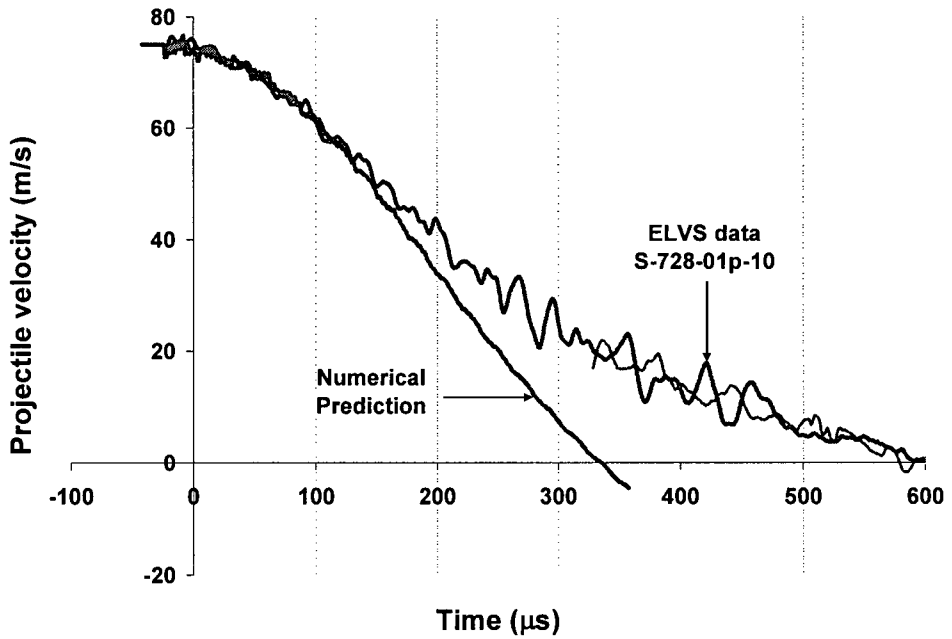

Figure 5 - 6: Velocity-time response of an RCC projectile in a non-perforating impact simulation of a 1-layer S-728 target struck at 76 m/s.

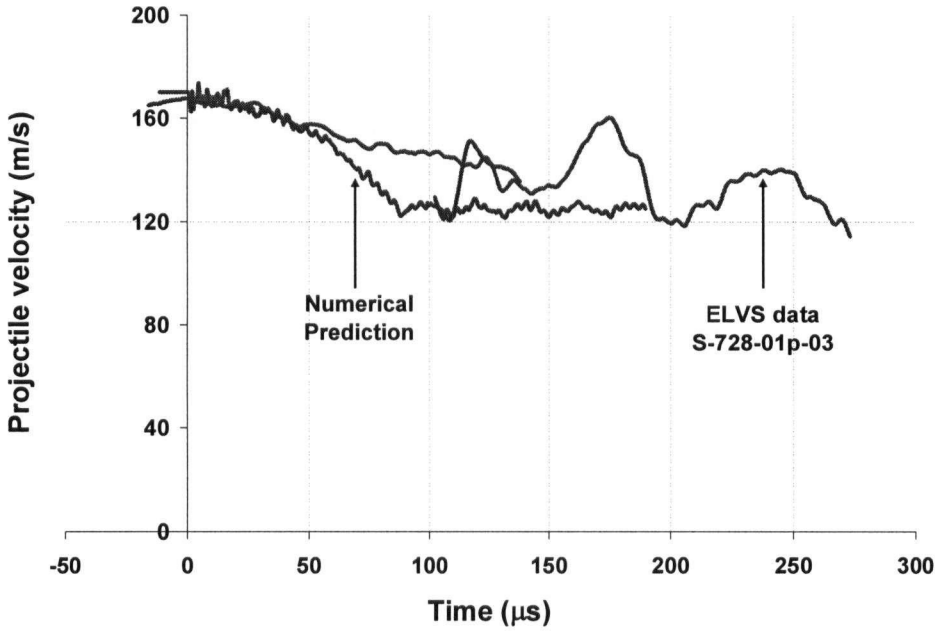

Figure 5 - 7: Velocity-time response of an RCC projectile in a perforating impact simulation of a 1-layer S-728 target struck at 170 m/s.

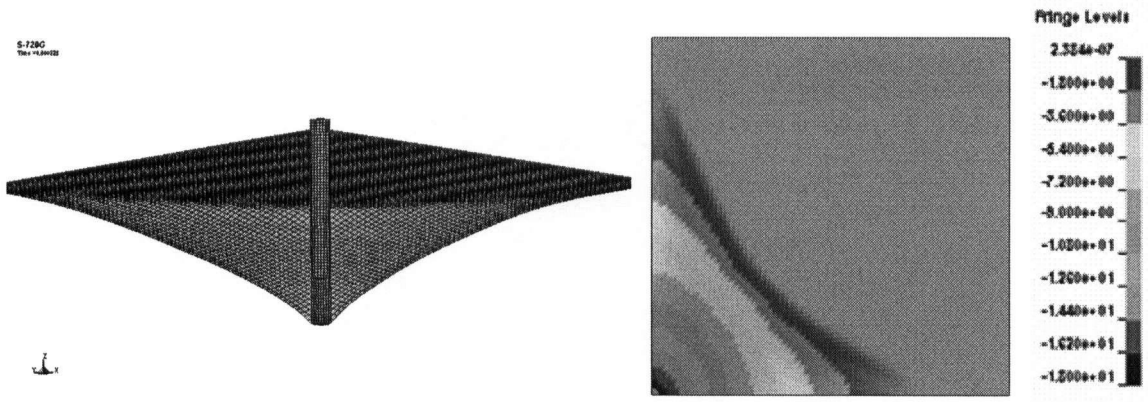

Figure 5 - 8: Transverse deformation profile (left) and corresponding fringe plot (right) for a 1-ply S-720 panel impacted at 100 m/s after 225 μs.

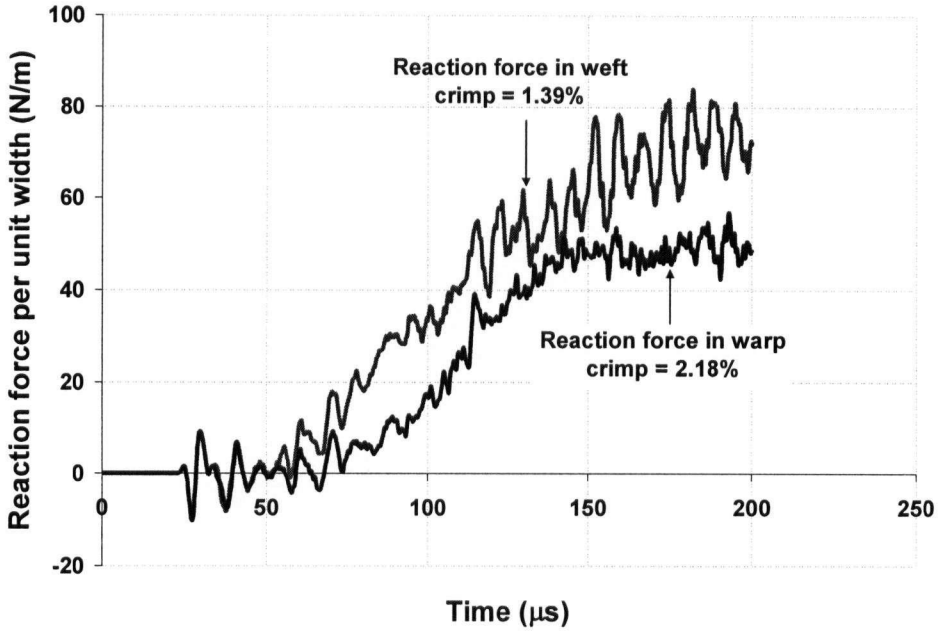

Figure 5 - 9: Comparison of the normalized reaction force in warp and weft of S-720 fabric.

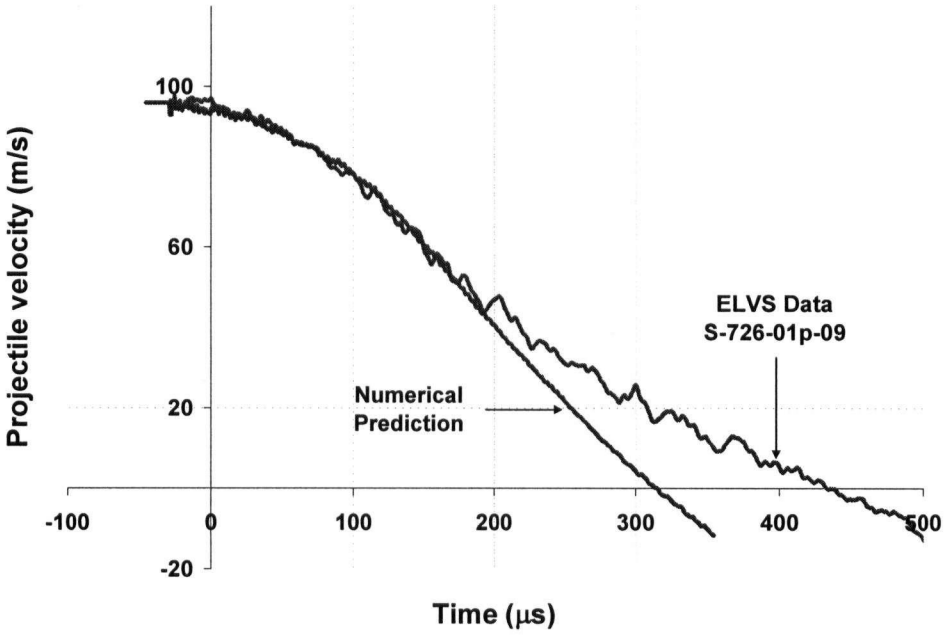

Figure 5 - 10: Velocity-time response of an RCC projectile in a non-perforating impact simulation of a 1-layer S-726 target struck at 96 m/s.

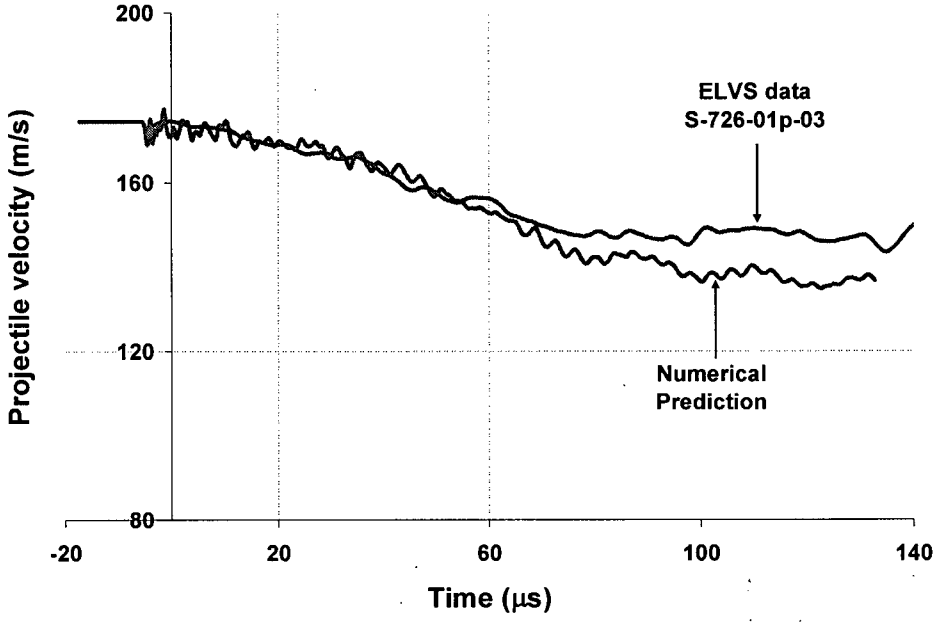

Figure 5 - 11: Velocity-time response of an RCC projectile in a perforating impact simulation of a 1-layer S-726 target struck at 174 m/s.

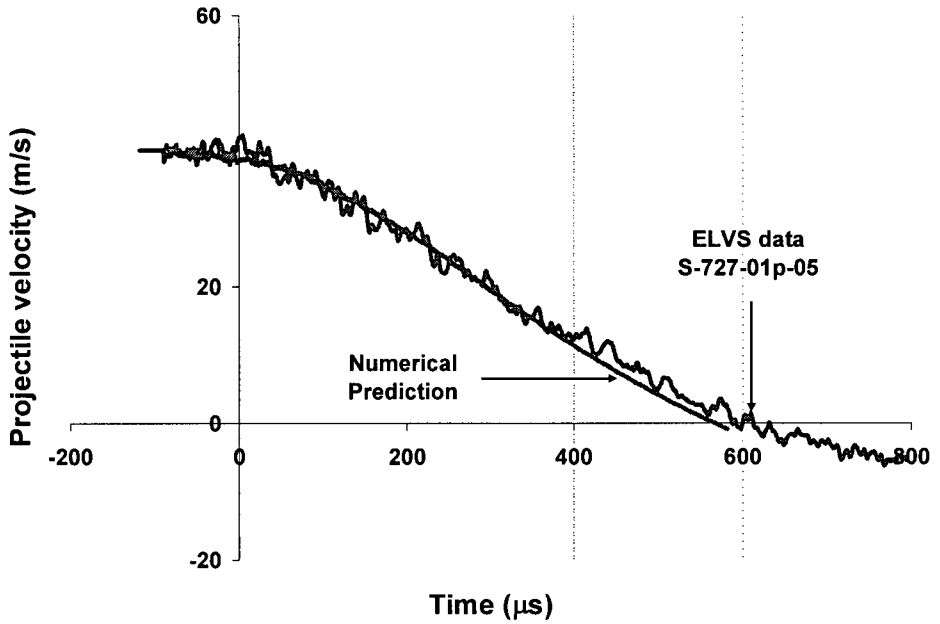

Figure 5 - 12: Velocity-time response of an RCC projectile in a non-perforating impact simulation of a 1-layer S-727 target struck at 40 m/s.

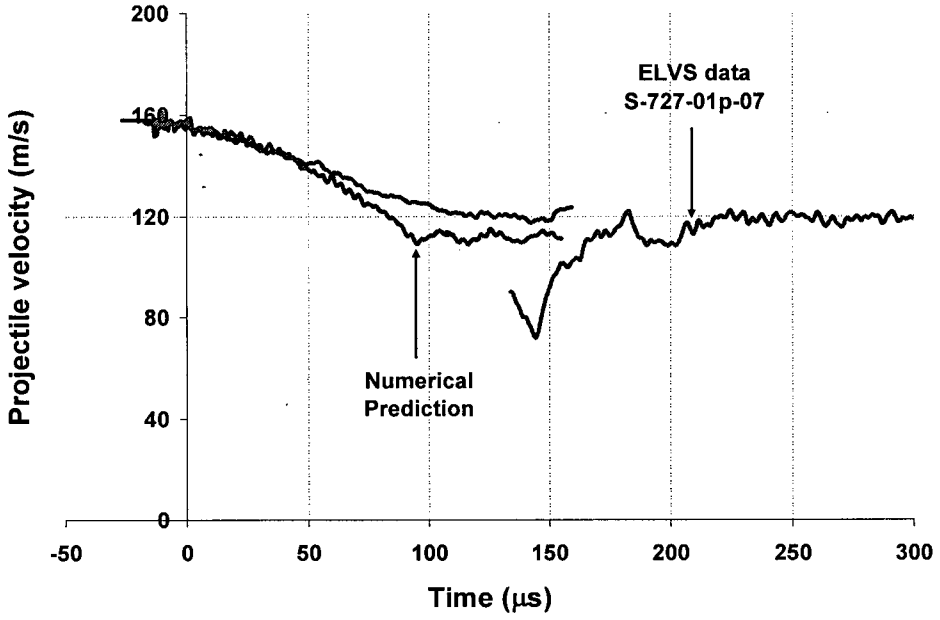

Figure 5 - 13: Velocity-time response of an RCC projectile in a perforating impact simulation of a 1-layer S-727 target struck at 158 m/s.

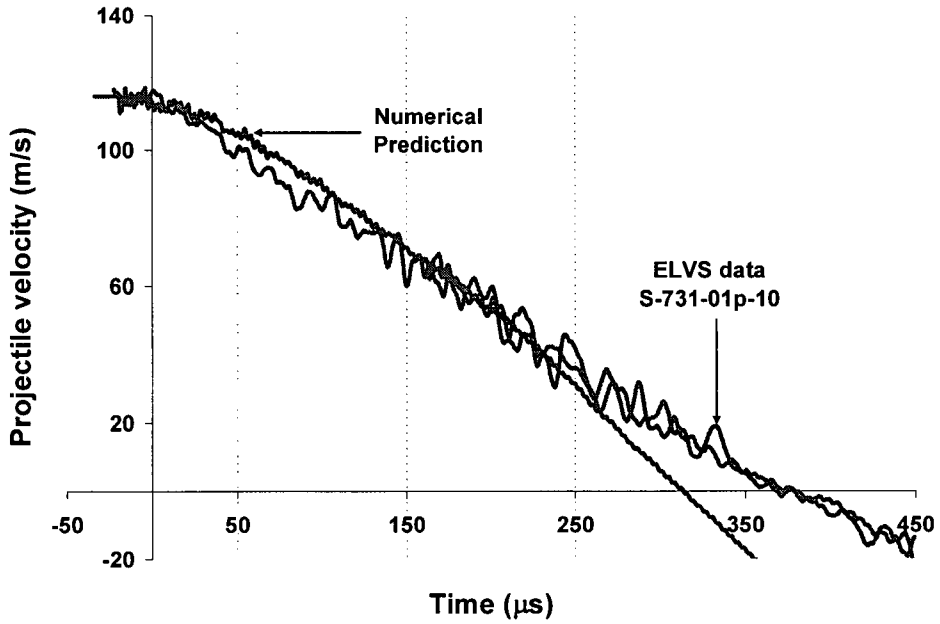

Figure 5 - 14: Velocity-time response of an RCC projectile in a non-perforating impact simulation of a 1-layer S-731 target struck at 116 m/s.

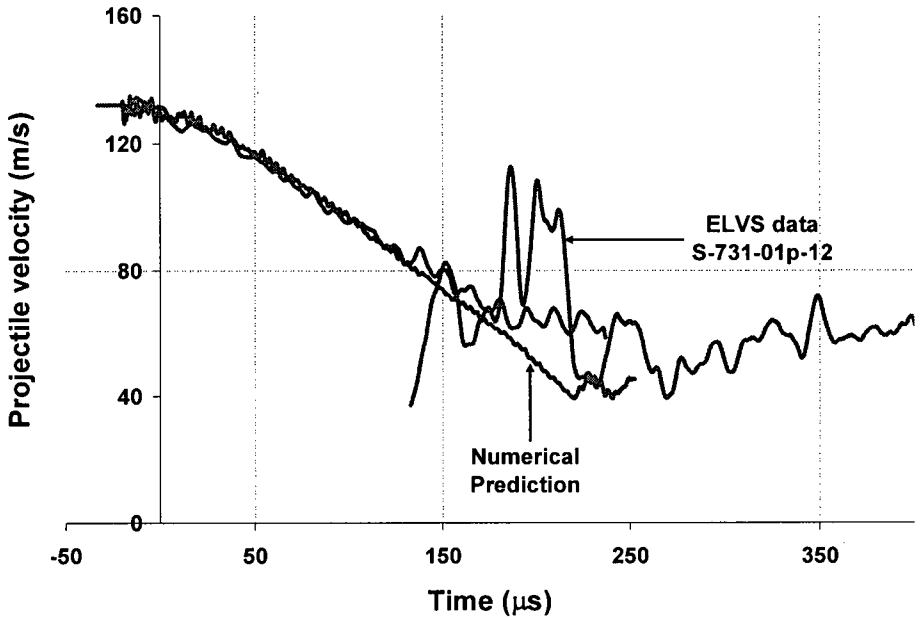

Figure 5 - 15: Velocity-time response of an RCC projectile in a perforating impact simulation of a 1-layer S-731 target struck at 132 m/s.

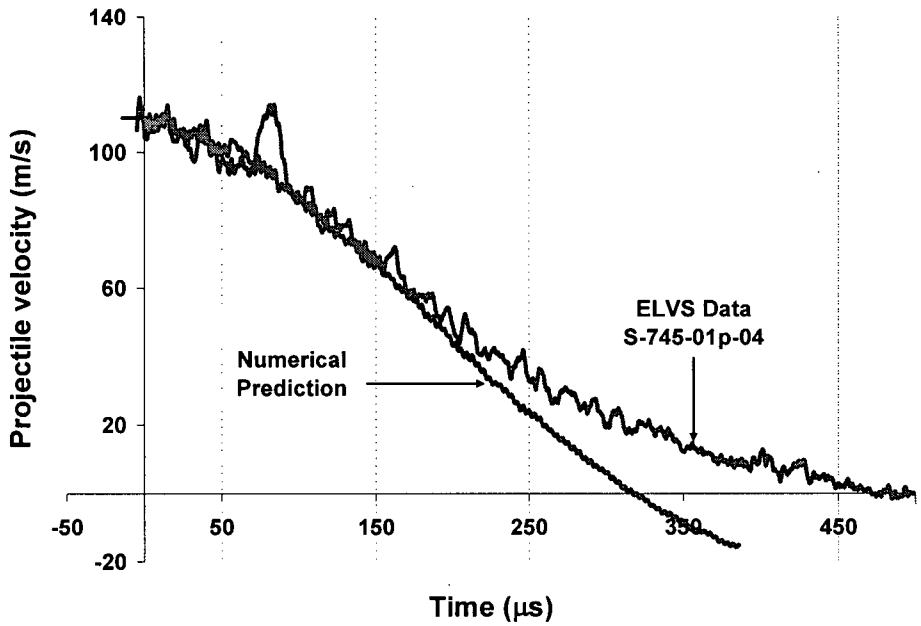

Figure 5 - 16: Velocity-time response of an RCC projectile in a non-perforating impact simulation of a 1-layer S-745 target struck at 110 m/s.

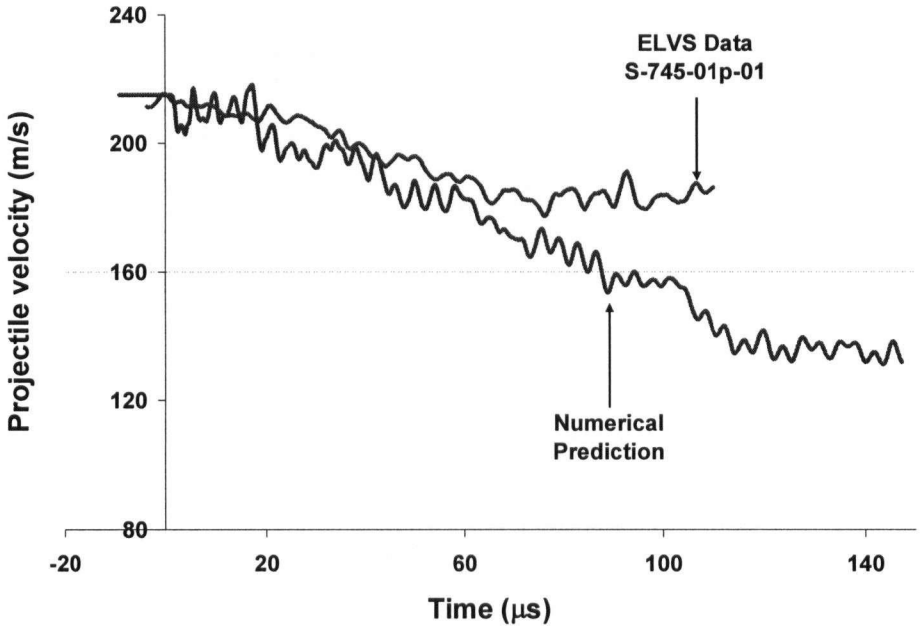

Figure 5 - 17: Velocity-time response of an RCC projectile in a perforating impact simulation of a 1-layer S-745 target struck at 215 m/s.

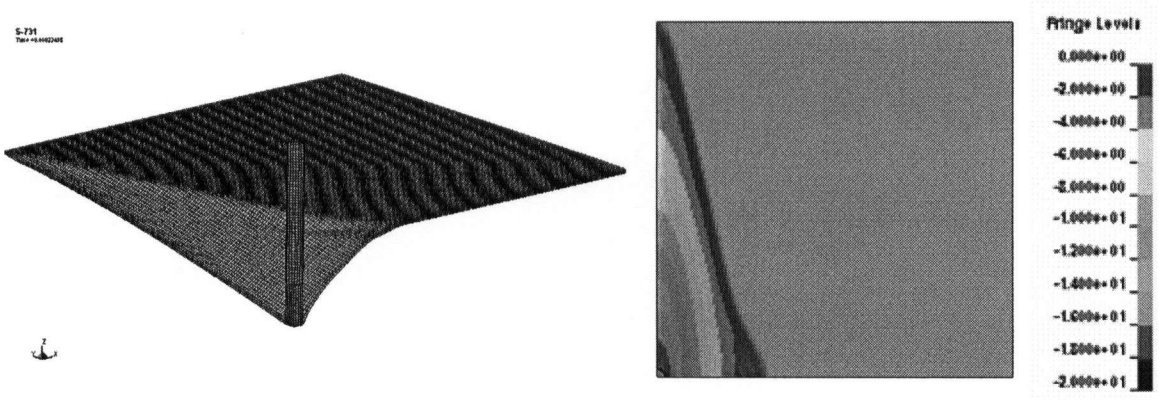

Figure 5 - 18: Transverse deformation profile (left) and corresponding fringe plot (right) for a 1-ply S-731 panel impacted at 100 m/s after 225 μs.

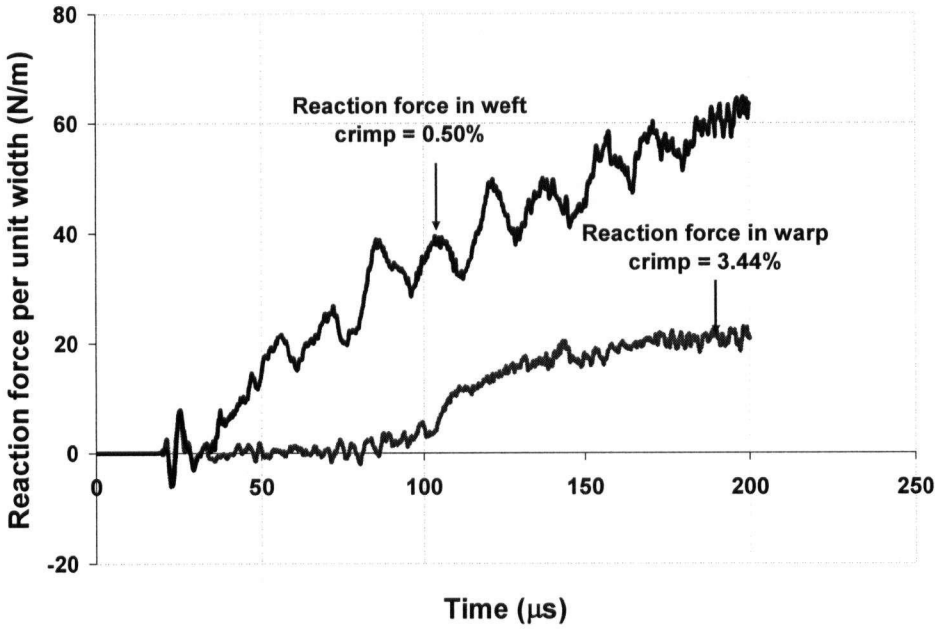

Figure 5 - 19: Comparison of the normalized reaction force in warp and weft of S-726 fabric.

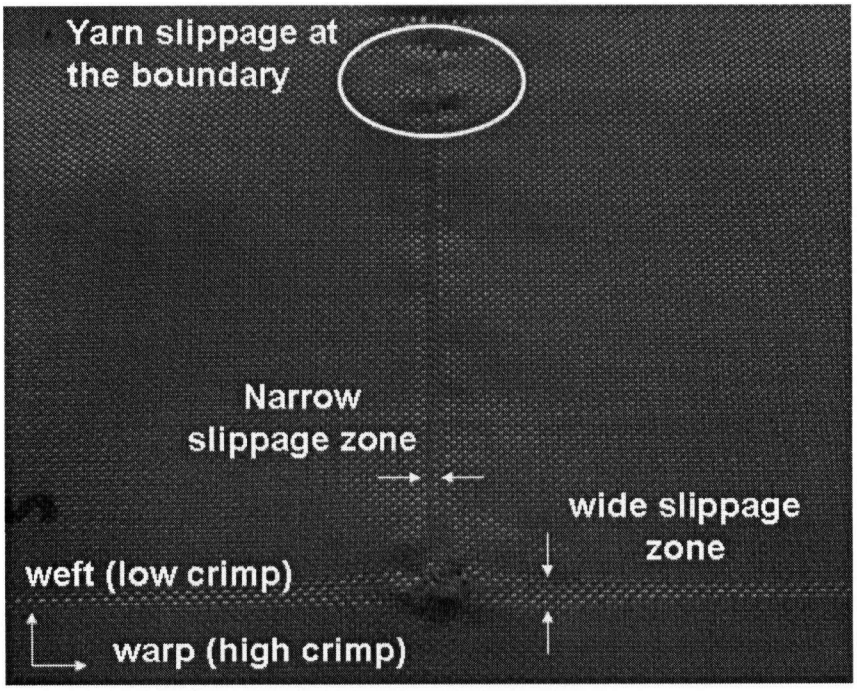

Figure 5 - 20: Post-mortem examination of the 1-layer S-726 panels impacted at 175 m/s.

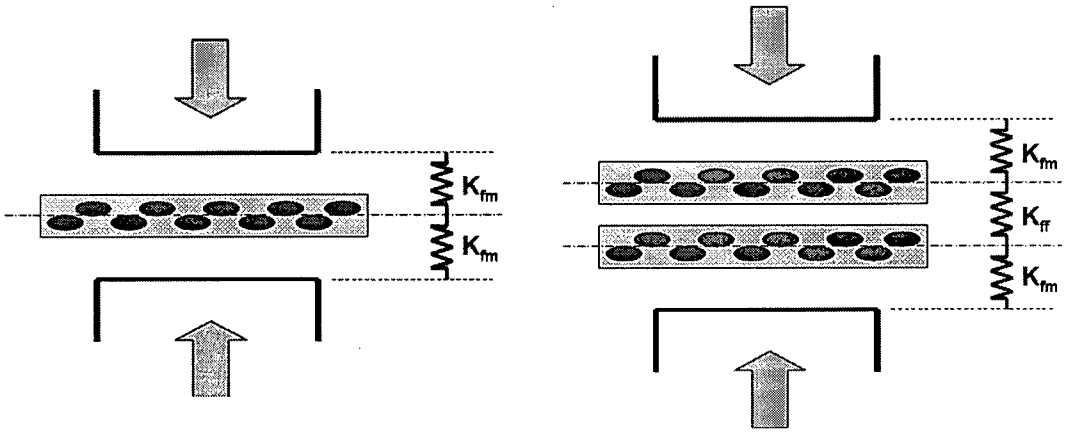

Figure 5 - 21: Schematics of the mechanical model considered for the transverse compression of single and two-ply fabric specimens.

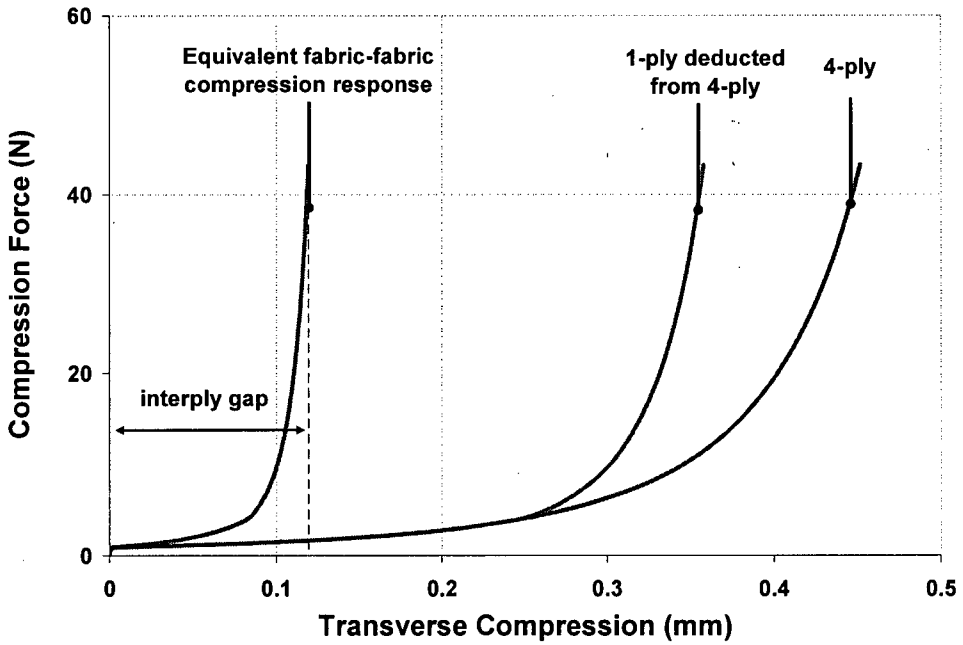

Figure 5 - 22: Calculation of inter-ply gap from transverse compression experiments, obtained for 4-ply S-728 fabric.

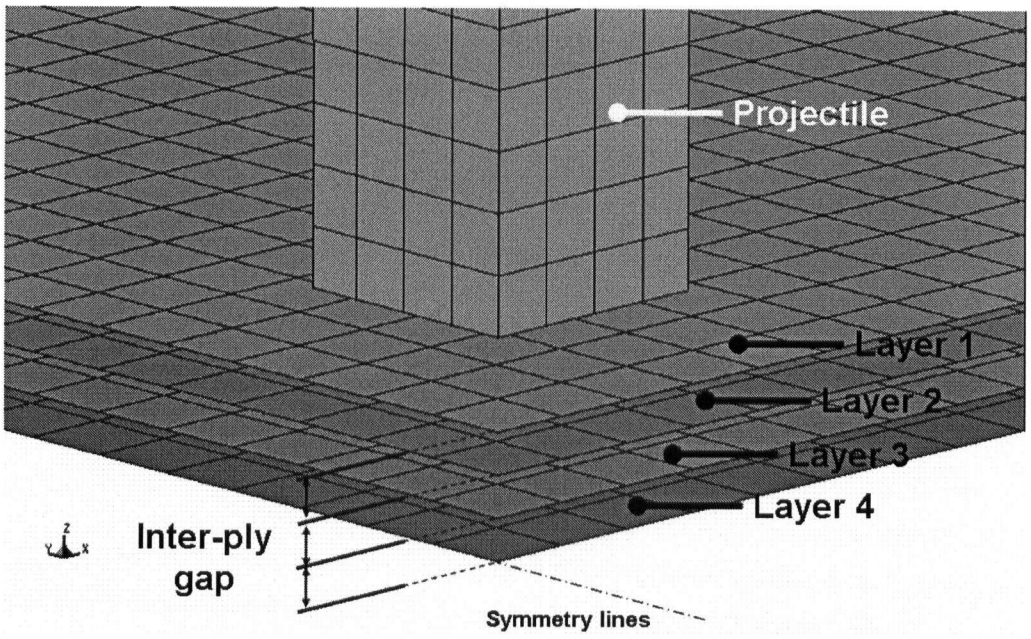

Figure 5 - 23: A schematic arrangement of multiple layers made from shell elements to construct a 4-ply S-726 4-layer model (quarter of the model is shown due to symmetry).

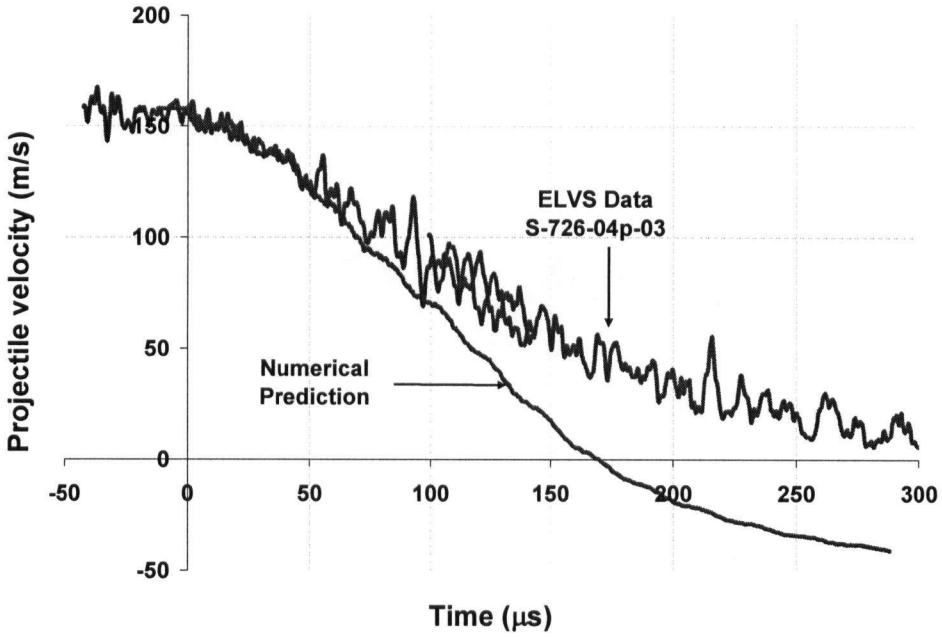

Figure 5 - 24: Velocity-time response of an RCC projectile in a non-perforating impact simulation of a 4-layer S-726 target struck at 158 m/s.

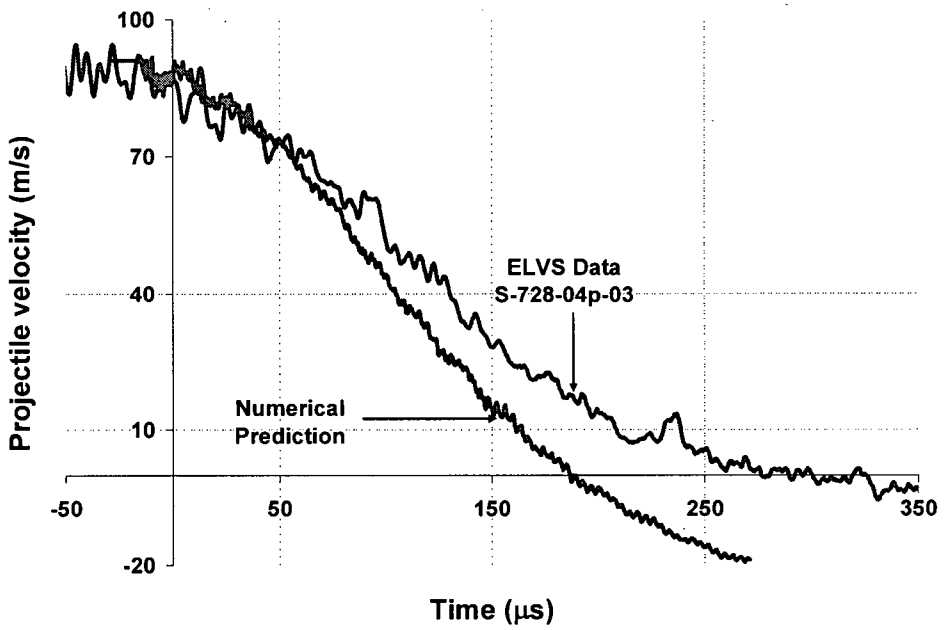

Figure 5 - 25: Velocity-time response of an RCC projectile in a non-perforating impact simulation of a 4-layer S-728 target struck at 91 m/s.

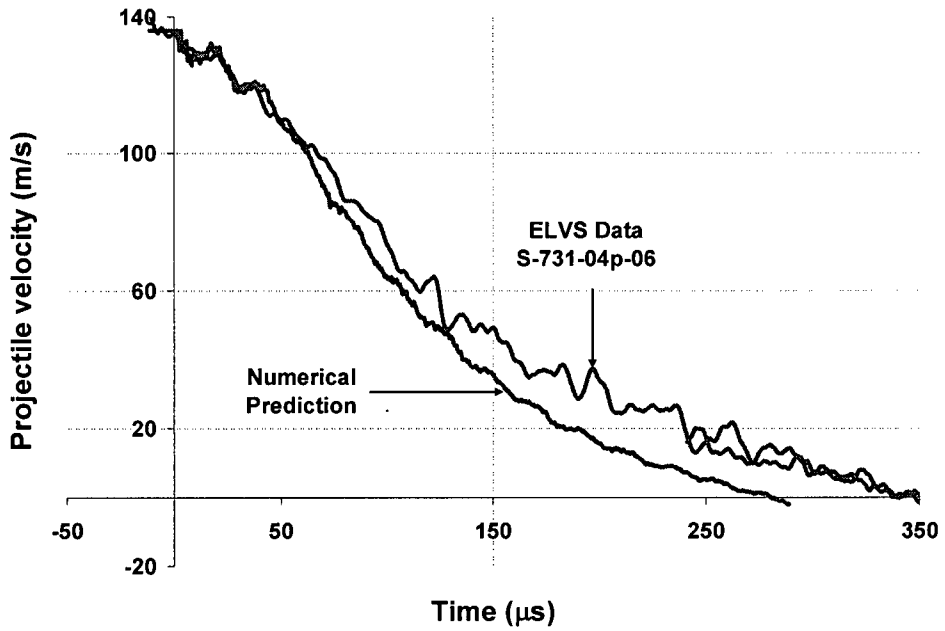

Figure 5 - 26: Velocity-time response of an RCC projectile in a non-perforating impact simulation of a 4-layer S-731 target struck at 136 m/s.

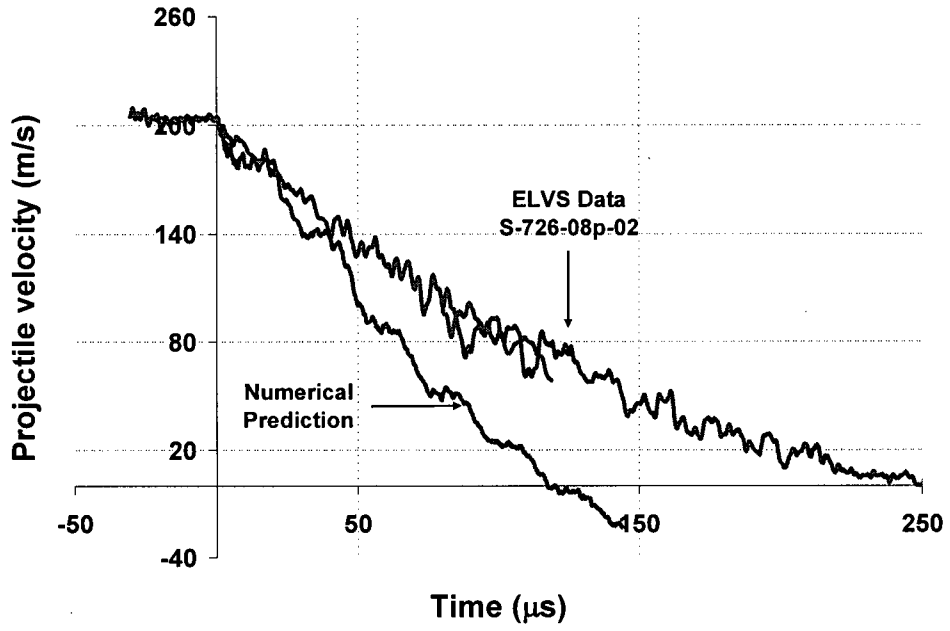

Figure 5 - 27: Velocity-time response of an RCC projectile in a non-perforating impact simulation of an 8-layer S-726 target struck at 204 m/s.

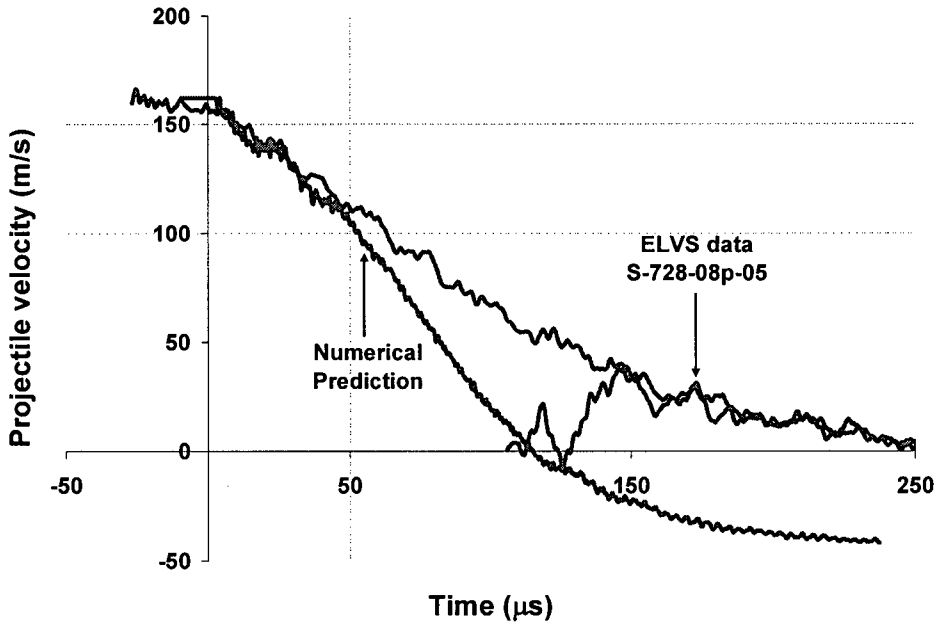

Figure 5 - 28: Velocity-time response of an RCC projectile in a perforating impact simulation of an 8-layer S-728 target struck at 162 m/s.

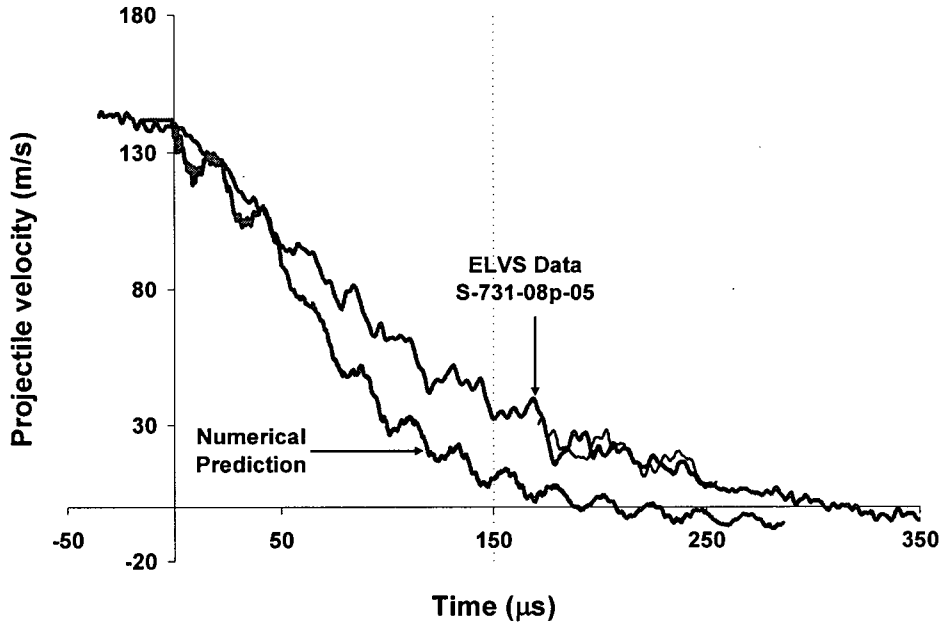

Figure 5 - 29: Velocity-time response of an RCC projectile in a perforating impact simulation of an 8-layer S-731 target struck at 142 m/s.

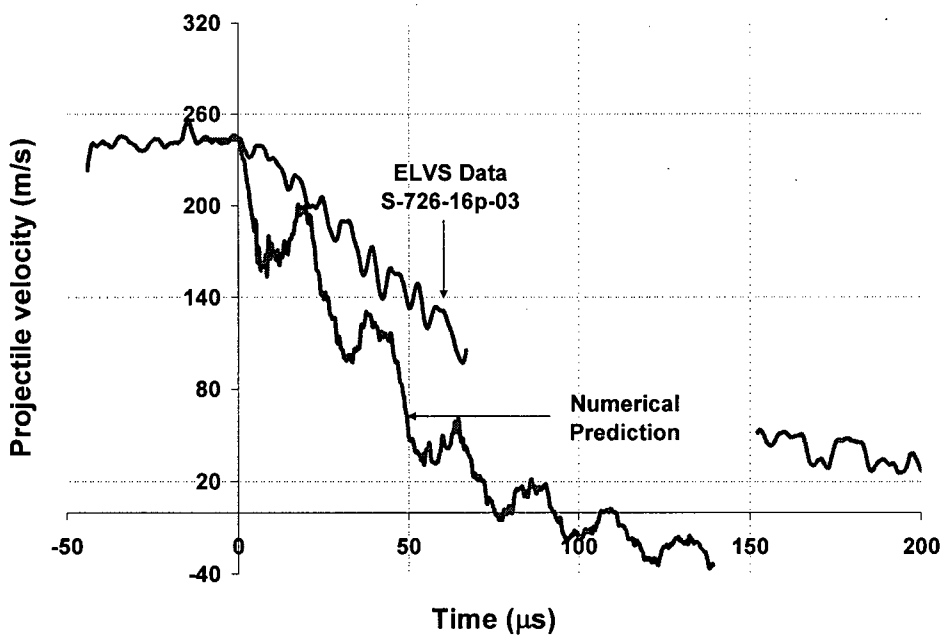

Figure 5 - 30: Velocity-time response of an RCC projectile in a perforating impact simulation of a 16-layer S-726 target struck at 243 m/s.

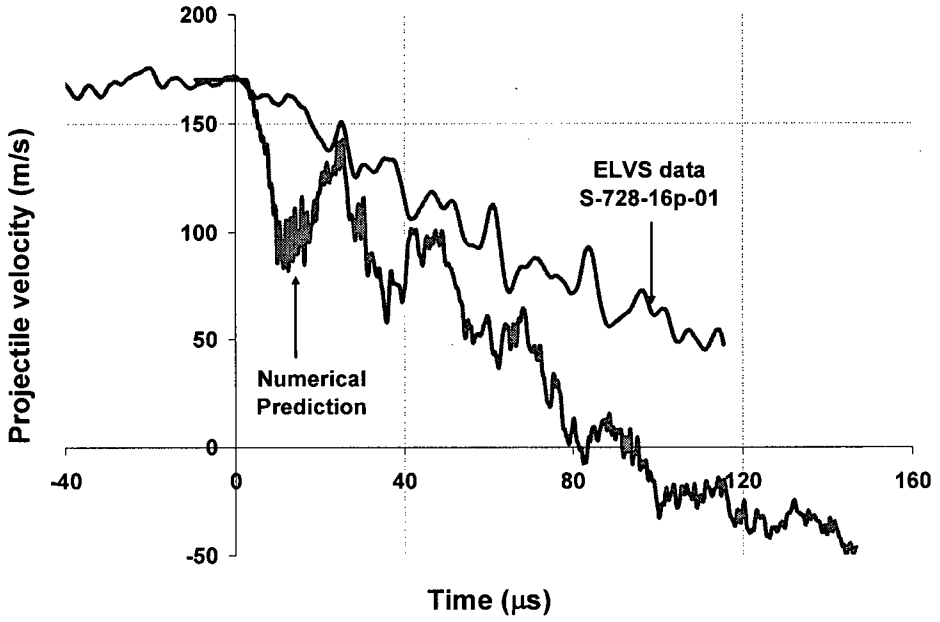

Figure 5 - 31: Velocity-time response of an RCC projectile in a perforating impact simulation of a 16-layer S-728 target struck at 170 m/s.

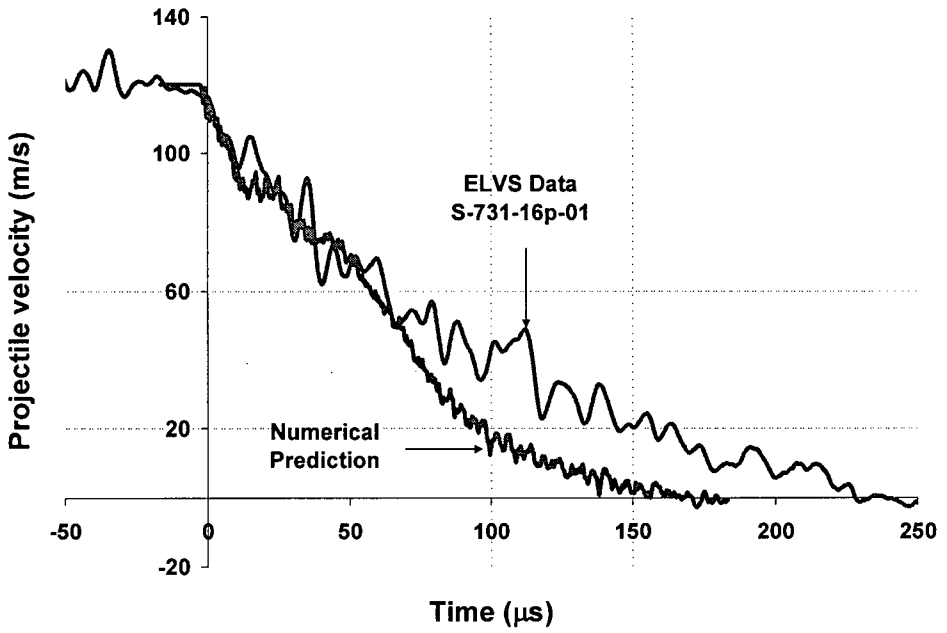

Figure 5 - 32: Velocity-time response of an RCC projectile in a perforating impact simulation of a 16-layer S-731 target struck at 120 m/s.

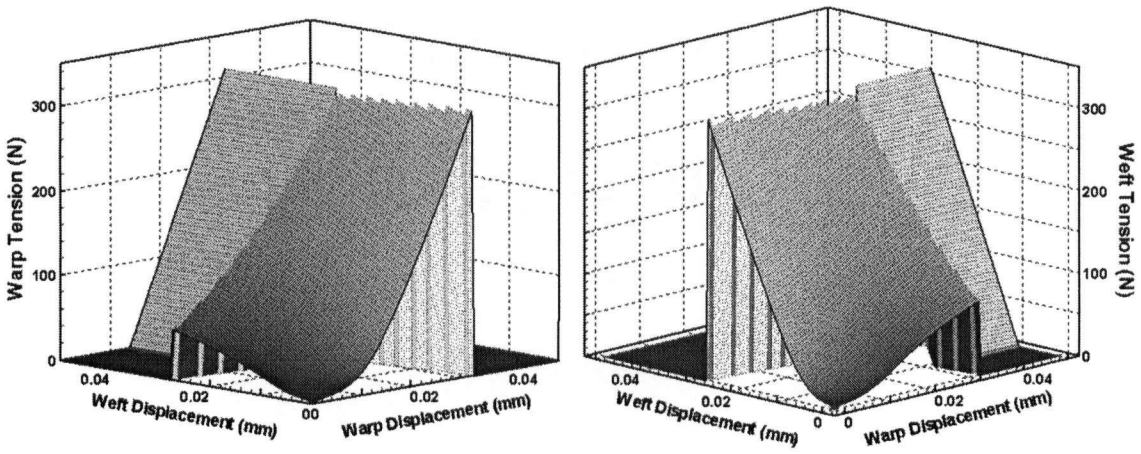

Figure 5 - 33: Warp and weft tension surfaces as a function of the in-plane extensional displacements, developed for S-720 fabric.

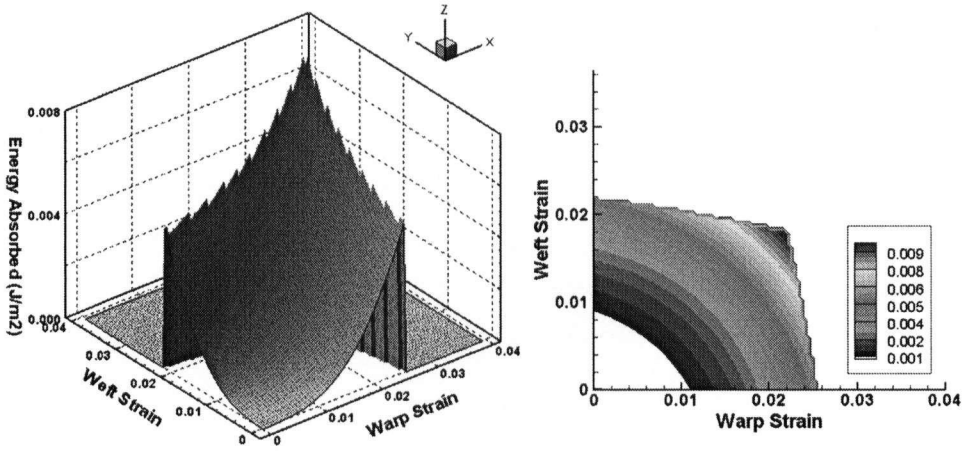

Figure 5 - 34: Energy absorbed per unit area (J/m^2) by S-720 fabric under symmetrically applied extension, expressed in terms of strain in the warp and weft directions; 3D surface (left) and 2D contour plot (right).

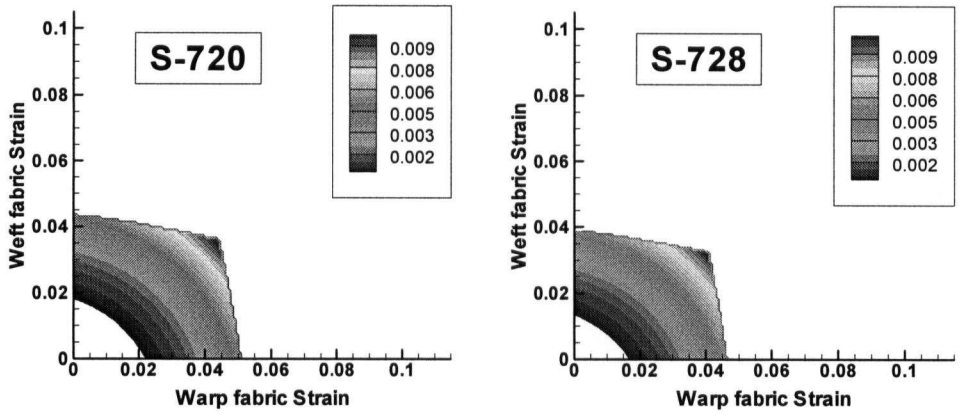

Figure 5 - 35: Contours of strain energy stored in a unit area of S-720 and S-728 fabrics as a function of the warp and weft strains.

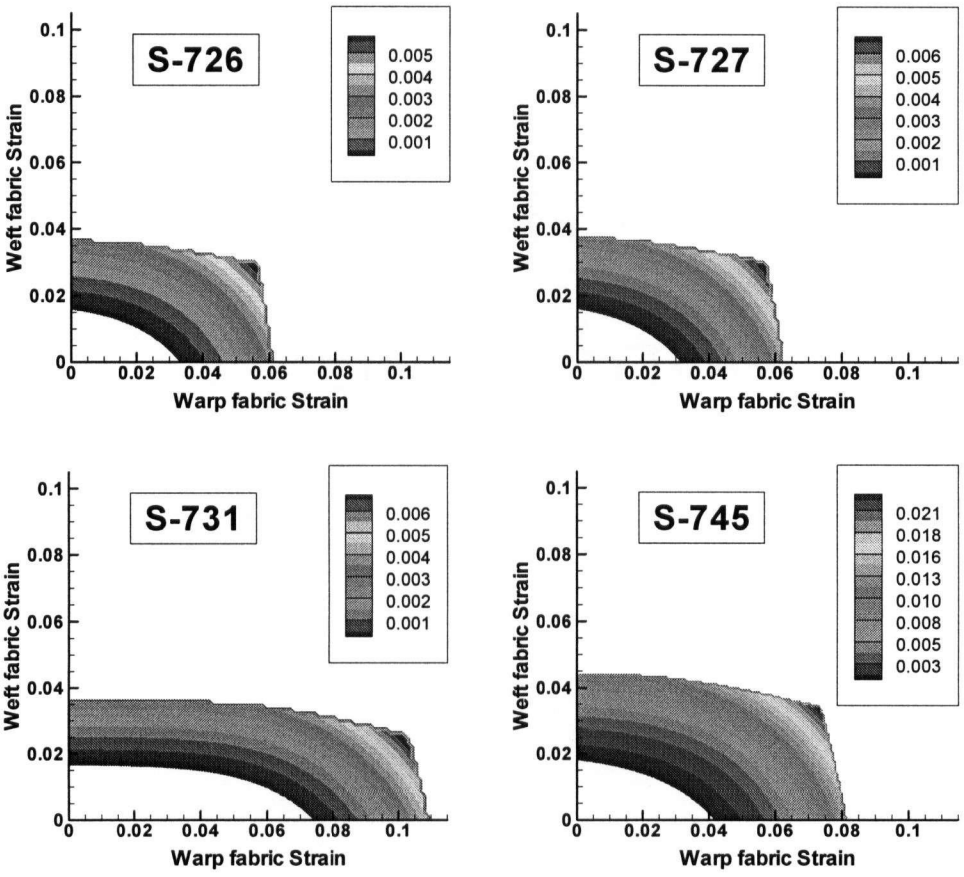

Figure 5 - 36: Energy-strain contour plots of a unit area of S-726, S-727, S-731 and S-745 fabrics.

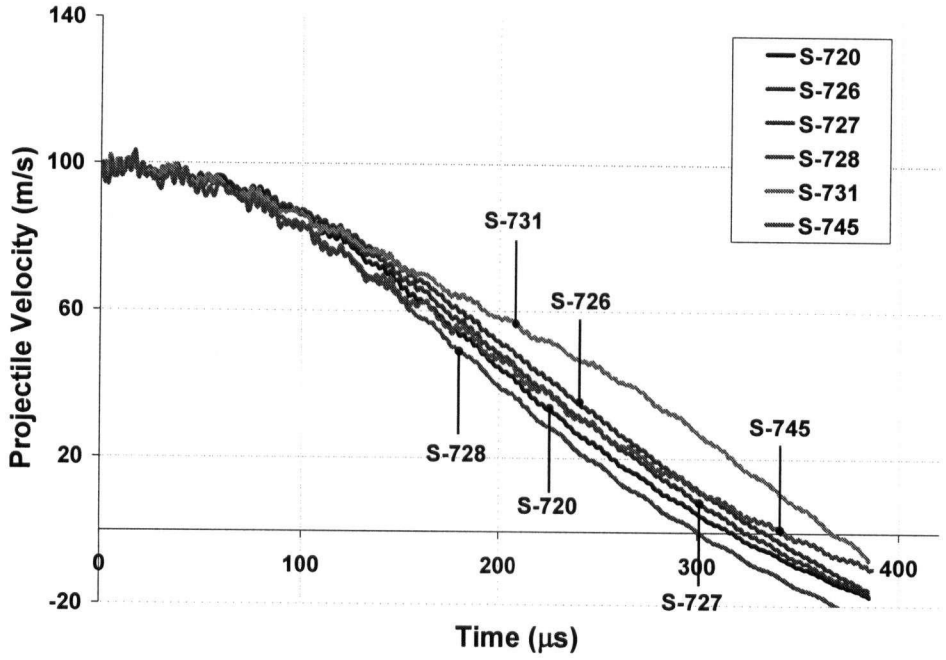

Figure 5 - 37: Velocity-time prediction of the shell-based fabric model showing the response of all six Kevlar® 129 panels impacted by an RCC at 100 m/s.

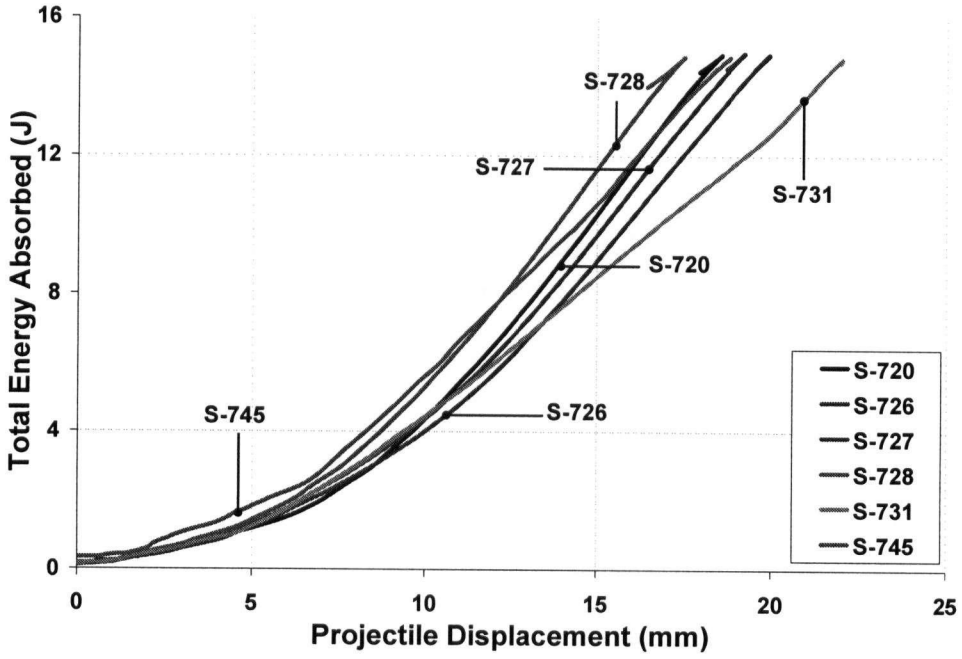

Figure 5 - 38: Target's energy absorption plotted against projectile displacement obtained from numerical simulation of the RCC projectile impacting the six Kevlar® 129 panels at 100 m/s.

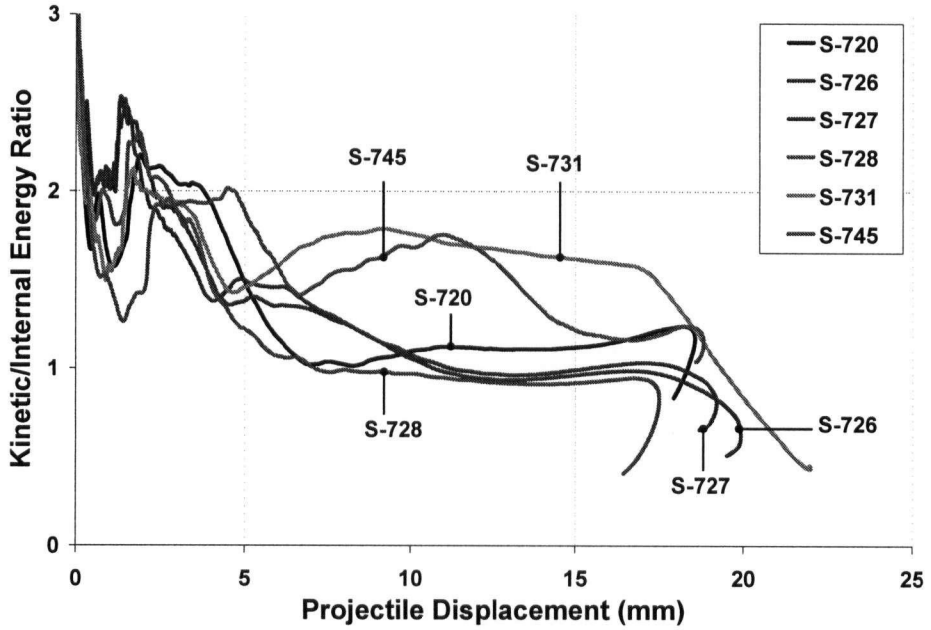

Figure 5 - 39: Kinetic to internal energy ratio of the target's absorbed energy plotted against projectile displacement obtained from numerical simulation of the RCC projectile impacting the six Kevlar® 129 panels at 100 m/s.

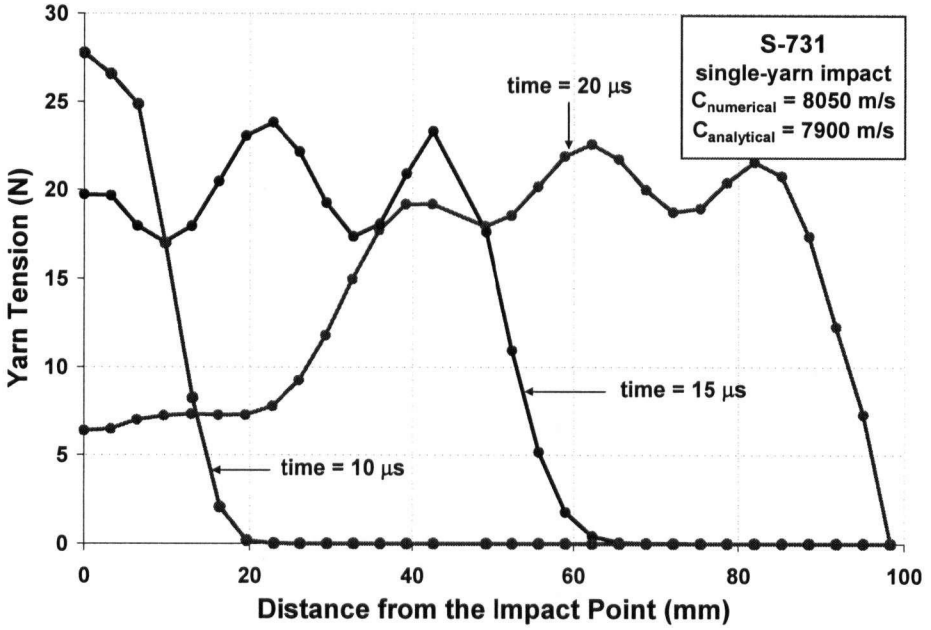

Figure 5 - 40: Propagation of the strain wave evident from the evolution of the yarn tension along the yarn at different time instances in an impact simulation of RCC projectile on a single yarn of S-731 fabric modelled by the shell elements.

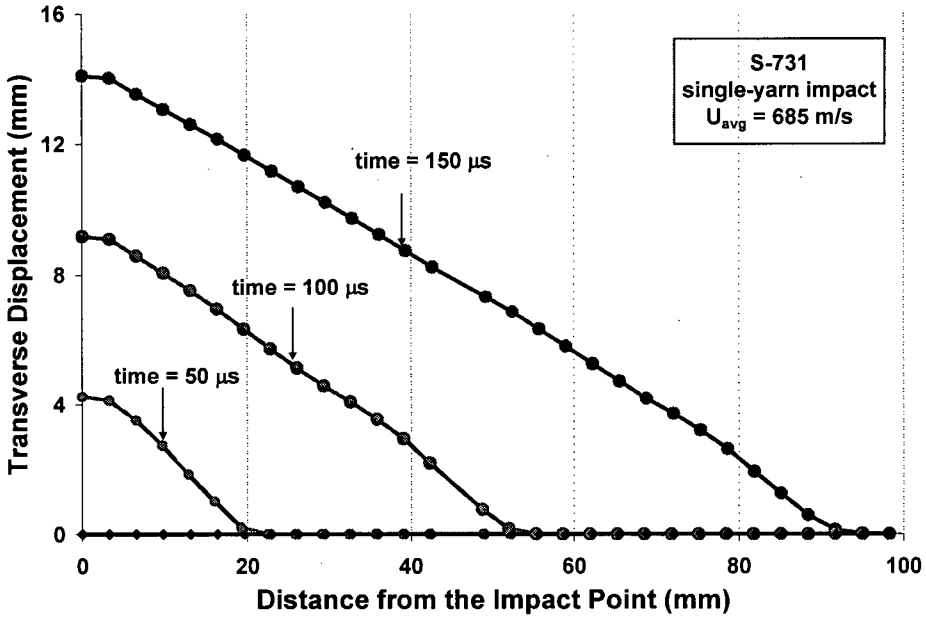

Figure 5 - 41: Transverse deformation of an S-731 single yarn impacted by an RCC, showing the growth of the deformation cone.

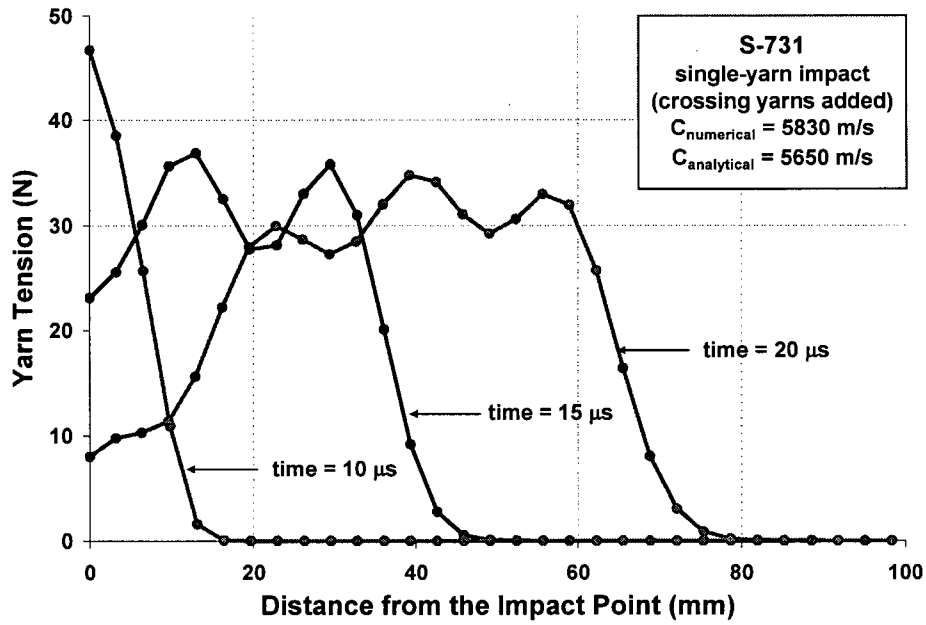

Figure 5 - 42: Propagation of the strain wave evident from the evolution of the yarn tension along the yarn at different time instances in an impact simulation of RCC projectile on an S-731 single yarn (with the addition of the mass of the crossing yarns) modelled by the shell elements.

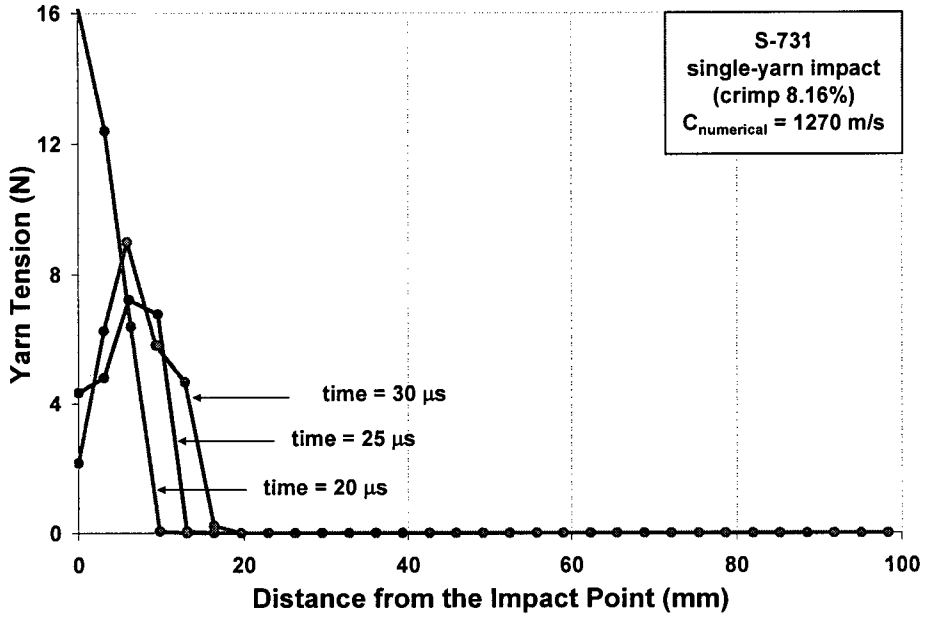

Figure 5 - 43: Propagation of the strain wave evident from the evolution of the yarn tension along the yarn at different time instances in an impact simulation of RCC projectile on a crimped (crimp = 8.16%) S-731 single yarn (with the addition of the mass of the crossing yarns) modelled by the shell elements.

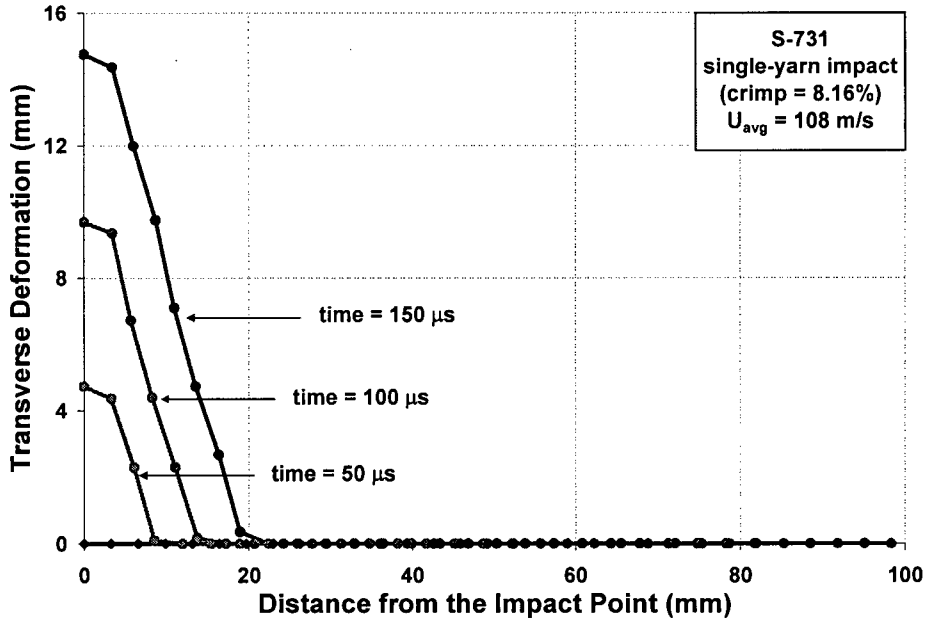

Figure 5 - 44: Transverse deformation of a crimped (crimp = 8.16%) S-731 single yarn impacted by an RCC, showing the growth of the deformation cone.

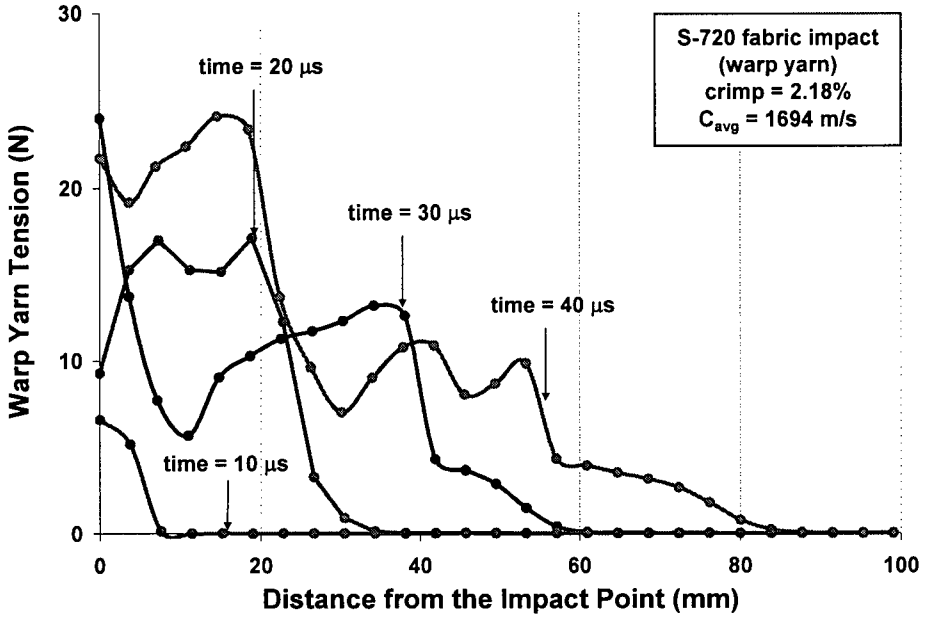

Figure 5 - 45: Propagation of the strain wave evident from the evolution of the tension along the warp yarn in the impact simulation of an RCC projectile on a 1-ply S-720 fabric modelled by the shell elements.

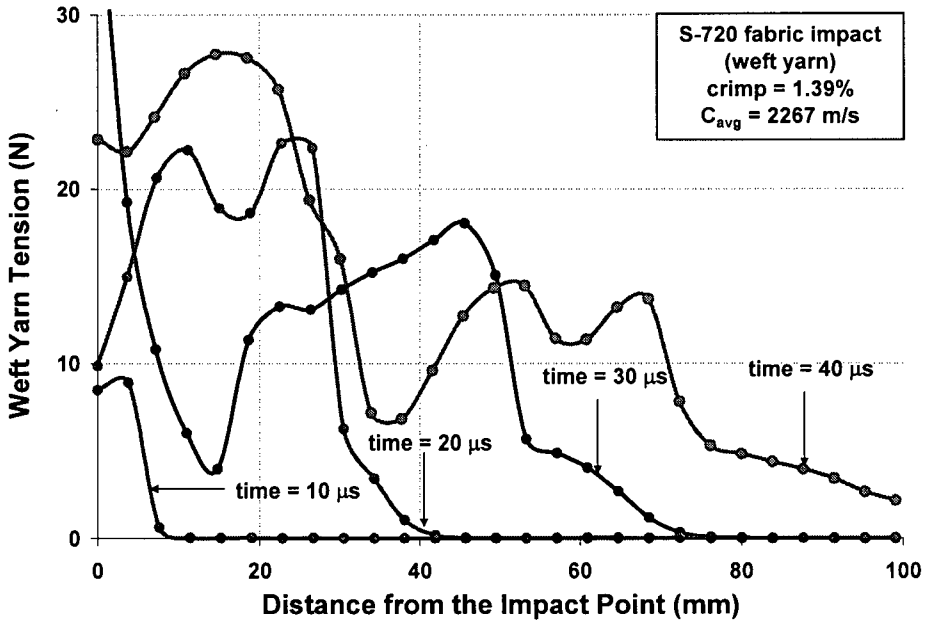

Figure 5 - 46: Propagation of the strain wave evident from the evolution of the tension along the weft yarn in the impact simulation of an RCC projectile on a 1-ply S-720 fabric modelled by the shell elements.

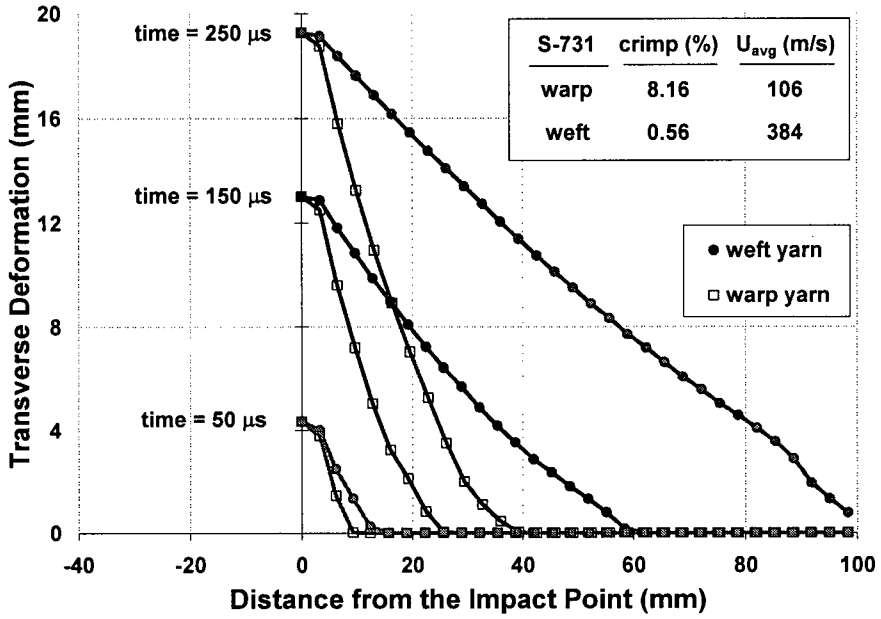

Figure 5 - 47: Transverse deformation of a 1-ply S-731 panel plotted for a warp and weft yarn in the impact simulation of an RCC at strike velocity of 100 m/s.

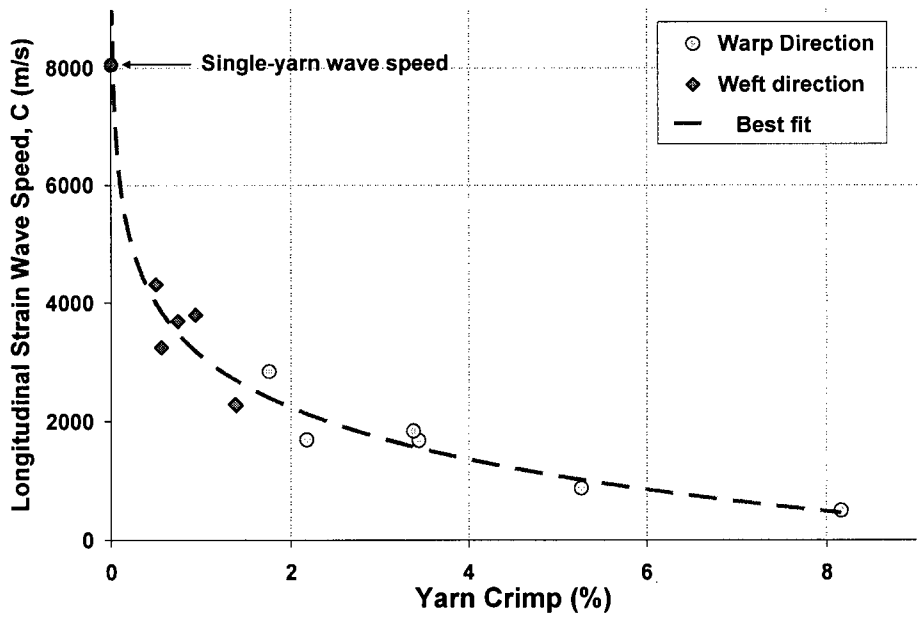

Figure 5 - 48: Longitudinal wave speed measured from the numerical model of the fabric plotted against the yarn crimp.

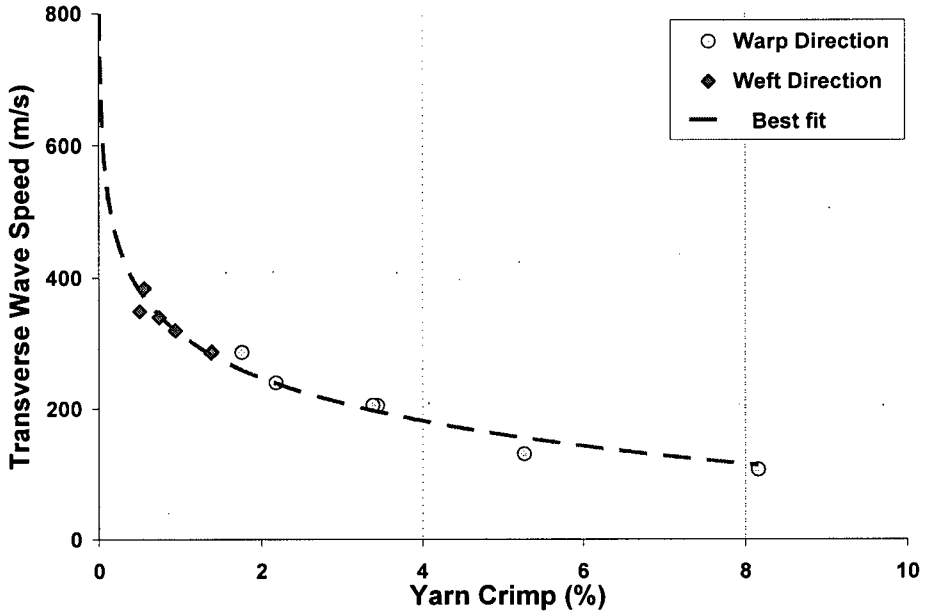

Figure 5 - 49: Transverse wave speed measured from the numerical model of the fabric plotted against the yarn crimp.

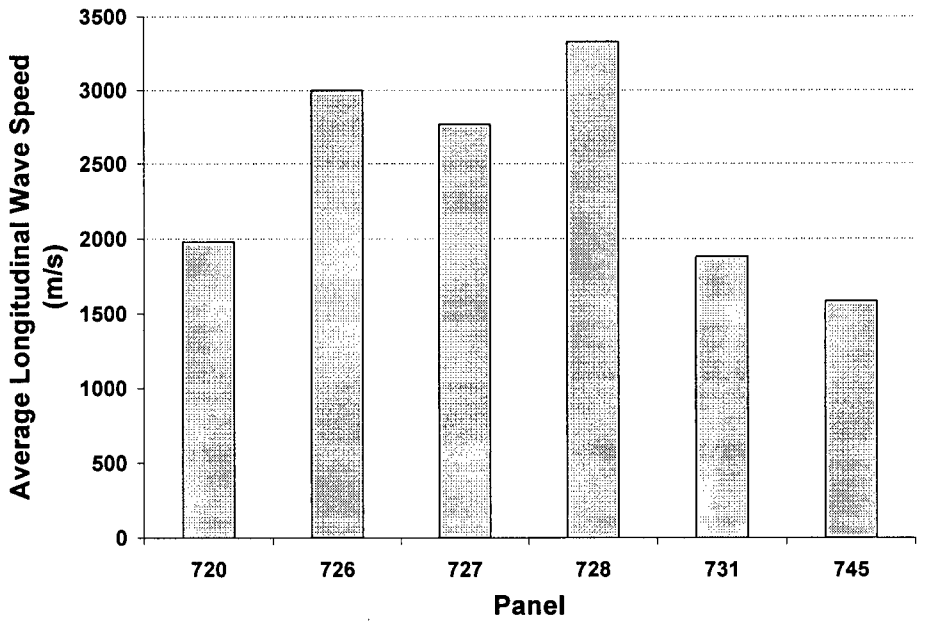

Figure 5 - 50: Average longitudinal wave speed measured from the numerical model of the fabric for the 100 m/s iso-velocity impact simulations.

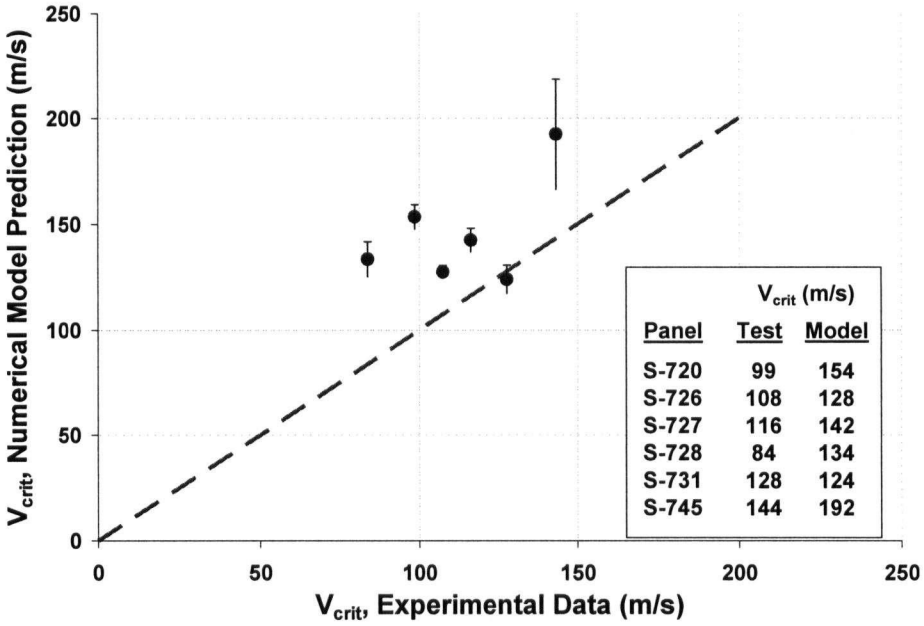

Figure 5 - 51: Critical velocity of the 1-ply Kevlar® 129 panels obtained from experimental data and estimated by the shell-based numerical model.

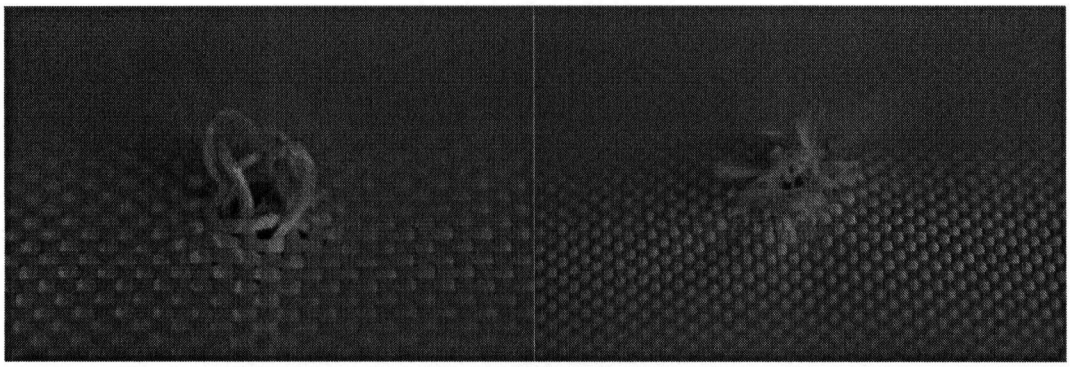

Figure 5 - 52: Post-mortem examination of the Kevlar® panels; perforation by yarn pullout (left) and by yarn rupture (right).

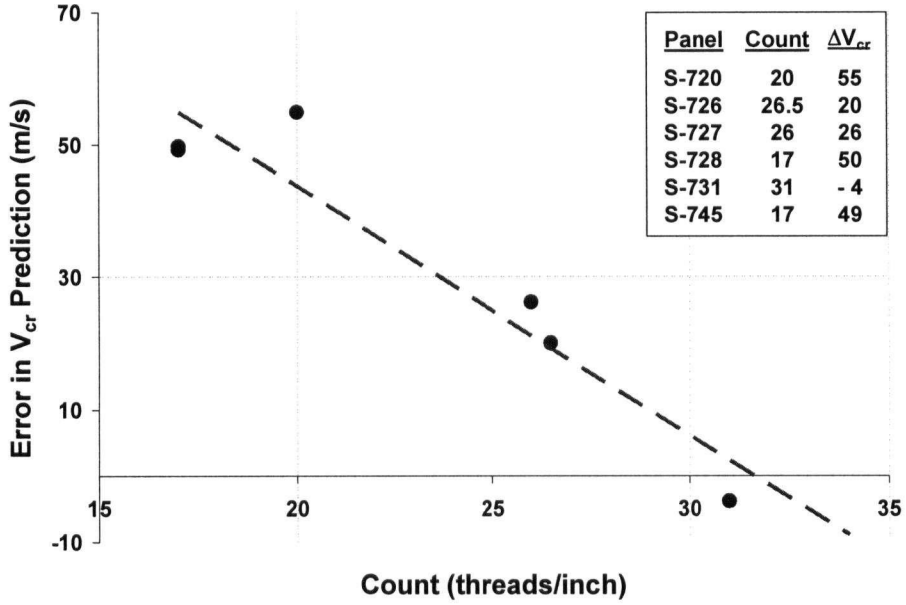

Figure 5 - 53: Error in the prediction of critical velocity of the 1-ply Kevlar® 129 panels compared to experimental data, plotted against their average count number.

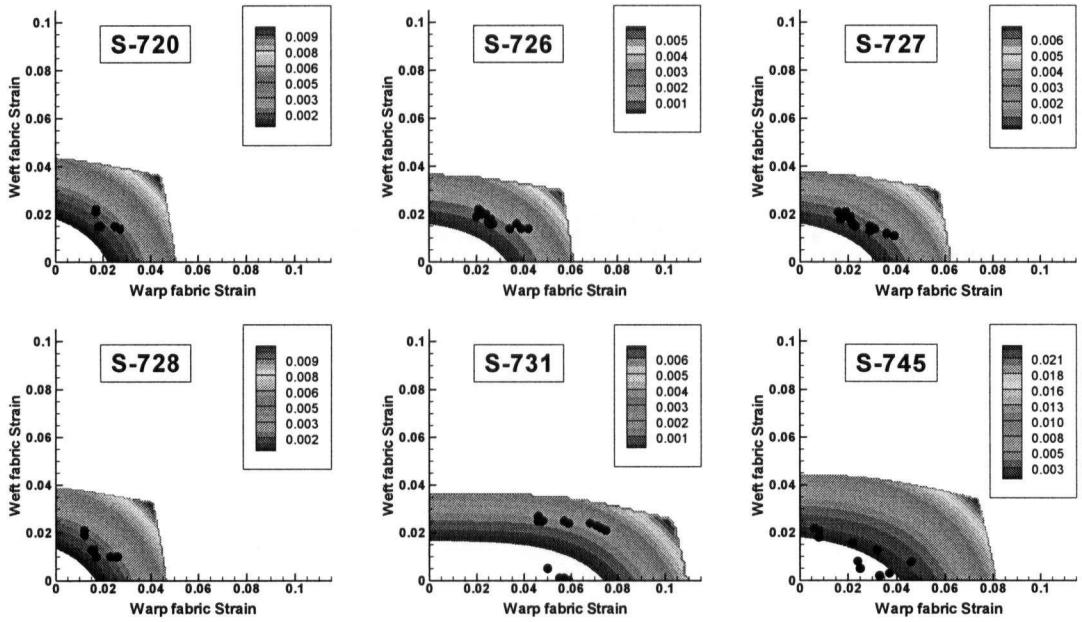

Figure 5 - 54: Energy-strain contour plots of a unit area of the six Kevlar® 129 fabric panels as a function of fabric strain, also showing the strain pairs corresponding to the most critical elements around the projectile (shells with highest energy) during an RCC impact simulation at 100 m/s.

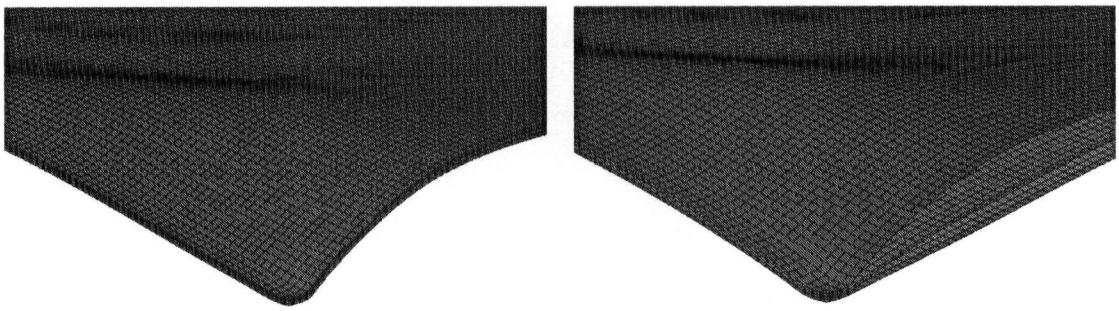

Parallel System **Alternating System**

Figure 5 - 55: Transverse deformation of the an S-726 4-layer target impacted at 100 m/s showing the increased interaction of adjacent layers in the alternating packing method.

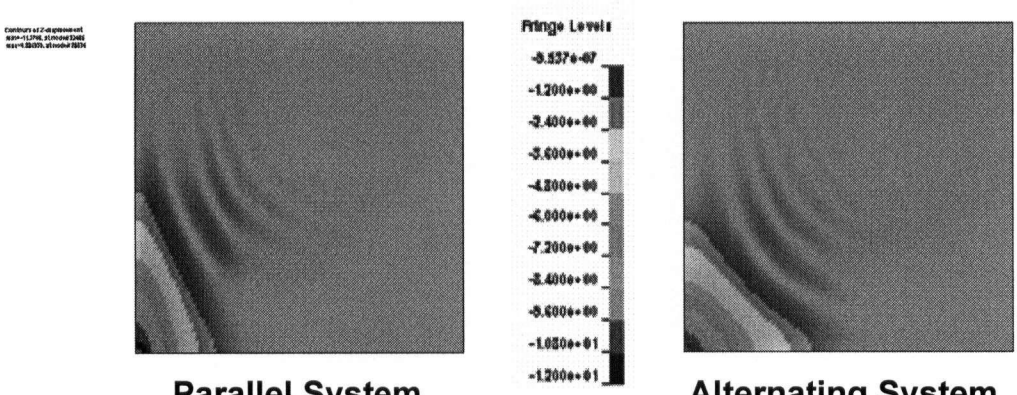

Parallel System **Alternating System**

Figure 5 - 56: Contours of transverse deformation of the third layer away from the strike face of an S-726 4-layer target impacted at 100 m/s showing the benefit of alternating packing method.

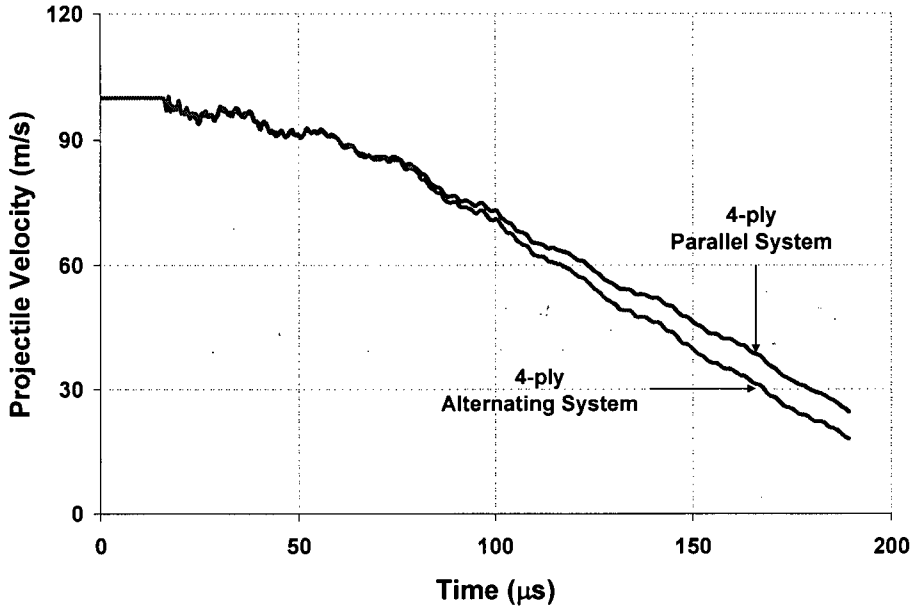

Figure 5 - 57: Comparison of the projectile response for different panel orientation in S-726 4-layer target.

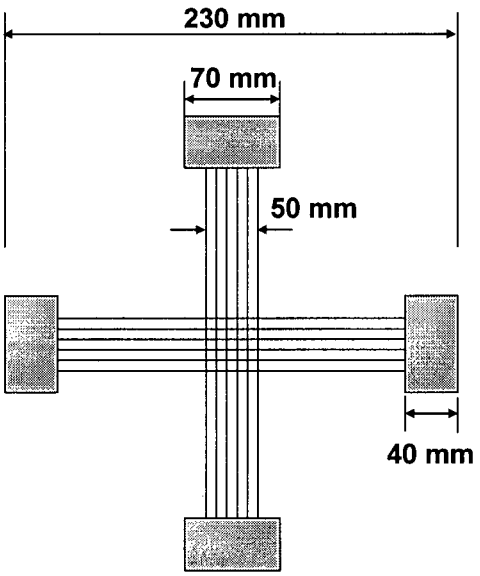

Figure 5 - 58: Cross-shaped fabric specimen used in the biaxial experiments conducted by Buet-Gautier and Boisse [37].

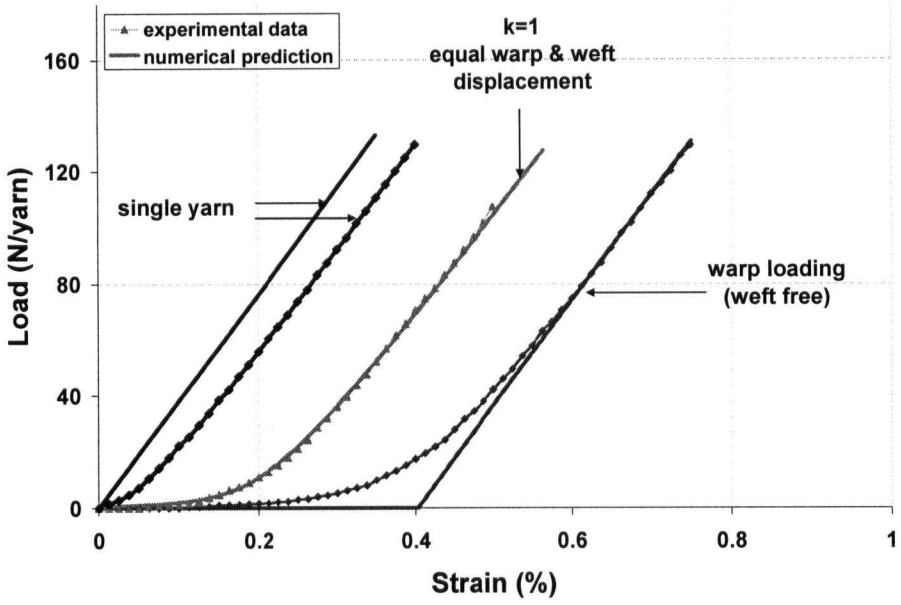

Figure 5 - 59: Predictions of the numerical model on the biaxial loading of the balanced plain weave glass fabric, after calibrating the input parameters to match the iso-displacement loading case ($k = 1$).

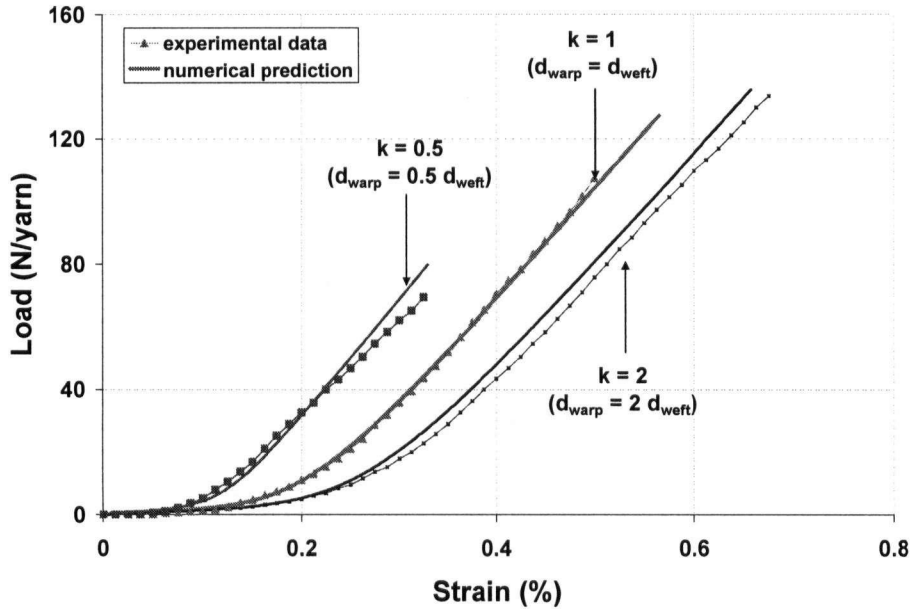

Figure 5 - 60: Predictions of the numerical model on the biaxial loading of the balanced plain weave glass fabric, extended to other two loading scenarios ($k = 0.5 \& 2$).

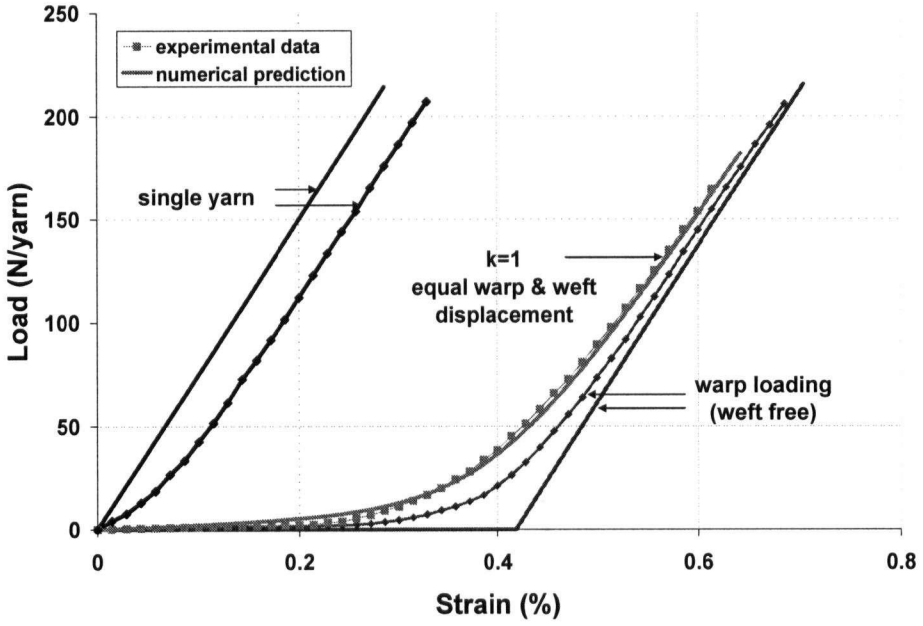

Figure 5 - 61: Predictions of the numerical model on the warp extension of the non-balance plain weave glass fabric, after calibrating the input parameters to match the iso-displacement loading case ($k = 1$).

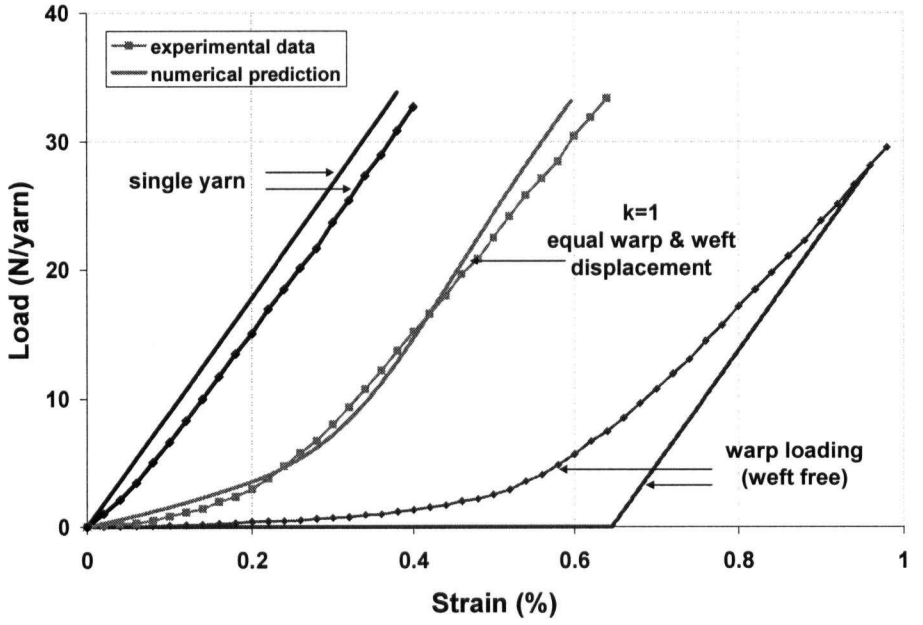

Figure 5 - 62: Predictions of the numerical model on the weft extension of the non-balance plain weave glass fabric, after calibrating the input parameters to match the iso-displacement loading case ($k = 1$).

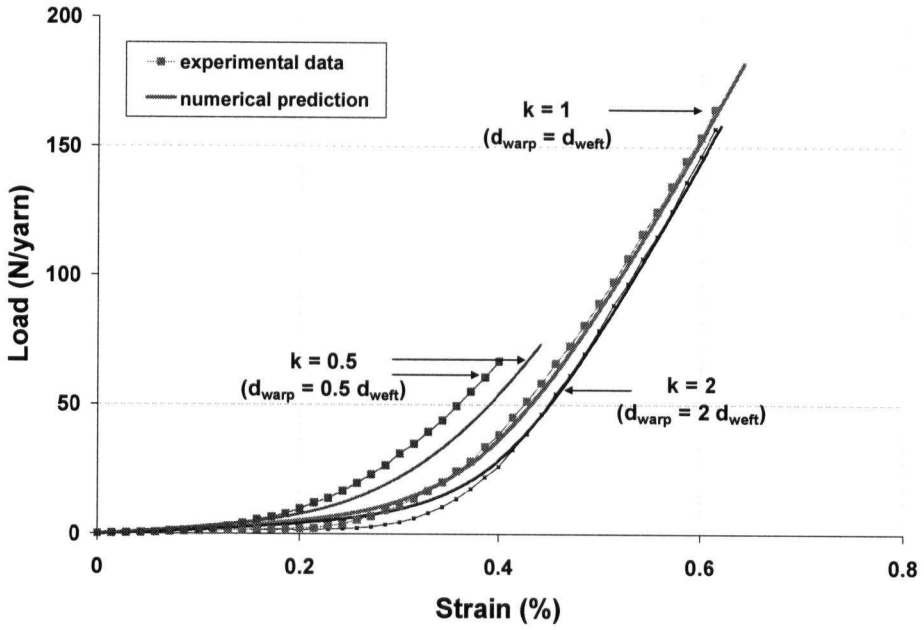

Figure 5 - 63: Predictions of the numerical model on the warp extension of the non-balance plain weave glass fabric, extended to other two loading scenarios ($k = 0.5 \& 2$).

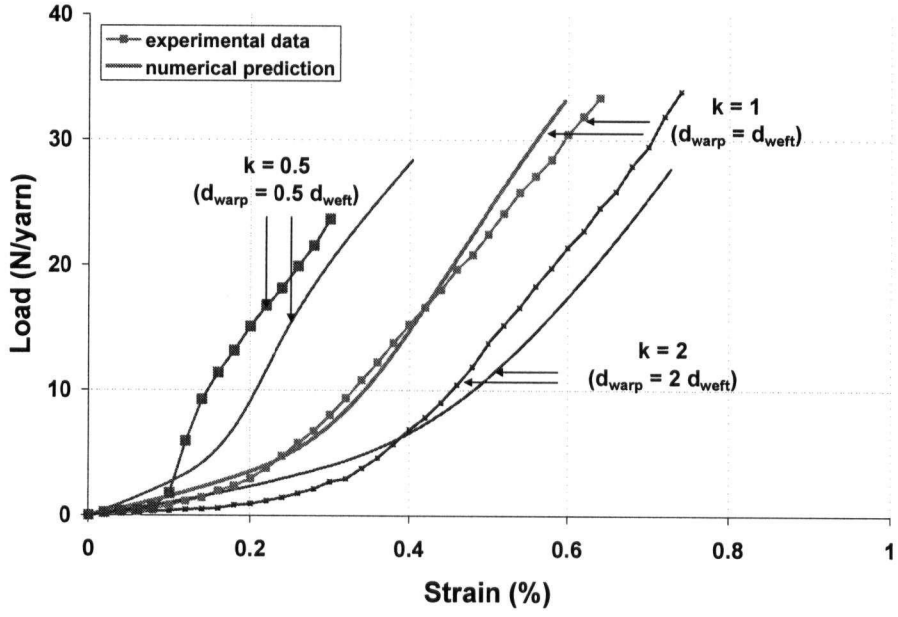

Figure 5 - 64: Predictions of the numerical model on the weft extension of the non-balance plain weave glass fabric, extended to other two loading scenarios ($k = 0.5 \& 2$).

CHAPTER 6 - SENSITIVITY ANALYSIS AND NUMERICAL CASE-STUDIES

6.1 INTRODUCTION

Determination of the material and geometric properties of the fabric panel is not a trivial task. Almost all mechanical and geometrical properties of a fabric have some level of uncertainty associated with them. Since the analysis procedure established in this thesis is based on a deterministic approach, one needs to incorporate this lack of knowledge on the accuracy of the input values in the interpretation of the model predictions. The basic step in assisting the user to better assess the level of confidence in the numerical results is to understand the sensitivity of the fabric response to various input parameters. A parametric study is thus performed to better understand the dependency of the fabric response on input parameters.

This chapter aims to provide some understanding into the physics of the ballistic response of the woven fabrics through examination of the influence of various parameters on a fabric's dynamic behaviour. Furthermore, the

numerical model is used later in the chapter to qualitatively explore the roots of pencilling phenomenon, a by-product of the weight reduction in the personal armours due to the use of new yarns and fibres with superior material properties.

6.2 FABRIC ENERGY ABSORPTION MECHANISM

The overall energy transferred into a fabric target during an impact event is stored in the forms of internal (strain) and kinetic energies. Detailed examination of the history of the absorbed energy by the targets reveals two distinct characteristic behaviours. As illustrated in Figure 6 - 1, the velocity time-history response of the projectile impacting a single-ply S-728 target at 100 m/s can be divided into two distinct zones of behaviour. In Zone I, the projectile velocity shows a gradual decrease with time with a shallow slope, while the deceleration in Zone II seems to be more rapid. Further examination of the fabric response shows that throughout Zone I, the fabric deformation eliminates the inherent "slack" in the system as a result of the yarn crimp and initiates the interaction of the warp and weft yarns. This can be seen in snapshots of the fabric's in-plane motion (see contours of in-plane velocities in Figure 6 - 2) and similarly warp and weft tensile force (depicted in Figure 6 - 3) at the instance when the longitudinal strain wave reaches the warp and weft boundaries. Due to the difference between the values of warp and weft crimp, this wave would travel at different speeds in the two main fabric directions.

Dependency of the longitudinal and transverse wave speeds on the yarn crimp was previously discussed in Chapter 6 (see Figure 6 - 48 and Figure 6 - 49).

Considering the kinetic and internal energy distribution in the fabric, the overlap of the two zones of behaviour can be better illustrated, shown in Figure 6 - 4 as the ratio of the kinetic to internal energy components. It appears that the fabric absorbs energy primarily in the form of kinetic energy in the initial stages of impact. Overlaying the zones identified on the velocity-time response plot over the energy ratio-time curve further reinforces the hypothesis that the kinetic energy is the dominant component of energy in the fabric during the initial stages of impact as the crimped yarns are stretching taut and the projectile's velocity loss is mainly due to the momentum exchange with the fabric. The stiffness of the stretched fabric yarns would come into play in the later stages of impact when the warp and weft yarns are fully taut and engaged in the energy absorption.

A similar trend can also be seen in the development of tension in the warp and weft yarns. As shown in Figure 6 - 5, the tension (plotted for the weft yarn of S-728 in this case) suddenly builds up in the yarns upon impact due to momentum exchange between the projectile and the fabric. The yarn tension then more or less remains constant (or increasing with at a low rate) within zone I as the yarn is being stretched and the crimp being taken out, after which the tension starts increasing monotonically in zone II. Similar observations are reported in other studies [1] and the nature of behaviour is attributed with the strain wave generation, propagation and reflection. The plot shown in Figure 6 - 5 only covers the initial 100 μs of the impact to focus on the initial response of the yarns; the tensile force will later reach a peak value and start decreasing, given that it remains below the failure limit. Depending on the projectile's striking velocity, failure of the yarns in a penetrating impact can occur at the

initial peak (for high impact velocities) before any significant strain wave propagation in the target occurs (zone I), or later in zone II (moderate strike velocities) within the increasing segment of the yarn tensile response. As a result, the failure of yarns and eventually the perforation of the fabric in each of these two scenarios are affected by different sets of fabric properties. Thus, the influencing parameters need to be identified, as discussed in the following sections.

6.3 PARAMETRIC STUDY

As mentioned earlier, all the measured and calculated geometric and mechanical properties of the fabric fed into the shell-based fabric model have various levels of uncertainties associated with them. The analysis methodology established here is based on a deterministic approach; however, in order to increase the user's confidence in the predictions of the numerical model, the effects of these inherent uncertainties on the outcome of the analysis need to be investigated. In addition, considering the two zones of behaviour discussed above, one can optimize the performance of a fabric system knowing the influence of various mechanical and geometric parameters on the overall energy absorption of the system. This section highlights the influence of some of these parameters on the performance prediction of the fabric systems, and reviews the variability level of each parameter in an effort to identify their overall importance.

6.3.1 Effect of Yarn Stiffness

As mentioned previously, the input material properties employed to perform impact simulations on single and multi-ply fabric targets are based on the properties of the virgin yarns. It is well known that the process of weaving the yarns into fabric deteriorates these properties due to the wear and abrasion caused by the contact between the yarns and different components of the manufacturing machinery. One of the main properties affected by this process is the yarn stiffness. Both the elastic modulus and cross-sectional area of the yarns wound be affected where fibres of the yarn are damaged during weaving [68, 69]. The yarn stiffness reduction can be directly measured in the laboratory by comparing the tension-displacement response of the virgin yarns with that of yarns extracted from the woven fabric. However, such data were not available for the study performed here and therefore properties of virgin yarns were used throughout the analyses.

This section investigates the influence of the yarn stiffness on the overall response of the fabric. This sensitivity analysis is performed by varying the elastic modulus of the yarns only, as a representative of the yarn stiffness. In the case of Kevlar® 129, the fibres are reported to have an elastic modulus of 96.0 GPa in the virgin state. The effect of a nominal ±20% change in the elastic modulus of the yarns on the biaxial warp tension-displacement response (fixed weft) of an S-728 fabric unit-cell is shown in Figure 6 - 6. As expected, a higher elastic modulus results in a stiffer force-displacement response as seen in this figure. The same trend is also reflected on the ballistic response of the fabric, as depicted in Figure 6 - 7, showing the projectile velocity-time response predicted

for impact of an RCC projectile on a 1-ply S-728 fabric at 100 m/s. It can be seen that a rather significant reduction of 20% in the yarn stiffness would only slightly affect the deceleration of the projectile. Investigating the evolution of strain in the yarns passing through the impact point, one can predict the penetration characteristics of a fabric target. As seen in the plot of the yarn strain-time response of Figure 6 - 8, the deformation of the yarns is affected by the modulus reduction throughout the impact, with the lower modulus resulting in a higher strain level. This would imply that stiffness degradation of the yarns causes the fabric to fail sooner for almost all the strike velocities, causing failure both in zone I and zone II. As a result, it can be concluded that the stiffness reduction would affect both the energy absorption characteristics and critical velocity of a fabric.

6.3.2 Effect of Yarn Crimp

Undulation of the yarns in a woven fabric is perhaps one of the most critical parameters affecting its highly non-linear biaxial behaviour. The presence of yarn crimp is mainly responsible for the deviation of the fabric response from that of a flat net-like structure and is the fundamental reason behind the inherent "slack" in an un-stretched fabric. Realistic representation of the yarn undulation in a woven fabric is thus the essential part of any crimp measurement methodology.

Determination of yarn crimp in the warp and weft directions is not a trivial task. Several factors such as over-handling of the fabric, choice of the measurement technique, and human factors can highly affect the measured crimp values of identical fabrics. Figure 6 - 9 shows an example of slight

human-affected measurement disparities resulting from two crimp measurements performed by the author and those reported by Kongshavn [42] for the same set of Kevlar® 129 fabrics. Despite the good agreements between the results, a difference of up to 20% exists between the two measured crimp values.

In order to probe the sensitivity of the unit-cell mechanical behaviour and the fabric's impact response to the variability in the yarn crimp values, changes of ±20% are considered in the warp and weft crimp values of the S-728 fabric. As seen in Figure 6 - 10, an increase in the yarn crimp would result in a softer in-plane extensional response. Similar conclusions can be drawn from the non-perforating ballistic response of the S-728 subjected to impact of an RCC projectile at a strike velocity of 100 m/s (Figure 6 - 11). Studying the strain time-history of the central weft yarn going through the impact point (Figure 6 - 12) reveals that although increasing the crimp reduces the energy absorption capacity of the fabric at a given time or projectile displacement, it results in a lower strain level in the yarns throughout the impact event. This suggests that the critical velocity of a fabric would increase with the introduction of more crimp into it. However, this improvement would come at a cost of increasing the back-face deformation of the fabric target. In a way, addition of crimp to the fabric is equivalent to adding more "ductility" to the system, leading to more overall energy absorption with an increase in the fabric's transverse deformation. It should be noted that this analysis is based on a pin-jointed crossover approach and other deformation mechanisms such as yarn slippage, which is specifically amplified by higher yarn crimp values, are not considered.

6.3.3 Effect of Fabric Areal Density

One of the fundamental components of the dynamic response of any structure is its inertial (mass) properties. In the case of fabrics, the mass properties of the targets are usually represented by their areal density, defined as the mass of the system per unit area. In most cases, the laboratory measurements and the theoretically calculated areal densities of Kevlar® 129 panels are in good agreement (Figure 6 – 1 for the case of six Kevlar® 129 panels studied here), showing small and often negligible disparities (a maximum of 4% in the case of S-720). This small margin of error can be translated into a high level of confidence in the theoretical values used in the numerical model.

In order to further investigate the influence of a fabric's areal density on its overall energy absorption characteristics, an approach similar to those employed for elastic modulus and yarn crimp sensitivity is employed. Ballistic response of a 1-ply S-728 fabric target under the impact of an RCC projectile flying at 100 m/s was studied while perturbing its areal density by ±20%. Figure 6 - 13 shows the sensitivity of the projectile deceleration on the changes of areal density. As expected, the heavier fabric is capable of absorbing more energy at a given time. The strain time-history of the central yarn in the weft direction shown in Figure 6 - 14 indicates that despite differences in the response for various values of areal density, no immediate improvement can be seen in the yarn strain evolution and the variability in the areal density is not expected to dramatically change the critical velocity of the fabric target.

Considering the above sensitivity analysis, areal density is perhaps one of the least concerning input parameters, and a reasonable level of confidence is

associated with its measured and calculated values. The possible sources of error in areal density stems from the inaccuracies in panel size and weight measurements, crimp measurement (in the case of calculated areal density), and the uncertainty in the yarn linear density reported by the manufacturer.

6.3.4 Discussion

Elastic modulus and crimp of the yarns and areal density of the fabric are three basic input parameters that determine the mechanical behaviour of fabrics under static and dynamic loadings. The analysis above shows that the influence of these three parameters on the energy absorption of the fabric (evident from the velocity time-history of the projectile) is more or less similar. However, there are different levels of accuracy associated with each of these parameters.

Elastic modulus of the fabric yarns is the parameter that gets affected by several factors in the manufacturing process, from constructing individual yarns out of fibres to weaving yarns into fabrics. Every step of the manufacturing process deteriorates the properties of the yarns to a certain degree, the amount of which should be determined from the examination of the yarns extracted from the final product. Crimp, on the other hand, is created during the weaving process and even in the final product can be affected by factors such as handling of the fabric. It is suggested that these two parameters be measured for every fabric individually to acquire a high level confidence in their values. Further investigation of the effects of other disturbing factors, such as stitching during the production of personal armours, on their overall performance is also highly advantageous to the accuracy of the numerical predictions. Areal density, on the other hand, seems to be more easily

determinable and improving accuracies on geometry and crimp values of yarns can lead to a better agreement between measured and calculated areal densities.

Two zones of behaviour were identified in this section, during which the response of the fabric is dominated by various parameters. Examining the sensitivity of projectile velocity deceleration to any of the above-studied parameters (elastic modulus, yarn crimp and areal density), little difference can be noticed within zone II (after 60 μs in the case of S-728). To better understand the differences in zone I, the projectile velocity-time response in initial 100 μs of the impact event is plotted for varying elastic modulus, yarn crimp and areal density in Figure 6 - 15, Figure 6 - 16 and Figure 6 - 17, respectively. It appears that the only parameter that most affects the energy absorption of the fabric in zone I is the areal density, where the projectile decelerates more rapidly as the fabric's mass increases.

The critical velocity of a fabric is inversely affected by the level of tension in the yarns. From the sensitivity analysis performed here, one can conclude that for an equal value of strain-to-failure, the fabric with higher elastic modulus would have higher critical velocity (see lower tension for higher modulus in Figure 6 - 8). A similar conclusion can be drawn for fabrics with higher crimp (see Figure 6 - 12). The same can not be said for changes in the areal density, as no clear advantage can be gained in yarn tension history before its peak (Figure 6 - 14) with the change in areal density.

As mentioned previously, the failure of the yarns in zone I occurs at strike velocities significantly higher than the critical velocity of a 1-ply fabric. In

reality, personal armours are made of many layers of fabric to withstand the impact of threats they are exposed to. The critical velocity for a multi-ply fabric pack is significantly higher than that of a single-ply target. As a result, the range of projectile strike velocities that a multi-ply pack is able to defeat can cause a single-ply target to instantaneously fail upon impact (zone I). Since the response of the fabric in zone I seems to be more efficiently improved by the areal density (Figure 6 - 17), it is more economically advantageous to place fabric materials with inferior mechanical properties but equal areal density on the strike face of a multi-ply fabric armour, as suggested by Cunniff [71]. This is a basic example of the advantages provided by the numerical model in the design and manufacturing of body armours.

6.4 Sensitivity to Other Parameters

6.4.1 Transverse Compression of Yarns

Perhaps the most unpredictable aspect of yarn mechanical behaviour inside a woven fabric is determining its transverse mechanical response. Individual Kevlar® 129 yarns (or any other yarn with untwisted fibre structure for that matter) are loosely made from juxtaposition of parallel fibres without any cohesion and are not capable of sustaining any transverse loading. Inside the fabric weave, however, the constraint provided by the weave structure changes the transverse behaviour of the yarns. As a result, the transverse mechanical properties of the yarns are highly dependent on many factors, such as weave tightness, voids between the fibres in the yarns, and transverse properties of the fibres themselves. Unfortunately, there is still no robust testing method

available to measure the transverse compressive behaviour of the yarns directly inside the fabric. The method employed in this thesis to predict this transverse yarn behaviour from the 3D crossover model is highly dependent on the success of the finite element model and susceptible to the possible inaccuracies in the numerical model. Knowing the influence of this aspect of modeling on the overall response of a fabric can help the user determine how much this uncertainty would affect the final conclusions of his/her analysis. This section aims to address this issue by exploring the effects of transverse yarn properties on the in-plane extensional and ballistic response of fabric panels.

The biaxial response of a fabric crossover with compressible yarns would fall between two extreme cases: crossover model with non-compressible yarns and one with decoupled warp and weft yarns. The true fabric response with the inclusion of yarn compressibility (compressible model) is thus compared to these two cases on unit-cell and fabric levels to investigate the sensitivity of the response to the transverse compression properties of the yarns. For this purpose, S-728 and S-731 fabrics are considered and the in-plane extensional responses of their unit-cells are investigated. S-728 represents a highly balanced low-crimp fabric while S-731 is an example of an unbalanced high-crimp one amongst the six Kevlar® 129 fabrics studied in this thesis.

Figure 6 - 18 and Figure 6 - 19 show the warp and weft tensile response as a function of warp extension in a unit-cell loading case where the weft yarn is held fixed. As can be seen, the decoupled response of the warp yarn in this loading scenario is comprised of an initial no-resistance zone up to the point where the yarns are stretched tight, after which the response is identical to that

of a single straight (taut) yarn. The weft yarn does not experience any tension in the decoupled model due to the absence of warp-weft yarn interaction, when the unit-cell is being loaded in the warp direction only. The incompressible model, on the other hand, exhibits pure crimp exchange and with no change in the transverse distance between the yarn centerlines, and intuitively shows the stiffest response amongst the three modeling approaches. As expected, the response of the unit-cell with compressible yarns falls in between the two other cases. This can be seen in the plot of energy surfaces predicted by the three models in Figure 6 - 20.

A slice from these surfaces (parallel to the warp displacement axis at zero weft displacement) will result in the graph of Figure 6 - 21 where the energy stored in the unit-cell is plotted versus the warp displacement for fixed weft yarn. These figures show that the energy surface corresponding to the model with compressible yarns is consistently in the middle of the two other models. Performing impact simulations on single-ply S-728 panels also indicate similar results. While the panels with compressible and decoupled yarns show the stiffest and most compliant responses, respectively, the one with compressible yarns falls between these two cases (see Figure 6 - 22 and Figure 6 - 23). However, investigating the components of the overall energy absorbed by the target (Figure 6 - 24) reveals that the panel with decoupled warp and weft yarns has a significantly larger kinetic energy component compared to the other two models, mainly due to the freedom of the fabric material to move without considerable resistance, a direct result of the absence of warp-weft yarn interaction.

A similar analysis is performed on the highly imbalanced S-731 fabric. Figure 6 - 25 and Figure 6 - 26 show the tensile response of the warp and weft yarns under extension, respectively, with the perpendicular yarn held fixed in each case. The response of the S-731 unit-cell model with compressible yarns appears to be very close to that of the model with decoupled yarns, especially for the case of low-crimp weft yarn loading. The overall absorbed energy surfaces of the unit-cell with compressible, non-compressible and decoupled warp and weft assumption shown in Figure 6 - 27 also indicate the close proximity of the fabric behaviour with compressible yarns to that of decoupled warp and weft. The energy absorbed by the unit-cell subjected to extension only in the warp direction (Figure 6 - 28) is closer to the decoupled yarns model than the non-compressible yarns, while the same energy plot of the compressible model and decoupled yarns model overlap for weft extension (Figure 6 - 29).

A similar behaviour is observed for a 1-ply panel impacted by an RCC projectile at 100 m/s, where the projectile velocity-time response of the fabric with compressible yarns appear much closer to that of the decoupled warp and weft model than the model with non-compressible yarns (Figure 6 - 30). It appears that the high level of crimp in the fabric, along with significant crimp imbalance between the warp and weft directions leads to the low yarn interaction, causing them to respond more or less in a decoupled fashion. The balance of kinetic to internal energy components in the impact simulation shows a larger kinetic component, similar to that of a fabric with decoupled warp and weft yarns (Figure 6 - 31).

6.4.2 Shear Properties

Shear properties of the fabric are amongst the major factors influencing the overall behaviour of fabrics. The fabric shear model adopted in this study is based on the trellis mechanism (see Chapter 5, Figure 4 - 8). The four characteristic parameters that construct fabric shear response are the stiffening and locking shear strains (γ_1 and γ_2) and initial and locked shear moduli (G_1 and G_2) and are determined using a simplified mechanistic approach that considers the geometry and physical interaction of parallel and crossing yarns (see Section 4.3.2). In the absence of any experimental data on the shear behaviour of the six Kevlar® 129 fabrics investigated here, all input values would merely provide an approximation of the real fabrics' shear response. In this section, results of a sensitivity analysis on the shear model input values are presented for the ballistic impact of RCC projectiles on 1-ply fabric targets.

A compilation of maximum shear strains in each of the six Kevlar® 129 fabric types reached during the impact simulation of an RCC projectile striking the target at 100 m/s is provided in Figure 6 - 32 alongside their respective stiffening and locking shear strains (γ_1 and γ_2). As is evident from this picture, the maximum shear strain in all fabrics (except S-731) is slightly higher than the stiffening shear strain value. In order to further investigate the influence of the shear response of shell elements on the overall response of the target, two extreme cases with low and high shear resistance of the trellis mechanism is considered. The panel chosen for this study was S-728 fabric impacted by an RCC at 100 m/s. For the low shear resistance case, the locked shear modulus is set equal to the lower initial modulus (i.e. $G_1 = G_2 = 8.66$ MPa for S-728),

leading to a very soft linear response of the shells in shear. Conversely in the high resistance scenario, the initial modulus is set equal to that of the locked configuration (i.e. $G_1 = G_2 = 8.66$ MPa for S-728) to obtain high shear resistance in all the shell elements throughout the fabric deformation.

Figure 6 - 33 shows a plot of the projectile's velocity prediction in the impact simulation of a 1-ply S-728 target comparing the trellis fabric model with the low and high resistance models discussed above. As seen, the response of the fabric with trellis model is more or less identical to that of the low shear resistance case, since the maximum shear deformation of the fabric observed in the simulations is significantly smaller than the locking strain. On the other hand, the high modulus case results in a much stiffer response and decelerates the projectile relatively more rapidly.

The deformation profile of the fabrics also changes noticeably with the increase in the shear stiffness. Figure 6 - 34 shows such a difference, where the diamond-shape transverse cone in the fabric with trellis shear model is transformed into an almost circular cone in the high-shear fabric. While the rhomboidal shape of the cone is a signature of the low shear orthotropic fabrics in ballistic impact, a transverse cone with a circular base is the fundamental characteristic of an isotropic membrane structure.

Figure 6 - 35 shows the low dependence of the S-728 fabric's dynamic response on the stiffening and locking strain values. As seen in this figure, reducing these limiting strains to 30% of their original value does not significantly affect the deceleration of the projectile. It can be concluded that in the case of the six Kevlar® 129 fabrics studied here in the ballistic impact with fixed boundary

conditions, the shear mode of deformation is not a dominant energy absorbing mode. This, however, might not be true for other fabrics with lower shear locking angles. In addition, other boundary conditions can also result in higher shear deformation of the fabrics and lead to a higher dependency of a fabric's ballistic performance to its shear properties. The user should pay particular attention to the fact that the shear model in this study is simplified for practical reasons. It is suggested that the mechanical behaviour of fabrics under shearing modes of deformation be studied using a more elaborate approach if the model proposed in this study is being utilized in a different application where significant shearing of fabrics is likely to occur.

6.4.3 Fabric Slippage at the Boundary

Perfect clamping of the fabric in the fixed boundaries is difficult to achieve for single and multi-ply targets. Effect of clamping pressure on the ballistic performance of various fabric targets was investigated [42] and it was observed that although higher pressures can significantly reduce the slipping of the fabric at the fixed boundaries, there is usually a certain level of slippage observed in most panels. Clearly, the slippage of the fabric at the boundaries would directly affect its ballistic performance and any analysis/simulation of such impact event should incorporate this phenomenon.

In order to investigate this boundary slippage, the fixed edges of the target were traced over the fabric before and after the impact. Figure 6 - 36 shows a typical boundary slippage that occurred in a 1-ply S-728 panel at a strike velocity of 36.9 m/s. Post-mortem examination of the tested panels showed a highly variable amount of slipping, both in terms of slip length and its width.

However, it was observed that the width of the slip zone is commonly proportional to the amount of fabric pull-in (slip length).

The boundary force profile of a 1-ply S-728 fabric impacted at 100 m/s is shown in Figure 6 - 37 for the weft yarns. As seen in this figure, the tension builds up at the boundary as the impact progresses. The central yarns seem to carry significantly higher reaction forces, which would later stabilize at a lower tension level as the distance from the central yarn increases. The width of the high tension zone would be affected by the projectile size and other fabric and impact properties. The boundary slip during the impact was incorporated in the numerical simulations by allowing the boundary nodes to move in during the event, with a triangular profile depicted in Figure 6 - 38. The width of the slipping zone was chosen to be 60 mm, in order to cover all the yarns with relatively high reaction forces.

Two characteristic variables defining this boundary slip during these simulations were assumed to be the pull-in amount and the time interval in which the slip occurs. Intuitively, the slipping would soften the ballistic response of the panels, as shown in Figure 6 - 39 for the weft yarn slippage during the impact of an RCC projectile on a 1-ply S-728 fabric at a strike velocity of 100 m/s. To obtain these results, the time interval during which the weft slippage occurs was chosen to be the initial 0-200 μs. Despite this fact, it can be observed that there is little effect on the deceleration of the projectile in zone I, and that the slippage would mostly influence the response of the fabric in zone II. However, it is clear that the slip time-interval of 0-200 μs is not

realistic since the tension in the central yarns is too low (if not zero) in the initial stages of impact.

Figure 6 - 40 shows the reaction force applied to the central weft yarn at the fixed boundary of the S-728 target. It can be seen that the peak force applied to the yarn is within the 150-250 μs timeframe. The influence of the slip time-interval on the velocity-time response of the projectile is depicted in Figure 6 - 41. It can be seen clearly that the onset of softening of the fabric response is directly linked to the beginning of the slip time-interval.

It was previously discussed in Chapter 6 that the model prediction of the fabric response was consistently stiffer than the ELVS measurement, specifically in the latter stages of impact where a clear slope-change was evident in the projectile velocity-time response (e.g. see Figure 5 - 6 and Figure 5 - 10). This sudden softening of the target can be attributed to the boundary slippage. Figure 6 - 42 shows the numerical predictions for the impact of an RCC projectile at a strike velocity of 36 m/s on a 1-ply S-728 fabric, with and without boundary slip consideration, compared to the ELVS data. The value of boundary slip considered in this simulation was 5 mm, which is the average of the slip values measured during the post-mortem examination of this specific panel. The slipping was assumed to occur linearly between the times of 200 to 650 μs. It can be seen that inclusion of the boundary slip improves the predictions of the model. However, the mechanics of such slip is not known at this point and an in-depth study of the slipping phenomenon is required both on the experimental and numerical fronts, before more conclusions can be drawn.

6.4.4 Inter-Layer Gap

Interlayer gap is an important parameter affecting the impact simulation of multi-ply fabric targets. A method was previously discussed in Chapter 6 to determine the gap between the layers using the data obtained from the transverse compression experiments of multi-ply fabric specimens. The numeric value of interlayer gap obtained from that approach for the six fabrics studied ranged between 0.10 mm and 0.14 mm. The model predictions of the projectile deceleration during the impact indicated a fabric response that appeared to be reasonably stiffer than the ELVS measurements. One of the sources of such discrepancy was associated with the small value of initial interlayer gap between the layers of the fabric pack.

In order to further investigate the effects of interlayer gap on the behaviour of the fabric pack, sensitivity of the velocity-time response of the projectile impacting a 16-ply S-728 fabric at 170 m/s to different values of interlayer gap is determined. The simulations are performed for the initial gap of 0.12 mm (as determined from the transverse compression data, see Table 5 - 2), as well as for a gap of 0.5 mm and 1.0 mm added to the initial interlayer gap. As seen in Figure 6 - 43, the addition of 0.5 mm gap significantly reduces the abrupt oscillations in the velocity-time plot of the projectile, eliminating the sudden jumps in the response. The source of such sudden jumps in the response is linked to the amplitude of the stress wave generated in the projectile upon impact that travels from its tip to the tail.

Comparing the deceleration of the projectile tip and tail to that of its centre of mass (see Figure 6 - 44) for the impact simulation discussed above, it is evident

that the two ends of the projectile oscillate around its centre of mass. Since the front ELVS measurements provide the deceleration of the projectile's tail and it appears to be smoother than the model response predictions with the gap value calculated from the transverse compression data, it is concluded that in reality there is more spacing between the adjacent plies of a multi-ply fabric pack. The reason behind the inaccuracies in the interlayer gap calculated from the transverse compression data is due to the lack of information on the starting point of the test data. Since the initial thickness of the fabric specimen is unknown, it is highly probable that a major portion of the initial part of the compression data is discarded, leading to interlayer gap values that are significantly smaller than the real values. This topic should be considered in more detail in the future, in order to determine the realistic interlayer gap that exists in multi-ply fabric targets.

6.5 PENCILLING PHENOMENON

Restricting the Behind Armour Blunt Trauma (BABT) to an acceptable level is one of the important goals of any bullet-proof vest design. Lewis et al. [72, 73] reported on the observation of a pencilling-type injury while investigating the response of personal armour systems at low velocities. The characteristics of the back-face deformations observed deviated significantly from the conventional shallow hemispherical crater and showed a sharp and highly localized deformation mode. Further studies were carried out and similar results were produced in ballistic impact tests firing 9 mm and 0.357" Magnum ammunitions at armour systems made from 20 plies of Kevlar® fabrics on a

variety of different tissue simulants (Plastilina®, ballistic gelatine, ballistic soap), as well as tests using pig tissue and cadaver as the backing. Lewis et al. concluded from their studies that this type of injuries should be considered in the design of bullet-proof vests. They argued that while the new designs of bullet-proof vests pass the acceptance criteria on the depth of back-face penetration, this deformation is highly localized compared to the shallow hemispherical deformation observed in the traditional vests. They concluded that this sharp localized deformation can cause puncture wounds in the body and can cause significant underlying injuries specifically over the ribcage. They linked the occurrence of the pencilling phenomenon to the light weight and flexibility of the new bullet-proof vests.

In order to investigate the mechanisms that trigger such behaviour, ballistic impact response of an RCC projectile striking a 4-ply target was compared to that of a 1-ply fabric, both supported by a block of backing material to incorporate the interaction of the armour with the body. The backing block was meshed as a cube with dimensions of 300 mm x 300 mm x 180 mm. The material model used for the backing block was the elasto-plastic material model in LS-DYNA with material properties provided in Table 6 - 1. The RCC projectile was considered to be rigid with a mass of 8.1 grams (equal to that of a 0.357" Magnum bullet). Since the improvements in the yarn mechanical properties in recent years have resulted in bullet-proof vests that are lighter than the traditional ones ([72, 73]), the elastic modulus and areal density of the 1-ply fabric was varied to probe the influence of each of the two parameters on the depth and shape of the back-face deformation.

Table 6 - 2 provides the specifics of the numerical cases that were run to investigate the effects of elastic modulus and areal density on the back-face deformation. The failure of the yarns in the target was not considered in this study to prevent the projectile from perforating the target. The projectile's strike velocity was set to 300 m/s to match that of the 0.357" Magnum bullet. Figure 6 - 45 shows the displacement of the projectile for simulations of impact on 4-ply target and backing only cases, as well as a mass-equivalent 1-ply target (areal density multiplied by four) with and without the increase in elastic modulus. The high-modulus equivalent 1-ply case was considered to account for the higher stiffness of the 4-ply target to that of a 1-ply target. As seen in this figure, depth of penetration increases by moving from 4 to 1-ply target, indicating the effect of target thickness. Figure 6 - 46 shows the projectile displacement obtained from the simulation of impact on 4-ply target, as well as 1-ply targets with and without modulus increase. It should be noted that the areal density of the 4-ply target is four times those of the 1-ply targets.

It is evident from this plot that reduction of the target mass significantly affects the projectile penetration depth. This mass reduction also affects the shape of the deformation in the backing material. As seen in Figure 6 - 47, the shape of the deformation crater in the backing material is steeper in the lighter target (1-ply) than the heavier one (4-ply). From the above comparisons, one can conclude that the occurrence of the pencilling phenomenon will be highly dependent on the mass of the layers resisting the motion of the projectile (non-perforated layers in the case of partial penetration), as well as the in-plane mobility (i.e. flexibility) of those layers, since they tend to bunch up around the projectile and conform to the steep and narrow shape of the deformation cone.

In order to reduce the pencilling effect in the body armours, the in-plane displacement of the individual layers should be constrained. This can be done through various methods, such as more efficient stitching of the layers together. Inclusion of layers with high shear resistance (low shear locking angle) at the armour-body interface should also decrease the dominance of this mode of deformation, since high in-plane shear would reduce the flexibility of the target and resist the deformation of the bottom layers that have the tendency to shear significantly to wrap around the projectile and amplify the pencilling deformation.

6.6 RECOMMENDATIONS FOR INDUSTRIAL APPLICATION

The goal of this study, as mentioned in Section 1.3, is to provide an efficient numerical tool for the analysis of fabric targets that is of use to personal armour designers. The verification, validation and sensitivity studies performed in this thesis prior to this point indicate the ability of the 2D shell crossover model to successfully predict the deformational response of fabric panels. The overall modelling approach established in this thesis is capable of providing solutions to industrial design problems. This section summarizes the requirements for setting up a fabric model and the analysis of an impact event in an industrial setting.

Design of a fabric starts with the choice of warp and weft yarns, their linear density, the weave type (plain, twill, etc.), and fabric thread count in warp and weft directions. Once the fabric is woven, several measurements can be made to determine the fabric crimp and in-plane gap between the yarns in the two

directions. Knowledge of these parameters is sufficient for setting up the shell-based model of the fabric. The steps required to set up a model are presented below:

- Calculate the fabric unit cell dimensions. A fabric unit cell is made of a single yarn crossover and its length in each direction is calculated from the thread count in the opposite direction. Each shell element would represent a single fabric unit cell, thus the fabric can be meshed from these elements with known dimensions.

- Determine the material properties (stiffness and strength) of the yarns. If mechanical properties of the yarns after weaving are not available, the properties of virgin yarns can be used, considering the sensitivity of the response to the yarn stiffness (Figure 6 - 7).

- Calculate the initial yarn heights (h_i) using their length and crimp values (Equation 4 – 5). The shell thickness is then determined as the summation of the yarn heights multiplied by two.

- Determine the shear locking angle. This is done using the gap between parallel yarns, according to the process illustrated in Section 4.3.2.

- In the case of multi-ply targets, determine the interlayer gap. This can be done either through performing fabric transverse compression tests, manually measuring the thickness of the multi-ply fabric pack, or assuming a pre-determined interlayer gap. Regardless of the

methodology, however, the user should always consider the gap sensitivity analysis performed earlier (Figure 6 - 43).

- Calculate the parameters required for the transverse compressive model of the yarns. These parameters are perhaps the most difficult to determine. For panels of Kevlar® 129, the transverse compression model derived in this thesis by fitting the predictions to the compression test data of the six panels studied can be used. If the fabric transverse compression data is not available, analysis of the two extreme cases of fabric with decoupled and with non-compressible yarns can be carried out to obtain the range of the response (see Figure 6 - 22 and Figure 6 - 30) and use engineering judgment to determine a reasonable approximation for the behaviour of the target.

Following the above steps, the user would have all the input data needed to set up a finite element model of the target and carry out the simulation of the ballistic event. The designer can use this model to help identify the weaknesses of a specific design and possibly improve/optimize the armour performance, though more work still needs to be done

6.7 SUMMARY

Due to the uncertainties associated with the determination of many mechanical and geometric fabric properties, sensitivity of the fabric response to these parameters was investigated in this chapter. The energy absorption mechanisms dominating the dynamic response of the fabric were investigated

and two distinct zones of behaviour were identified. The effects of various input parameters on the overall response were examined within this framework.

The influence of yarn elastic modulus and crimp, and fabric areal density were investigated. It appeared that while the areal density is the only parameter that would noticeably affect the zone I response, all three parameters would equally affect the zone II response. While determination of the fabric areal density and yarn elastic modulus are more trivial through laboratory measurement and mechanical testing of the yarns extracted from the fabric, yarn crimp is more difficult to measure as it can be affected by many factors such as handling of the fabric, etc. It was found that for a constant strain-to-failure value, increasing the elastic modulus and yarn crimp can lead to a higher critical velocity.

Transverse compressive behaviour of the yarns appeared to have significant influence on the interaction of the yarns. Yarns that are transversely compliant transform a fabric's response through reducing the interaction of the crossing yarns. This is more dominant in unbalanced high crimp fabrics than the balanced low crimp ones. Determination of the transverse behaviour of yarns inside the fabric is a difficult process and the user should determine the bounds of the response by performing simulations with decoupled and/or non-compressive yarns.

Sensitivity of the ballistic response of the fabrics to the components of the shear model was investigated. As discussed, the shearing of the fabric in the specific ballistic experiments simulated in this study seemed to be within the low-shear portion of the fabrics' response. As a result, increasing the shear resistance up

to a certain limit did not affect the ballistic response of the fabric. It was also suggested that a more sophisticated shear model be implemented in the shell elements, in the cases where the proposed model is being used in applications where the fabric would undergo high shear deformations.

The influence of the almost inevitable fabric slippage at the fixed boundaries during the ballistic impact experiments on the overall response of the fabric was investigated in Section 6.4.3. It was observed that the slippage of the fabric at the boundaries can significantly affect the response of the fabric, and was suggested that the experimental information on the boundary slippage be precisely recorded and analysed. This phenomenon not only would affect the energy absorption of the fabrics but can also affect the critical velocity determination for a specific fabric target.

Pencilling phenomenon, a common characteristic back-face deformation of the new lightweight body armours was also investigated in this chapter. The numerical simulations confirmed that the occurrence of the pencilling behaviour is linked to the light weight and flexibility of the target, and found that addition of high-shear-resistant layers can reduce the probability of occurrence of such phenomenon.

Table 6 - 1: Mechanical properties of the dummy backing material used to investigate pencilling phenomenon.

Property	Value
E (MPa)	100.0
Density (g/mm^2)	3.0E-03
Yield strain	0.20
Erosion strain	0.95

Table 6 - 2: Elastic modulus and density of the yarns considered in the simulations performed to investigate the pencilling phenomenon.

Simulation	Target	Elastic modulus (GPa)	Total Areal density (g/m^2)
Case 1	1-ply	480.0	1155
Case 2	1-ply	96.0	1155
Case 3	1-ply	480.0	231
Case 4	1-ply	96.0	231
Case 5	4-ply	96.0	1155

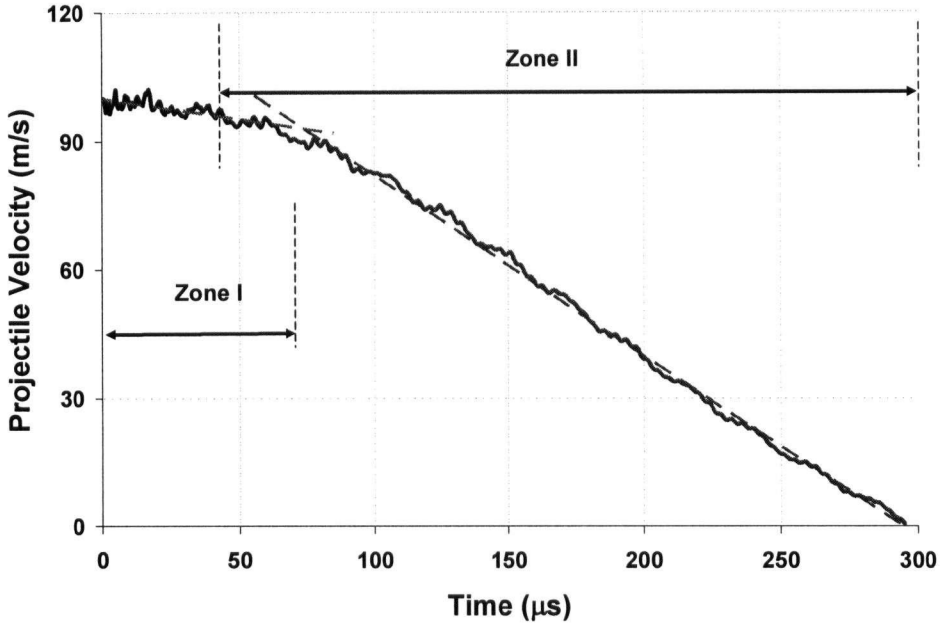

Figure 6 - 1: Velocity-time response of the RCC projectile impacting a 1-ply S-728 fabric at 100 m/s. Two zones of behaviour are identified, dominated by mass (zone I) and stiffness (zone II) of the target.

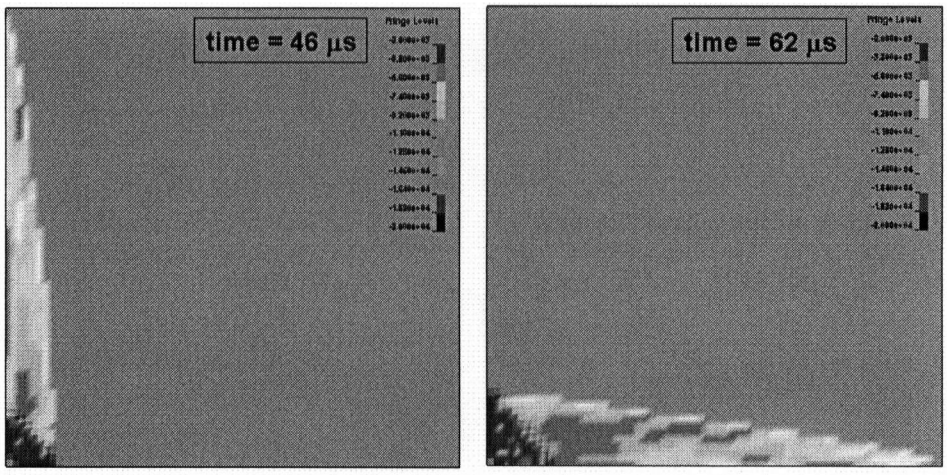

Figure 6 - 2: Contours of in-plane fabric velocity in warp (right) and weft (left) directions reaching the panel boundaries, predicted for the impact of an RCC projectile on a 1-ply S-728 fabric at 100 m/s.

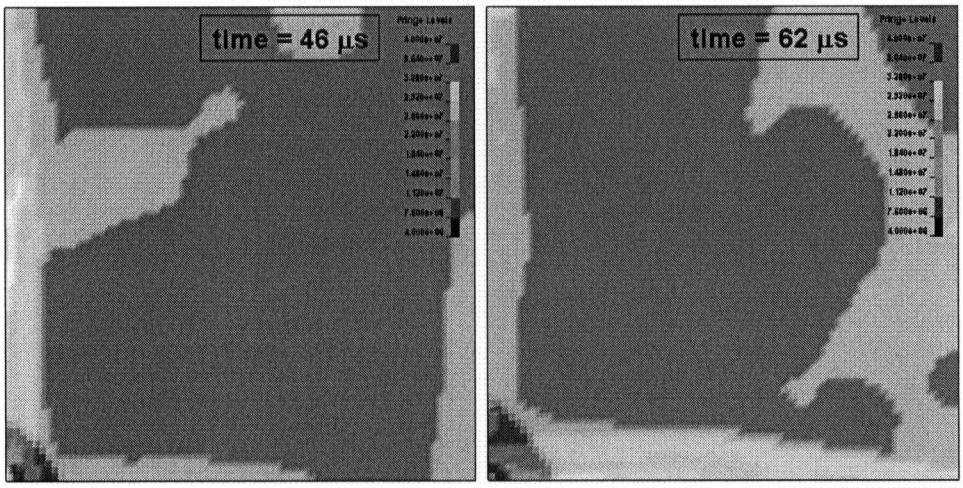

Figure 6 - 3: Contours of tension in warp (right) and weft (left) yarns reaching the panel boundaries, predicted for the impact of an RCC projectile on a 1-ply S-728 fabric at 100 m/s.

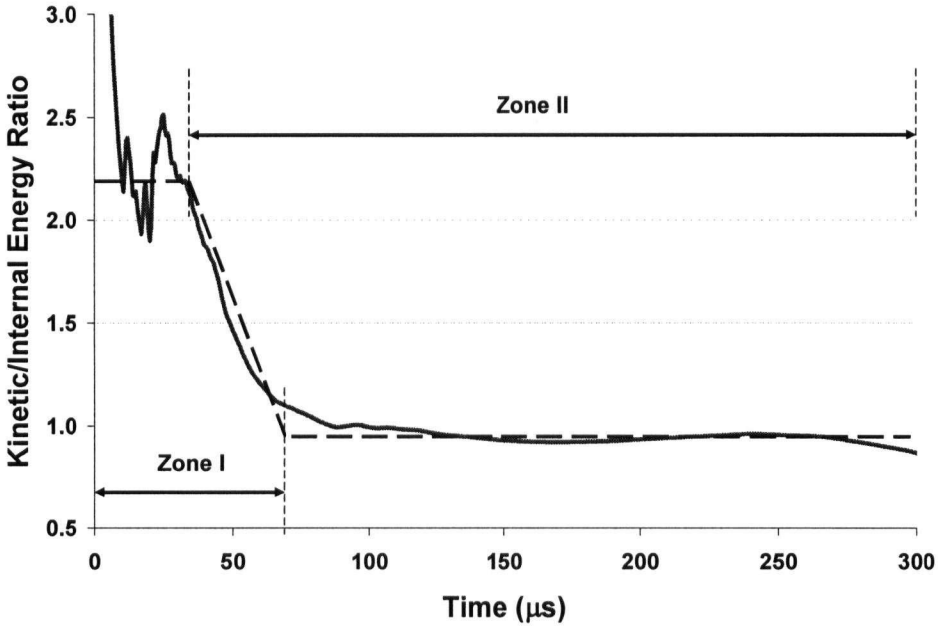

Figure 6 - 4: Kinetic/strain energy ratio of the total energy absorbed by a 1-ply S-728 fabric impacted at 100 m/s by an RCC projectile.

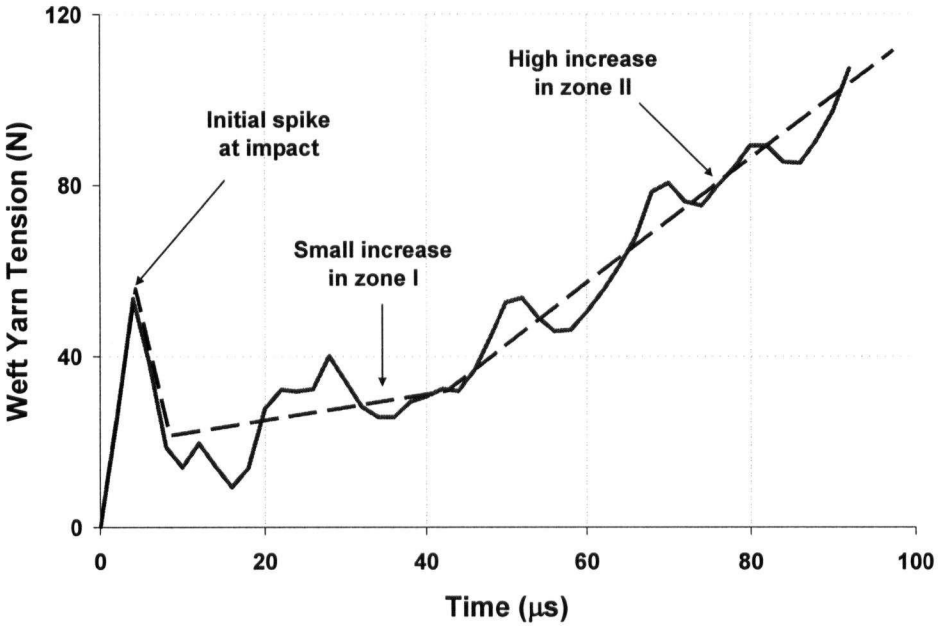

Figure 6 - 5: Tension-time response of the weft yarn of a 1-ply S-728 fabric impacted at 100 m/s by an RCC projectile.

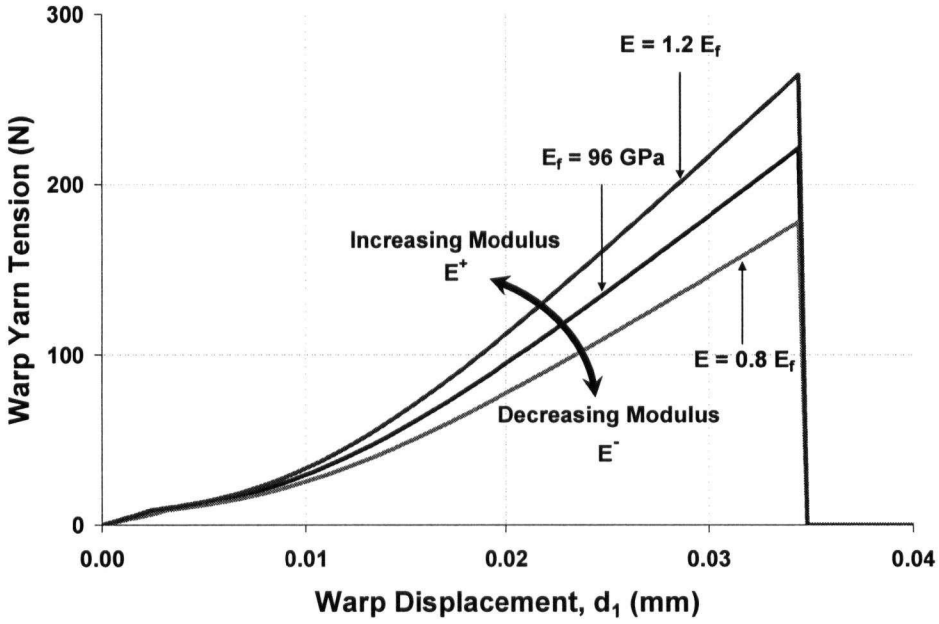

Figure 6 - 6: Tension-displacement response of an S-728 unit-cell loaded in the warp direction with fixed weft yarn, showing the effects of ±20% change in the elastic modulus of the yarns.

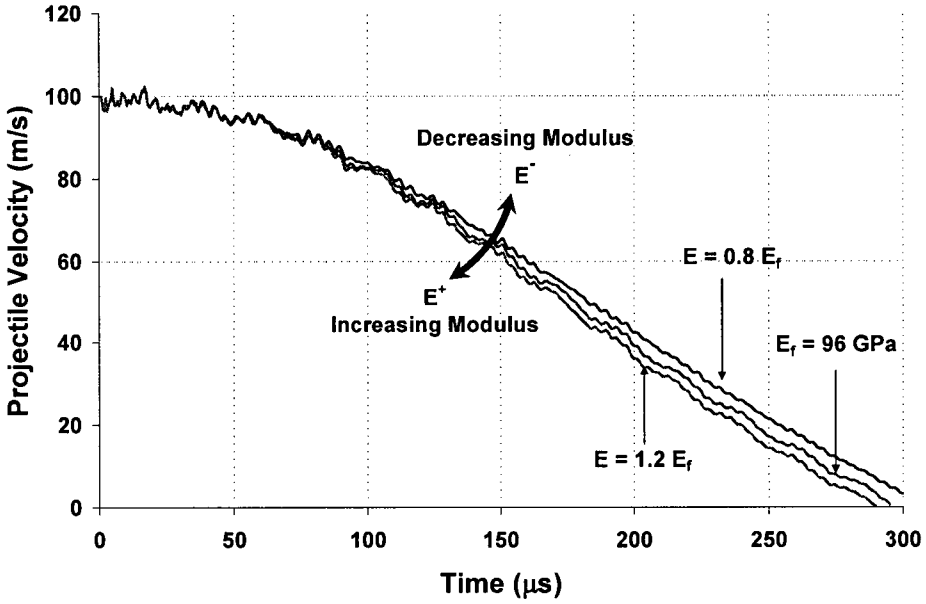

Figure 6 - 7: Velocity-time response of the RCC projectile impacting a 1-ply S-728 fabric at 100 m/s, showing the effects of ±20% change in the elastic modulus of the yarns.

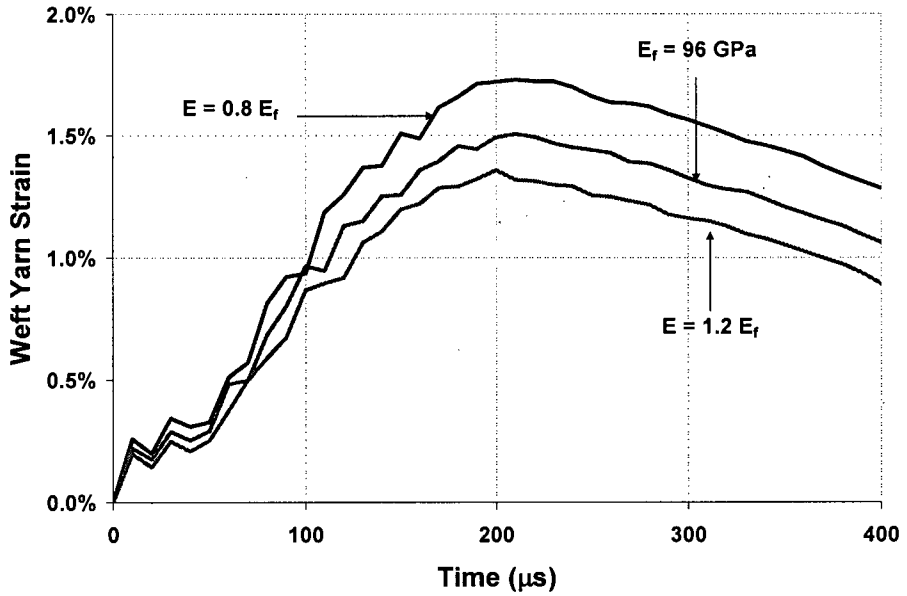

Figure 6 - 8: Strain-time response of the central weft yarn of an S-728 in an impact simulation of an RCC striking a 1-ply target at 100 m/s, showing the effects of modulus change.

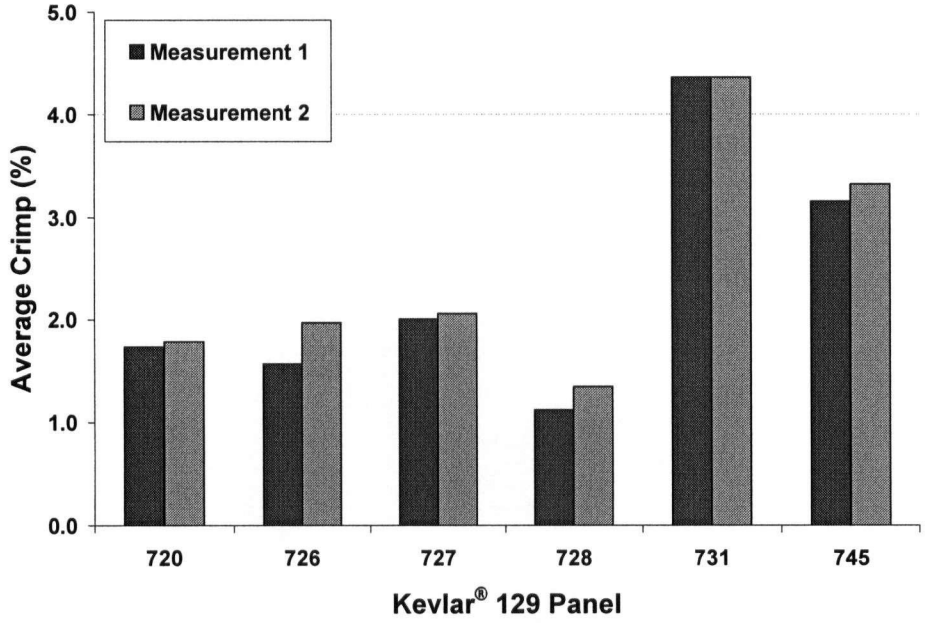

Figure 6 - 9: Crimp measurement performed independently on the six Kevlar® 129 fabric panels by two different individuals, showing a maximum deviation of 20% from each other.

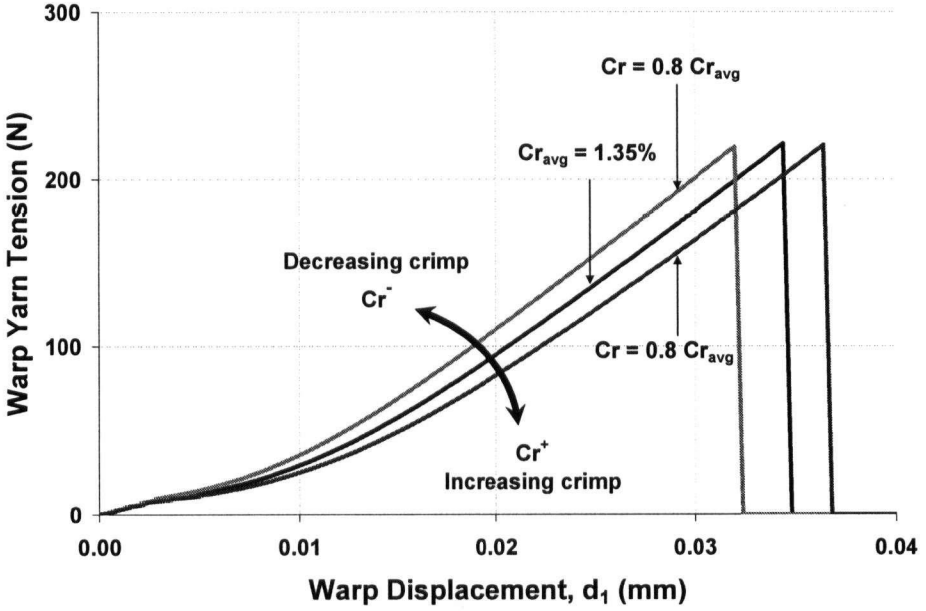

Figure 6 - 10: Tension-displacement response of an S-728 unit-cell loaded in the warp direction with fixed weft yarn, showing the effects of ±20% change in the yarn crimp.

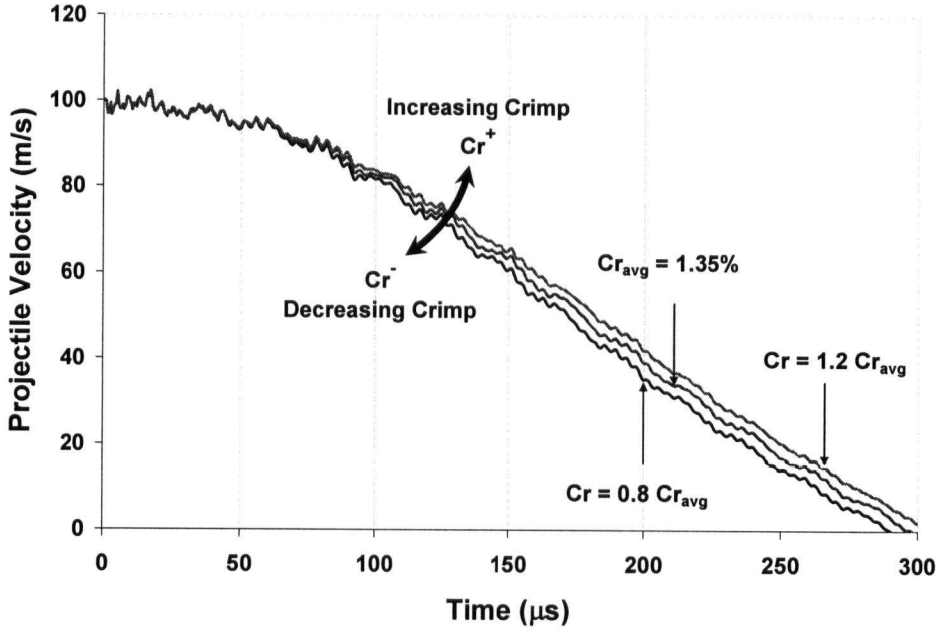

Figure 6 - 11: Velocity-time response of the RCC projectile impacting a 1-ply S-728 fabric at 100 m/s, showing the effects of ±20% change in the yarn crimp.

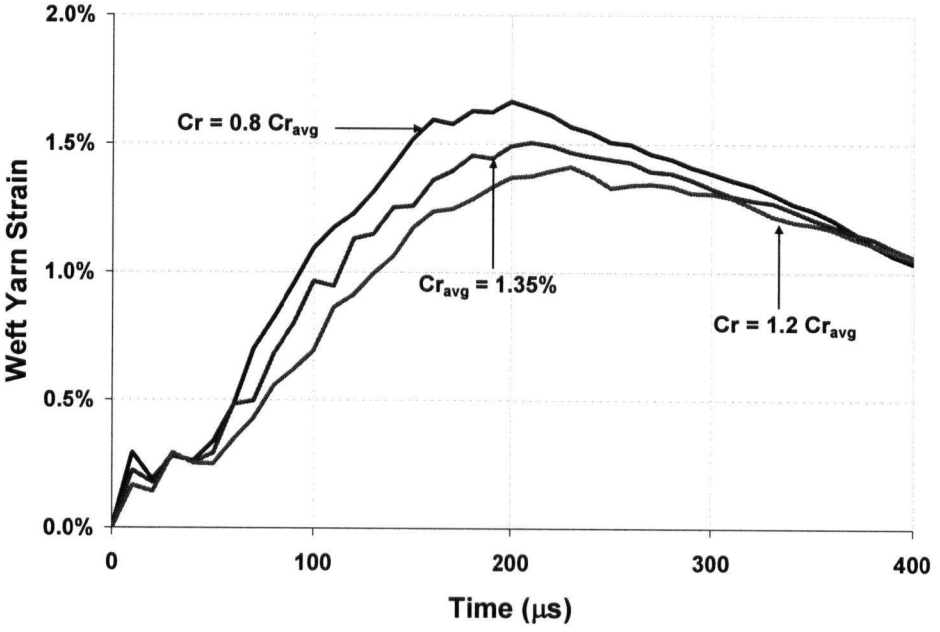

Figure 6 - 12: Strain-time response of an S-728 central weft yarn in an impact simulation of an RCC striking a 1-ply target at 100 m/s, showing the sensitivity of the fabric response to crimp.

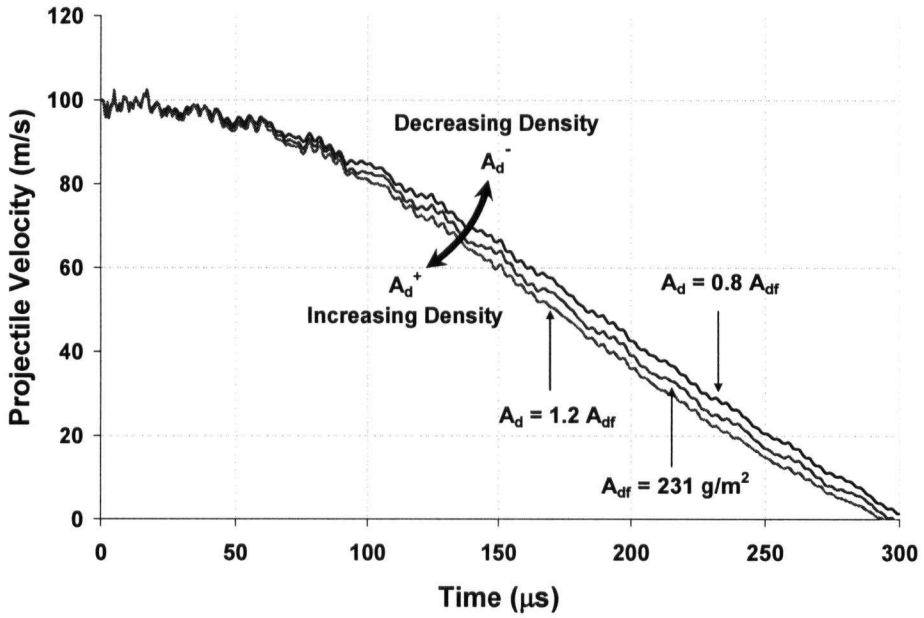

Figure 6 - 13: Velocity-time response of the RCC projectile impacting a 1-ply S-728 fabric at 100 m/s, showing the effects of ±20% change in the fabric areal density.

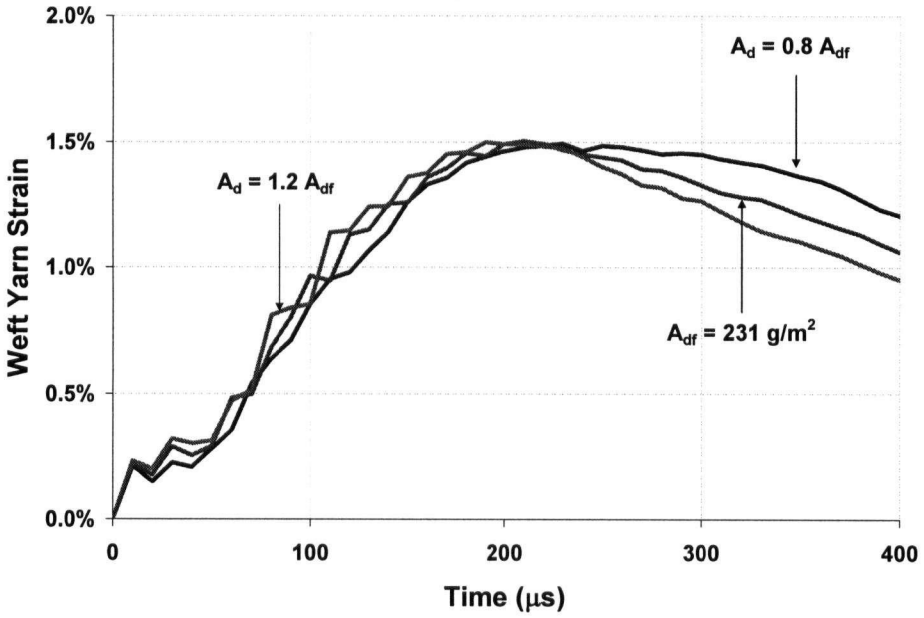

Figure 6 - 14: Strain-time response of an S-728 central weft yarn in an impact simulation of an RCC striking a 1-ply target at 100 m/s, showing the sensitivity of the fabric response to areal density.

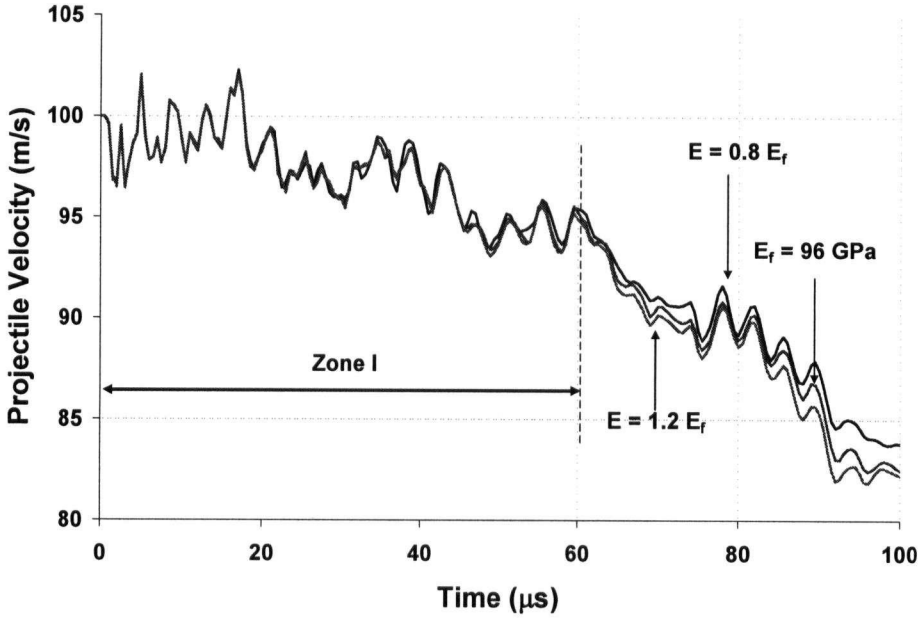

Figure 6 - 15: Initial 100 μs of the velocity-time response of the RCC projectile impacting a 1-ply S-728 fabric at 100 m/s, showing the effects of ±20% change in the fabric elastic modulus.

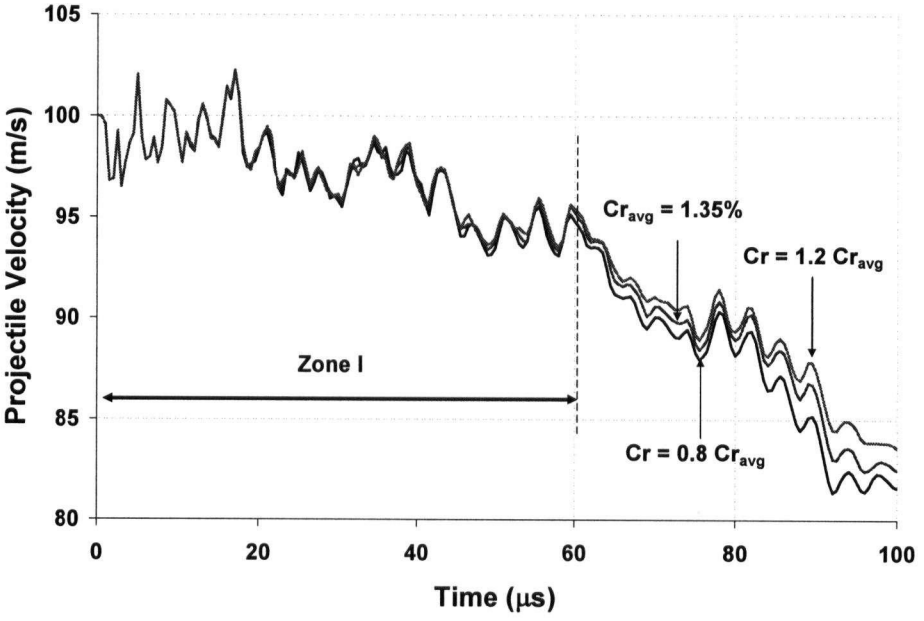

Figure 6 - 16: Initial 100 μs of the velocity-time response of the RCC projectile impacting a 1-ply S-728 fabric at 100 m/s, showing the effects of ±20% change in the fabric crimp value.

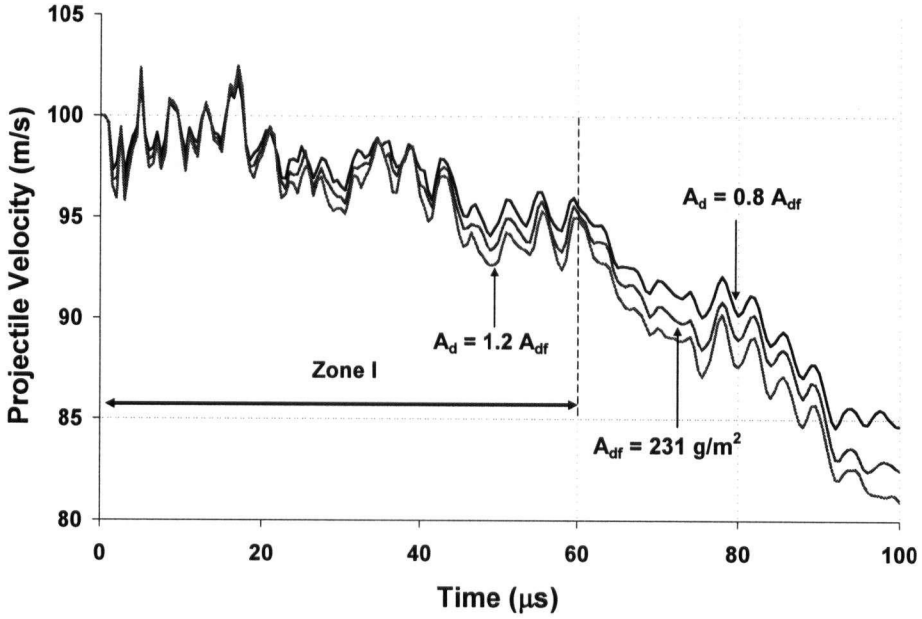

Figure 6 - 17: Initial 100 μs of the velocity-time response of the RCC projectile impacting a 1-ply S-728 fabric at 100 m/s, showing the effects of ±20% change in the fabric areal density.

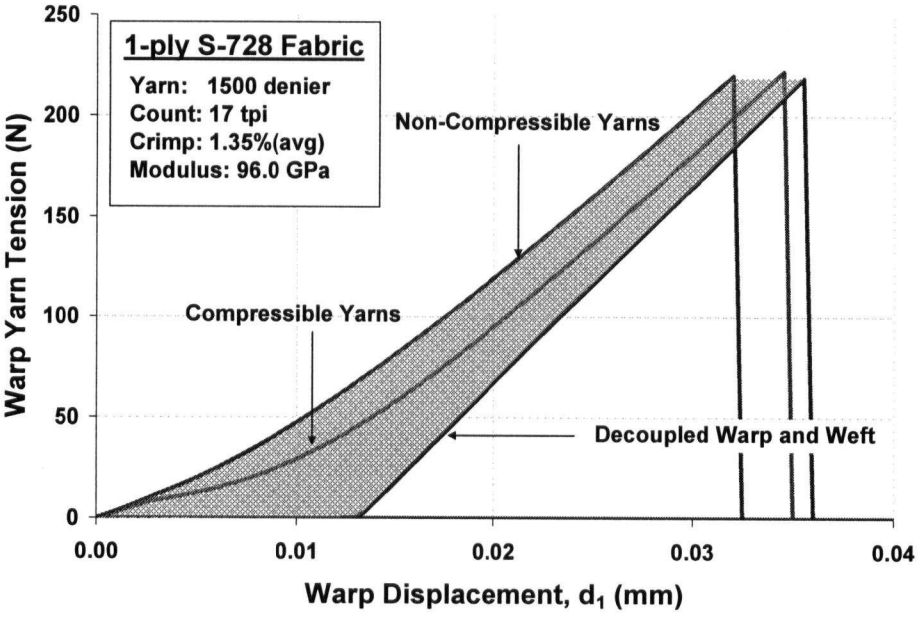

Figure 6 - 18: Tensile response of the warp yarn of an S-728 fabric unit-cell subjected to displacement in the warp direction (weft yarn fixed), assuming compressible, non-compressible and decoupled crossover yarns.

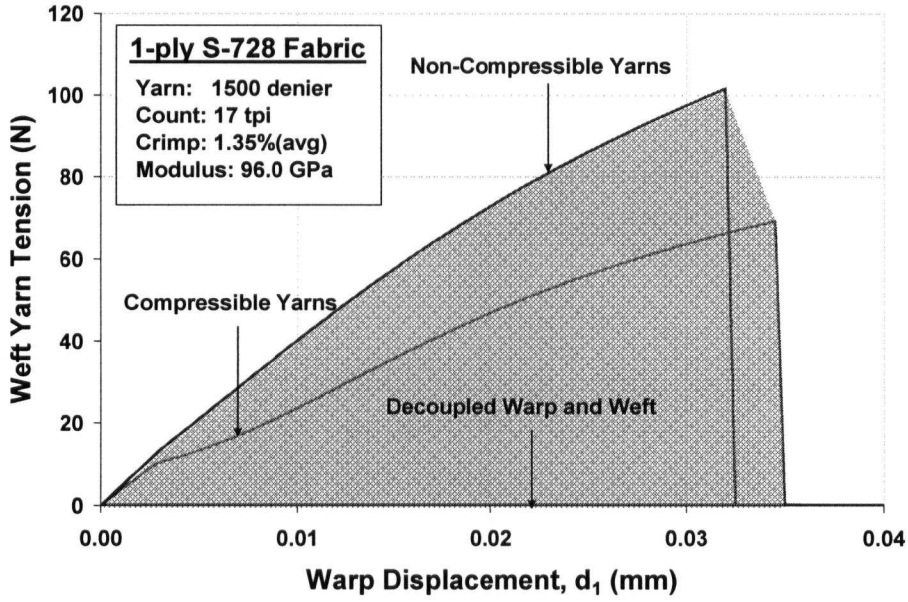

Figure 6 - 19: Tensile response of the weft yarn of an S-728 fabric unit-cell subjected to displacement in the warp direction (weft yarn fixed), assuming compressible, non-compressible and decoupled crossover yarns.

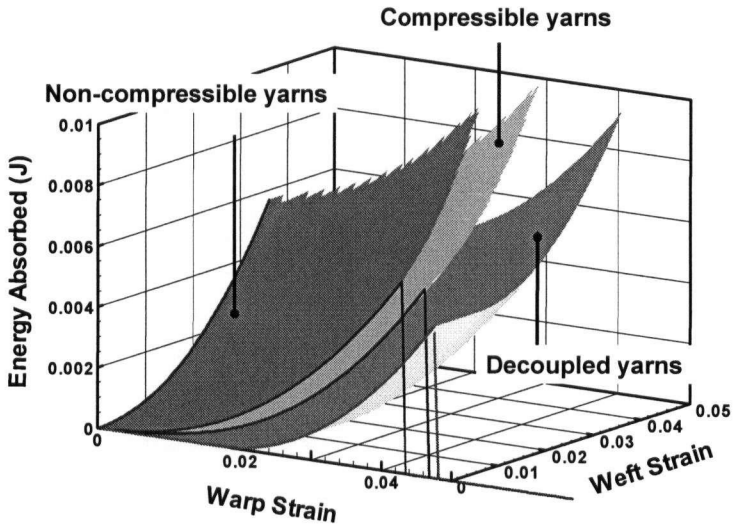

Figure 6 - 20: Surfaces of energy stored in an S-728 fabric unit-cell subjected to warp and weft displacement, assuming compressible, non-compressible and decoupled crossover yarns.

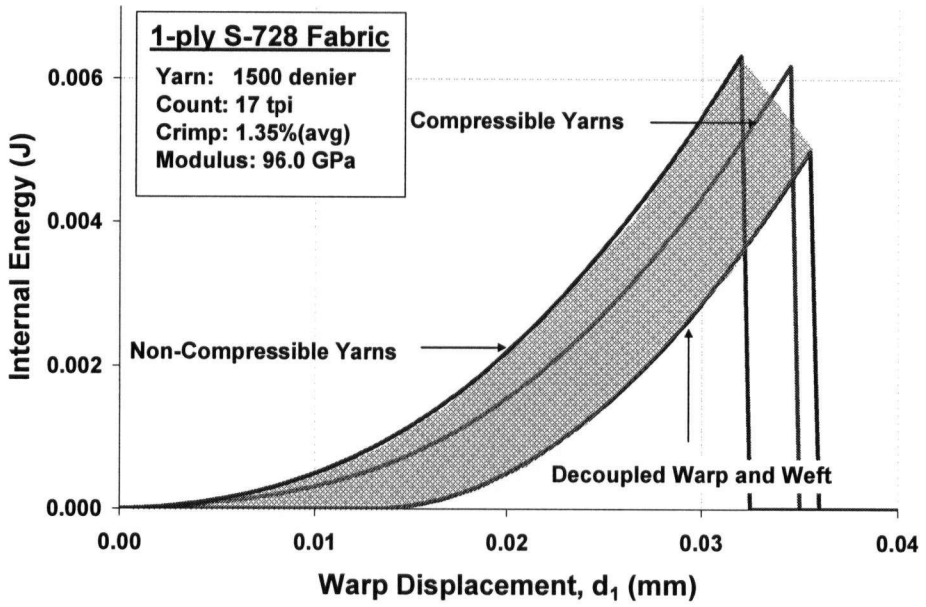

Figure 6 - 21: Energy stored in an S-728 fabric unit-cell subjected to displacement in the warp direction (weft yarn fixed), assuming compressible, non-compressible and decoupled crossover yarns.

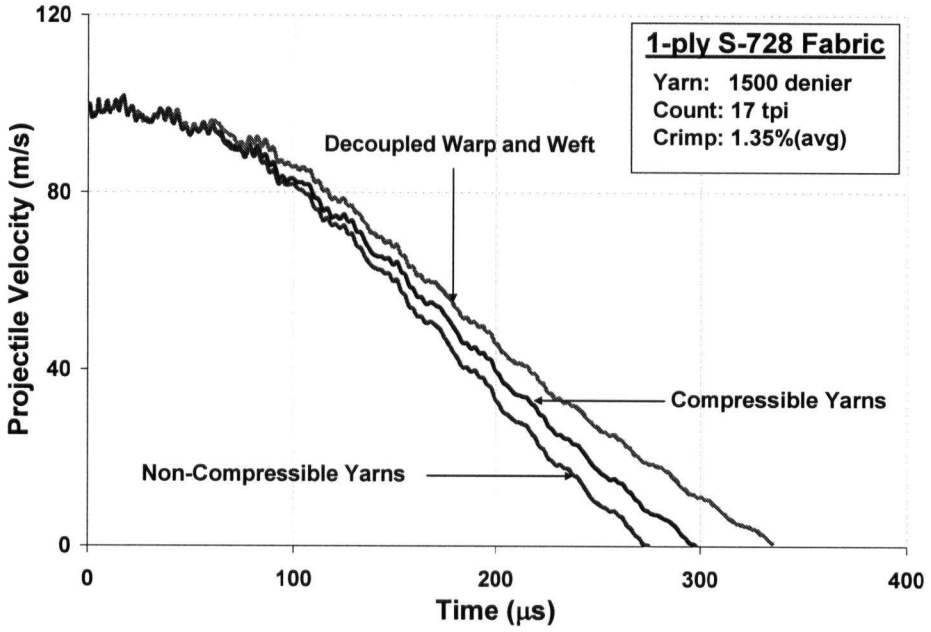

Figure 6 - 22: Velocity-time response of an RCC projectile impacting a 1-ply S-728 fabric at 100 m/s, predicted assuming compressible, non-compressible and decoupled crossover yarns.

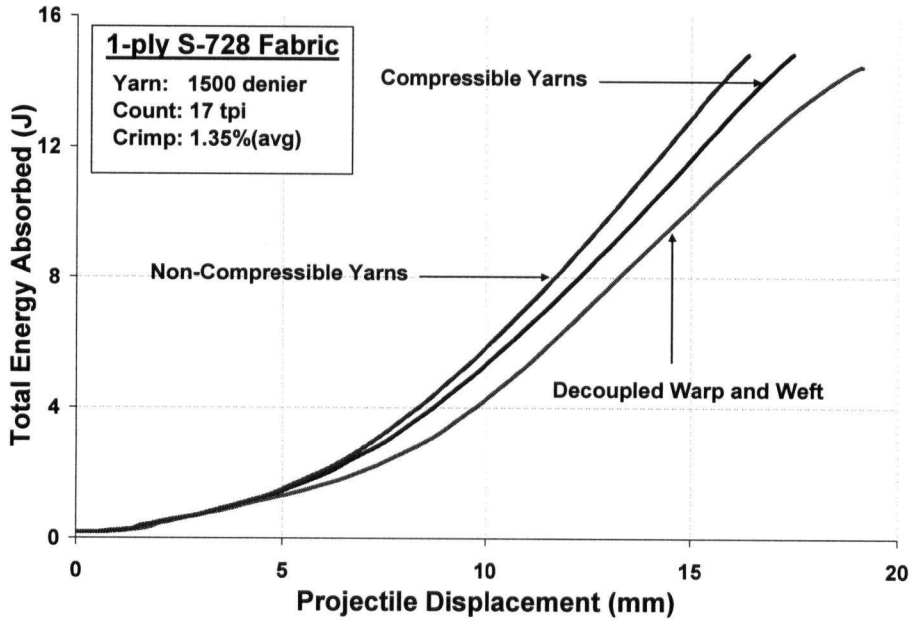

Figure 6 - 23: Energy-time response of an RCC projectile impacting a 1-ply S-728 fabric at 100 m/s, predicted assuming compressible, non-compressible and decoupled crossover yarns.

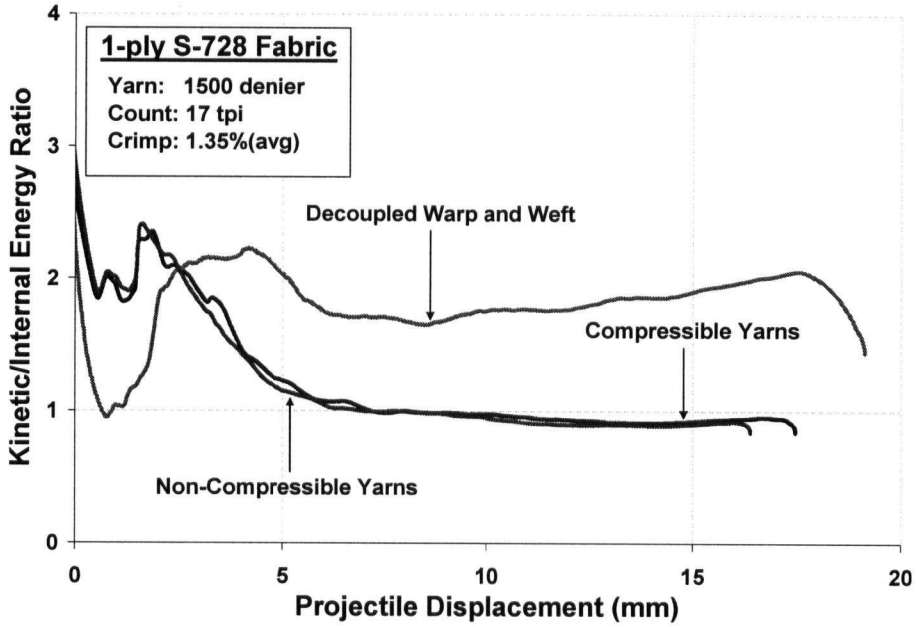

Figure 6 - 24: Ratio of the kinetic to internal energy components stored in the fabric in the impact simulation of an RCC projectile striking a 1-ply S-728 fabric at 100 m/s, predicted assuming compressible, non-compressible and decoupled crossover yarns.

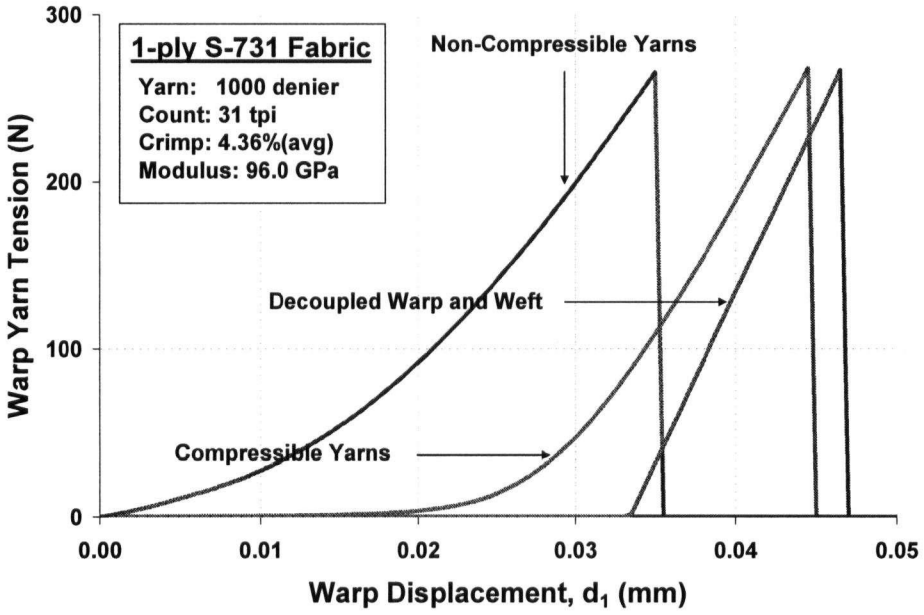

Figure 6 - 25: Tensile response of the warp yarn of an S-731 fabric unit-cell subjected to displacement in the warp direction (weft yarn fixed), assuming compressible, non-compressible and decoupled crossover yarns.

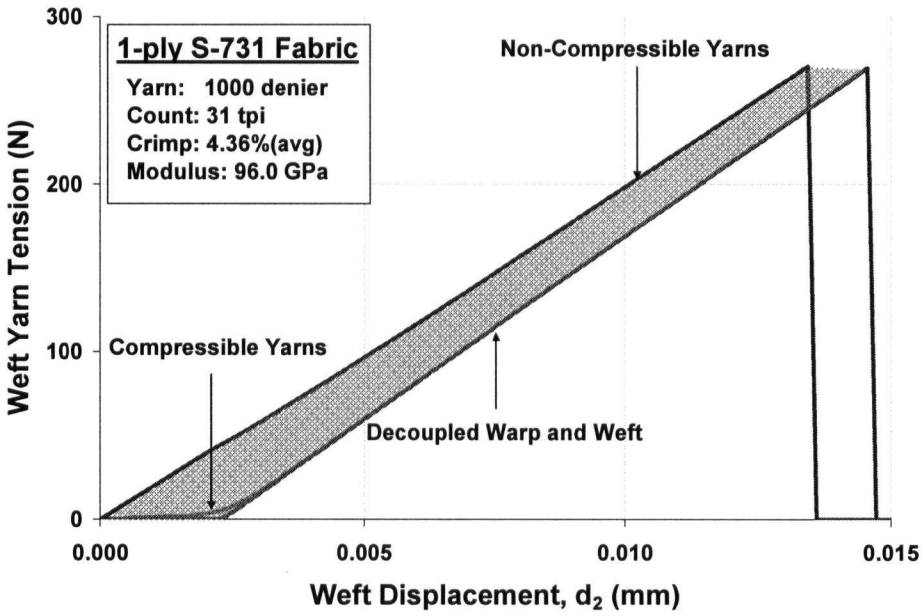

Figure 6 - 26: Tensile response of the weft yarn of an S-728 fabric unit-cell subjected to displacement in the weft direction (warp yarn fixed), assuming compressible, non-compressible and decoupled crossover yarns.

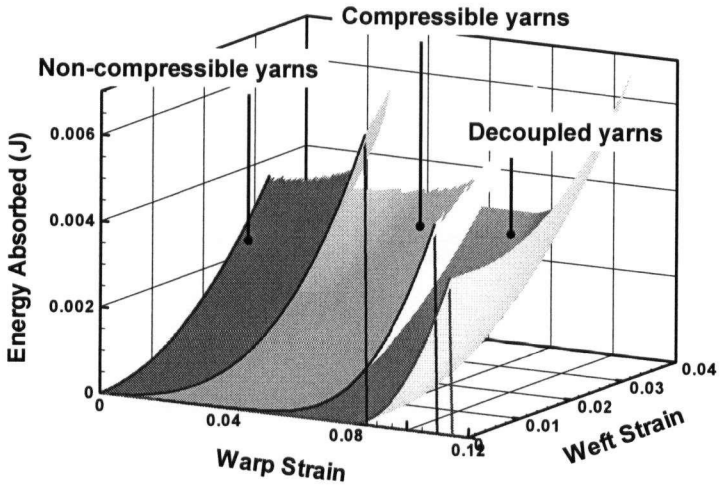

Figure 6 - 27: Surfaces of energy stored in an S-731 fabric unit-cell subjected to warp and weft displacement, assuming compressible, non-compressible and decoupled crossover yarns.

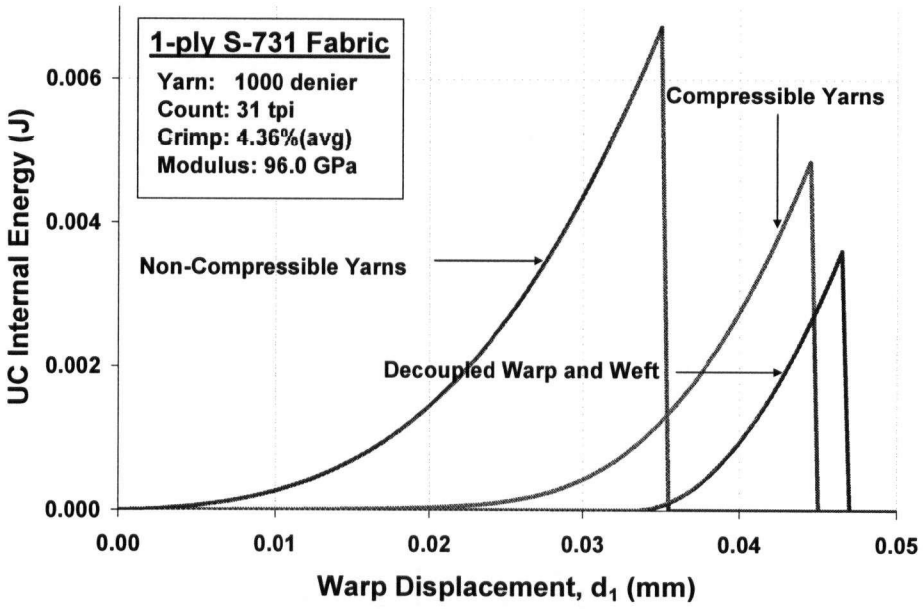

Figure 6 - 28: Energy stored in an S-731 fabric unit-cell subjected to displacement in the warp direction (weft yarn fixed), assuming compressible, non-compressible and decoupled crossover yarns.

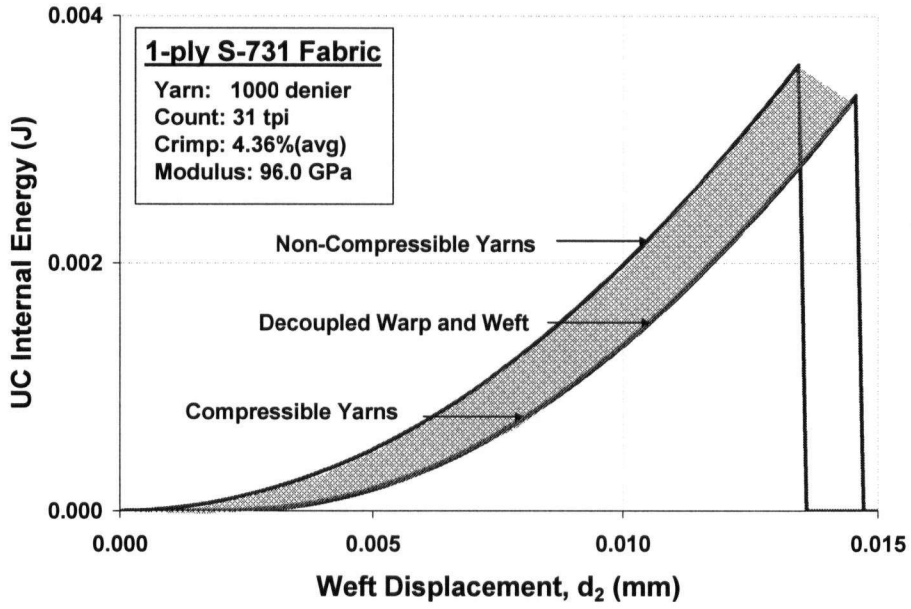

Figure 6 - 29: Energy stored in an S-731 fabric unit-cell subjected to displacement in the weft direction (warp yarn fixed), assuming compressible, non-compressible and decoupled crossover yarns.

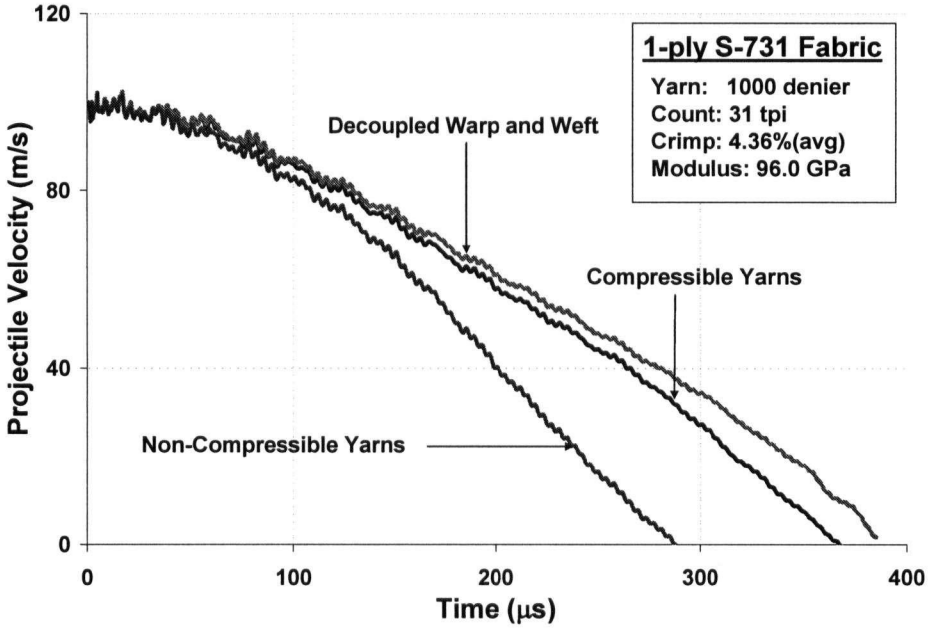

Figure 6 - 30: Velocity-time response of an RCC projectile impacting a 1-ply S-731 fabric at 100 m/s, predicted assuming compressible, non-compressible and decoupled crossover yarns.

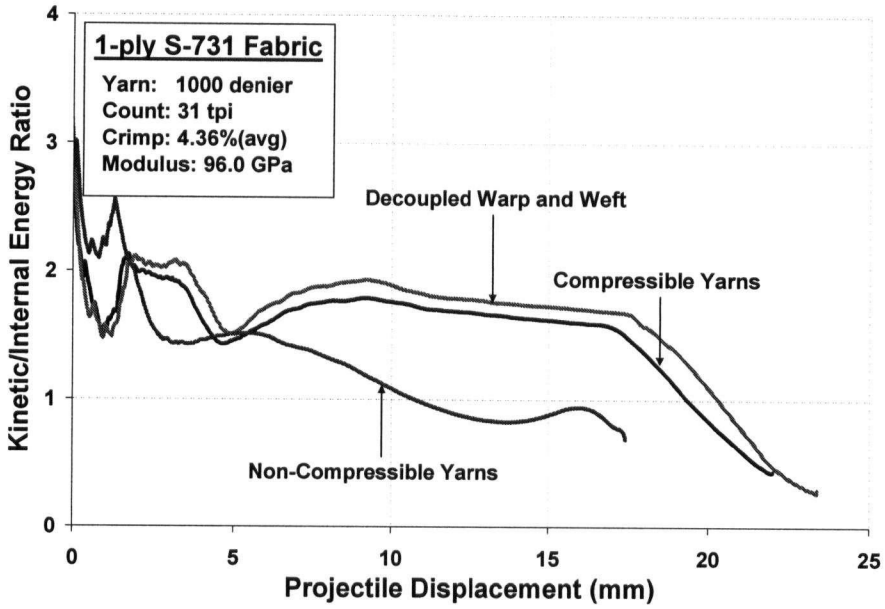

Figure 6 - 31: Ratio of the kinetic to internal energy components stored in the fabric in the impact simulation of an RCC projectile striking a 1-ply S-731 fabric at 100 m/s, predicted assuming compressible, non-compressible and decoupled crossover yarns.

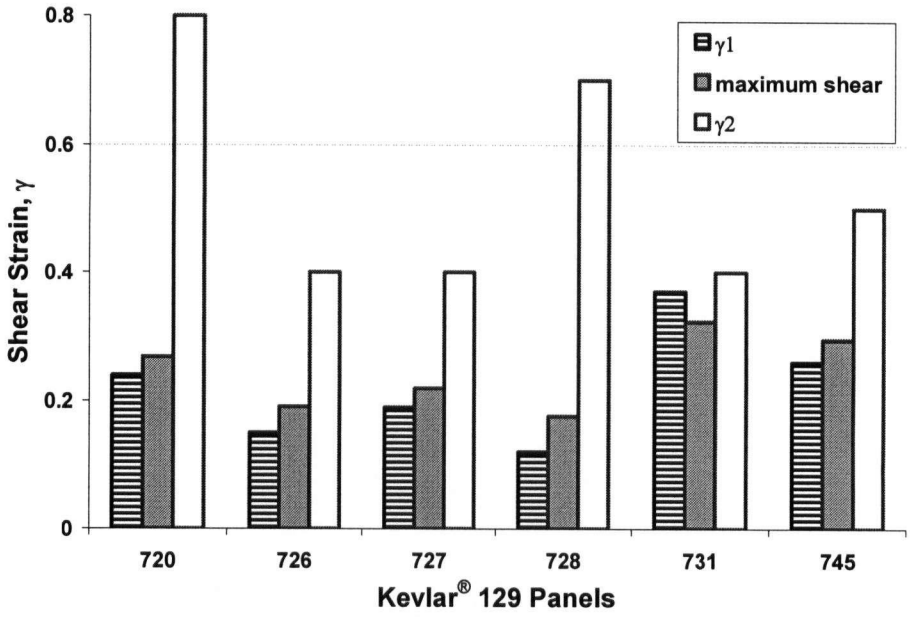

Figure 6 - 32: Maximum shear strain observed in the six Kevlar® 129 panels impacted by an RCC flying at 100 m/s, compared to the stiffening and locking shear strains, γ_1 and γ_2.

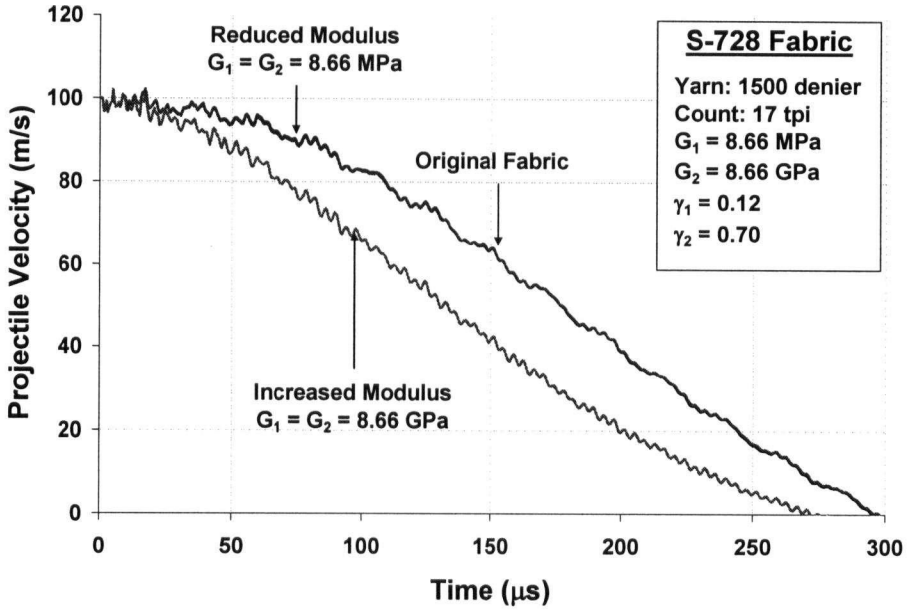

Figure 6 - 33: Velocity-time response of an RCC projectile impacting a 1-ply S-728 fabric at 100 m/s, showing two extreme cases of low and high fabric shear modulus values.

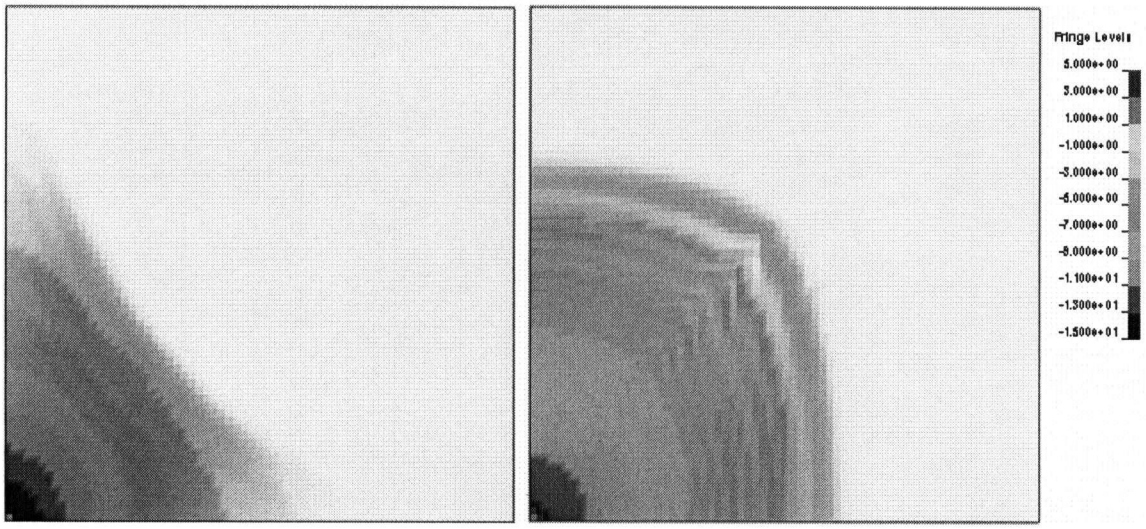

Figure 6 - 34: Deformation patterns shown by contours of z-displacement considering low (left) and high (right) fabric shear modulus.

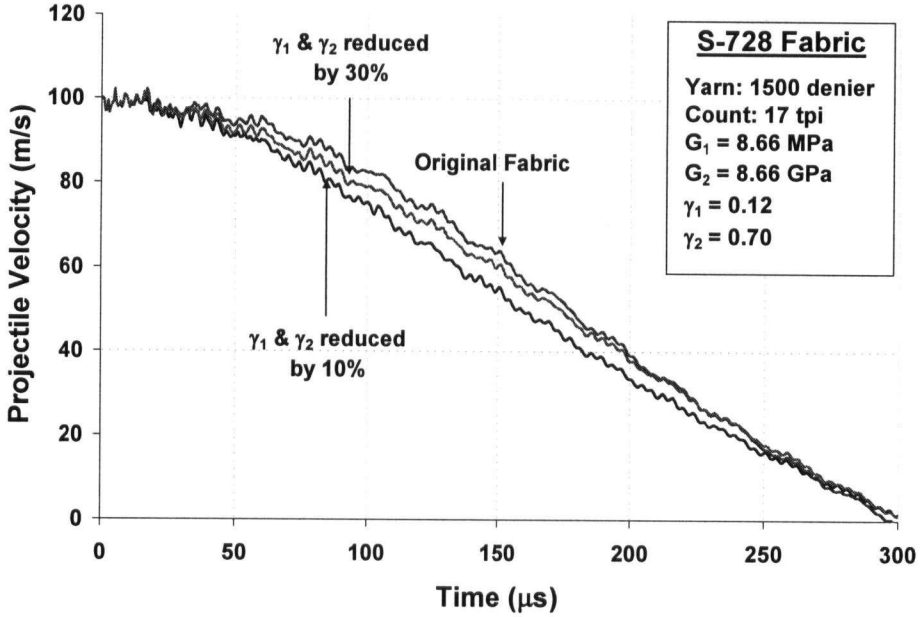

Figure 6 - 35: Velocity-time response of an RCC projectile impacting a 1-ply S-728 fabric at 100 m/s, showing the effect of stiffening and locking angles on the response of the projectile.

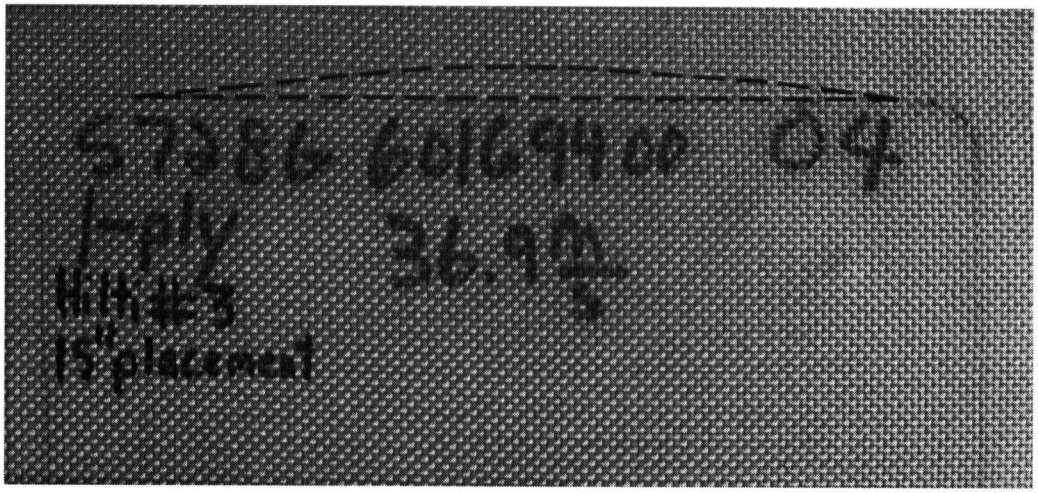

Figure 6 - 36: Boundary slippage marked during a ballistic impact experiment on a 1-ply S-728 panels at a strike velocity of 36.9 m/s.

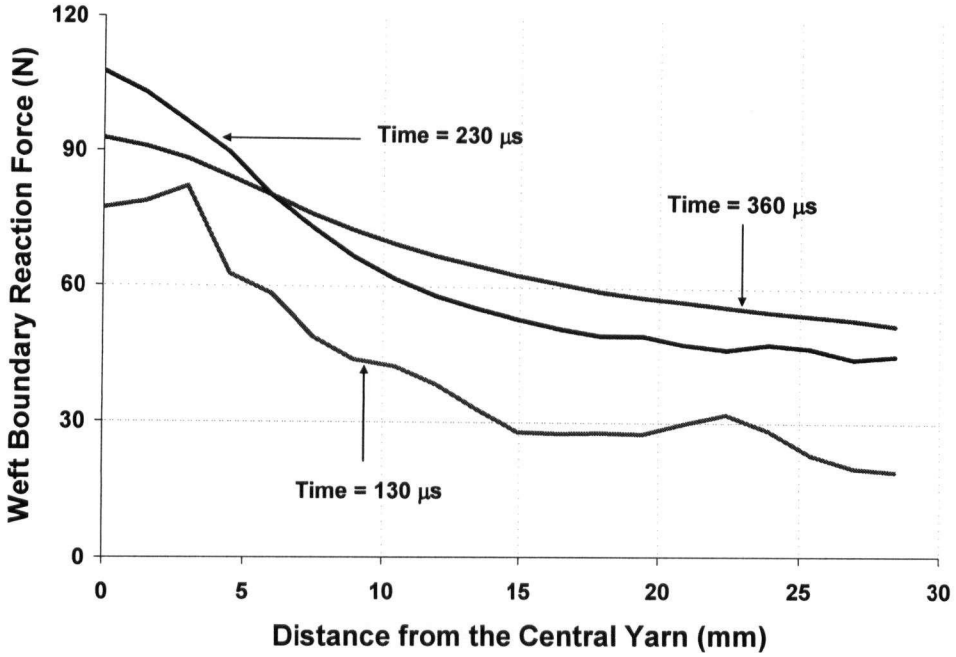

Figure 6 - 37: Boundary reaction in the weft direction of an S-728 1-ply fabric impacted by an RCC projectile at 100 m/s.

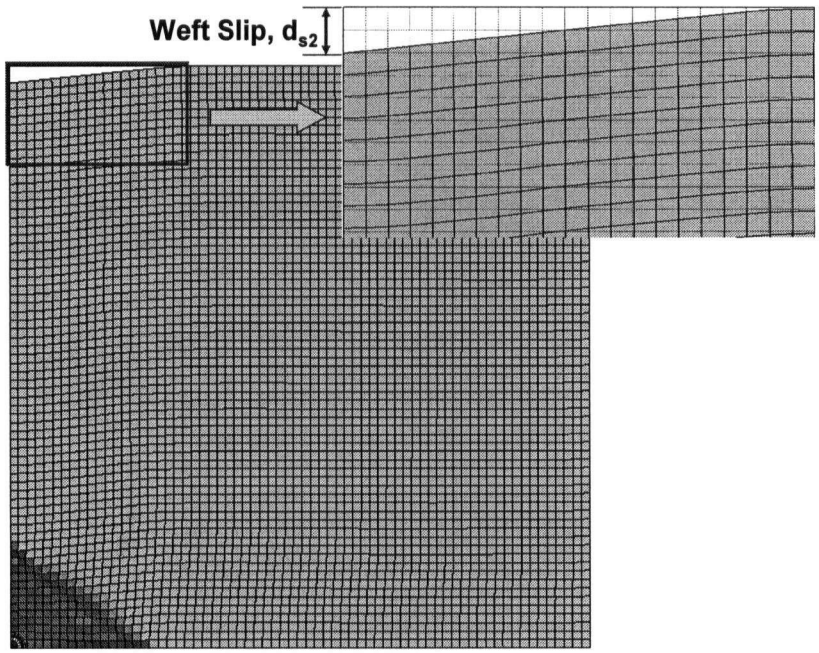

Figure 6 - 38: Simulation of slip at the boundary of an S-728 1-ply fabric through prescribing the in-plane motion of the nodes at the boundaries (weft slip shown here).

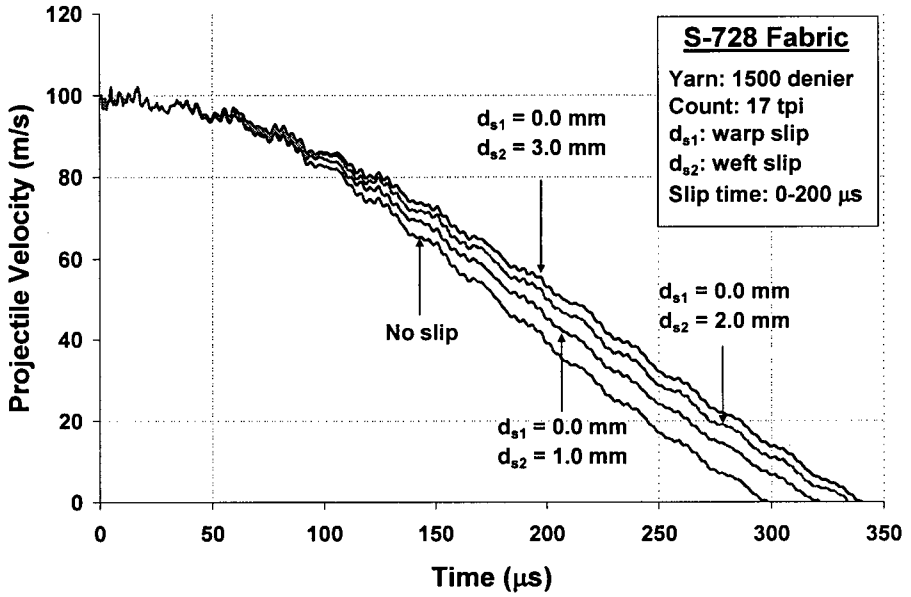

Figure 6 - 39: Velocity-time response of an RCC projectile impacting a 1-ply S-728 fabric at 100 m/s, showing the effect of weft boundary slip on the response of the projectile.

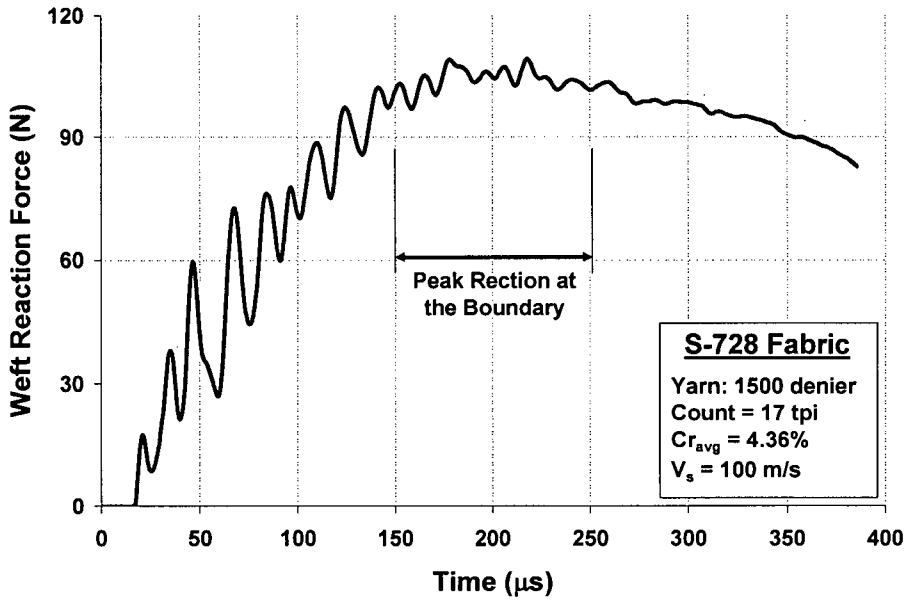

Figure 6 - 40: Reaction force-time response of the central weft yarn in an impact simulation of an RCC projectile striking a 1-ply S-728 fabric at 100 m/s.

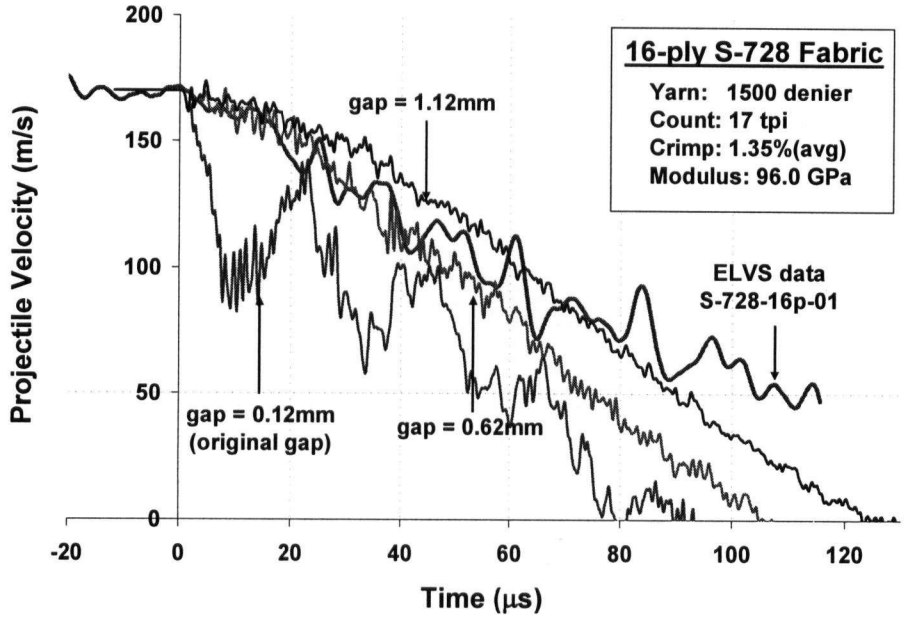

Figure 6 - 43: Velocity-time response of an RCC projectile impacting a 16-ply S-728 fabric at 170 m/s, showing the effect of interlayer gap on the projectile deceleration.

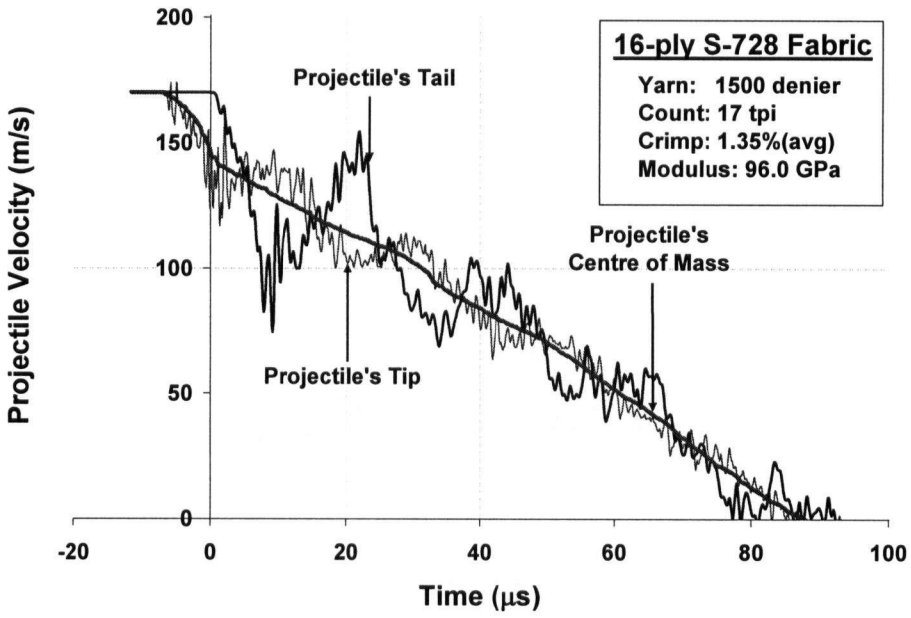

Figure 6 - 44: Velocity-time response of an RCC projectile impacting a 16-ply S-728 fabric at 170 m/s, showing responses of its tip, tail, and centre of mass.

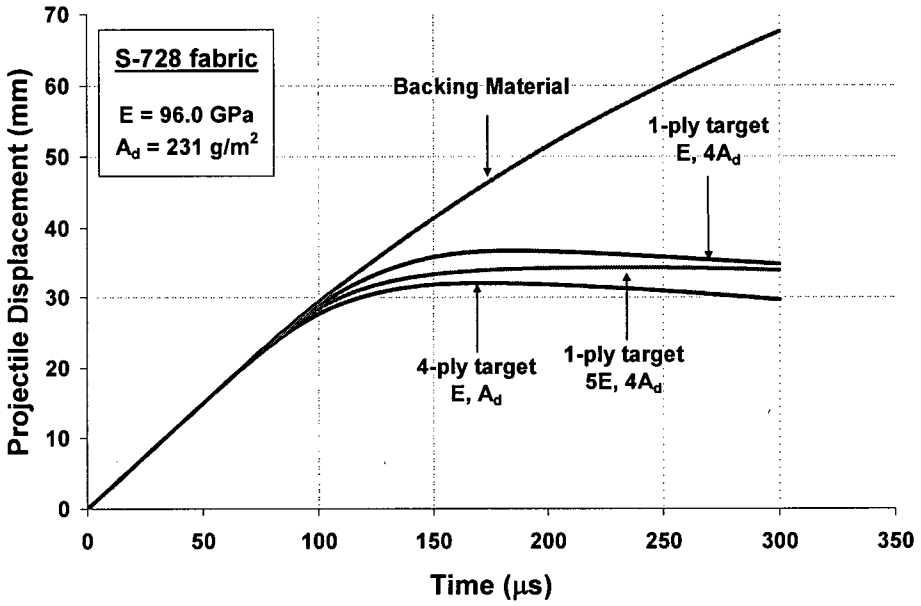

Figure 6 - 45: Displacement-time response of an 8g RCC projectile impacting 4-ply and mass-equivalent 1-ply targets at 300 m/s.

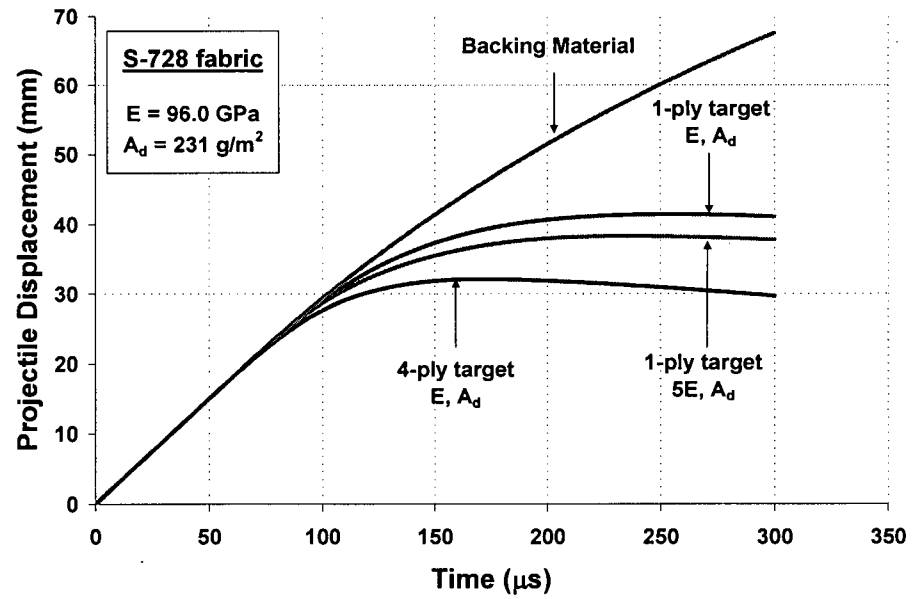

Figure 6 - 46: Displacement-time response of an 8g RCC projectile impacting 4-ply and 1-ply targets at 300 m/s.

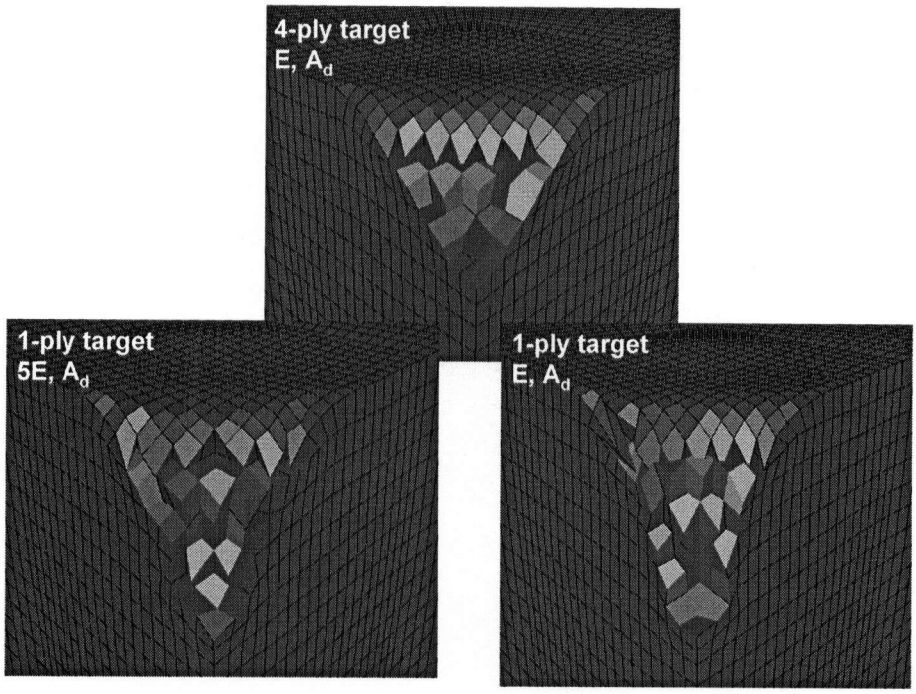

Figure 6 - 47: Post-mortem deformation observed in the backing material in the impact simulation of an 8g RCC projectile striking a 4-ply (top) and 1-ply (bottom) S-728 targets at 300 m/s.

CHAPTER 7 - SUMMARY, CONCLUSIONS AND FUTURE WORK

7.1 SUMMARY

The work presented in this thesis introduces a new approach to the numerical modelling of textile materials that are specifically designed for ballistic applications. This approach takes advantage of the available experimental information and the development of novel modelling techniques to characterize the mechanical behaviour of a single fabric crossover embedded in a fabric unit cell in order to simulate ballistic impact experiments on multi-ply packs of fabric.

To study the behaviour of the fabric unit cell, a detailed 3D finite element model is developed that explicitly considers the warp and weft yarns in a single crossover. This 3D crossover model consists of bar and solid elements with specialized constitutive models that capture the axial and transverse properties of the yarns. The 3D crossover model proved successful in capturing many details of fabric geometry and yarn interaction during the fabric

deformation, but appeared extremely inefficient due to the large amount of computational resources that it needed to carry out the analysis, to a point that it is impractical for simulations of real size (full size) fabric.

An efficient shell element is also developed to represent the mechanical response of a single yarn crossover in a more efficient manner. The material model developed for this shell element is based on a sine-based representation of the yarn profiles and considers their interaction as they deform under the applied displacements. While the response predictions of the shell elements agrees well with those obtained from the 3D fabric crossover model, they are significantly more efficient to run thus making them suitable for the simulation of real-size multi-ply fabric panels.

The efficient shell elements are used to perform simulations of ballistic impact on single and multi-ply fabric targets. The predictions of the model are compared with the experimental data obtained from instrumented ballistic experiments. Overall, the model has proved to be successful in capturing the essence of the dynamic response of fabric targets and where discrepancies have been detected their source have been probed.

A detailed sensitivity study has been performed on several geometric and mechanical properties of the fabric. This analysis revealed many characteristic features of the fabrics that are influential in their specific energy absorption properties during a ballistic event. The model has also been used to study the pencilling phenomenon and the factors that affect its occurrence in lightweight armour systems.

7.2 CONCLUSIONS

The study presented in this thesis has resulted in a robust numerical tool for simulating the complex deformational behaviour of fabrics under impact. The numerical model enables the user to perform an in-depth investigation of the physics of fabric deformation and gain knowledge on the importance of various design parameters.

In general, the 3D crossover model proved to be invaluable in determining the mechanical behaviour of the fabric particularly under loading scenarios that do not lend themselves to impact experiments. Development of the constitutive model for solid elements that provides the transverse mechanical response of the yarns paves the way for studying the unit cell response of any fabric weave, as long as the shape of the yarns in the weave is known. In other words, there is no limit on applicability of the 3D crossover model, as long as the finite element mesh of the fabric unit cell can be generated.

Development of the 2D shell crossover model has been instrumental in carrying out the simulations of ballistic impact experiments and the related sensitivity studies efficiently. The efficiency of the shell elements makes them a practical choice for creating models of real-life dimensions and analyzing full-scale impact events. The shell elements are highly versatile and can be easily extended to incorporate other weave types for future research and development.

Some of the specific conclusions drawn from this thesis are listed below:

- The transverse mechanical response of the yarns inside the fabric has proved to be very difficult to characterize. The data from transverse compression tests used in this study provide a useful guide on how to calibrate such a yarn response. Despite the usefulness of the transverse compression tests, more study needs to be performed to better understand the transverse behaviour of yarns, in particular, and that of the fabric as an assembly of yarns.

- The method developed in this study for inter-layer gap determination in multi-ply fabric systems takes advantage of the data from the transverse fabric compression tests. However, it appeared that the gap values calculated result in multi-ply panel response predictions that are much stiffer than those of the real panels. It is speculated that in reality, the gap between the layers is larger than the ones estimated, and this discrepancy is associated with the truncation of the initial segment of the transverse force-displacement data available to this study.

- The success of a numerical simulation is highly dependent on the validity of its underlying assumptions. Therefore, it is extremely important that these assumptions be based on reality and remain valid throughout the analysis. The assumption of sine-based yarn profile in developing the material model for the shell elements proved not to be valid for loose fabrics (low count and small yarn linear density) and resulted in a deviation of the predictions from the experimental measurements.

- Perhaps one of the most important fabric parameters that could influence the appearance of different deformational and failure mechanisms is yarn

crimp. This factor, overlooked by the majority of previous studies, directly controls a fabric's energy absorption characteristics by affecting its longitudinal and transverse wave speeds. Furthermore, the crimp imbalance in warp and weft yarns causes the overloading of one direction compared to the other one and leads to a non-optimal fabric system.

- Two distinct zones of behaviour have been identified for the energy absorption of the fabrics. Specifically, it is found that the amount of energy absorbed in the initial stages of impact (zone I) is mostly influenced by the mass of the fabric. This reinforces the suggestion by Cunniff [71] to place material with inferior mechanical properties on the strike face of the multi-ply fabric targets, since the projectile perforation in these top layers occur in zone I of their energy absorption response.

Overall, it was concluded that in order to truly optimize the energy absorption characteristics of a fabric panel, one needs to consider many fabric and yarn properties and their relative influence on the overall fabric mechanical response. The numerical models developed in this thesis provide suitable tools for investigating the fabric behaviour and can reduce the reliance on the experimental efforts in the design and optimization process of the personal armour systems.

7.3 CONTRIBUTIONS TO THE STATE-OF-THE-ART

The strength of this study is its ability to successfully merge the experimental data and their interpretation with the numerical models to obtain a realistic

representation of the fabric's static and dynamic deformational behaviour. Availability of the experimental measurements *during the impact event* [51] provides a unique opportunity to validate the detailed time history of the predictions of various quantities of interest. Typically, the success of ballistic response predictions are based on how well they predict the residual velocity of the projectile as it exits the target or essentially the total energy absorbed by the target. The high resolution validation process afforded by the ELVS system can expose the smallest flaws in the numerical model, ones that would not be discovered in the absence of such detailed experimental data. The result of this study is a computational model that has met such high standards for validation and the limitations of its applicability are well established. Furthermore, all the variables used in this approach are based on the physical reality of the fabric, whose values have been calibrated by appropriate experimental measurements.

The main advantage of the work conducted throughout this thesis is the way in which the two unit cell models (2D shell crossover and 3D fabric crossover models) complement each other. The detailed 3D fabric crossover model not only provides information on the transverse compression of the yarns as input to the 2D shell crossover model, it also serves to verify the predictions of the shells on the mechanical response of a single fabric crossover. The 3D crossover model provides an invaluable tool to gauge the suitability of the assumptions made in deriving the fundamentals of the shell model, as well as identifying the limits of their validity.

The formulation of the shell elements based on the sine-based yarn profiles developed in this study is unique, and is in accordance with the yarn shapes

observed in the cross-sectional micro-images of fabrics [42], as well as the predictions of the detailed 3D crossover model. Traditionally, yarns with truss-like bilinear configuration have been used in the representative shell elements [57]. These models lead to theoretical yarn geometries that are different from what is observed in the real fabrics and given the high dependency of the response on the yarns configuration, result in inconsistent crossover response. Furthermore, the comparison between the 3D fabric crossover model and the 2D shell elements would not be meaningful due to their significantly different geometries. The fabric models assembled from the shell elements with sine-based formulation have been shown to capture the ballistic response of fabric targets successfully, making them a good candidate for future studies. Compared to the traditional discrete models, the shell prediction of the fabric response under ballistic impact shows a slight improvement for the fabrics considered in this study. However, this is due to the fact that the coupled biaxial behaviour of the crossing yarns considered along with the inclusion of yarn transverse compression affect the fabric response in opposite ways. Therefore, little difference is observed in the projectile deceleration prediction compared to that of the discrete pin-jointed model that fails to capture these two features of fabric behaviour. As a result, the shell crossover model developed here provides a more realistic mechanics of the fabric compared to that obtained from the discrete model.

The contributions made to the 3D crossover and the 2D shell crossover models are summarized in Table 7 - 1 and Table 7 - 2. For a comparison of the model efficiencies, the reader is referred to Table 4 - 3 for execution times required to

complete the analysis of impact on fabric models constructed from the 2D and 3D crossover models, as well as the discrete pin-jointed model.

Overall, the numerical model provided in this study is a robust state-of-the-art tool for analysing the mechanical response of fabric structures, in general, and their ballistic behaviour, in particular.

7.4 RECOMMENDATIONS FOR FUTURE WORK

The approach introduced in this thesis is only a stepping stone towards a fully inclusive and comprehensive model of fabrics. Despite the success of the proposed models in fulfilling the initial goals, improvements are needed to be made in order to expand the applicability of the approach. The recommendations for future work are:

- One of the influential factors in the mechanical response of fabrics was found to be the transverse compression of the yarns. Further studies should be conducted on designing more suitable experiments to capture the yarns true transverse behaviour inside a fabric. Measurement of the fabric thickness before and after the experiments was found to be extremely valuable, specifically in determining the inter-layer gap in multi-ply fabric packs.

- The transverse compression model needs to be revisited, and a mechanics-based model be developed to capture the interaction of the yarns in a specific weave structure during compression. The model implemented in the solid elements to capture the transverse mechanical response of the

yarn also needs to be improved and based on the physics of interaction between the individual fibres of a yarn.

- Degradation of the material and geometrical properties of yarns during the weaving process should be further investigated. As mentioned before, it is known that the weaving process damages the yarns and causes degradation of their mechanical properties [68, 69], which in turn introduce an undetermined amount of error in the predictions of the numerical model. The true properties of the yarns need to be determined by performing experiments on the yarns extracted from the fabric.

- One of the assumptions made in establishing the crossover models of fabric in this study is the assumption of frictionless contact between the crossing yarns. Effects of this inter-yarn friction on the overall behaviour of a yarn crossover should be further investigated and the error introduced by such assumption be evaluated.

- The shear component of the fabric unit cell was found to have little effect on the energy absorption of the fabrics for the loading cases studied in this thesis. However, this might not be true for other applications where the fabric is subjected to extreme shear deformations, or fabrics with low shear locking angles. The shear model implemented in the shell elements is based on a simple trellis mechanism. A more mechanistic shear model that considers the interaction of the yarns during the scissoring deformation mechanism needs to be developed.

- One of the shortcomings of the model developed is its oversimplified yarn failure criterion. The instantaneous strain-to-failure model incorporated in the shell element is highly sensitive to any oscillations of numerical noise that is introduced in the calculations from a variety of sources such as contact. As a result, premature failure of yarns was observed, specifically for targets with higher number of layers. Implementation of an appropriate failure model that is not affected by the oscillations in the response is highly beneficial to the accuracy of the predictions, especially in the penetrating impact simulations.

- The efficiency of the model can be further increased by implementing a more optimized mathematical solution to the differential equations. The biaxial behaviour of a yarn crossover can ideally be represented by the response surfaces that provide the tension history of the yarns as a function of the applied displacements. Instead of calculating the response at each time-step during the analysis, this can be done as a pre-processing step and implemented into the shell UMAT as a direct mathematical function or look up table, to further reduce the execution time.

- Some of the simplifying assumptions used in developing the material constitutive model of the shell elements should be further investigated. For instance, the assumptions of symmetric unit cell displacements and the sine shape of the yarn profile should be relaxed to determine their effects on the unit cell and ultimately fabric response.

- The approach employed in this study is a purely deterministic one. In reality, the material and geometric properties of the fabrics and yarns

have some uncertainty associated with them, due to the presence of flaws, material handling, measurement techniques, etc. Incorporation of the uncertainties in numerical analysis is a subject of great interest in the field of computational mechanics. Prediction of the ballistic response of fabrics would greatly benefit from the current research in this area.

Table 7 - 1: Comparing the 3D crossover model developed in this study to that of the current literature.

Property	Current 3D Model	3D Models in Literature
Elements	Solid and bar	Solid
Spurious modes of deformation	Eliminated	Present, reduced by hourglass control
Yarn material model	Orthotropic	Orthotropic
Yarn transverse material model	Coupled non-linear model (dependent on fibre volume fraction)	Decoupled linear elastic (Poisson's ratio =0)
Transverse mechanical properties	Calibrated with compression experiments	Generally not calibrated

Table 7 - 2: Comparing the 2D shell model developed in this study to that of the current literature.

Property	Current Shell Model	Shell Models in Literature
Warp and weft yarns	Coupled	Coupled and decoupled
Yarn shape	Sinusoidal	Mainly linear
Transverse compression calibration	3D crossover model, or experiments	Generally not calibrated
Verification	3D crossover model	none

Bibliography

1. Shahkarami, A. (1999), "A numerical investigation of ballistic impact on textile structures," M.A.Sc. Thesis, The University of British Columbia.
2. Roylance, D., A. Wilde, and G. Tocci (1973), "Ballistic impact of textile structures," *Textile Research Journal*, 43(1), 34-41.
3. Roylance, D. and S. S. Wang (1980),"Penetration mechanics of textile structures," Ballistic Materials and Penetration Mechanics, Elsevier Scientific Publishing Co., 273-292.
4. Billon, H. H. and D. J. Robinson (2001), "Models for the ballistic impact of fabric armour," *International Journal of Impact Engineering*, 25, 411-422.
5. Johnson, G. R., S. R. Beissel, and P. M. Cunniff (1999), "A computational model for fabrics subjected to ballistic impact," *Proceedings of 18th International Symposium on Ballistics*, 962-969.
6. Shim, V. P. W., V. B. C. Tan, and T. E. Tay (1995), "Modelling deformation and damage characteristics of woven fabric under small projectile impact," *International Journal of Impact Engineering*, 16(4), 585-605.
7. Shim, V. P. W., V. B. C. Tan, and T. E. Tay (1995), "Perforation of woven fabric by spherical projectiles," *ASME*, AMD-vol. 205, Impact, waves and fracture, 453-456.
8. Tan, V. B. C., V. P. W. Shim, and N. K. Lee (2001), "Computational analysis of oblique projectile impact on high strength fabric," *Proceedings of Impact engineering and Application*, 327-332.
9. Tan, V. B. C., V. P. W. Shim, and T. E. Tay (2003), "Experimental and numerical study of the response of flexible laminates to impact loading," *International Journal of Solids and Structures*, 40, 6245-6266.
10. Tan, V. B. C., V. P. W. Shim, and X. Zeng (2005), "Modelling crimp in woven fabrics subjected to ballistic impact," *International Journal of Impact Engineering*, 32, 561-574.

11. Zeng, X. S., V. P. W. Shim, and V. B. C. Tan (2005), "Influence of boundary conditions on the ballistic performance of high-strength fabric targets," *International Journal of Impact Engineering*, 32, 631-642.

12. Cepus, E., A. Shahkarami, R. Vaziri, and A. Poursartip (1999), "Effect of boundary conditions on the ballistic response of textile structures," *Proceedings of International Conference on Composite Materials (ICCM 12).*

13. Novotny, W. (2002), "A numerical and experimental investigation of the impact behaviour of hybrid and multi-ply fabric structures," M.A.Sc. Thesis, The University of British Columbia.

14. Novotny, W., E. Cepus, A. Shahkarami, Vaziri R., and Poursartip A. (2005), "Numerical modelling of the early impact behaviour of multi-ply fabric armours," *Proceedings of Impact Loading of Lightweight Structures,* 403-420.

15. Cunniff, P. M. and J. Ting (1999), "Development of a numerical model to characterize the ballistic behavior of fabrics," *Proceedings of 18th International Symposium on Ballistics San Antonio, TX, 15-19 November 1999,* 822-828.

16. Ting, C., J. Ting, P. M. Cunniff, and D. Roylance (1998), "Numerical characterization of the transverse yarn interaction on textile ballistic response," *International SAMPE Technical Conference,* 30, 57-67.

17. Tan, V. B. C. and T. W. ching (2006), "Computational simulation of fabric armour subjected to ballistic impact," *International Journal of Impact Engineering,* 32, 1737-1751.

18. Shockey, D. A., D. C. Erlich, and J. W. Simons (2000), "Improved barriers to turbine engine fragments," U.S. Department of Transportation, SRI International, Menlo Park, California.

19. Shockey, D. A., D. C. Erlich, and J. W. Simons (1999), "Lightweight fragment barriers for commercial aircraft," *Proceedings of 18th International Symposium on Ballistics,* 1192-1199.

20. Duan, Y., M. Keefe, T. A. Bogetti, and B. A. Cheeseman (2005), "Modeling the role of friction during ballistic impact of a high-strength plain-weave fabric," *Composite Structures,* 68(3), 331-337.

21. Duan, Y., M. Keefe, T. A. Bogetti, and B. A. Cheeseman (2005), "Modeling friction effects on the ballistic impact behavior of a single-ply

high-strength fabric," *International Journal of Impact Engineering*, 31(8), 996-1012.

22. Duan, Y., M. Keefe, T. A. Bogetti, B. A. Cheeseman, and B. Powers (2006), "A numerical investigation of the influence of friction on energy absorption by a high-strength fabric subjected to ballistic impact," *International Journal of Impact Engineering*, 32, 1299-1312.
23. Duan, Y., M. Keefe, T. A. Bogetti, and B. Powers (2006), "Finite element modeling of transverse impact on a ballistic fabric," *International Journal of Mechanical Sciences*, 48, 33-43.
24. Boisse, P., K. Buet, A. Gasser, and J. Launay (2001), "Meso/macro-mechanical behaviour of textile reinforcements for thin composites," *Composites Science and Technology*, 61(3), 395-401.
25. Boisse, P., B. Zouari, and A. Gasser (2005), "A mesoscopic approach for the simulation of woven fibre composite forming," *Composites Science and Technology*, 65, 429-436.
26. Gasser, A., P. Boisse, and S. Hanklar (2000), "Mechanical behaviour of dry fabric reinforcements. 3D simulations versus biaxial tests," *Computational Materials Science*, 17(1), 7-20.
27. Boisse, P., A. Gasser, and G. Hivet (2001), "Analyses of fabric tensile behaviour: Determination of the biaxial tension-strain surfaces and their use in forming simulations," *Composites - Part A: Applied Science and Manufacturing*, 32(10), 1395-1414.
28. Peng, X. and J. Cao (2002), "A dual homogenization and finite element approach for material characterization of textile composites," *Composites Part B: Engineering*, 33(1), 45-56.
29. Tabiei, A. and I. Ivanov (2002), "Computational micro-mechanical model of flexible woven fabric for finite element impact simulation," *International Journal for Numerical Methods in Engineering*, 53, 1259-1276.
30. Ivanov, I. and A. Tabiei (2004), "Loosely woven fabric model with viscoelastic crimped fibres for ballistic impact simulations," *International Journal for Numerical Methods in Engineering*, 61, 1565-1583.
31. King, M. J., P. Jearanaisilawong, and S. Socrate (2005), "A continuum constitutive model for the mechanical behavior of woven fabrics," *International Journal of Solids and Structures*, 42, 3867-3896.

32. King, M. J. (2003), "An energy-based constitutive model for the in-plane mechanical behaviour of woven fabrics," Master of Science Thesis, Massachusetts Institute of Technology.

33. King, M. J. and S. Socrate (2004), "A shell formulation to model the three-dimensional deformation response of woven fabrics," *Proceedings of IMECE 2004*, 1-10.

34. Lim, C. T., V. P. W. Shim, and Y. H. Ng (2003), "Finite element modeling of the ballistic impact of fabric armor," *International Journal of Impact Engineering*, 28, 13-31.

35. Brueggert, M. and Tanov R.R. (2001), "An LS-DYNA user defined material model for loosely woven fabric with non-orthogonal varying weft and warp," *Proceedings of 7th International LS-DYNA Users Conference*, 8-1-8-13.

36. Tanov R.R. and M. Brueggert (2003), "Finite element modeling of non-orthogonal loosely woven fabrics in advanced occupant restraint systems," *Finite Elements in Analysis and Design*, 39, 357-367.

37. Buet-Gautier, K. and P. Boisse (2001), "Experimental analysis and modeling of biaxial mechanical behavior of woven composite reinforcements," *Experimental Mechanics*, 41(3), 260-269.

38. Xue, P., J. Cao, and J. Chen (2005), "Integrated micro/macro-mechanical model of woven fabric composites under large deformation," *Composite Structures*, 70(1), 69-80.

39. Luo, S. Y. (2000),"Finite Elastic Deformation," Comprehensive Composite Materials, A. Kelly and C. Zweben, eds., Elsevier, 683-718.

40. Stubbs, N. (1989),"Elastic and inelastic response of coated fabrics to arbitrary loading paths," Textile Structural Composites, T. W. Chou and F. K. Ko, eds., Elsevier, 331-354.

41. Simons, J. W., D. C. Erlich, and D. A. Shockey (2001), "Finite element design model for ballistic response of woven fabrics," *Proceedings of 19th International Symposium on Ballistics*, 1415-1422.

42. Shahkarami, A., E. Cepus, I. Kongshavn, R. Vaziri, and A. Poursartip (2004), "Ballistic response of multi-layer fabrics," Final Report, Submitted to DuPont, DRDC-Valcartier and PSP.

43. "http://www.dupont.com/kevlar/whatiskevlar.html"

44. Van Wyk, C. M. (1946), "Notes on the compressibility of wool," *Journal of the Textile Institute*, 37, T285-T292.

45. Hoffman, R. M. and L. F. Beste (1951), "Some relations of fiber properties to fabric hand," *Textile Research Journal*, 21(2), 66-77.

46. Gutowski, T. G. (1985), "A resin flow/fiber deformation model for composites," *SAMPE Quarterly*, 16(4), 58-64.

47. Saunders, R. A., C. Lekakou, and M. G. Bader (1998), "Compression and microstructure of fibre plain woven cloths in the processing of polymer composites," *Composites: Part A*, 29A, 443-454.

48. Saunders, R. A., C. Lekakou, and M. G. Bader (1999), "Compression in the processing of polymer composites 1. A mechanical and microstructural study for different glass fabrics and resins," *Composites Science and Technology*, 59, 983-993.

49. Pearce, N. and J. Summerscales (1995), "The compressibility of a reinforced fabric," *Composites Manufacturing*, 6(1), 15-21.

50. Starratt, D., T. Sanders, E. Cepus, A. Poursartip, and R. Vaziri (2000), "An efficient method for continuous measurement of projectile motion in ballistic impact experiments," *International Journal of Impact Engineering*, 24(2), 155-170.

51. Cepus, E. (2003), "An experimental investigation of the early dynamic impact behaviour of textile armour systems: Decoupling material from system response," Ph.D. Thesis, The University of British Columbia.

52. Cook, R. D., D. S. Malkus, and M. E. Plesha (1989), Concepts and applications of finite element analysis, John Wiley & Sons.

53. Bathe, K. J. (1996), Finite element procedures, Prentice-Hall, Inc.

54. Hallquist, J. O. (2003), LS-DYNA Keyword User's Manual (Version 970), Livermore Software Technology Corporation.

55. Kawabata, S. (1989),"Nonlinear mechanics of woven and knitted materials," Textile Structural Composites, T. W. Chou and F. K. Ko, eds., Elsevier Science Pub. Co., 67-116.

56. Hallquist, J. O. (1998), LS-DYNA Theoretical Manual, Livermore Software Technology Corporation.

57. Kawabata, S., M. Niwa, and H. Kawai (1973), "The finite-deformation theory of plain-weave fabrics Part I: The biaxial-deformation theory," *Journal of the Textile Institute*, 64(2), 21-46.

58. Kawabata, S., M. Niwa, and H. Kawai (1973), "The finite-deformation theory of plain-weave fabrics Part II: The uniaxial-deformation theory," *Journal of the Textile Institute*, 64(2), 47-61.

59. Kawabata, S., M. Niwa, and H. Kawai (1973), "The finite deformation theory of plain-weave fabrics Part III: The shear-deformation theory," *Journal of the Textile Institute*, 64(2), 62-85.

60. Press, W. H., S. A. Teukolsky, W. T. Wetterling, and B. P. Flannery (1992), Numerical recipes in FORTRAN 77: The art of scientific computing, Cambridge University Press.

61. Wylie, C. R. and L. C. Barrett (1995), Advanced engineering mathematics, McGraw-Hill, Inc.

62. Prodromou, A. G. and J. Chen (1997), "On the relationship between shear angle and wrinkling of textile composite preforms," *Composites - Part A: Applied Science and Manufacturing*, 28(5), 491-503.

63. McBride, T. M. and J. Chen (1997), "Unit-cell geometry in plain-weave fabrics during shear deformations," *Composites Science and Technology*, 57(3), 345-351.

64. Belytschko, T. B., J. Lin, and C. S. Tsay (1984), "Explicit algorithms for nonlinear dynamics of shells," *Computational Methods in Applied Mechanical Engineering*, 42, 225-251.

65. Hughes, T. J. R. and W. K. Liu (1981), "Nonlinear finite element analysis of shells: Part I. Three-dimensional shells," *Computer Methods in Applied Mechanics and Engineering*, 26, 331-362.

66. Hughes, T. J. R. and W. K. Liu (1981), "Nonlinear finite element analysis of shells- Part II. Two-dimensional shells," *Computer Methods in Applied Mechanics and Engineering*, 27, 167-181.

67. Lebrun, G., M. N. Bureau, and J. Denault (2003), "Evaluation of bias-extension and picture-frame test methods for the measurement of intraply shear properties of PP/glass commingled fabrics," *Composite Structures*, 61(4), 341-352.

68. Lee, L., S. Rudov-Clark, A. P. Mouritz, M. K. Bannister, and I. Herszberg (2002), "Effect of weaving damage on the tensile properties of three-dimensional woven composites," *Composite Structures*, 57, 405-413.

69. Rudov-Clark, S., A. P. Mouritz, L. Lee, and M. K. Bannister (2003), "Fibre damage in the manufacture of advanced three-dimensional woven composites," *Composites: Part A*, 34, 963-970.

70. Roylance, D., P. Hammas, J. Ting, H. Chi, and B. Scott (1995), "Numerical Modeling of Fabric Impact," *Proceedings of High Strain Rate Effects on Polymer, Metal and Ceramic Matrix Composites and Other Advanced Materials*, 155-160.

71. Cunniff, P. M. (1999), "Decoupled response of textile body armor," *Proceedings of 18th International Symposium on Ballistics*, 814-821.

72. Lewis, E. A., I. Horsfall, and C. Watson (2006), "Pencilling: A novel behind armour blunt trauma injury," *Proceedings of 22nd International Symposium on Ballistics*, 1326-1332.

73. Lewis, E. A. (2005), "Pencilling: A novel behind armour blunt trauma injury," PhD Thesis, Cranfield University.

74. Chapman, S. J. (2000), MATLAB Programming for Engineering, Brooks/Cole Publishing Company.

75. Lomov, S. V., A. V. Gusakov, G. Huysmans, A. Prodromou, and I. Verpoest (2000), "Textile geometry preprocessor for meso-mechanical models of woven composites," *Composites Science and Technology*, 60, 2083-2095.

76. Brown, D., M. Morgan, and R. McIlhagger (2003), "A system for the automatic generation of solid models of woven structures," *Composites: Part A*, 34, 511-515.

APPENDIX A - 3D CROSSOVER MESH PRE-PROCESSOR

Creation of the finite element mesh of a physical model is one of the major steps in the mechanical analysis of any system. This task gets even more cumbersome when the geometries of the bodies studied are complicated. To create the unit-cell of a woven fabric, multiple trials of mesh generation might be needed due to the existing uncertainties on the accuracy of some input parameters. Availability of a specialized pre-processor to create the mesh of a fabric unit-cell would greatly facilitate the creation of a consistent F.E. mesh of a yarn crossover.

A finite element mesh pre-processor was developed that would create unit-cells of plain-weave fabrics. In developing the pre-processor, basic assumptions are derived from investigating cross-sectional micro-images of various fabric panels. The following sections highlight the findings from the micro-images and the basics of the 3D unit-cell pre-processor.

A.1 FABRIC CROSS-SECTIONAL MICRO-IMAGES

Geometrical properties of yarn in the woven fabric are one of the basic information needed to develop 3D models of fabric unit-cells. A yarn's

geometry and profile in a woven fabric is mainly influenced by its material properties and the weave architecture, as well as many other processing parameters. As a result, the final shape of yarns in the weave is a product of the above-mentioned factor and the interaction of the orthogonally woven yarns. The woven profile and configuration of the yarns in the weave was investigated by optical microscopy of fabric samples. This section discusses the highlights of the procedure and the results obtained from imaging the cross-sections of various plain-weave fabrics of Kevlar® 129.

In order to obtain images of the fabric cross-section, 4cm by 4cm squares of fabric were cut from the fabrics and submerged in a translucent araldite epoxy resin [42]. After the resin cured, the samples were sectioned parallel to the warp and weft directions, exposing the cross-section of the woven fabric. Images of the weave architecture and yarn profiles were then obtained by observing the samples in a Wilde™ dissecting microscope. A sample of the warp and weft images obtained for the S-728 fabric is presented in Figure A - 1.

The digital images obtained from the optical microscope were analysed and various parameters such as crimp and relative position of the yarns were measured, as seen in Figure A - 2. The dimensions measured on the micro-images are summarized in Table A - 1. From the geometrical values measured, many fabric and weave properties such as yarn crimp, thread count, and void content of the yarns can be estimated using the fabric cross-sectional micro-images.

The yarn crimp and void ratios determined from the micro-images are provided in Table A - 2. The crimp values obtained from the micro-images

appeared generally to have a larger value than the hand measured ones. This discrepancy was related to the facts that the yarn crimp in the images might have altered during cutting and handling of fabric samples, or may reflect local effects. The yarns may have also absorbed some liquid during the potting procedure, further changing the yarn crimp observed in the images.

The void content of the yarn was calculated using the cross-sectional area of the yarn (A_T) measured from image analysis compared the total theoretical solid area of the fibres in the yarn (A_f) obtained from the yarn linear density. The yarn's initial void is thus calculated from the following equation:

$$Void = \frac{A_T - A_f}{A_T} - 1 \qquad \text{(A - 1)}$$

The void ratios calculated show a surprisingly high level of void in the yarns (57% to 71.5%) leading to the suspicion that the yarns might have absorbed some liquid during the potting process.

An important observation in the micro-images was the presence of yarn overlay. As seen in Figure A - 3, the fibres in the yarns tend to spread apart at the centre of each crossover point, thus overlaying their adjacent yarns. This leads in to a non-uniform yarn cross-section and is mostly observed in the panel direction with low crimp value.

However, despite all the discrepancies observed, the micro-images of fabric cross-section provide invaluable qualitative information on the yarn shapes and profiles in the woven fabric. This information was used to establish the

basis for the generation of the F.E. mesh of the yarn crossovers and development of the pre-processor, as presented in the following section.

The location of the cut is usually aligned with the centerline of a warp or weft yarn. However, there is usually some error involved with the sectioning process. Depending on the normal distance of the cutting line from the yarn centreline, the thickness yarn profile visible in the image, as well as the cross-sectional dimensions and their alignment gets affected. The change in the profile thickness and yarn alignment is clearly evident in Figure A - 4, where the cutting plane makes an angle with the warp yarn.

A.2 FINITE ELEMENT UNIT-CELL MESH PRE-PROCESSOR

A pre-processor was developed in MATLAB [74] environment to create the geometry and F.E. meshes of plain-weave fabric unit-cells, later used to analyse the biaxial response of fabrics. As mentioned earlier, the pre-processor takes advantage of the findings from the cross-sectional micro-images to approximate the shape of the yarns in the fabric.

There have been several studies on developing pre-processors to create the profile of yarns in a certain fabric weave structure. Lomov et al. [75] presented a pre-processor named CETKA (meaning net in Russian) that is capable of predicting the yarn profile in complex 3-dimensional weave patterns. The algorithm is later further developed to become the foundation for a commercially available pre-processor called WISETEX. The fabric topography is described and the equilibrium of yarns in the weave is satisfied through mathematical representation of warp/weft interaction in a fabric. Mechanical model are thus developed for plain fabric and textile composite unit-cell. This

pre-processor is capable of creating models of highly complex weave structure, requiring a wealth of yarn and fabric information, some of which might not be easily obtainable.

Brown et al. [76] also developed a pre-processor that generates solid models of fabrics. The aim of Brown's study was to provide a system to generate solid models of the woven fabric and extract geometric data from it to optimize the architecture of the fabric composite reinforcement. The options considered for the cross-sectional shape and yarn profile are discussed, leading to the utilization of sinusoidal shape functions.

The cross-sectional micro-images of the fabric cross-sections were used to set the framework for the pre-processor development. Qualitatively, it can be concluded that the yarn profiles can be realistically represented by sinusoidal functions. The yarn cross-sections appeared to be either elliptical or sine-based. It was also observed that the yarn cross-section may change along the yarn, depending on the interaction between the crossing yarns. This change can be so sever that lead to the yarn overlay, as discussed earlier.

The input data used in the pro-processor are the fabric and yarn geometrical parameters obtained from the laboratory measurements. Figure A - 5 shows a general overview of the process of creating a single yarn crossover. The first action undertaken by the pre-processor is to calculate the cross-section and profile of the yarns from the input values provided. The profile created is then discretized and intermediate cross-sections are generated along the yarn, paving the way to the addition of solid elements and generation of the fabric unit-cell.

Several simplifying assumptions are made in order to create the finite element mesh of the yarns that closely match the observations from the cross-sectional micro-images. The basic assumptions are listed below:

- Yarn profiles are considered to be best represented by a sine function.
- Yarn cross-sections are considered to be elliptical, or sine-shaped.
- Yarn cross-sections (perpendicular to its centerline) stay constant along the yarn (i.e. no yarn overlay).

The yarn profile (see Figure A - 6) is defined by the following function:

$$z = a_2 \sin(b_2 x)$$

Parameter b_2 is calculated from setting the period of the sine function equal to the axis-to-axis distance of two adjacent yarns in the perpendicular direction (unit-cell length), w_2, as follows:

$$b_2 = \frac{\pi}{w_2}$$

w_2 is directly calculated from the yarn count number. The amplitude of the sine function, a_2, is a function of the crimped length of the yarn, S_{cr}. The length of the sine curve is set equal to the yarn crimped length, as follows:

$$S_{cr} = \int_0^{w_2} \sqrt{1 + (a_2 b_2)^2 \cos^2(b_2 x)}\, dx$$

Two options are considered for the yarn cross-section: sinusoidal and elliptical (Figure A - 7).

In both cases, the width of the yarn, a_1, is determined from the unit-cell width, w_1, and the gap between parallel yarns, g_1:

$$a_1 = w_1 - g_1$$

b_1 is determined from the yarn area considerations, such that the voided area of the yarn does not interpenetrate the geometry of the crossing yarn.

Figure A - 8 depicts the process of producing the F.E. mesh of a fabric unit-cell and all its components. Basically, the 3D model of the fabric crossover is comprised of 3-D solid (brick) elements. A set of input referred to as "control input data" specifies the additional components to be included in the unit-cell model. The user-controlled options are the addition of linear bar elements to represent the axial stiffness of the yarns, and shell elements to the yarn ends. The user can also choose to create a unit-cell model that includes one or four crossovers of plain weave fabrics. The pre-processor provides node and element data in formats recognizable by either LS-DYNA or ABAQUS commercial finite element codes. The first step in creating the unit-cell mesh is to create the geometry of the yarns through calling the subroutine that locates the nodes defining the volume of the yarns. The pre-processor then proceeds with filling the volume of the yarns with solid elements. If prompted by the user, the linear beams and yarn-end shell elements are added to the yarn in the next step. In the final step, the yarns are plotted for visual inspection by the user and the input files are created.

One important characteristic of every finite element mesh is the element size. The pre-processor would automatically calculate the element size if prompted,

or would use some user-defined values to create the F.E. mesh of the fabric unit-cell. The node numbering is designed such that the elements' local 2-direction is aligned with the yarn's axial direction. Nodes located at the yarn ends are grouped in node-sets and are utilized to define the yarn motion in the finite element analysis.

The geometrical information obtained from the study of cross-sectional micro-images of all fabric panels are used to create finite element meshes of their unit-cells. One of such unit-cells is presented in Figure A - 9, where the micro-image of the warp cross-section of S-720G fabric is compared with the finite element mesh created using information obtained from the micro-images. It can be seen that the finite element mesh generated match the yarn profile and cross-section seen in the actual micro-image.

Table A - 1: Fabric and weave parameters obtained from the micro-images (data provided by Kongshavn [42]).

Panel	Direction	Yarn Width (mm)	Yarn Thickness (mm)	Crossing Yarn's Thickness (mm)	Total Thickness (mm)	Threads (per mm)
720	warp	1.37	0.32	0.19	0.51	0.78
	weft	1.23	0.33	0.14	0.47	0.78
726	warp	1.08	0.19	0.14	0.33	1.05
	weft	0.95	0.30	0.10	0.40	1.03
727	warp	1.18	0.28	0.12	0.40	0.99
	weft	0.92	0.29	0.13	0.42	1.02
728	warp	1.49	0.33	0.13	0.46	0.64
	weft	1.64	0.32	0.10	0.42	0.69
731	warp	0.98	0.27	0.15	0.42	1.22
	weft	0.74	0.33	0.14	0.47	1.50
745	warp	1.80	0.55	0.11	0.66	0.68
	weft	1.43	0.59	0.17	0.76	0.60

Table A - 2: Yarn crimp values and void ratios calculated from the micro-images (data provided by Kongshavn [42]).

Panels	Direction	Crimp (%)	Void Ratio (%)
720	warp	3.21	63.9
	weft	2.68	60.4
7265	warp	4.21	57.5
	weft	1.48	64.9
7272	warp	2.04	70.3
	weft	2.13	61.0
728	warp	3.05	65.3
	weft	2.70	69.3
731	warp	9.90	63.5
	weft	3.04	54.1
745	warp	10.16	70.0
	weft	2.68	63.2

Table A - 3: Material and geometrical properties input to the pre-processor for S-720G.

Property	Warp	Weft
Yarn (denier)	1420	1420
Count (tpi)	20	20
Crimp (%)	3.21	2.68
Cross-section	Sine	Sine

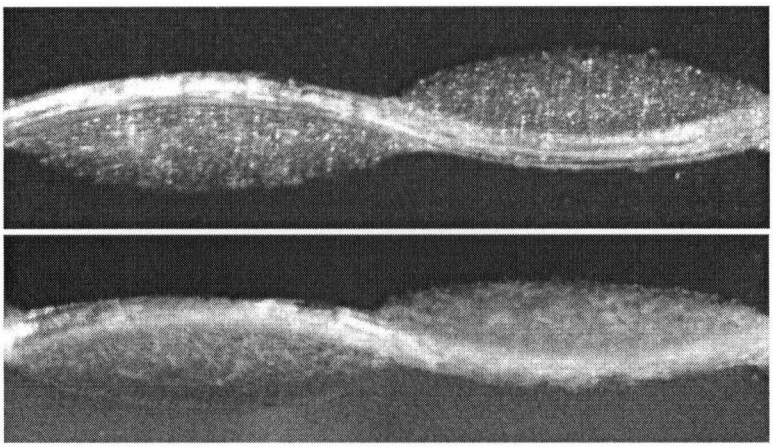

Figure A - 1: Cross-sectional micro-images of S-728 panel (top: warp, bottom: weft) [42].

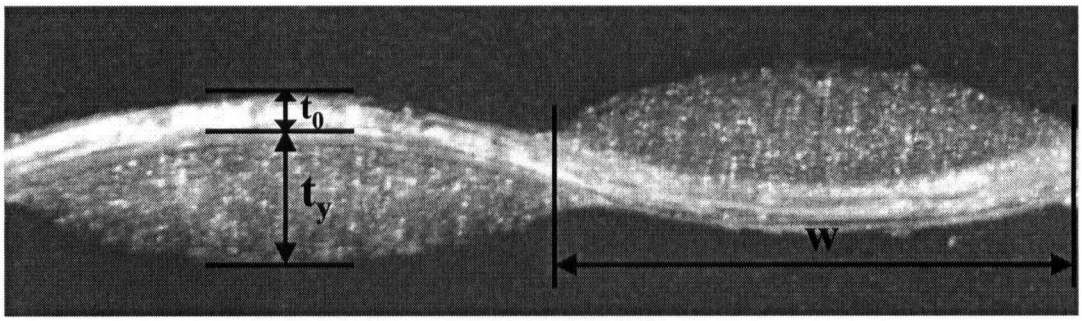

Figure A - 2: Measurement of various dimensions on the micro-images of S-728 (warp) panels [42].

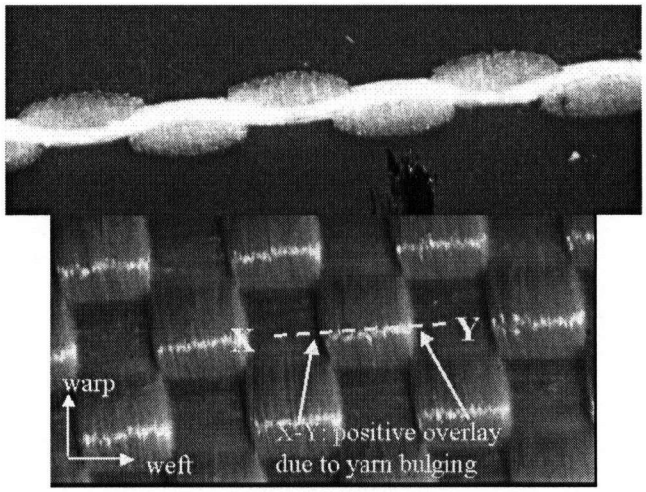

Figure A - 3: Yarn overlay in fabric S-731; cross-section (top) and plan view (bottom) [42].

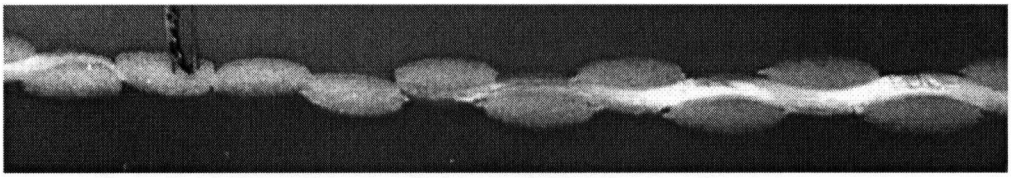

Figure A - 4: Micro-image of the S-731 fabric cross-section, cut at an angle [42].

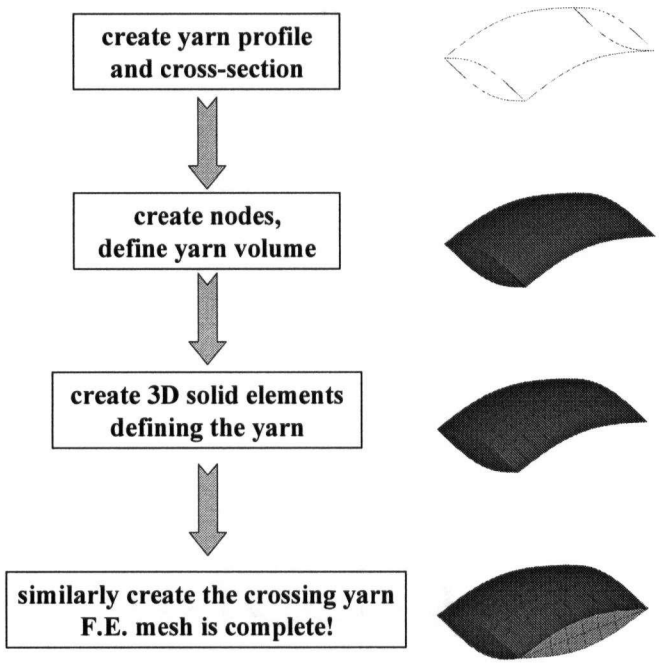

Figure A - 5: Process of creating a single yarn crossover in the pre-processor.

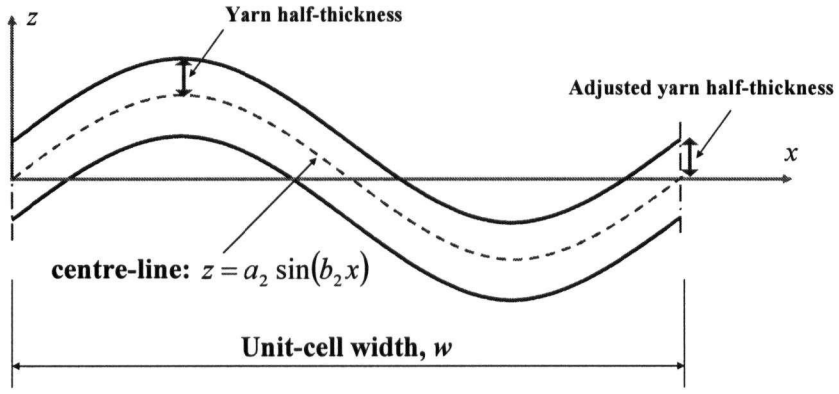

Figure A - 6: Sinusoidal yarn profile used to create the yarn centreline in the mesh pre-processor.

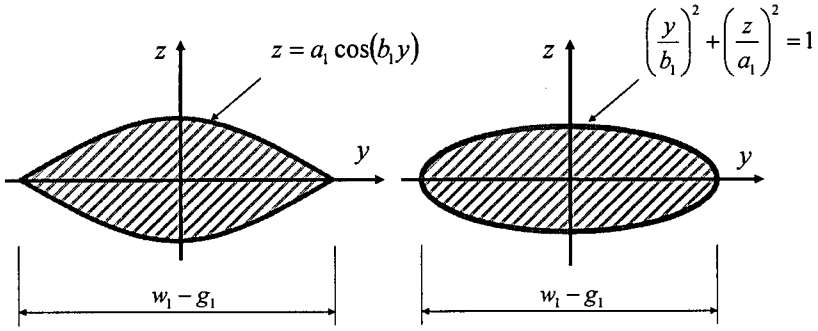

Figure A - 7: Sine-based (left) or elliptical (right) cross-section definition of yarns.

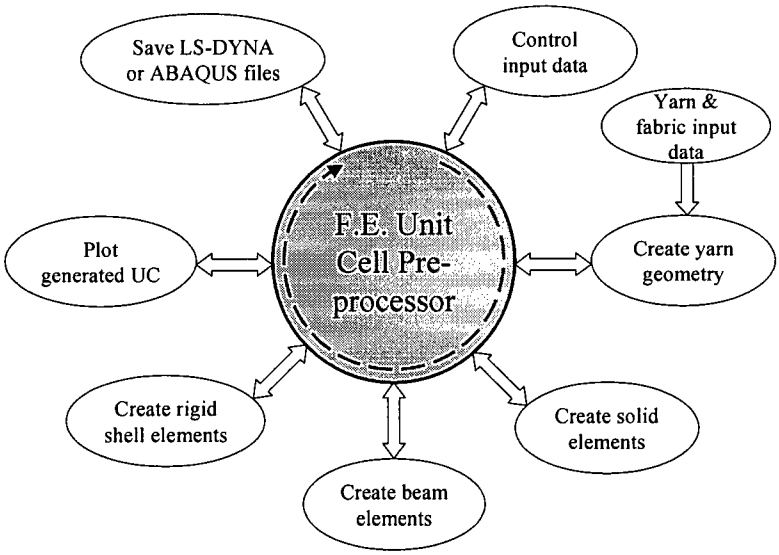

Figure A - 8: Process of generating the F.E. mesh of a fabric unit-cell.

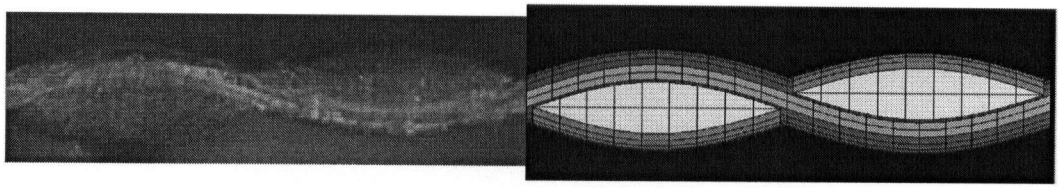

Figure A - 9: Cross-sectional micro-image of S-720 weft fabric compared to the generated finite element mesh.

APPENDIX B - PSEUDO-CODES

The following sections present the algorithms that are implemented in the User Material Models of LS-DYNA for beams and solids of the 3D fabric crossover model and the shells of the 2D shell crossover model.

B.1 BEAM ELEMENT

1. **Read** the current strain rates, $\underline{\Delta\varepsilon}^n$, **calculate** the total strains $\underline{\varepsilon}^n = \underline{\varepsilon}^{n-1} + \underline{\Delta\varepsilon}^n$.

2. Check the failure of the beams: **if** $\varepsilon_1^n \geq \varepsilon_f$ **then** erode the element.

3. **Calculate** the axial stress component using a viscoelastic constitutive model: $\sigma_1^n = \sigma_1^{n-1} + E\Delta\varepsilon_1 + \mu\sqrt{E\rho l}\dfrac{\Delta\varepsilon_1}{\Delta t}$, where μ is the viscosity coefficient.

4. Eliminate axial compression: **if** $\sigma_1^n \leq 0$ **then** $\sigma_1^n = R_c \times \sigma_1^n$ where R_c is the compression reduction factor.

5. Include yarn crimp: **if** $\varepsilon_1^n \leq \varepsilon_{cr}$ **then** $\sigma_1^n = 0.01 \times \sigma_1^n$.

6. **Calculate** shear components: $\sigma_i^n = \sigma_i^{n-1} + R_s \times \Delta\varepsilon_i^n$ where $i = 4, 6$.

7. The updated stress tensor is **returned** to LS-DYNA to continue the analysis.

B.2 SOLID ELEMENT

1. **Read** the current strain rates, $\underline{\Delta\varepsilon}^n$, **calculate** the total strains $\underline{\varepsilon}^n = \underline{\varepsilon}^{n-1} + \underline{\Delta\varepsilon}^n$.

2. **Call** the deformation gradient subroutine, **read** $\underline{F}^n$ and **calculate** the Jacobian $J^n = \left|\underline{F}^n\right|$.

3. **Calculate** average cross-sectional change in the 1-3 plane (2-dir aligned with the yarn axis) by $\Delta A = \dfrac{J^n}{\exp\left(\varepsilon_2{}^n\right)}$.

4. **Calculate** the current fibre volume fraction: $V_f{}^n = \dfrac{V_f{}^0}{\Delta A}$.

5. **Calculate** the elastic modulus in the yarn axis direction (2-dir): if $\varepsilon_2{}^n \geq 0$ then $E_2 = R_c E_f V_f{}^n$ else $E_2 = E_f V_f{}^n$.

6. **Calculate** the transverse elastic modulus: if $V_f{}^n \leq V_f{}^0$ (transverse yarn expansion) then $E_1 = R_T E_c$ where R_T is a reduction factor. Else $E_1 = \dfrac{a}{b - V_f{}^n}$. Set $E_3 = E_1$.

7. **Calculate** the stress tensor: $\sigma_i{}^n = E_i \varepsilon_i{}^n$ where $i = 1...6$ (shear moduli E_4, E_5, and E_6 inputted by the user).

8. The updated stress tensor is **returned** to LS-DYNA to continue the analysis.

B.3 SHELL ELEMENT

1. **Read** the current strain rates (increments), $\underline{\Delta\varepsilon}^n = \begin{bmatrix} \Delta\varepsilon_x{}^n & \Delta\gamma^n \\ 0 & \Delta\varepsilon_y{}^n \end{bmatrix}$.

2. **Read** the material coordinates (warp and weft vectors, $\underline{q_i}^{n-1} = \begin{bmatrix} q_{i_x}{}^{n-1} & q_{i_y}{}^{n-1} \end{bmatrix}^T$) from the history variables.

3. **Calculate** the incremental deformation gradient from $\underline{F}^n = \underline{I} + \underline{\Delta\varepsilon}^n = \begin{bmatrix} 1+\Delta\varepsilon_x{}^n & \Delta\gamma^n \\ 0 & 1+\Delta\varepsilon_y{}^n \end{bmatrix}$.

4. **Update** the location of the warp and weft vectors by $\underline{q_i}^n = \underline{F}^n \underline{q_i}^{n-1}$.

5. **Calculate** the transformation matrix $\underline{\Theta_i}^n = \begin{bmatrix} \cos\theta_i{}^n & \sin\theta_i{}^n \\ -\sin\theta_i{}^n & \cos\theta_i{}^n \end{bmatrix}$, where $\theta_i^n = \tan^{-1}\left(\frac{q_{i_x}{}^n}{q_{i_y}{}^n}\right)$ and $i = 1,2$ represents the warp and weft directions.

6. **Calculate** the strain tensor transformed to the warp or weft direction $\underline{\Delta\varepsilon_i}^n = \underline{\Theta_i}^n \underline{\Delta\varepsilon}^n \underline{\Theta_i}^{nT}$.

7. **Calculate** the incremental stretch along each yarn from $\lambda_i^n = \sqrt{1+2\Delta\varepsilon_{i1}^n} \approx 1+\Delta\varepsilon_{i1}^n$, where $\Delta\varepsilon_{i1}^n$ is the transformed strain tensor component in the yarn direction.

8. **Calculate** the total stretch of each yarn by $\Lambda_i^n = \Lambda_i^{n-1}\lambda_i^n$, where Λ_i^{n-1} is obtained from the history variables.

9. **Calculate** the unit-cell displacement along each yarn from $d_i^n = (\Lambda_i^n - 1)w_{0i}$, where w_{0i} is the initial half-length of the unit–cell.

10. **Read** the range of d_i^n for which the iterations should be performed. **If** d_i^n out of the specified range **then** $F_{c_i}{}^n = 0$ (indicating the absence of contact between the yarns) and **go to** line 25 (bypass the iterations).

11. **If** any of the two yarns have previously failed **then** determine the tension in the other yarn from the single yarn response ($T_i = \frac{E_i A_i}{S_{0i}}(w_i - S_{0i})$ if $w_i > S_{0i}$, else $T_i = 0$) and **go to** line 25 (skip the iterations).

12. Set up the Newton-Raphson iterative scheme. **Set** initial values of h_i.

13. **Start loop** over *iter*, **Calculate** the current yarns lengths from $S_i = 2\int_0^{w_i}\sqrt{1+\left(\frac{\pi h_i}{2w_i}\right)^2 \sin^2\left(\frac{\pi}{2w_i}x\right)}dx$ and its derivative $\frac{dS_i}{dh_i}$.

14. **Calculate** the yarns tensile force from $T_i = \frac{E_i A_i}{S_{0i}}(S_i - S_{0i})$.

15. **Calculate** the yarn angle with the fabric plane at the edges of the unit cell from $\sin\alpha_i = \frac{\pi h_i}{\sqrt{(2w_i)^2 + (\pi h_i)^2}}$.

16. **Calculate** the yarn contact force, $F_{c_i} = 2T_i \sin\alpha_i$.

17. **Calculate** the transverse yarn compression, $d_{c_i} = a - \frac{b}{\sqrt[3]{F_{c_i}}}$.

18. **Calculate** the equilibrium objective function, $f_1 = F_{c_1} - F_{c_2}$.

19. **Calculate** the compatibility objective function, $f_2 = h_1 + h_2 + d_{c_1} + d_{c_2} + g - h_{01} - h_{02}$.

20. **Calculate** tolerance value for each objective function: $Tol_1 = K_{tol} \times |F_{c_1} + F_{c_2}|$ and $Tol_2 = K_{tol} \times |h_1 + h_2|$, where $K_{tol} = 0.001$ in this study.

21. Check the solution convergence criteria. **If** $f_1 < Tol_1$ and $f_2 < Tol_2$ **then** (convergence is achieved) **go to** line 25.

22. **Else** (convergence not satisfied) **calculate** the h_i correction values, $\underline{dh} = \underline{J} \times \underline{f}$ where $\underline{J} = \begin{bmatrix} \frac{\partial f_1}{\partial h_1} & \frac{\partial f_1}{\partial h_2} \\ \frac{\partial f_2}{\partial h_1} & \frac{\partial f_2}{\partial h_2} \end{bmatrix}$ and $\underline{f} = \begin{bmatrix} f_1 \\ f_2 \end{bmatrix}$.

23. **Calculate** new h_i using $\underline{h} = \underline{h} - \underline{dh}$.

24. **Go to** 13.

25. Check for contact between the yarns. **If** contact force between the yarns are negative (i.e. $F_{c_i} \le 0$) **then** calculate the single yarn response ($T_i = \frac{E_i A_i}{S_{0i}}(w_i - S_{0i})$ if $w_i > S_{0i}$, else $T_i = 0$).

26. Check for yarn failure. **If** $T_i > Tu_i$ **then** $T_i = 0$ and flag the yarn failed.

27. **If** both yarns have failed **then** erode the shell element from the mesh.

28. **Calculate** the stress tensor for each yarn using $\underline{\sigma_i}^n = \begin{bmatrix} \frac{T_i}{A_i} & 0 \\ 0 & 0 \end{bmatrix}$.

29. **Transform** the stress tensors back to the shell local coordinate system: $\underline{\bar{\sigma}_i}^n = \underline{\Theta_i}^T \underline{\sigma_i}^n \underline{\Theta_i}$.

30. **Calculate** the average stress tensor: $\underline{\sigma_{avg}}^n = \frac{\underline{\bar{\sigma}_1}^n + \underline{\bar{\sigma}_2}^n}{2} = \begin{bmatrix} \sigma_{avg_1}^n & \sigma_{avg_{12}}^n \\ 0 & \sigma_{avg_2}^n \end{bmatrix}$

31. **Calculate** the shear component from the trellis mechanism and add it to the in-plane shear stress. The trellis shear component (Equation 4-35) as a function of the shear strain, γ^n, (where $\gamma^n = \gamma^{n-1} + \Delta\gamma^n$) is:

    If $|\gamma^n| < \gamma_1$ **then** $\tau_{12}^n = \tau_{12}^{n-1} + G_1\gamma^n$,

    else if $\gamma_1 < |\gamma^n| < \gamma_2$ **then** $\tau_{12}^n = \tau_{12}^{n-1} + G_1\gamma^n + \frac{G_2 - G_1}{\gamma_2 - \gamma_1}\frac{(\gamma^n - \gamma_1)^2}{2}$,

else $\tau_{12}{}^{n} = \tau_{12}{}^{n-1} + G_2\gamma^{n} + (G_1 - G_2)\dfrac{\gamma_1 + \gamma_2}{2}$.

32. The updated stress tensor $\underline{\sigma}^{n} = \begin{bmatrix} \sigma_{avg_1}{}^{n} & \sigma_{avg_{12}}{}^{n} + \tau_{12}{}^{n} \\ 0 & \sigma_{avg_2}{}^{n} \end{bmatrix}$ is **returned** to LS-DYNA to continue the analysis.